Defects in strongly correlated and spin-orbit entangled quantum matter

Dissertation

Michael Becker

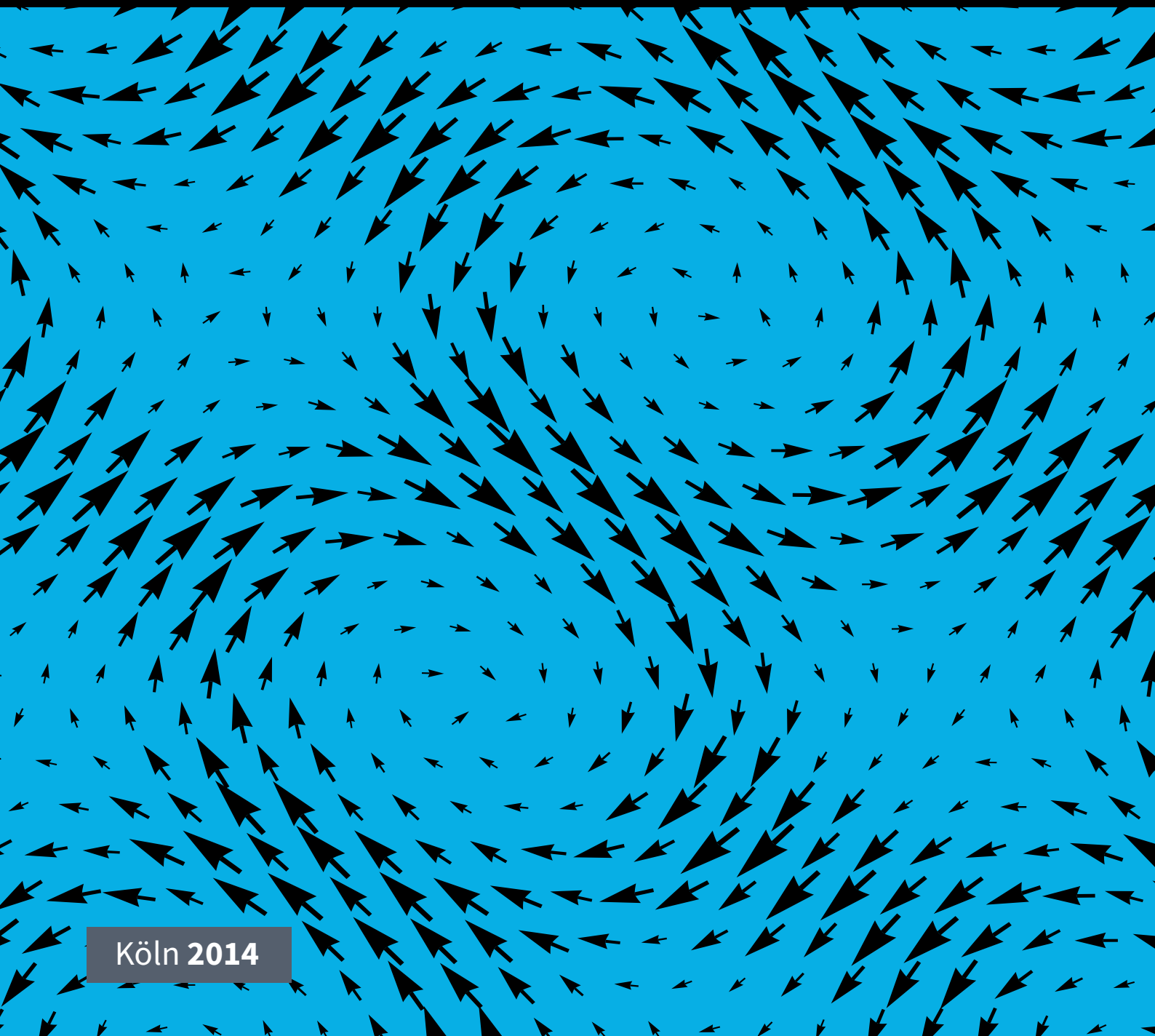

Köln **2014**

Defects in strongly correlated and spin-orbit entangled quantum matter

Inaugural-Dissertation

zur

Erlangung des Doktorgrades

der Mathematisch-Naturwissenschaftlichen Fakultät

der Universität zu Köln

vorgelegt von

Michael Becker

aus Bendorf

Köln 2014

Berichterstatter: Prof. Dr. Simon Trebst

Priv.-Doz. Dr. Ralf Bulla

Tag der mündlichen Prüfung: 26. 11. 2014

Abstract

The inherent complexity of interacting quantum many-body systems poses an outstanding challenge to both theory and experiment. Especially in the presence of strong electronic correlations, highly interesting and perplexing physical phenomena can occur.

In this thesis, we focus on three different examples of strongly correlated electron systems in which different types of defects occur. First, we investigate the Heisenberg-Kitaev model formulated on a triangular lattice. Using a mixture of numerical and analytical techniques we map out the entire phase diagram for the classical and quantum models. We provide an analytical foundation to the intriguing $\mathbb{Z}_2$-vortex ground state, in which strong spin-orbit coupling leads to the formation of a lattice of topological point defects. This state was observed previously in classical Monte Carlo simulations. We furthermore propose the iridate $Ba_3IrTi_2O_9$ to be a prime candidate for the realization of such a state.

The second part deals with the physics of a defect in the form of a localized magnetic moment which is embedded into a metallic environment: the Kondo effect. Although this effect has been a cornerstone of condensed matter physics for more than 50 years, its properties in real-space are still not fully understood. What is the Kondo screening cloud—the extended many-body state of entangled conduction electrons? We present numerical results in 1D and 2D for the charge density oscillations created by the impurity. We find that the entire RG flow of the problem is recovered in these oscillations, elucidating the internal structure of the screening cloud.

Finally, we investigate the competition between the Kondo effect and Majorana physics. Majorana bound states are highly interesting objects which exhibit unusual statistics and could be used as a building block of a topological quantum computer. Recently, signatures of their existence were observed in experiment, and we here examine how Kondo physics (which might play a role in real systems) interact with such Majorana bound states.

Kurzzusammenfassung

Die Komplexität wechselwirkender Quanten-Vielteilchensysteme stellt eine enorme Herausforderung sowohl für Theorie als auch für Experimente dar. Insbesondere in Systemen von stark wechselwirkenden Elektronen können ungewöhnliche neue physikalische Phänomene auftreten.

In dieser Arbeit betrachten wir drei unterschiedliche Beispiele solcher stark korrelierter Systeme, in denen jeweils verschiedene Arten von Defekten auftreten. Als erstes widmen wir uns dem Heisenberg-Kitaev-Modell, formuliert auf dem Dreiecksgitter. Mit numerischen und analytischen Methoden sind wir in der Lage, das vollständige Phasendiagramm zu untersuchen, sowohl für das klassische als auch das quantenmechanische Modell. Wir liefern eine analytische Grundlage für den $\mathbb{Z}_2$-Vortex-Zustand, in welchem starke Spin-Bahn-Wechselwirkung dazu führt, dass sich ein Gitter aus topologischen Punktdefekten aufbaut. Dieser Zustand wurde kürzlich das ersten Mal in klassischen Monte-Carlo-Simulationen beobachtet. Wir schlagen vor, dass solch ein Zustand in dem Übergangsmetalloxid $Ba_3IrTi_2O_9$ existieren könnte.

Im zweiten Teil widmen wir uns der Physik eines Defektes in Form eines an eine metallische Umgebung gekoppelten lokalen magnetischen Moments: dem Kondo-Effekt. Dieser Effekt ist seit seiner Beschreibung vor über 50 Jahren ein Grundpfeiler der Festkörperphysik. Dennoch wird die dazugehörige Physik im Ortsraum weiterhin kontrovers diskutiert. Was genau ist die Kondo-Screening-Cloud – der örtlich ausgedehnte, verschränkte Zustand zwischen magnetischem Moment und Leitungsband-Elektronen? Wir präsentieren numerische Resultate für Ladungsdichte-Oszillationen in 1D und 2D, in denen wir den gesamten Renormierungsgruppenfluss des Problems wiederfinden. Damit können wir Aussagen über die innere Struktur der Screening-Cloud tätigen.

Schließlich beschäftigen wir uns mit der Frage, wie der Kondoeffekt mit der Majoranaphysik konkurriert. Gebundene Majoranazustände sind hochinteressante Objekte mit ungewöhnlicher Statistik, die als mögliche Bausteine eines topologischen Quantencomputers in Frage kommen. In 2012 konnten experimentell überzeugende Hinweise auf deren Existenz nachgewiesen werden. Wir betrachten den Einfluss des Kondoeffekts, welcher im experimentellen Aufbau eine Rolle spielen könnte, auf solche Majoranazustände.

Contents

Chapter 1.

Introduction

Condensed matter systems with strong electronic correlations have brought forth some of the most remarkable physics of the last decades. From the Kondo effect, in which a single localized magnetic degree of freedom forms an entangled state with conduction electrons in its vicinity, to the physics of Mott insulators, where the strong Coulomb repulsion pins electrons down thereby suppressing charge transport, to spin liquids, an exotic quantum state that shows no magnetic order even at zero temperature.

Given the fact that already the Helium atom, the second-simplest element, does not allow a closed analytical solution, it is truly fascinating that physicists have been able to successfully describe and understand condensed matter systems comprised of *exponentially many*, much more complicated constituents. In these many-body systems, the individual constituents can conspire to create entirely new, *emergent* phenomena [1], such as fractional charges [2], heavy fermions [3], non-abelian anyons [4], or the still somewhat mysterious high-T_c superconductors [5]. Such physics *cannot* be understood constructively from looking at a single component of the system as they are true many-body effects.

Whereas some of these systems, such as topological insulators [6] or Majorana edge states [7], can be well-described in terms of non- or weakly-interacting theories, in many other cases the strong interactions cannot be neglected. In fact, in these cases they are crucial for the occurrence of novel physics. A remarkable example is given by the physics of the so-called Mott insulators. The electrons in crystalline materials can typically travel through the system by "hopping" from one lattice site to the next. Under certain circumstances, however, the strong Coulomb repulsion forbids two electrons to be on the same lattice site at a time, thereby effectively pinning electrons down and suppressing charge transport, and the only remaining degree of freedom is the magnetic moment of the electron's spin. These localized magnetic degrees of freedom can display a broad variety of vastly different behavior, being either magnetically ordered in a broken-symmetry state, or completely fluctuating even at zero temperature; a spin liquid state in which *no* symmetry is broken. Materials and phenomena which exhibit such physics are currently one of the central research topics of both experimentalists and theorists. While this great interest was spurred strongly by the discovery of high-T_c superconductivity in which electron correlations play an important role [8], numerous other fascinating and novel phenomena can occur in strongly correlated systems, with a multitude of possible applications in devices such as superconducting magnets or even quantum computers.

In part one of this thesis we introduce a selection of models of strongly correlated systems that play a major part in the remainder of the text. Already in the simplest case of a single localized magnetic degree of freedom, historically termed an "impurity", the highly non-trivial Kondo effect manifests: below a characteristic temperature scale, a complex many-body singlet forms and the magnetic degree of freedom is screened. This effect has witnessed a revival in the last years due to the advent of nano-scale devices such as quantum dots, allowing for accurate control of the relevant parameters and new possible

applications of Kondo physics [9]. We present the Anderson impurity model and discuss how it leads to local moment formation and the low energy Kondo physics. Focusing then on the Mott insulators mentioned above, we present the infamous Hubbard model, a deceptively simple Hamiltonian which at present is far from fully understood [8]. Considering the limit of a strong Coulomb interaction, we find the Heisenberg Hamiltonian, an effective model of the spin degrees of freedom. Finally, incorporating orbital ordering effects, we discuss a similar model with anisotropic exchange interaction: the Kitaev model.

We then present the two numerical techniques we used extensively for the results in this thesis: the numerical renormalization group (NRG) and the density matrix renormalization group (DMRG). The former was devised by Kenneth Wilson in 1975 [10] and to this day is the weapon of choice for impurity problems. Almost two decades later, Steve White invented the DMRG in 1992 [11], where based on Wilson's NRG he formulated an algorithm to calculate ground state properties of generic lattice Hamiltonians in 1D. Although both methods are typically used in very different contexts, they are born from the same ideas and can thus be considered from a common point of view.

Part two considers a model comprised of both Heisenberg and Kitaev terms, formulated on the triangular lattice. We discuss how in certain transition metal oxides strong spin-orbit coupling leads to a formation of a state characterized by effective $j = 1/2$ degrees of freedom. Furthermore, in some of these materials, the specific exchange interaction between these degrees of freedom might be described in terms of the Heisenberg-Kitaev model. Whereas the honeycomb version of this model has been subject of great theoretical and experimental discourse, we here focus on the triangular lattice. Thus far, only results for the classical model are known [12, 13], most of them numerical. We present a thorough analysis of the entire phase diagram, including analytical and numerical approaches for both the classical *and* quantum case.

In part three, we turn our focus to the Kondo effect. Although it has been one of the arguably most researched condensed matter topics of the 20th century [9], its real-space physics is still discussed controversially. In a broad parameter regime, an Anderson impurity behaves partly like a potential scatterer. This scattering induces static charge density oscillations around the impurity, known as Friedel oscillations [14]. Building on previous findings [15], we present numerical results for the Friedel oscillations in which we recover the full renormalization group flow of the impurity problem, allowing for a detailed analysis of the structure of the notorious Kondo screening cloud — the quantum many-body singlet thought to be exponentially far extended in real-space.

The fourth and final part investigates the interplay between Kondo physics and Majorana bound states at the edges of quantum wires. Majorana fermions are exotic particles which are their own anti-particles. While they are conjectured to exist as possible high-energy particles, it has become clear that they might also occur in the form of quasiparticle excitations in condensed matter systems. In fact, in a seminal experiment, signatures in transport measurements of so-called Kitaev wires have strongly indicated the existence of Majorana bound states in these systems [16]. Although the evidence is compelling, several factors might influence the results, among them disorder and the Kondo effect. Thus, these side effects must be ruled out to achieve an unambiguous detection of Majorana modes. We consider the interplay of Kondo and Majorana physics in an experimentally relevant setup, and show that in the experimentally relevant regimes the low-energy physics is indeed dominated by the Majorana bound state.

Part I.

Models and numerical methods

Chapter 2.

Models of strongly correlated electrons

In a typical solid the intricate subtleties of quantum mechanics are combined with a vast number of $\sim 10^{23}$ particles. Since these particles interact in various ways, an exact microscopic description of such materials seems intractable. However, it turns out that a large number of materials have properties that are comparatively insensitive to the Coulomb repulsion between electrons. In these cases, theories such as Fermi liquid theory, in which electrons are replaced by quasi-particles emerging from collective excitations, provide a remarkably good description of the low-temperature physics. In fact, many of the most intensively studied phenomena in condensed matter physics in recent years can be described to a significant degree in terms of non- or weakly-interacting models: among them are topological insulators and superconductors [6], Majorana fermions in 1D wires [7], and graphene [17].

However, in many materials the correlations between the electrons are dominating factors and cannot be neglected. These strong correlations cannot be treated perturbatively anymore and in many cases lead to drastically different physics! In fact, already a single strongly correlated site coupled to a system of otherwise effectively non-interacting particles can give rise to such physics known as the Kondo effect, which has kept physicists busy for decades before it could finally be solved. A different example of strongly correlated systems is given by the transition metal oxides, in which the strong Coulomb correlations lead to a variety of intriguing physical phenomena, the arguably most famous one being the high-T_c superconductivity discovered in doped cuprates. The unusual electronic and magnetic properties of many strongly correlated materials have also found many real-life applications such as superconducting magnets and magnetic storage [18].

In this chapter we introduce the models of strongly correlated systems considered in the main body of this thesis. This also provides a background for the discussion of numerical techniques in the next chapter. Starting with a non-interacting system which contains only a single site with a strong Coulomb interaction (the single-impurity Anderson model and the Kondo model, cf. Parts III and IV), we then present the infamous Hubbard model and its strong-coupling limit, the Heisenberg spin-Hamiltonian. Finally, we introduce the Kitaev model, a special case of a so-called compass model, which is similar to the Heisenberg model, but the spin interactions are anisotropic and depend on lattice properties (cf. Part B).

2.1. Quantum impurity problem

The arguably simplest non-trivial paradigm of a strongly correlated system is the introduction of a single strongly correlated impurity into an otherwise non-interacting system. Such systems are already very hard to solve and contain rich physics. The poster child of quantum impurity physics is the infamous Kondo effect: the unexpected mini-

mum that was measured in the electronic resisitvity of gold as the temperature is lowered. The dominant contribution to the resistivity in metals comes from the scattering of conduction electrons on phonons. As the temperature is lowered, these phonon modes are suppressed and a finite residual resistivity due to lattice defects in the metal remains. However, in the presence of magnetic impurities, it was found [19] that below a certain temperature the resistivity increased. Thirty years later, Jun Kondo could attribute this effect to the spin-scattering of conduction electrons on the impurity spin [20] which leads to a logarithmic divergence in the resistivity below a characteristic temperature, the so-called Kondo temperature T_K. Although the origin of the resistance minimum was now understood, the unphysical logarithmic divergence still posed a serious problem. A concerted effort by many workers, especially a scaling analysis by Anderson [21], suggested that upon lowering the temperature, a local magnetic moment builds up on the impurity, and subsequently, below T_K, this local moment is *screened* from the rest of the system by the formation of a spin-singlet state with conduction band electrons. The definitive confirmation of this picture eventually came with Wilson's numerical renormalization group method (NRG) [10, 22], see Chap. 3.

2.1.1. Single-impurity Anderson model

The Hamiltonian of a generic quantum impurity system can always be cast into a form consisting of three parts: the Hamiltonian of the host system, the Hamiltonian of the isolated impurity and a coupling between the two,

$$H = H_{\mathrm{host}} + H_{\mathrm{imp}} + H_{\mathrm{host-imp}}. \tag{2.1}$$

In the context of Kondo physics, the formation of a local moment on the impurity and the screening by conduction electrons can be well understood within the framework of a special quantum impurity Hamiltonian: the single-impurity Anderson model (SIAM), introduced by Anderson in 1961 [23]. In the SIAM, the host system is described by non-interacting particles and for infinite or periodic systems the Hamiltonian is diagonal in momentum space,

$$H_{\mathrm{host}} = \sum_{\mathbf{k}\sigma} \varepsilon_{\mathbf{k}} c^\dagger_{\mathbf{k}\sigma} c_{\mathbf{k}\sigma}, \tag{2.2}$$

where $c^\dagger_{\mathbf{k}\sigma}$ creates an electron with spin $\sigma = \uparrow / \downarrow$ and momentum $\mathbf{k}$ in the conduction band, and $\varepsilon_{\mathbf{k}}$ is the dispersion relation. This approach is justified by Landau's Fermi liquid theory: At sufficiently low temperature the long-range Coulomb interaction between the electrons in the metal is screened and the effective degrees of freedom in the system can be viewed in terms of quasi-particles which move around in the host system nearly freely [3]. Neglecting the small remaining interaction between these quasi-particles turns out to be a reasonable approximation.

The second part in Eq. (2.1) is the impurity part of the Hamiltonian. In the SIAM it describes a single orbital with level energy ϵ_f and a Coulomb interaction U:

$$H_{\mathrm{imp}} = \epsilon_f \hat{n}_f + U \hat{n}_{f\uparrow} \hat{n}_{f\downarrow}, \tag{2.3}$$

where $\hat{n}_f = \sum_\sigma \hat{n}_{f\sigma}$ is the occupation number operator with $\hat{n}_\sigma = f^\dagger_\sigma f_\sigma$, and $f^\dagger_\sigma$ creates an electron with spin σ on the impurity orbital. When the impurity orbital is embedded in the host metal, the two systems are coupled via a hybridization $V_{\mathbf{k}}$. We can neglect the $\mathbf{k}$-dependence of the hybridization if the impurity couples only locally to a translationally invariant system, and in this thesis we always assume a constant hybridization $V_{\mathbf{k}} = V$.

The Hamiltonian $H_{\mathrm{host-imp}}$ is then given by

$$H_{\mathrm{host-imp}} = V \sum_{\sigma} \left(f_{\sigma}^{\dagger} c_{\mathbf{0}\sigma} + c_{\mathbf{0}\sigma}^{\dagger} f_{\sigma} \right), \tag{2.4}$$

where now $c_{\mathbf{0}\sigma}^{\dagger} = \frac{1}{\sqrt{\mathcal{V}}} \sum_{\mathbf{k}} c_{\mathbf{k}\sigma}^{\dagger}$ (with the system's volume $\mathcal{V}$) creates an electron in the host system orbital coupling to the impurity. Without loss of generality we can always define the origin of the host system's coordinate system such that the hybridizing orbital is located at $\mathbf{r} = \mathbf{0}$.

Local moment formation in the SIAM

To understand how the SIAM allows for the formation of a magnetic moment on the impurity, we consider the isolated impurity Hamiltonian H_{imp}. Defining $|0\rangle$ as the unoccupied impurity orbital, the impurity can be in one of the following four states, given here with their corresponding energies:

$$\begin{aligned} |0\rangle &\qquad E = 0, \\ f_{\uparrow}^{\dagger} |0\rangle = |\uparrow\rangle &\qquad E = \epsilon_f, \\ f_{\downarrow}^{\dagger} |0\rangle = |\downarrow\rangle &\qquad E = \epsilon_f, \\ f_{\uparrow}^{\dagger} f_{\downarrow}^{\dagger} |0\rangle = |\uparrow\downarrow\rangle &\qquad E = 2\epsilon_f + U. \end{aligned}$$

To obtain a spin doublet ground state (i.e. either $|\uparrow\rangle$ or $|\downarrow\rangle$), single occupation must be favored ($\epsilon_f < \epsilon_F$, where ϵ_F is the Fermi energy), but the Coulomb energy must be strong enough to disfavor energetic excitations to the doubly-occupied state ($\epsilon_f + U > \epsilon_F$). Setting the Fermi level to $\epsilon_F = 0$, the requirement for the ground state to be a local magnetic moment can thus be compactly expressed as

$$-U < \epsilon_f < 0. \tag{2.5}$$

In the special case when $\epsilon_f = -U/2$ the impurity is called *particle-hole symmetric*, as the transformation $\hat{n}_f \to 2 - \hat{n}_f$ leaves the Hamiltonian invariant.

2.1.2. Kondo model

The SIAM provides a description of the quantum impurity system for arbitrary energies and occupation of the impurity orbital. However, we have argued that at the heart of the Kondo effect lies the spin-flip scattering on a magnetic impurity moment. Since we have identified the parameter regime in which the SIAM can sustain a local moment, we can derive an effective, simplified Hamiltonian for this special case. To this end, we project the Hamiltonian onto the subspace in which the impurity is singly-occupied. This is done via the so-called *Schrieffer-Wolff* transformation [24]. Taking into account virtual excitations to the zero- and doubly-occupied manifolds up to second order, this projection yields the following effective Hamiltonian, called the *Kondo Hamiltonian*:

$$H = H_{\mathrm{host}} + K \sum_{\mathbf{k}\mathbf{k}'\sigma} c_{\mathbf{k}\sigma}^{\dagger} c_{\mathbf{k}'\sigma} + J \mathbf{S}_f \cdot \mathbf{s}_0, \tag{2.6}$$

where $\mathbf{S}_f$ and $\mathbf{s_0}$ are the spin-$\frac{1}{2}$ operators for the impurity local moment and the host system orbital spin which couples directly to the impurity. These two operators are defined

as

$$\mathbf{S}_f = \sum_{\sigma,\sigma'} f^\dagger_\sigma \boldsymbol{\sigma}_{\sigma\sigma'} f_{\sigma'}, \tag{2.7}$$

$$\mathbf{s_0} = \sum_{\sigma,\sigma'} c^\dagger_{\mathbf{0}\sigma} \boldsymbol{\sigma}_{\sigma\sigma'} c_{\mathbf{0}\sigma'}, \tag{2.8}$$

with the vector of Pauli matrices $\boldsymbol{\sigma} = (\sigma^x, \sigma^y, \sigma^z)$. The first term H_{host} is again given by Eq. (2.2) and the second term in Eq. (2.6) is a purely potential scattering contribution. The effective Heisenberg exchange coupling J and the potential scattering strength K are given (to second order in V) by [3]

$$J = V^2 \left(\frac{1}{U + \epsilon_f} + \frac{1}{-\epsilon_f} \right), \tag{2.9a}$$

$$K = \frac{V^2}{2} \left(\frac{1}{-\epsilon_f} - \frac{1}{U + \epsilon_f} \right). \tag{2.9b}$$

Eqs. (2.9) show that in the particle-hole symmetric case, $\epsilon_f = -U/2$, the potential scattering term vanishes, $K = 0$, and the spin interaction simplifies to

$$J = \frac{4|V|^2}{U}. \tag{2.10}$$

Since the parameters U and ϵ_f are constrained by Eq. (2.5), J is always positive and thus the interaction is always antiferromagnetic. This fact is an essential result as it leads to the singlet formation and screening of the impurity spin at low energies.

At this point we want to stress that the Kondo Hamiltonian in Eq. (2.6) is a low-temperature effective model of the full single-impurity Anderson model defined by Eqs. (2.1)-(2.4). Whereas the latter also describes charge fluctuations on the impurity at high energies, the former assumes a strictly singly-occupied impurity and models only the low-energy spin-spin interactions. The high-energy physics of both models differ, but the low-energy behavior and ground states of both models are identical.

2.1.3. Poor man's scaling and the renormalization group

Having introduced two related models—the single-impurity Anderson model and its low-energy counterpart, the Kondo model—which describe a metallic host containing magnetic impurities, we now turn to the explanation for the occurrence of the resistance minimum. The experimentally observed correlation between the existence of a Curie-Weiß behavior in the impurity susceptibility (a local moment) and the appearance of the resistance minimum suggested the origin of the latter to be related to magnetic impurities. Perturbational treatments of the Anderson and Kondo models, however, could not reproduce the minimum. Only when Kondo in 1964 [20] extended the perturbational calculations within the Kondo model to third order in J, the spin degeneracy of the impurity could be shown to lead to the appearance of $\log(T/D)$ terms. The resistivity is then given by

$$R(T) = R_0 \left[1 + 2J\rho_0 \ln \left(\left| \frac{k_B T}{D} \right| \right) \right], \tag{2.11}$$

where R_0 is the resistivity calculated to second order and ρ_0 is the density of states at the Fermi level and k_B the Boltzmann constant.

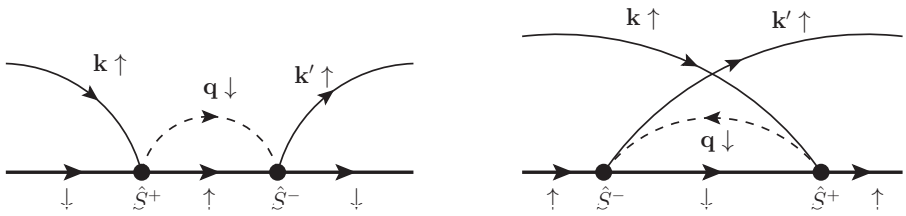

Figure 2.1.: Virtual second-order excitations into the high-energy band segments in poor man's scaling. The thick horizontal lines represent the state of the impurity spin. The interactions with conduction band states (thin lines) flip the impurity spin, leading to a virtual excitation into the eliminated band edge (dashed line). Subsequently, the impurity spin is flipped back into its original state. The left diagram shows the process of an electron in a quantum state $|\mathbf{k}\uparrow\rangle$ being scattered into the band edge and then back into the state $|\mathbf{k}'\uparrow\rangle$. The right diagram, on the other hand, describes the process of a particle from the band edge being scattered into the bulk of the band (leaving a hole in the band edge) and then being scattered back into the band edge.

This result finally explained the origin of the resistance minimum by attributing it to spin-spin interactions which dominate the physical processes at low enough temperatures. Unfortunately, it also implied the divergence of all physical quantities for $T \to 0$. The problem of how to extend the calculations to the regime $T \ll T_K$ attracted the attention of many theorists and quickly became known as the *Kondo problem*. It could eventually be overcome with the help of the *poor man's scaling* technique developed by Anderson in 1970 [21]. In this approach the band width is progressively reduced, and second-order virtual excitations to the band edges are eliminated perturbatively. In each step, an energy interval of size δD is cut off from the band at the edges. The reduced band thus runs from $(-D+|\delta D|) \to (D-|\delta D|)$. Excitations to the eliminated states are taken into accout perturbatively, and it turns out that the only non-trivial contributions arise from virtual second-order excitations into the high-energy intervals and back. Fig. 2.1 shows diagrammatic representations of these processes.

Once the band width is reduced, the resulting Hamiltonian has exactly the same form as the original. However, the coupling parameters are renormalized $J \to \tilde{J}$ and the Hamiltonian is now defined on a reduced bandwidth $2\tilde{D} = 2(D - |\delta D|)$. The reduction step is then applied repeatedly, and in the limit of infinitesimally small energy intervals, $|\delta D| \to \mathrm{d}D$, yields a differential equation for the coupling parameter J, viz.

$$\frac{\mathrm{d}J}{\mathrm{d}\ln(D)} = -2\rho_0 J^2 + \mathcal{O}\left(\rho_0^2 J^3\right). \tag{2.12}$$

This differential equation defines a *flow* of the coupling parameter as the temperature/energy scale is progressively reduced. Integrating Eq. (2.12) we find a so-called *scaling invariant* of the Kondo effect, the Kondo temperature T_K:

$$D\exp\left(-\frac{1}{\rho_0 J}\right) = \tilde{D}\exp\left(-\frac{1}{\rho_0 \tilde{J}}\right) \sim T_K. \tag{2.13}$$

The invariance of T_K under the reduction of the energy scale implies that, for low enough temperatures, all properties of the system must depend *only* on this parameter T_K. A

better estimate of T_K is obtained from perturbation theory to third order, giving

$$T_K = D\sqrt{\rho_0 J}\exp\left(-\frac{1}{\rho_0 J}\right). \tag{2.14}$$

The renormalization group

Building on the scaling ideas by Anderson discussed in the previous section, we can formulate the more general concept of the renormalization group (RG) method, which was largely pioneered in the context of critical systems in condensed matter physics by Kadanoff [25] and Wilson [10]. It is a mapping R of a Hamiltonian $H(\mathbf{K})$ which is specified by a set of coupling parameters $\mathbf{K} = (K_1, K_2, \ldots)$, into a new Hamiltonian of the same form but with different (renormalized) coupling parameters $\tilde{\mathbf{K}}$, formally:

$$R(\mathbf{K}) = \tilde{\mathbf{K}}. \tag{2.15}$$

The series of points $\mathbf{K}$ defines trajectories in parameter space, also called the *RG flow* (in the sense that these trajectories have a direction and are smooth). Typically, the transformation R consists of integrating out local (microscopic) degrees of freedom in order to eventually obtain a description of the system on a macroscopic level. An example for such a transformation was given in the last subsection by the reduction of the band width. Other examples include Wilson's real-space renormalization group procedure (see Chap. 3), and the Kadanoff block spin transformation in which the RG scheme consists of an explicit coarse-graining of space. Both these schemes are discussed in more detail in Ref. [10].

A key concept within the RG framework is that of *fixed points*. A fixed point is a point $\mathbf{K}^*$ where the RG transformation leaves the coupling parameters invariant,

$$R(\mathbf{K}^*) = \mathbf{K}^*. \tag{2.16}$$

At these points, further application of the RG scheme will not change the description of the system anymore. One generally distinguishes between *stable* and *unstable* fixed points. The trajectories in the vicinity of a stable fixed point are drawn towards it—the system flows to the stable fixed point. In the neighborhood of an unstable fixed point, however, trajectories are eventually driven away and flow to the stable fixed point.

2.1.4. Fixed Points of the RG flow

Applying the renormalization group idea to the symmetric flat-band Anderson model renormalizes the parameters $U \to \tilde{U}$ and $V \to \tilde{V}$. We find three distinct fixed points [3, 22], and in Fig. 2.2 we show the RG flow diagram for the symmetric Anderson model. The three fixed points can be interpreted in a physically intuitive way:

Free orbital (FO): At high temperatures, $T \sim D$, charge fluctuations to and from the impurity are dominant and the system is described by the (unstable) free orbital fixed point. At this fixed point, the impurity can be in all four possible states. The charge fluctuations lead to peaks in the impurity density of states $\rho_{\mathrm{imp}}(\epsilon)$ at $\epsilon = \epsilon_f$ and $\epsilon = \epsilon_f + U$, which are commonly known as the Hubbard satellites.

Local moment (LM): Lowering the temperature (or energy scale) by applying the RG scheme iteratively, below a certain energy scale charge fluctuations are frozen out

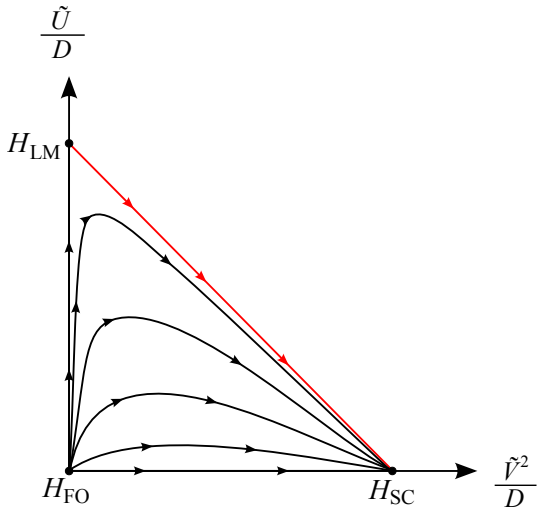

Figure 2.2.: Renormalization group flow of the symmetric Anderson model [3]. The only stable fixed point is the strong coupling fixed point at $V^2 \to \infty$. The red line indicates the RG flow shared with the Kondo model where only the local moment and strong coupling fixed points are present. In the Kondo model, $J \sim V^2/U$ is the renormalized parameter.

and the impurity orbital becomes singly-occupied, forming a local magnetic moment. The system flows away from the FO fixed point to the (unstable) *local moment* fixed point. In the RG flow the LM fixed point lies at $\tilde{U} \to \infty$. In this regime, the Kondo model serves as an adequate low-energy theory of the Anderson model. Accordingly, the Kondo model with $J = 0$ (cf. Eqs. (2.10)) is described by the same LM fixed point.

Strong coupling (SC): Further lowering the temperature, as soon as the Kondo temperature scale at T_K is reached, spin-scattering processes become dominant and the formation of the Kondo singlet groundstate is represented by the system flowing to the stable *strong-coupling* fixed point. In the impurity density of states the formation of the singlet leads to a narrow peak of width T_K around the Fermi level: The so-called Kondo resonance. The SC fixed point is the $V^2 = \infty$ limit of the Anderson model, and accordingly the $J = \infty$ limit of the Kondo model.

Fig. 2.3 shows the impurity entropy in the single-impurity Anderson model as a function of ω for three different sets of impurity parameters. At high energies, $\omega \sim D$, the system is at the FO FP, and the four possible states of the impurity yield an entropy $S_{\mathrm{imp}} = \log(4) = 2\log(2)$. At a non-universal energy scale, the impurity degrees of freedom reduce to that of a single spin-$\frac{1}{2}$, and $S_{\mathrm{imp}} = \log(2)$. Finally, below the Kondo scale the impurity is screened, the resulting singlet state has an entropy of $S_{\mathrm{imp}} = \log(1) = 0$.

2.1.5. The Kondo resonance

The spin exchange between the conduction electrons and the localized impurity spin qualitatively change the energy spectrum of the system [9]. The combined scattering processes generate a new state, known as the *Kondo resonance*, at the Fermi level ϵ_F. This new state also substantiates the intuitive picture we have established so far: the electrons mainly contributing to the low-temperature conductivity of a metal have energies around the Fermi level. Since the Kondo resonance also forms at the Fermi energy,

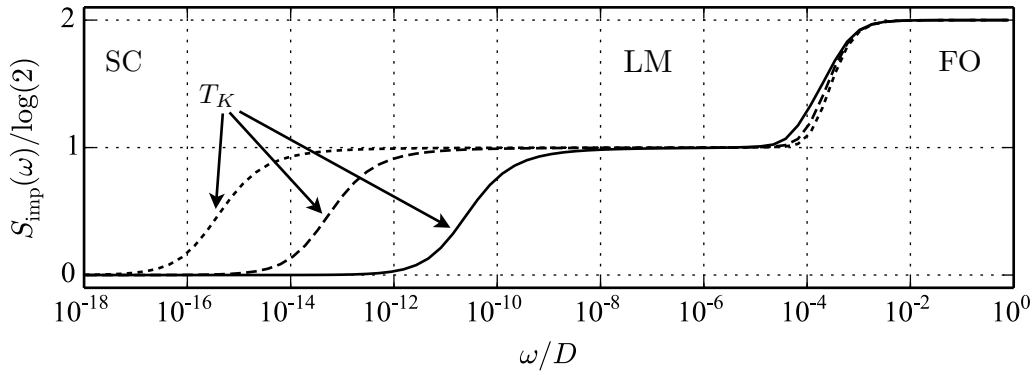

Figure 2.3.: Impurity entropy in the single-impurity Anderson model as a function of ω for three different sets of impurity parameters. The data was obtained with the Numerical Renormalization Group for a constant hybridization function, and the parameters of the Anderson model were $\epsilon_f/D = -0.8 \times 10^{-3}$, $V/D = 3 \times 10^{-3}$ and $U/D = 1 \times 10^{-3}, 1.125 \times 10^{-3}$ and 1.25×10^{-3} (solid, dashed, and dotted lines).

it is precisely these electrons that are affected most, leading naturally to an increased resistivity. Various experimental measurements of the Kondo resonance [26, 27] have recently been obtained by measuring the linear-response conductance G and the differential conductance dI/dV through a quantum dot, which was tuned to form a spin-$\frac{1}{2}$ impurity.

2.2. The SU(2) Heisenberg Spin Model

In the previous section we considered the case of a system of non-interacting fermions coupled to a single impurity—a localized orbital with strong Coulomb interaction. The description of a metal in terms of a Fermi liquid, i.e. non-interacting fermionic quasiparticles, is a vital approach that has proven to be very successful in many cases. However, when electron-electron interactions become dominant this description is not useful anymore. The physics of such strongly correlated electrons is, in fact, a bona fide example of the inapplicability of Fermi liquid theory [8].

2.2.1. Hubbard model

A very fruitful starting-point for the description of such systems is given by the Hubbard model; a deceptively simple tight-binding Hamiltonian with only on-site interactions. It has been proposed by J. Hubbard in 1963 to understand the physics of transition metal monoxides [28], but it has since been applied to many different systems and problems, e.g. heavy fermions [3] and high-T_c superconductivity [29]. It has been attacked with the full range of analytic and numerical techniques available to condensed matter theorists, but in spite of its simplicity it is at present far from being completely understood [8]. The Hubbard-Hamiltonian is given by

$$H_{\rm Hubbard} = -t \sum_{\langle ij \rangle, \sigma} c^\dagger_{i\sigma} c_{j\sigma} + U \sum_i \hat{n}_{i\uparrow} \hat{n}_{i\downarrow}, \tag{2.17}$$

where $c^\dagger_{i\sigma}$ creates an electron with spin σ at lattice site i, and $\hat{n}_{i\sigma} = c^\dagger_{i\sigma} c_{i\sigma}$ is the occupation number operator. The first term describes the hopping of electrons between two nearest-neighbor sites i and j, with the hopping amplitude t. The second term represents the strong Coulomb interaction between two electrons on the same site.

2.2.2. Mott insulators and Heisenberg Hamiltonian

One of the many successes of the Hubbard model was the description of Mott insulators: materials that under conventional band theory are expected to be conducting, however show insulating behavior in experiment. The explanation of this discrepancy in terms of strong interactions between electrons follows immediately from the Hubbard model.

Starting from the Hubbard Hamiltonian in Eq. (2.17) at half-filling (i.e. an electron concentration of on average one electron per lattice site), we examine the effect of interactions. To this end, we consider the dimensionless interaction parameter U/t. In the weakly interacting limit, $U/t \ll 1$, one can resort to standard Fermi liquid theory and the interaction term in Eq. (2.17) can be viewed as a mere perturbation to the non-interacting system. In the opposite limit of $U/t \gg 1$, however, the electrons in the system will be localized at each site. The immense energy penalty from the Coulomb repulsion is thus avoided at the expense of the (much smaller) kinetic energy t. In this case charge carriers cannot travel through the system and the system becomes insulating; this is known as a Mott insulator [30]. The groundstate of the half-filled Hubbard model for $U \gg t$ is thus a system where each site is occupied by one electron, carrying a spin-$\frac{1}{2}$. To derive an effective theory for this situation we treat the hopping of electrons in perturbation theory, and integrating out second-order virtual excitations into intermediate states in which a site becomes doubly-occupied yields the Heisenberg spin-Hamiltonian:

$$H_{\text{Heisenberg}} = J \sum_{\langle ij \rangle} \mathbf{S}_i \cdot \mathbf{S}_j, \tag{2.18}$$

where $\mathbf{S}_i = (S^x_i, S^y_i, S^z_i)$ is the vector of spin-$\frac{1}{2}$ operators at site i, and

$$J = \frac{2t^2}{U}. \tag{2.19}$$

The interaction in Eq. (2.18) is antiferromagnetic, since $J > 0$. The origin of this fact can be explained very simply [8]: For two neighboring sites occupied with electrons of parallel spin, an intermediate state of both electrons on one site is strictly forbidden by the Pauli principle. The same process is allowed, though, for electrons of anti-parallel spin. In the latter case, such a process leads to an energy gain of $\Delta E = -2t^2/U$.

2.3. The Kitaev Honeycomb Model

The interaction terms in the Heisenberg model are isotropic, i.e. symmetry operations of the underlying lattice do not change the Hamiltonian. Now, we discuss a special model with anisotropic interactions, i.e. where the relative spatial alignment of two interacting spins determines the type of interaction. This model was first presented by A. Kitaev in 2006, after he had found an exact solution to it [31] while considering it in the context of fault-tolerant quantum computation.

Not only is the fact that an exact solution to a (non-trivial) 2D model exists remarkable by itself, this so-called *Kitaev model* furthermore possesses an abundance of compelling

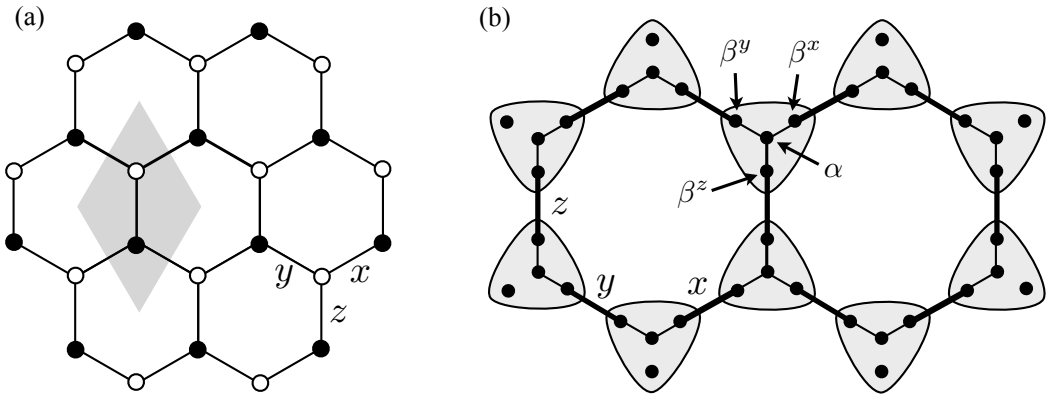

Figure 2.4.: (a) The honeycomb lattice of the Kitaev model. Each site belongs to one of two sublattices, shown here as empty or filled disks. The gray diamond shows the unit cell containing two sites. (b) A graphical representation of the Majorana fermionization. The large gray bubbles represent a spin-$\frac{1}{2}$ and each black dot represents one Majorana fermion.

physical properties: It can be solved by mapping to non-interacting Majorana fermions, its ground state is a true quantum spin liquid with topological order [32], and it contains both abelian and non-abelian anyonic excitations in the presence of a magnetic field. At the time of Kitaev's original publication it was not clear how to realize this model in a real system [31]. Recently, however, Khaliullin and co-workers suggested [33] that the Kitaev model might be in part realized in certain transition metal oxide systems with orbital degrees of freedom. This discovery spurred a lot of research and is one of the main motivations for the problems considered in this thesis (see Part II). In the following, we present the model along with a sketch of the solution.

2.3.1. The model

The Kitaev model consists of spin-$\frac{1}{2}$ degrees of freedom located at the vertices of a honeycomb lattice, Fig. 2.4(a). The lattice can be subdivided into two sublattices with the unit cell containing two sites. Interactions occur between nearest-neighbor spins and are divided into three types depending on the direction of the link between the sites. Each type of interaction is an Ising-like coupling of one spin component and we call them "x-links", "y-links" and "z-links", see Fig. 2.4(a). The full Hamiltonian is given by

$$H_{\text{Kitaev}} = J_x \sum_{x-\text{links}} S_i^x S_j^x + J_y \sum_{y-\text{links}} S_i^y S_j^y + J_z \sum_{z-\text{links}} S_i^z S_j^z, \tag{2.20}$$

with three independent coupling parameters J_x, J_y and J_z. As the honeycomb lattice is bipartite there is no geometrical frustration when considering only nearest-neighbor interactions. However, it is the anisotropic spin-interaction terms that highly frustrate the model. To see this, consider one spin interacting with its three neighbors: for each individual neighbor, the spin minimizes its energy by aligning along a different spin axis, which cannot be fulfilled with respect to all three neighbors at the same time.

2.3.2. Majorana fermions

The Dirac equation as a relativistic generalization of the Schrödinger equation describes all spin-$\frac{1}{2}$ particles (such as electrons) as well as their anti-particles (such as positrons). Whereas in general particles and their anti-particles are different, Ettore Majorana showed in 1937 [34] the existence of a solution of the Dirac equation which is its own anti-particle. This is most easily seen in terms of operators where the Majorana solution is a linear combination of two "regular" Dirac-fermions. Consider the fermionic operator c_i ($c_i^\dagger$) that destroys (creates) a Dirac particle and obeys the canonial anticommutation relation $\{c_i, c_j^\dagger\} = \delta_{ij}$. From this, we can construct the following linear combination:

$$\gamma_{i,1} = \frac{1}{\sqrt{2}}\left(c_i + c_i^\dagger\right), \qquad \gamma_{i,2} = \frac{1}{\sqrt{2}i}\left(c_i - c_i^\dagger\right). \tag{2.21}$$

These new operators γ_i are purely real solutions to the Dirac equation. They are thus hermitian and also obey fermionic statistics

$$\{\gamma_\mu, \gamma_\nu\} = \delta_{\mu\nu}, \qquad \gamma_\mu^\dagger = \gamma_\mu. \tag{2.22}$$

Eq. (2.22) shows explicitly that the Majorana fermions are indeed their own anti-particle. From Eqs. (2.21) we furthermore see that we can express a regular Dirac fermion as the combination of two Majoranas as

$$c_i = \frac{1}{\sqrt{2}}\left(\gamma_{i,1} + i\gamma_{i,2}\right), \qquad c_i^\dagger = \frac{1}{\sqrt{2}i}\left(\gamma_{i,1} - i\gamma_{i,2}\right). \tag{2.23}$$

In its original paper, Ettore Majorana speculated that his findings might apply to neutrinos, which at that time were themselves only hypothetical. Remarkably, more than 80 years later, it is to this day still not certain whether neutrinos are in fact Majorana fermions or not [35]. Furthermore, the theory of supersymmetry in high energy physics also has put forth candidates for Majorana fermions, such as the so-called weakly interacting massive particles (WIMPs) in the context of dark matter [36].

In the field of condensed matter physics, the search for Majorana fermions has recently attracted much interest as it was suggested that they occur as quasiparticle excitations in a variety of systems. Although the use of Majorana fermions in condensed matter theory is mostly motivated from a purely mathematical standpoint [35], the possibility of real materials exhibiting such physics leads to a realistic chance of further exploring and even utilizing their exotic features.

We discuss how the Kitaev model can be solved in terms of Majorana fermion operators in the following sections, and in Part IV we focus on a different system at the center of the current search for Majorana fermions.

2.3.3. Representation of spins by Majorana fermions

Following Kitaev's original solution, we employ the Majorana fermions initially as a mathematical tool which turns out to be essential for the solution of the Kitaev model. To this end, we represent one spin at site i by four Majorana fermions which we call α_i, β_i^x, β_i^y, and β_i^z. The spin operators can now be written in terms of these Majoranas as

$$S_i^\gamma = i\beta_i^\gamma \alpha_i, \tag{2.24}$$

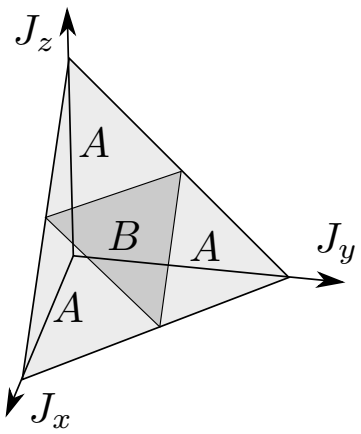

Figure 2.5.: Phase diagram of the Kitaev model. Shown is a cut at $J_x + J_y + J_z = \text{const}$ through the positive octant. The gapped phase A and the gapless phase B are discussed in the main text. The other octants have equivalent phase diagrams.

where $\gamma \in \{x, y, z\}$. Fig. 2.4(b) gives a graphical representation of this transformation. A side-effect of this mapping is that with the introduction of the Majorana operators we doubled the Hilbert space. This, however, can be remedied by restricting the Hilbert space to its physical sector, which can be done by requiring the new spin operators to fulfill the spin SU(2) algebra. In the Majorana representation, the Kitaev Hamiltonian Eq. (2.20) becomes

$$H = \frac{i}{4} \sum_{\langle ij \rangle} J_\gamma \underbrace{\left(i\beta_i^\gamma \beta_j^\gamma\right)}_{=\hat{u}_{ij}} \alpha_i \alpha_j, \tag{2.25}$$

where the sum runs over nearest-neighbors $\langle ij \rangle$ and, as before, $\gamma \in \{x, y, z\}$ corresponds to the type of link. Remarkably, the operators $\hat{u}_{ij}$ commute with each other and the Hamiltonian, and we can therefore split the Hilbert space into eigenspaces of each $\hat{u}_{ij}$ which are indexed by their eigenvalues ± 1. Replacing the operators $\hat{u}_{ij}$ by their eigenvalues u_{ij} yields a Hamiltonian quadratic in the Majorana modes. This non-interacting problem is then exactly solvable.

2.3.4. Spectrum and phase diagram

The freedom of fixing every u_{ij} leaves us with the question which configuration minimizes the ground state energy? In fact, from a theorem by Lieb [37] it follows that the ground state is achieved by a field configuration where $u_{jk} = 1$ for all links where j belongs to the even sublattice, and k to the odd sublattice. This configuration obviously has a translational symmetry and we find the fermionic spectrum by Fourier transformation of the operators in the Hamiltonian

$$H = \frac{i}{4} \sum_{\langle ij \rangle} J_\gamma u_{ij} \alpha_i \alpha_j. \tag{2.26}$$

The spectrum is then readily found as

$$\varepsilon(\mathbf{k}) = \pm 4 \left| J_x e^{i\mathbf{k}\cdot\mathbf{a}_1} + J_y e^{i\mathbf{k}\cdot\mathbf{a}_2} + J_z \right|, \tag{2.27}$$

with the two lattice vectors of the honeycomb lattice $\mathbf{a}_1 = (\frac{1}{2}, \frac{\sqrt{3}}{2})$ and $\mathbf{a}_2 = (-\frac{1}{2}, \frac{\sqrt{3}}{2})$. From here, we can immediately identify the parameter regime in which the spectrum is gapless (i.e. a solution exists for $\varepsilon(\mathbf{k}) = 0$), which is the case exactly when the following three triangle inequalities are fulfilled

$$\begin{aligned} |J_x| &\leq |J_y| + |J_z| \\ |J_y| &\leq |J_x| + |J_z| \\ |J_z| &\leq |J_x| + |J_y| \,. \end{aligned}$$

We call the gapless phase B, and the gapped phases A, and show them in Fig. 2.5 for a cut through the parameter space for which $J_x + J_y + J_z = \mathrm{const}$.

2.3.5. Spin liquid ground states

A remarkable property of the Kitaev model was first elucidated in Ref. [32]: In its ground state, dynamical two spin correlation functions are short ranged and vanish exactly beyond nearest-neighbor separation, independent of the values of J_x, J_y and J_z. Therefore, the ground state, in both phases A and B, is given by a short-ranged quantum spin liquid with no long range spin order [38].

In the phase A the spin liquid is gapped and has a $\mathbb{Z}_2$ topological order. In fact, in the limit that one coupling is much stronger than the two others, e.g. $J_x, J_y \ll J_z$, the Hamiltonian can be mapped to the toric code [31], a thoroughly studied model of a topological quantum error correcting code [39]. The phase B, on the other hand, is gapless, and it contains quasi-particle excitations in the form of non-abelian anyons, objects of tremendous interest in the context of topological quantum computation, see also Part IV.

Thus, the combination of an exact solution and the great number of rich physics, such as the non-abelien anyonic excitations in the gapless spin liquid state, have made this model a central focus of theoretical and experimental condensed matter research in recent years.

Chapter 3.

Numerical methods: DMRG and NRG

Strongly-correlated many-body quantum systems on low-dimensional lattices present a challenging task for both analytical and numerical treatment. The presence of strong interactions leads to failure of perturbation theory. Field-theoretic approaches have led to great insights but oftentimes rely on severe approximations. Numerically, a lattice system of finite size can in principle always be solved exactly by means of diagonalization. However, the Hilbert space of the problem grows exponentially in system size and thus severely restricts the system sizes feasible for simulation to the order of currently $\mathcal{O}(10)$. Although computational power steadily increases, this exponential barrier cannot be overcome and one has to turn to approximate solutions.

Kadanoff's block spin renormalization group was a first major step to understanding how to successfully apply renormalization group ideas from other fields in condensed matter physics. In his paper [25], he shows a way to define components of the theory at large distances by iterative aggregation of components at shorter distances. By grouping spins into blocks and then transforming the system so that each group of spins is now represented by a single effective spin, one effectively "zooms out" of the system and eventually reaches a description of the long length scale (or, conversely, low-energy) physics. This approach was further corroborated by Kenneth G. Wilson while working on the Kondo problem, and led to the invention of the numerical renormalizaton group (NRG) algorithm [10]. However, the concepts and ideas that enabled the NRG to be to this day the most powerful weapon to tackle Kondo physics fail for essentially all many-body lattice systems. Even a single free particle in a box cannot be described by Wilsons's approach. Eventually, Steven R. White realized that an important change in the approach was needed to enable it to treat general one-dimensional lattice systems to great accuracy. In 1992 he invented the density matrix renormalization group (DMRG) technique [11] which since then has proven to be the most powerful numerical method for one-dimensional systems know to date. Recently, with a deeper understanding of the underlying mathematical and physical structures, and the growth in computational powers available, the DMRG algorithm could be extended to also treat 2D systems (however only systems of small width).

Although the problems for which NRG and DMRG are best suited are very different, and although both algorithms have strongly differing features, at their core they are intimately related. In this chapter, we introduce both techniques from the point of view of their common foundation and in the modern language of *matrix product states*.

3.1. Reducing the size of the Hilbert space

The Hilbert space of a quantum lattice system comprised of N sites with a local Hilbert space of dimension d is exponentially large with a dimension $D = d^N$. However, it turns out that not the entire Hilbert space is required to describe the ground state of a realistic

Hamiltonian, and renormalization group methods for many-body systems (see Chap. 2.1) have the goal to identify precisely the relevant degrees of freedom of a given system. To this end, it is important to better understand how we can reduce the full Hilbert space to a relevant sub-manifold.

3.1.1. Entanglement entropy

How much a state is spread throughout the full Hilbert space can be quantified by means of the entanglement entropy. Consider a system X which is comprised of two subsystems A and B such that $X = A \cup B$. Assuming this system to be in a pure state $|\psi\rangle$, the entanglement entropy is defined as the von Neumann entropy of either subsystem (since it is the same for either subsystem). First, we can formulate the reduced density matrices for each subsystem by tracing out the other subsystem,

$$\hat{\rho}_A = \mathrm{Tr}_B \, |\psi\rangle \langle\psi| \,, \qquad \hat{\rho}_B = \mathrm{Tr}_A \, |\psi\rangle \langle\psi| \,. \tag{3.1}$$

The operators $\hat{\rho}_A$ and $\hat{\rho}_B$ have the same eigenvalues, λ_i, and by applying iteratively a singular value decomposition (SVD) [40] the full state $|\psi\rangle$ can be written in the so-called Schmidt decomposition as

$$|\psi\rangle = \sum_i \lambda_i \, |a\rangle_i \otimes |b\rangle_i \,, \tag{3.2}$$

where $|a\rangle_i$ and $|b\rangle_i$ are eigenvectors of ρ_A and ρ_B, respectively. This formulation is related to the matrix product states we discuss below, where a state is written in terms of tensor products of local objects. From the spectrum of the reduced density matrices one can now rigorously define the entanglement entropy as

$$S = \mathrm{Tr} \, \rho_A \log \rho_A = -\sum_i \lambda_i^2 \log \lambda_i^2 . \tag{3.3}$$

If $|\psi\rangle$ is a non-entangled state, the density matrices only have one non-vanishing eigenvalue which—due to normalization—is $\lambda_0 = 1$, and accordingly the entanglement entropy vanishes, $S = 0$. On the other hand, a maximally entangled state will have an exponentially large number of equal eigenvalues, leading to the (maximal) entanglement entropy $S = \log D$.

3.1.2. Area laws

At first glance, one might argue that a calculation of the entanglement spectrum must be performed in the full Hilbert space and we have thus gained nothing. However, one can prove for one-dimensional systems and certain two-dimensional systems that low-energy eigenstates of gapped Hamiltonians with local interactions obey so-called *area laws* for the entanglement entropy [41, 42]. In particular, the entanglement entropy of the ground states of such systems grows proportionally to the *surface* of the cut rather than the subsystem's volume. Taking for instance the two subsystems A and B as in Fig. 3.1, we find $S(A) \sim \partial A = L + W$. For a 1D system, this in fact implies $S_A = S_B = \mathrm{const.}$

It is important to stress that the fact that most systems have an area law leads to dramatic consequences, as it heavily constrains the number of possible candidates for the ground state in the Hilbert space. Indeed, the manifold of states with an entanglement entropy that grows with boundary rather than volume makes up only an exponentially small part of the full Hilbert space [40, 43]. Therefore, by reducing the Hilbert space of the

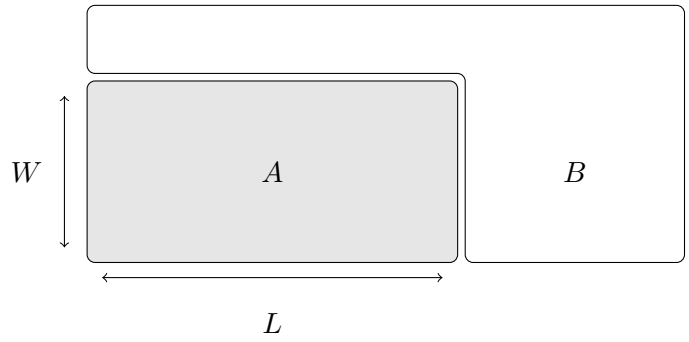

Figure 3.1.: Subsystems A and B comprising the full system $X = A \cup B$. If the system obeys an area law, the entanglement entropy of subsystem A grows with the boundary between A and B, $S_A \sim W + L$, and not with the volume of A, $S_A \sim W \cdot L$.

problem to the relevant manifold of states obeying an area law, we can massively reduce the required computational resources.

In fact, it turns out [44] that using the formalism of matrix product states (or more generally tensor networks), which we describe below, one automatically targets exactly such states. Accordingly, when constructing numerical RG methods to focus on the most relevant degrees of freedom, it is natural to formulate them in the context of matrix product states.

3.2. Matrix product states

To introduce the formalism of matrix product states, consider a lattice of L sites where each site has a local Hilbert space of dimension d. While the following discussion is valid for arbitrary dimensions of the system, for our purposes we assume the lattice to be one-dimensional. Any pure state of this system can be formulated as

$$|\psi\rangle = \sum_{\sigma_1,\ldots,\sigma_L} c_{\sigma_1,\ldots,\sigma_L} \, |\sigma_1\rangle \, |\sigma_2\rangle \ldots |\sigma_L\rangle \,, \tag{3.4}$$

where the sum runs over all d^L states in the full Hilbert space and we have an exponentially large number of coefficients $c_{\sigma_1\ldots\sigma_L}$. A matrix product state is a representation of this state by means of *local* objects, where the coefficients $c_{\sigma_1\ldots\sigma_L}$ are expressed in terms of matrices $A_i^{\sigma_1}$ as

$$c_{\sigma_1\ldots\sigma_L} = A_1^{\sigma_1} A_2^{\sigma_2} \ldots A_{L-1}^{\sigma_{L-1}} A_L^{\sigma_L}. \tag{3.5}$$

and thus the state $|\psi\rangle$ is given in a matrix product state formulation by

$$|\psi\rangle = \sum_{\sigma_1,\ldots,\sigma_L} A_1^{\sigma_1} A_2^{\sigma_2} \ldots A_{L-1}^{\sigma_{L-1}} A_L^{\sigma_L} \, |\sigma_1\rangle \, |\sigma_2\rangle \ldots |\sigma_L\rangle \,. \tag{3.6}$$

At this point, of course, this is a mere reformulation and the number of total coefficients is naturally still exponentially large. In fact, the dimensions of the matrices A grow exponentially, where $A_1^{\sigma_1}$ is a $(1 \times d)$ matrix, $A_2^{\sigma_2}$ is $(d \times d^2)$, and so forth. The dimensions grow for the first half of the matrices, then they decrease in the same manner until finally $A_{L-1}^{\sigma_{L-1}}$ is a $(d^2 \times d)$ matrix, and $A_L^{\sigma_L}$ is a $(d \times 1)$ vector. Thus, for a practical (numerical) treatment we have gained nothing so far.

To see how we can reduce the level of complexity by finding an optimal approximation, consider again the Schmidt decomposition in Eq. (3.2). From the reasoning above we know that for only slightly entangled states, only a few density matrix eigenvalues λ_i contribute most of the weight. By summing only over the M largest eigenvalues λ_i in Eq. (3.2), we can thus create an approximate state $|\tilde{\psi}\rangle \approx |\psi\rangle$, and it can be shown [40] that this is in fact an optimal approximation.

Turning back to the matrix product states we can in the same fashion limit the maximum matrix dimension of the matrices $A_i^{\sigma_i}$ to be $M \ll d^L$. The matrix size yields an upper bound for the rank of the reduced density matrices, and in this sense takes on the same role as the M in the Schmidt decomposition. By keeping only the largest M singular values in each decomposition, we can thus approximate the state $|\psi\rangle$ with a set of matrices $A_i^{\sigma_i}$ where each matrix is at most of dimension $(M \times M)$.

3.2.1. Matrix Product Operators (MPO)

With the representation of arbitrary states as matrix product states, we now turn to the representation of operators. In the basis of the MPS states, $\{|\sigma_i\rangle\}$, we can write any operators as [40]

$$\hat{O} = \sum_{\sigma_1,\ldots,\sigma_L} \sum_{\sigma_1',\ldots,\sigma_L'} W_1^{\sigma_1\sigma_1'} W_2^{\sigma_2\sigma_2'} \ldots W_{L-1}^{\sigma_{L-1}\sigma_{L-1}'} W_L^{\sigma_L\sigma_L'} |\boldsymbol{\sigma}\rangle \langle\boldsymbol{\sigma}'| \,, \tag{3.7}$$

where we have introduced the notation for a basis state

$$|\boldsymbol{\sigma}\rangle \equiv |\sigma_1\rangle |\sigma_2\rangle \ldots |\sigma_L\rangle \,. \tag{3.8}$$

The $W_i^{\sigma\sigma'}$ in Eq. (3.7) are matrices just like the matrices A_i^{σ} in Eq. (3.6) with the only difference that they depend on not one but two external indices, σ and σ', which can be understood as ingoing and outgoing physical states. The coefficients of the operator are then readily obtained as

$$\langle\boldsymbol{\sigma}|\hat{O}|\boldsymbol{\sigma}'\rangle = W_1^{\sigma_1\sigma_1'} W_2^{\sigma_2\sigma_2'} \ldots W_{L-1}^{\sigma_{L-1}\sigma_{L-1}'} W_L^{\sigma_L\sigma_L'}. \tag{3.9}$$

The application of an MPO to an MPS follows straight-forwardly from their definitions:

$$\begin{aligned} \hat{O}|\psi\rangle &= \sum_{\boldsymbol{\sigma}\boldsymbol{\sigma}'} \left(W_1^{\sigma_1\sigma_1'} W_2^{\sigma_2\sigma_2'} \ldots W_L^{\sigma_L\sigma_L'} \right) \left(A_1^{\sigma_1} A_2^{\sigma_2} \ldots W_L^{\sigma_L} \right) |\boldsymbol{\sigma}\rangle \\ &= \sum_{\boldsymbol{\sigma}} N^{\sigma_1} N^{\sigma_2} \ldots N^{\sigma_L} |\boldsymbol{\sigma}\rangle \,, \end{aligned} \tag{3.10}$$

where the new matrices N^{σ} have the multiplied dimension of the MPS and the MPO. Noteably, the form of the MPS stays invariant at the prize of an increased matrix size. In typical applications, however, the new MPS can be truncated again to the original matrix dimensions. The operation of summing over exponentially many basis vectors $|\sigma_1, \sigma_2, \ldots, \sigma_L\rangle$ has been reduced to a polynomial operation, of order $Ld^2 D_W^2 M^2$ where D_W is the dimension of the MPO [40].

3.2.2. Graphical representation of MPS and MPO

While generally the usage of MPS requires a lot of notational overhead, a much more convenient diagrammatic notation exists. From this point, we use the general word tensor

for each quantity occurring in the MPS description. In this sense, numbers are tensors of rank 0, vectors are tensors of rank 1, matrices of rank 2, etc.[1] In the diagrammatic notation, the tensors are represented by shapes and indices of the tensors are represented by lines emerging from the shapes. Lines connecting two tensors imply a summation over the corresponding index. In Fig. 3.2 we show examples of the basic diagrams we use, including an example of a matrix-vector multiplication showcasing the summation over an index.

In Fig. 3.3 we show the representation of the matrix product state, Eq. (3.6), and the representation of a matrix product operator, (3.7), both for a chain of length $L = 5$. The usage of squares instead of circles for the MPO is merely a help of better distinction of the two types of objects; the relevant property is the number of legs protruding from each tensor.

3.2.3. Canonical form of an MPS

Thus far, aside from the dimensionality we have not put any constraints on the matrices $A_i^{\sigma_i}$ in the MPS. However, in the light of the variational ground state search of the DMRG, it is useful to have the MPS be in the so-called *canonical form*. This form assures the correct normalization required in the DMRG process. We start with a general MPS with no normalization assumptions,

$$|\psi\rangle = \sum_{\sigma_1,\ldots,\sigma_L} M_1^{\sigma_1} \ldots M_L^{\sigma_L} |\sigma_1\rangle \ldots |\sigma_L\rangle \,. \tag{3.11}$$

Performing an SVD on the first matrix $M_1^{\sigma_1}$ yields

$$M_1^{\sigma_1} = USV^\dagger, \tag{3.12}$$

and we replace the original matrix $M_1^{\sigma_1}$ by the new matrix $A_1^{\sigma_1} \equiv U$. Next we generate a new matrix $\tilde{M}_2^{\sigma_2}$ by multiplying $SV^\dagger$ from the left to the matrix M^{σ_2},

$$\tilde{M}_2^{\sigma_2} = SV^\dagger M_2^{\sigma_2}. \tag{3.13}$$

After transforming all matrices in the original expression, we have generated the state

$$|\psi\rangle = \sum_{\sigma_1,\ldots,\sigma_L} A_1^{\sigma_1} \tilde{M}_2^{\sigma_2} \ldots M_L^{\sigma_L} |\sigma_1\rangle \ldots |\sigma_L\rangle \,. \tag{3.14}$$

The important reward from this procedure is the fact that due to the SVD the matrix $A_1^{\sigma_1}$ has the property that $(A_1^{\sigma_1})^\dagger A_1^{\sigma_1} = \mathbb{1}$. Iterative continuation of this scheme leads to the final MPS representation in (left-)canonical form

$$|\psi\rangle = \sum_{\sigma_1,\ldots,\sigma_L} A_1^{\sigma_1} \ldots A_L^{\sigma_L} |\sigma_1\rangle \ldots |\sigma_L\rangle \,, \tag{3.15}$$

where all matrices are normalized such that $(A_i^{\sigma_i})^\dagger A_i^{\sigma_i} = \mathbb{1}$ for $i = 1, \ldots, L$. In the SVD of the last $(d \times 1)$-matrix $M_L^{\sigma_L}$, the product $SV^\dagger$ yields a single number, which is precisely the norm of the initial state.

The same procedure can be applied starting from the last matrix M^{σ_L} and moving to

[1] This nomenclature is rooted in the more general theory of tensor networks, of which the MPS framework is a subset.

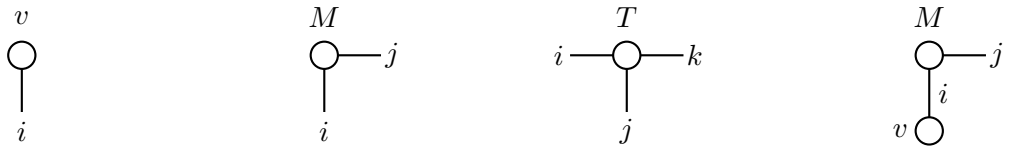

Figure 3.2.: Diagrammatic representation of (from left to right) a vector v_i, a matrix M_{ij} and a rank-3 tensor T_{ink}. The right-most picture shows a contraction of a vector v with a matrix M, the result being a vector $w_j = \sum_i v_i M_{ij}$.

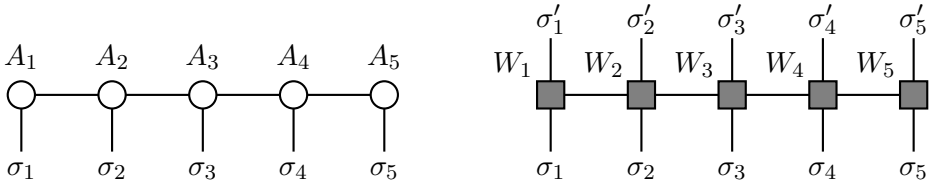

Figure 3.3.: Left: Graphical representation of a matrix product state $|\psi\rangle$ for a chain of length $L = 5$. Right: Representation for a matrix product operator $\hat{O}$ for the same chain.

the left. In this case, the matrices $M_i^{\sigma_i}$ are being iteratively replaced by the matrices $V^\dagger$ from the SVD, and the neighboring matrix to the left is transformed into

$$\tilde{M}_{i-1}^{\sigma_{i-1}} = M_{i-1}^{\sigma_{i-1}} US. \tag{3.16}$$

After each matrix is transformed, the final state is in the right-canonical form, given by

$$|\psi\rangle = \sum_{\sigma_1,\ldots,\sigma_L} V_1^{\sigma_1} \ldots V_L^{\sigma_L} |\sigma_1\rangle \ldots |\sigma_L\rangle \,, \tag{3.17}$$

where all matrices V again fulfill the relation $(V_i^{\sigma_i})^\dagger V_i^{\sigma_i} = \mathbb{1}$, which again follows from the SVD.

Let us remark at this point, that instead of starting from the left or the right end, one can of course also start from an arbitrary point in the state, generating a so-called mixed canonical form.

3.3. Real-space renormalization

At this point we introduce the common renormalization idea behind Wilson's NRG and White's DMRG. Conceptually, both methods operate in the same way: Consider a finite

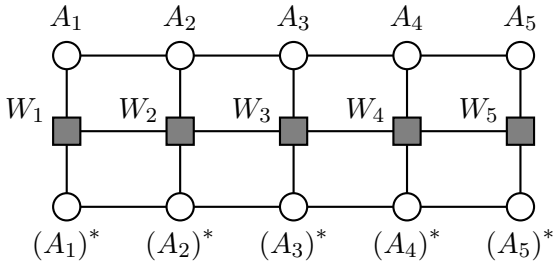

Figure 3.4.: Graphical representation of an expectation value $\langle\psi|H|\psi\rangle$

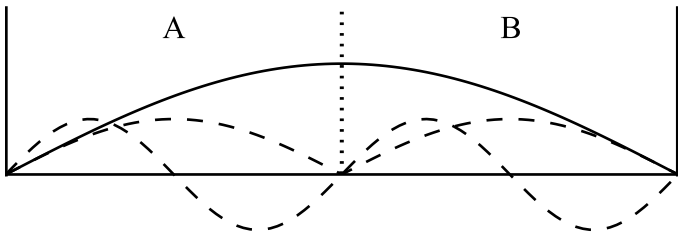

Figure 3.5.: Lowest lying states of the entire system $A \cup B$ (solid line), and the two lowest lying states of each subsystems A and B (dashed lines).

chain lattice of length L with open boundary conditions. The Hilbert space of each site i is given by $\mathcal{H}_i$ and has dimension $\dim \mathcal{H}_i = d$. The Hilbert space of the full system is then $\mathcal{H} = \bigotimes_{i=1}^{L} \mathcal{H}_i$, and has $\dim \mathcal{H} = d^L$. Starting with the isolated first site $i = 1$, the remaining sites are successively appended to the system. To avoid the exponential growth of the full Hilbert space, in each step the new Hilbert space is truncated to a maximum dimension M. Denoting the truncated Hamiltonian with dimension $\dim \tilde{\mathcal{H}} \leq M$ with a tilde, this step can be formally written for the first two sites as

$$\mathcal{H}_1 \otimes \mathcal{H}_2 \to \tilde{\mathcal{H}}_2, \tag{3.18}$$

where the index on the right-hand side denotes the (truncated) Hilbert space of the sites $i = 1, \ldots, n$. The general form of this transformation is thus

$$\tilde{\mathcal{H}}_{n-1} \otimes \mathcal{H}_n \to \tilde{\mathcal{H}}_n, \tag{3.19}$$

and once this procedure has been performed on the entire system, we have an approximated representation of the original system. But how do we decide how we truncate the Hilbert spaces? Since we are generally interested in the ground state of the system, one possible suggestion could be to keep only the part of the Hilbert space which corresponds to states of lowest energy. In fact, this is precisely what is done in Wilson's NRG. After a careful mapping of the physical system to a rather artificial chain lattice, by keeping only the lowest energy states in each step a faithful (even 'numerically exact') solution is found for the ground state.

However, this scheme fails for generic systems, which can be understood immediately by considering the simple case of a particle in a box. The crucial problem is visualized in Fig. 3.5, where the system has been divided into two subsystems A and B. The lowest-lying energy states (in fact, *all* states) of each subsystem vanish at the boundary. However, the ground state of the full system $A \cup B$ has its maximum amplitude in the center. It is immediately clear that no finite combination of the states from A and B can yield the ground state for $A \cup B$.

White's key insight for the DMRG algorithm was to base the truncation scheme not on the lowest-lying energies, but rather on those states that contribute most to the system. These states are those with the most weight in the reduced density matrix of each subsystem, which closes the loop to the matrix product representation we discussed above.

3.4. Density Matrix Renormalization Group

The original formulation of the DMRG by White is found in Ref. [11]. Based on Wilson's numerical renormalization group (see below), it was formulated from the viewpoint of real-space renormalization: Starting from a single site, more and more sites are successively added to the Hamiltonian while in each step truncating the Hilbert space to keep only those states with the largest spectral weight in the density matrices. After a desired system size is reached, the obtained state is optimized by iteratively optimizing each individual site in *sweeps* through the system. A comprehensive overview of this original formulation can be found in Ref. [45].

The further development of this method, however, has led to the realization that it, in fact, naturally operates on matrix product states [40]. The DMRG algorithm can be equivalenty reformulated as the variational optimization of a given MPS. For the results of this thesis, we used an implementation of the MPS-DMRG approach which has been developed with support from the Swiss Platform for High-Performance and High-Productivity Computing (HP2C) and based on the ALPS libraries [46, 47].

3.4.1. Variational optimization of a matrix-product state

Assume we have a Hamiltonian H given as an MPO. Furthermore, consider the class of normalized matrix product states with a maximum matrix dimension of M. To find the optimal approximation to the (true) ground state of H within this class of states, we need to find the state $|\psi\rangle$ which minimizes the energy,

$$E = \frac{\langle\psi|\hat{H}|\psi\rangle}{\langle\psi|\psi\rangle}. \tag{3.20}$$

After introducing a Lagrangian multiplier λ, this translates to extremizing

$$\langle\psi|\hat{H}|\psi\rangle - \lambda\,\langle\psi|\psi\rangle\,. \tag{3.21}$$

Such a minimization is generally computationally difficult and not very efficient, due to the big number of free parameters. However, a variational solution can be found by iteratively minimizing one tensor of $|\psi\rangle$ at a time, then proceeding to the next one. While this scheme is essentially identical to White's single-site DMRG algorithm, the optimization can also be carried out by considering two sites at a time (the two-site DMRG algorithm), which might converge better under certain circumstances. However, generally it is *a priori* not obvious, which of the two methods leads to a better convergence. Details on the two-site optimization can be found in Refs. [11, 45].

Let us now assume our MPS to be in (either left- or right-) canonical form, so that each tensor is properly normalized. In order to optimize a single tensor, i.e. minimize Eq. (3.21) with respect to this tensor, we fix all other tensors in the MPS, leaving out the currently considered one. As an example, we consider the situation of Fig. 3.6 and optimize the tensors $A_3^{\sigma_3}$. The effective Hamiltonian $\hat{H}_{\text{eff}}$ is then found by leaving out A_3, shown diagrammatically in Fig. 3.6. To optimize the local tensors, we first reshape all d matrices $A_3^{\sigma_3}$ into one big vector $\mathbf{A}_3$ of maximum length dM^2. The coefficients in this vector are the variational parameters and the minimization can be written as

$$\min_{A_3}\Big(\langle\psi|\hat{H}|\psi\rangle - \lambda\,\langle\psi|\psi\rangle\Big) = \min_{A_3}\Big(\mathbf{A}_3^\dagger H_{\text{eff}}\mathbf{A}_3 - \lambda\mathbf{A}_3^\dagger\cdot\mathbf{A}_3\Big)\,. \tag{3.22}$$

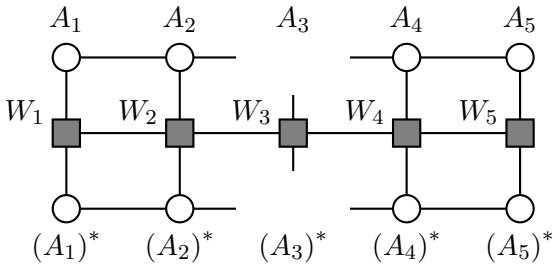

Figure 3.6.: Graphical representation of the effective Hamiltonian H_{eff} for the optimization of tensor A_3 in a 5-site system.

This minimization can now be performed by solving

$$\frac{\partial}{\partial \mathbf{A}_3^\dagger}\left(\mathbf{A}_3^\dagger H_{\text{eff}}\mathbf{A}_3 - \lambda \mathbf{A}_3^\dagger \cdot \mathbf{A}_3\right) = 0, \tag{3.23}$$

which leads to the eigenvalue problem

$$H_{\text{eff}}\mathbf{A}_3 = \lambda \mathbf{A}_3. \tag{3.24}$$

An exact numerical diagonalization of this problem for matrices of dimension dM^2 is in most cases out of the question. However, as we are usually only interested in the ground state, the eigenvalue problem can be solved by sparse-matrix techniques such as the Lanczos [48] or Jacobi-Davidson [49] algorithms, which are numerically fast but only give results for the lowest few eigenstates and eigenvectors.

3.4.2. Optimization procedure

Having discussed the optimization of a single tensor, we now turn to the optimization of the full MPS $|\psi\rangle$. This procedure can be broken down into the following steps:

1. **Initial MPS and normalization**
   Construct an *initial MPS* for the desired system, truncated to a maximum bond dimension of M. Typically this is done by either constructing a state using some knowledge about the physical system, or by generating a random MPS. This initial MPS is then transformed into *right-canonical* (see above) to ensure a proper normalization of its tensors.

2. **Right sweep**
   Starting at site $i = 1$, solve the eigenvalue problem for tensor A_1. Similar to the calculation of the canonical form above, the new A_1 is then decomposed by SVD into $A_1 = USV^\dagger$, where the matrix U becomes the new tensor A_1, and the $SV^\dagger$ is multiplied from the left to the next tensor A_2. This ensures proper normalization of the tensors (as by definition $U^\dagger U = \mathbb{1}$). Then, we move to the next site, $i \to i + 1$, and repeat this procedure until $i = L - 1$.

3. **Left sweep**
   Once the right sweep has optimized site $i = L-1$, the right sweep has transformed the entire system (with the exception of site $i = L$) into left-canonical form. We can thus simply repeat set previous step in the other direction, with the left sweep starting at site $i = L$. As in step 3, the tensor A_i is diagonalized, and after the SVD,

the matrix $V^\dagger$ becomes A_i. US are multiplied from the right to the tensor A_{i-1}. Again, this ensures normalization as $V^\dagger V = \mathbb{1}$. Repeat for the next site, $i \to i-1$, until $i = 1$.

The process of sweeping once right and then left are commonly referred to as one 'sweep' through the system. This sweeping is repeated until the energy converges. For a system with open boundary conditions, this procedure recovers precisely the single-site DMRG method, albeit formulated in the language of MPS [11, 40, 50]. Since in each step the parameters of one tensor are optimized, the energy can only be lowered in this process. For one-dimensional gapped Hamiltonians which have an area law, this method works extraordinarily well, producing results with an accuracy of 10^{-9} and better [50].

3.4.3. Ensuring ground state convergence

The bond dimension parameter M is a crucial factor determining the accuracy of the DMRG results. If M is too small for the system at hand, the resulting wavefunction may not be represented accurately. However, performing several calculations with increasing M can remedy this problem as one can examine the convergence behavior towards the exact result (we remind ourselves that in the limit $M \to \infty$ DMRG produces exact results). Another more subtle issue arises from the fact that the DMRG is globally a variational method and as such might get stuck in a metastable minimum [51].

A general technique to avoid metastable minima in DMRG calculations which is especially useful in the MPS formulation was given by S. White in Ref. [52]. In the next subsection we demonstrate the occurrence of effective long-range interactions in the simulation of 2D systems with the DMRG. Consider for instance a hopping term between two sites which are nearest-neighbors in the physical system, but far apart in the MPS representation. Correlations due to this interaction might be incorrectly suppressed in the calculations, since in the DMRG process the extra states required to allow for the hopping between the two physical sites might not help lower the energy of one tensor, unless they are already present in the tensor corresponding to the other site [53]. The solution suggested in Ref. [52] is to add a *noise* term to the density matrix at each step. This leads to correlations between sites further apart being artificially inserted, and thus the physical correlations are "kept alive" until the calculation has run once through the entire system. At this point, the addition of extra terms can generally be turned off.

3.4.4. 2D lattices

The DMRG is constructed to work on one-dimensional lattices, and to simulate higher-dimensional systems one must first map them to a chain. While this mapping introduces long-range interactions, which however increase the computational costs only slightly, a much bigger problem arises due to the entanglement scaling. In 1D systems with an area law the entanglement entropy is constant, but in 2D it grows with the boundary of the subsystem, i.e. linearly in system width. In the chain representation, in order to keep the accuracy of the calculation fixed, this growth in entanglement entropy can only be accommodated for by keeping more states in the calculation. In fact, the number of required states grows exponentially with the system width [54]. However, even with the exponential growth MPS can still successfully describe systems of moderate width. In typical applications, the used lattices have a long length $L \sim \mathcal{O}(10^2)$ and a somewhat smaller width $W \sim \mathcal{O}(1)$, with open boundary conditions in the length direction, and (if required) periodic boundary conditions in the width direction. A thorough discussion of

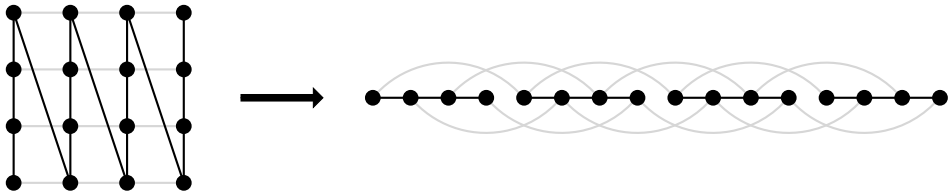

Figure 3.7.: One possible mapping of a 4×4 square lattice to a one-dimensional system, demonstrating the introduction of long-range interactions (gray lines) to the resulting 1D chain.

the application of DMRG to 2D systems can be found in Ref. [53]. In Fig. 3.7 we demonstrate one possible way of mapping a 4×4 square lattice system to a chain, where the gray lines in the right figure show the induced long-range interactions, and the black lines indicate the nearest-neighbor hoppings.

3.4.5. Calculating excited states

Aside from the ground state properties, one can also use the DMRG to calculate excited states. In fact, the calculation of the gap to the first excited state is oftentimes of fundamental importance for the classification of phases and their robustness [53].

A powerful way to calculate excited states in the DMRG takes direct advantage of the formulation in the MPS framework, which makes it possible to calculate overlaps of wave functions in separate calculations. After the ground state $|\psi_0\rangle$ of a Hamiltonian H is found in an MPS representation using DMRG, one defines a Hamiltonian

$$H' = H + wP_0, \tag{3.25}$$

where $P_0 = |\psi_0\rangle \langle\psi_0|$ is a projection operator to the ground state and $w > 0$ is an energy penalty for states which are not orthogonal to $|\psi_0\rangle$. For a large enough w, the ground state $|\psi_1\rangle$ of the modified Hamiltonian H' will be the second lowest eigenstate (which can be either an excited state or a second ground state in a degenerate system) of the original Hamiltonian H [53]. After the states $|\psi_0\rangle$ and $|\psi_1\rangle$ are found, one can proceed to calculate the next excited state by including both P_0 and a new projector $P_1 = |\psi_1\rangle \langle\psi_1|$ in the Hamiltonian.

Simply put, in each calculation a state with lowest energy is found with the constraint that it be orthogonal to a given set of other states. While this method provides a very efficient way of obtaining excited states and energy spectra, we briefly comment on the computational cost. The result for an excited state depends greatly on the accuracy of the lower-lying previously obtained states. Thus, for an accurate computation of many excited states the maximum matrix dimension M kept for all DMRG runs must be much higher than just for a ground state calculation. Furthermore, since with this method the excited states can only be computed sequentially (as the previously found states are the required input to the calculation), the number of excited states which are accessible to a high accuracy is limited to the order of $\mathcal{O}(1)$ in a realistic setting.

3.5. Numerical Renormalization Group

After having introduced the DMRG algorithm, we now — somewhat anachronistically — present the numerical renormalization group (NRG) algorithm, which was invented by K.

Wilson in 1975 [10] and later on laid the foundation for the development of the DMRG. While the DMRG algorithm is constructed for ground state calculations of generic lattice Hamiltonians, the NRG focuses on the solution of quantum impurity problems, see Sec. 2.1. The two main steps in a NRG run consist of mapping the quantum impurity problem onto a semi-infinite tight-binding chain. In the second step, this chain is iteratively diagonalized. This diagonalization is essentially equivalent to a sweep in the DMRG, with the main difference that the truncation of the Hilbert space is performed with respect to the lowest-lying energy states, rather than the density matrix eigenvalues. The relation between the NRG and other RG methods is straight-forward and it allows for the examination of an RG flow of thermodynamic observables.

3.5.1. Hybridization function

An important feature of the Hamiltonian for a quantum impurity problem given in Eqs. (2.2)-(2.4) is the fact that the host system is non-interacting and thus readily diagonalizable in momentum space, i.e.

$$H_{\text{host}} = \sum_{\mathbf{k}\sigma} \epsilon_{\mathbf{k}}\, c^{\dagger}_{\mathbf{k}\sigma} c_{\mathbf{k}\sigma}. \tag{3.26}$$

In this case the conduction band degrees of freedom can be integrated out, yielding the so-called hybridization function $\Delta(\omega)$. The latter contains *all* relevant information about the host system from the viewpoint of the impurity and is thus the only input needed to solve the impurity problem. The precise form of the hybridization function for the Hamiltonian given above is

$$\Delta(\omega) = \Delta^R(\omega) - i\Delta^I(\omega) = \lim_{\delta\to 0} \sum_{\mathbf{k}} \frac{|V_{\mathbf{k}}|^2}{\omega + i\delta - \epsilon_{\mathbf{k}}}. \tag{3.27}$$

In the case that the hybridization is independent of $\mathbf{k}$, $V_{\mathbf{k}} = V$, this becomes

$$\Delta(\omega) = |V|^2 \sum_{\mathbf{k}} \frac{1}{\omega - \epsilon_{\mathbf{k}}} - i\pi|V|^2 \sum_{\mathbf{k}} \delta(\omega - \epsilon_{\mathbf{k}}). \tag{3.28}$$

Real and imaginary parts of $\Delta(\omega)$ are related to each other by the Kramers-Kronig relation [3], and thus it suffices to know only the imaginary part, which is given by the local density of states of the host site coupling to the impurity. Assuming, as before, that the impurity couples to the site at $\mathbf{r} = \mathbf{0}$, this yields

$$\begin{aligned} \Delta^I(\omega) &= \pi V^2 \rho_{\mathbf{0}}(\omega) \\ &= -V^2\, \mathrm{Im}\, G^{(0)}(\mathbf{0}, \mathbf{0}; \omega), \end{aligned} \tag{3.29}$$

where we have used that the local density of states can be expressed in terms of the local retarded Green function. The superscript (0) here indicates that the host system is comprised of free conduction electrons. The calculation of such local Green functions will be discussed in much detail in Part III, along with the various low-energy properties of the hybridization functions we encounter.

In summary, the only required input to the NRG method is the (imaginary part of the) hybridization function $\Delta(\omega)$ and the parameters for the isolated impurity, U, ϵ_f and V.

3.5.2. Wilson chain

In order to use the aforementioned RG scheme to treat the problem of a magnetic impurity embedded in a generic d-dimensional host system, we first need to discretize the system. To this end, the host system (which is represented here by the hybridization function) is mapped onto a semi-infinite tight-binding chain, the so-called Wilson chain. This mapping is possible even for 2D and 3D host systems, since in the Kondo effect the s-wave modes are dominant at low energies and any angular dependence of system parameters is not important. The idea is to iteratively map energy intervals—going from high to low energies—to the discrete sites of the Wilson chain. Here, the interpretation is intuitive: going to greater distances on the Wilson chain directly translates to going to lower energies in the original problem. Or equivalently, in the real-space RG sense, each site in the Wilson chain can be associated with a real-space shell around the impurity. The first site in the Wilson chain then corresponds to the region closest to the impurity, and it in turn couples to a shell further away, and so forth [3, 10].

Logarithmic discretization

All of the information about the non-interacting host system that is relevant to the impurity problem is contained in the hybridization function. This implies that the particular form of the host Hamiltonian does not matter as long as the hybridization function does not change. The following reformulation of the Anderson impurity model will prove amenable to the discretization in the next step:

$$H = H_{\mathrm{imp}} + \sum_{\sigma} \int_{-D}^{D} \mathrm{d}\epsilon \; g(\epsilon)\, a^{\dagger}_{\epsilon\sigma} a_{\epsilon\sigma} + \sum_{\sigma} \int_{-D}^{D} \mathrm{d}\epsilon \; h(\epsilon) \left(f^{\dagger}_{\sigma} a_{\epsilon\sigma} + \mathrm{H.c.} \right), \tag{3.30}$$

with a generic dispersion $g(\epsilon)$, a hybridization $h(\epsilon)$ and fermionic operators $[a_{\epsilon\sigma}, a^{\dagger}_{\epsilon'\sigma'}] = \delta(\epsilon - \epsilon')\delta_{\sigma\sigma'}$. For this new formulation, the hybridization function $\Delta(\omega)$ is given by [55]

$$\Delta(\omega) = \pi \frac{\mathrm{d}\epsilon(\omega)}{\mathrm{d}\omega} h\left(\epsilon(\omega)\right)^2, \tag{3.31}$$

with $\epsilon(\omega)$ the inverse function to $g(\epsilon)$, i.e. $g(\epsilon(\omega)) = \omega$. The functions $g(\epsilon)$ and $h(\epsilon)$ must now be constructed in such a way that the hybridization function equals that in Eq. (3.29). For a constant $\Delta(\omega) = \Delta_0$, this can for instance be achieved by setting $g(\epsilon) = \epsilon$ and $h(\epsilon) = \sqrt{\Delta_0/\pi}$.

In the form of Eq. (3.30) the system can now be conveniently discretized. To this end, we introduce a discretization parameter $\Lambda > 1$ and define a set of intervals within the band with the discretization points (see Fig. 3.8(a))

$$\omega_n = \pm \Lambda^{-n}, \qquad n = 0, 1, 2, \ldots. \tag{3.32}$$

There is a certain freedom to the choice of the functions g and h in Eq. (3.31). Here, we follow Ref. [55] and shift all ϵ-dependence into the function $g(\epsilon)$. The function $h(\epsilon)$ is approximated as a step function, where for each interval $[\omega_n, \omega_{n+1}]$ it is given by the average of the hybridization function in that interval (see Fig. 3.8(b))

$$h_n^{\pm} = \frac{1}{d_n} \int^{n} \mathrm{d}\epsilon \, \frac{\Delta(\epsilon)}{\pi}, \tag{3.33}$$

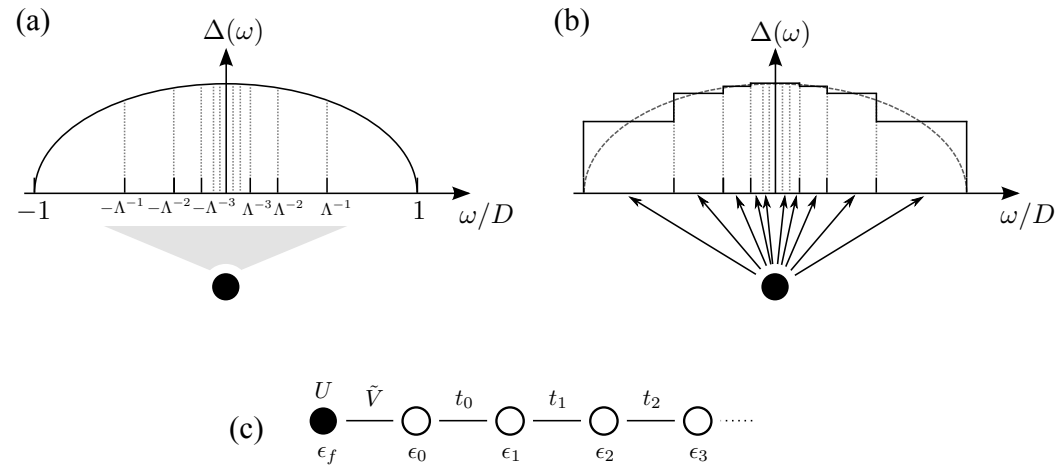

Figure 3.8.: Logarithmic discretization of the hybridization function coupling to the impurity (black disk). (a) The hybridization function $\Delta(\omega)$ (solid line, here as an example that of a semi-infinite chain, see Chap. 7.1.1). While the impurity couples to the full function, the band is logarithmically discretized with a parameter $\Lambda > 1$. (b) The hybridization function is then transformed into a discrete set of values. (c) From the discretized hybridization function the semi-infinite Wilson chain is constructed.

where the integration runs over the nth interval, and $d_n = \Lambda^{-n}(1 - \Lambda^{-1})$ is the width this interval. Finally, the discretized Hamiltonian is given by

$$\begin{aligned} H =& H_{\text{imp}} + \sum_{n\sigma} \left(\xi_n^+ a_{n\sigma}^\dagger a_{n\sigma} + \xi_n^- b_{n\sigma}^\dagger b_{n\sigma} \right) \\ &+ \frac{1}{\sqrt{\pi}} \sum_{n\sigma} \left(f_\sigma^\dagger \left(\gamma_n^+ a_{n\sigma} + \gamma_n^- b_{n\sigma} \right) + \left(\gamma_n^+ a_{n\sigma}^\dagger + \gamma_n^- b_{n\sigma}^\dagger \right) f_\sigma \right), \end{aligned} \tag{3.34}$$

where

$$\gamma_n^\pm = \sqrt{\pi d_n} h_n^\pm, \qquad \xi_n^\pm = \frac{\int^{\pm,n} \mathrm{d}\epsilon\, \Delta(\epsilon)\epsilon}{\int^{\pm,n} \mathrm{d}\epsilon\, \Delta(\epsilon)}. \tag{3.35}$$

The fermionic operators $a_{n\sigma}$ and $b_{n\sigma}$ act in the nth energy interval, for a derivation see Ref. [56]. In the next step, the Hamiltonian (3.34) is mapped onto a semi-infinite tight-binding chain.

Mapping to semi-infinite chain

From the discretized Hamiltonian in Eq. (3.34) we can readily read off the fermionic degree of freedom to which the impurity directly couples,

$$c_{0\sigma} = \frac{1}{\int \mathrm{d}\epsilon\, \Delta(\epsilon)} \left(\gamma_n^+ a_{n\sigma} + \gamma_n^- b_{n\sigma} \right). \tag{3.36}$$

The operators $c_{0\sigma}$ act on the zeroth orbital of the Wilson chain. The operators for the following sites can be iteratively constructed, alongside with the effective hopping amplitudes t_n between these sites and the level energies for each site, ϵ_n [56]. The hopping amplitudes (see Fig. 3.8(c)) decay exponentially with distance n—a direct consequence of the logarithmic discretization—and thus eventually guarantee a clear scale separation

in the energies. For certain special cases, the calculation of the t_n's can be performed analytically and in the limit of a completely flat hybridization function the level energies are $\epsilon_n = 0$ for all n, and the hopping amplitudes are given by

$$t_n = \frac{(1+\Lambda^{-1})(1-\Lambda^{-n-1})}{2\sqrt{1-\Lambda^{-2n-1}}\sqrt{1-\Lambda^{-2n-3}}}\Lambda^{-n/2}, \tag{3.37}$$

where we explicitly find the exponential dependence on n. Of course, in practice we cannot treat an infinite Wilson chain, therefore one truncates the chain after a certain number of sites when sufficiently low energy ranges are reached. Typical values of Λ are on the order of 2, and the Wilson chain typically reaches lengths of about 60 sites [56].

After the mapping, when truncating the Wilson chain at site N, we are left with what is essentially a single-impurity Anderson model for a semi-infinite inhomogeneous 1D tight-binding chain, given by the Hamiltonian [56]

$$\begin{aligned} H =& H_{\mathrm{imp}} + \tilde{V}\sum_{\sigma}\left(f_\sigma^\dagger c_{0\sigma} + \mathrm{H.c.}\right) \\ &+ \sum_{\sigma,n=0}^{N}\epsilon_n c_{n\sigma}^\dagger c_{n\sigma} + \sum_{\sigma,n=0}^{N-1}\left[t_n\left(c_{n\sigma}^\dagger c_{n+1\sigma} + \mathrm{H.c.}\right)\right], \end{aligned} \tag{3.38}$$

where the operator $c_{n\sigma}$ destroys a fermion with spin σ on the Wilson chain at site n, and the parameters ϵ_n and t_n are given above. The hybridization $\tilde{V}$ is given by

$$\tilde{V}^2 = \frac{1}{\pi}\int_{-D}^{D}\mathrm{d}\epsilon\,\Delta(\epsilon) \tag{3.39}$$

which, using Eq. (3.29), in the case of a constant bare hybridization $V_{\mathbf{k}} = V$ reduces to $\tilde{V} = V$.

3.5.3. Finding the ground state

After the transformations introduced in the previous subsections, we have successfully reformulated the Anderson impurity model as a finite lattice system, consisting of the strongly-correlated impurity and the Wilson chain. At this point the exponential decay of the hopping amplitudes along the chain come into play: Knowing the spectrum of a given part of the chain up to some length, the remaining sites only make exponentially small corrections due to the exponentially small energy scales further down the chain [40]. To find the ground state, the NRG recipe follows the ideas presented in Sec. 3.3: Starting with just the impurity and the first site, more sites are added iteratively and in each step the Hilbert space is truncated to keep only the M states of lowest energy. In contrast to general lattice Hamiltonians, this truncation scheme is perfectly suited for Kondo physics and their particular formulation as a Wilson chain.

Let us now formulate this scheme more precisely [57]: The dimension of the impurity's Hilbert space is $d_0 = 4$, and the local Hilbert spaces of each chain site is also of dimension $d = 4$. The Hamiltonian of the chain up to length n, $\tilde{\mathcal{H}}_n$, lives in a Hilbert space with basis states $|\sigma_i\rangle$, where $i = 0$ for the impurity and then $i = 1, \ldots, n$ for the sites in the chain.

Starting with a chain of length n such that its Hamiltonian $\tilde{\mathcal{H}}_n$ can be diagonalized exactly, we find the α eigenstates $|\psi_\alpha^n\rangle$. One then projects $\tilde{\mathcal{H}}_n$ on the M states of lowest energy and adds the next site at $n+1$ to the chain, yielding $\tilde{\mathcal{H}}_{n+1}$. The Hilbert space of

the new Hamiltonian $\tilde{\mathcal{H}}_{n+1}$ is of dimension dD and its eigenstates can be written as

$$|\psi_n^\beta\rangle = \sum_{\sigma_n=1}^{d} \sum_{\alpha=1}^{D} [A_n^{\sigma_n}]_{\alpha\beta} |\psi_{n-1}^\alpha\rangle |\sigma_n\rangle , \tag{3.40}$$

where $[A_n^{\sigma_n}]_{\alpha\beta}$ is a matrix composed of the coefficients in the expansion. From this formulation one immediately sees that the NRG process operates on matrix products states. In each step of the iterative diagonalization, the current state can be written (by repeatedly using Eq. (3.40)) as an MPS, viz.

$$|\psi_n\rangle = \sum_{\sigma_0,\ldots,\sigma_n} A_0^{\sigma_0} A_1^{\sigma_1} \ldots A_n^{\sigma_n} |\sigma_1 \ldots \sigma_n\rangle . \tag{3.41}$$

In the language of the density matrix renormalization group, we can think of the iterative diagonalization process in the NRG as a single right-sweep in which the truncation scheme keeps the lowest energies rather than those with largest weight in the reduced density matrix.

Renormalization group flow

In contrast to the variational optimization of a general MPS as discussed in the context of DMRG, the NRG procedure can be readily understood from a RG point of view. Whereas in the DMRG algorithm sweeps are performed back and forth until the energy converges, traversing along the chain in the NRG directly corresponds to the standard RG scheme in which going to greater distances implies consideration of lower energy scales. In this sense, from the NRG one can obtain the true RG flow as a function of energies, or equivalently temperature, recovering the fixed points of the corresponding quantum impurity problem discussed in Sec. 2.1.

3.5.4. Calculation of dynamic quantities

A physical quantity of which we make ample use in this thesis is the impurity spectral function of the Anderson impurity model,

$$A_{\mathrm{imp},\sigma}(\omega, T) = -\frac{1}{\pi} \operatorname{Im} G_{\mathrm{imp},\sigma}(\omega, T), \tag{3.42}$$

where $G_{\mathrm{imp},\sigma}(\omega, T)$ is the impurity Green function for the spin-species σ, evaluated at an energy ω and temperature T. Knowing the eigenstates, $|r\rangle$, and eigenenergies, E_r, of the Hamiltonian, the spectral function can be written in the Lehmann representation as [56]

$$A_{\mathrm{imp},\sigma}(\omega, T) = \frac{1}{\mathcal{Z}(T)} \sum_{r,r'} \left|M_{r,r'}\right|^2 \left(e^{-\beta E_r} + e^{-\beta E_{r'}}\right) \delta(\omega - (E_{r'} - E_r)), \tag{3.43}$$

with the partition function $\mathcal{Z}(T) \equiv \sum_r \exp(-\beta E_r)$ and the many-body matrix elements $M_{r,r'} = \langle r|f_\sigma|r'\rangle$. During the iterative diagonalization process, the spectral function can be calculated in each step, yielding a result which is valid for the energy range corresponding to the given step. For each step $n = 1, 2, \ldots$, the spectral density is thus evaluated at a frequency $\omega \sim \omega_n$, where ω_n is the characteristic energy scale of the Hamiltonian $\tilde{\mathcal{H}}_n$. This procedure yields a discrete spectrum. To generate a smooth spectrum, the δ distribution in Eq. (3.43) is replaced by a continuous function which is typically taken

to be a Gaussian [58] or logarithmic Gaussian [59] distribution.

Part II.

The Heisenberg-Kitaev model in triangular $j = 1/2$ Mott insulators

Chapter 4.

Transition metal oxides as $j = 1/2$ Mott insulators

The transition metals are found in the center of the periodic table and are defined by the presence of a partially filled (inner) d shell. Of great interest are the transition metal oxides (TMO), in which each transition metal ions is surrounded by a cage of oxygen ions (the so-called ligands). The physical phenomena found in the $3d$ TMOs range from high-T_c superconductivity in layered cuprates, colossal magnetoresistance in perovskite manganites, to the coexistence of magnetism and ferroelectricity [60]. In the crystal field created by the ligand cage the orbital degrees of freedom of the transition metals take on a prominent role [61]. Therefore, the diverse properties of the TMOs are largely a result of the strong electron-electron interaction between electrons occupying the same orbital.

While the physics of $3d$ TMOs form a venerable but still vibrant field of research, the heavier $4d$ and $5d$ TMOs introduce interesting and non-trivial new physics due to the strong spin-orbit coupling found in these elements. In fact, the TMOs with partially filled $5d$ shells are largely governed by a balanced interplay of electronic correlations, crystal field effects and spin-orbit coupling. All three contributions enter with roughly the same strength, facilitating a large variety of quantum states in these materials, such as Weyl semi-metals, axion insulators, or topological Mott insulators [62].

We focus here on a special situation in which the transition metal oxides become Mott insulators, in which strong spin-orbit coupling leads to the formation of an effective $j = \frac{1}{2}$ degree of freedom. Such a state was first observed by Kim et al. in 2008 [63], where despite the assumption that it should be metallic, the iridate Sr_2IrO_4 was found to be a Mott insulator exhibiting exactly the aforementioned physics. The discovery of this novel state has spurred a lot of research, and it was found to also occur in the hexagonal iridates Na_2IrO_3 [64] and Li_2IrO_3 [65]. There, the effective degrees of freedom form well-separated layers of honeycomb lattices. The orbital nature of the localized 'spins' introduces a strong spatial dependence of the interactions, and Khaliullin et al. suggested in Ref. [33] that these materials might be described by a combination of Heisenberg physics and the celebrated Kitaev model, see Sec. 2.3.

In this chapter, we recapitulate the formation of such $j = \frac{1}{2}$ states in transition metal oxides with partially filled $5d$ shells and discuss it as a possible ground state for the recently synthesized iridate $Ba_3IrTi_2O_9$, which contains transition metal oxides forming layers of a *triangular* lattice. With this motivation we discuss the physics of the Heisenberg-Kitaev model on the triangular lattice in the next chapter.

4.1. Effective spin moment in transition metal oxides

In this section, we demonstrate how the combined effects of crystal field splitting and spin-orbit coupling lead to the formation of a Mott insulating state in the $5d$ transition metals oxides, and finally to an effective spin-like degree of freedom.

4.1.1. Atomic orbitals

From quantum mechanics we know that the state of an electron in a hydrogen atom is described completely by a set of four quantum numbers: the principal quantum number n, the azimuthal quantum number ℓ, the magnetic quantum number m_ℓ and the electron's spin quantum number m_σ. In a real-space representation, the wavefunction of the electron can be split into a radial part $R_{n\ell}$, an angular part Y_ℓ^m and the spin wavefunction σ^{m_s}. In polar coordinates, $\mathbf{r} = (r, \theta, \phi)$, it is then given as:

$$\psi_{n\ell m_\ell m_\sigma}(r, \theta, \phi) = R_{n\ell}(2r/n) \cdot Y_\ell^{m_\ell}(\theta, \phi) \otimes \sigma^{m_\sigma}, \tag{4.1}$$

where the angular component component $Y_\ell^{m_\ell}$ is a spherical harmonic and the radial component R has a generally complex structure but always decays exponentially in r. The real-space part of these wave functions (i.e. omitting the spin part) defines the so-called *atomic orbitals*, which give the probability amplitude for an electron to be found in a given location within the atom.

The principal quantum number n can take on integer values $n = 1, 2, \ldots$, and it describes the different energy shells of the atom. The azimuthal quantum number ℓ determines the orbital angular momentum of the orbital. For a given energy level n, the groups of orbitals corresponding to different values of ℓ are labelled s, p, d and f, referring to $\ell = 0, 1, 2$ and 3, respectively. For $\ell > 3$ the naming continues in alphabetical order (omitting j). The so-called subshell defined by n and ℓ still has some degree of freedom which is captured by the magnetic quantum number m_ℓ. The latter can take on integer values $m_\ell = -\ell, \ldots, \ell$. Thus, the determination of a specific orbital requires all three quantum numbers n, ℓ, and m_ℓ. Due to the Pauli exclusion principle, each orbital can host at most two electrons of different spin quantum number, and thus the state of a single electron is entirely described by the four quantum numbers.

Neglecting at this point effects such as the relativistic spin-orbit coupling (see below) and placing the atom in a spherical potential, for a given n and ℓ, the total energy of the considered state is independent of the value of the magnetic quantum number. This degeneracy can be lifted by external effects, such as a crystal potential which arises when considering atoms in a material.

Although these orbitals are obtained for the hydrogen atom, they are at least qualitatively similar to the description of atoms with more than one electron, and can thus be used as a good approximation.

Hund's rule(s)

Shortly after the advent of quantum mechanics and the atomic orbital model, Friedrich Hund in 1925 formulated a set of rules [66,67] which are used to determine the electronic configuration of a multi-electron atom in its ground state. Although Hund formulated three rules, here we only consider the first rule, which can be stated as follows:

> For a given electronic configuration, the term with maximum multiplicity has the lowest energy.

The *multiplicity* is equal to $2S + 1$, where S is the total spin for all electrons. To fill up the degenerate energy levels in the ground state of the atom, according to Hund's rule, one first places one electron with a given spin, e.g. spin-$\uparrow$, in every orbital. Once all orbitals are occupied, one starts filling up the orbitals with electrons of opposite spin, in our example spin-$\downarrow$.

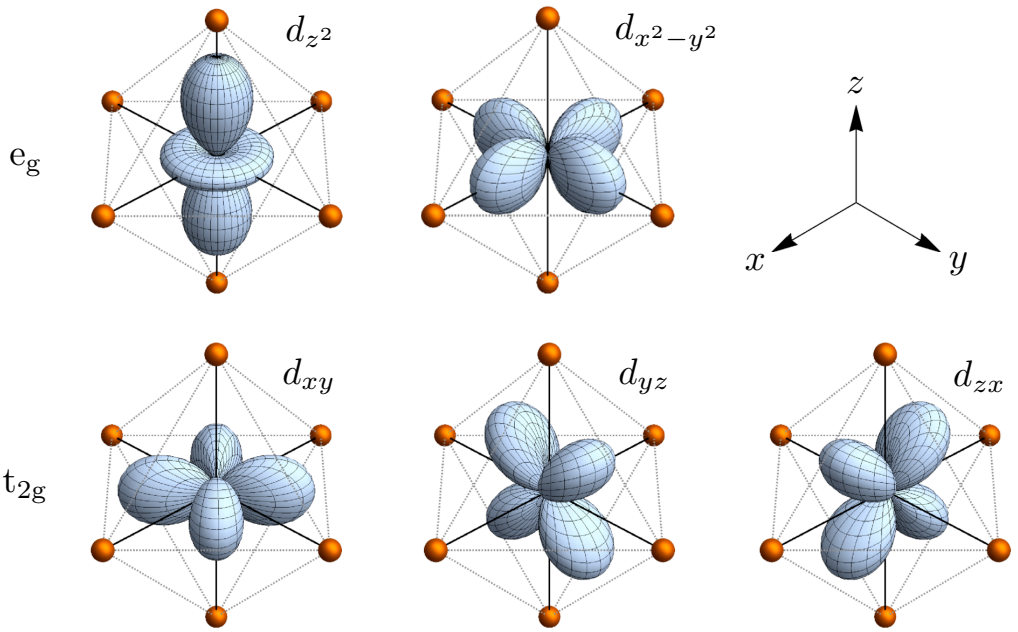

Figure 4.1.: The five d-orbitals for $n = 3$ in the octahedral oxygen cage of a transition metal oxide. The two e_g orbitals are spatially extended towards the oxygen atoms, raising their energy due to the Coulomb interaction. The three t_{2g} orbitals, however, are pointing away from the oxygens.

4.1.2. e_g and t_{2g} orbitals in a crystal field

The transition metals are defined by a partially filled inner d shell, thus we specifically consider here these d level orbitals embedded into a crystal background. For an atom in a *spherical* potential, the d level (with angular momentum quantum number $\ell = 2$) has five degenerate eigenfunctions $|\ell, m_\ell\rangle$, where $m_\ell = \pm 2, \pm 1, 0$. In most transition metal oxides however, the transition metal ion is surrounded by an octahedral cage of six oxygen ions—the so-called ligands—which create a crystal field with *cubic* (rather than spherical) symmetry acting on the d-electrons of the transition metal atom, lifting the 5-fold degeneracy. In this case, the eigenfunctions of a d-electron are not the $|\ell, m_\ell\rangle$ states anymore, but rather linear combinations of them yielding the following five real-valued orbitals [68]

$$\left.\begin{aligned} d_{z^2} &= |2,0\rangle \\ d_{x^2-y^2} &= \tfrac{1}{\sqrt{2}}\left(|2,2\rangle + |2,-2\rangle\right) \end{aligned}\right\} \mathrm{e}_g\text{orbitals} \tag{4.2}$$

$$\left.\begin{aligned} d_{xy} &= -\tfrac{i}{\sqrt{2}}\left(|2,2\rangle - |2,-2\rangle\right) \\ d_{yz} &= \tfrac{1}{\sqrt{2}}\left(|2,1\rangle + |2,-1\rangle\right) \\ d_{zx} &= -\tfrac{i}{\sqrt{2}}\left(|2,1\rangle - |2,-1\rangle\right), \end{aligned}\right\} \mathrm{t}_{2g}\text{orbitals} \tag{4.3}$$

which are shown in Fig. 4.1. All three t_{2g} orbitals have the same energy, as do the two e_g, but the energy of the t_{2g} orbitals is lower than that of the e_g orbitals, which can be understood from the following perspective: The two e_g orbitals are aligned along the z-axis and as a flat "cross" along the $x-$ and $y-$axes, respectively. The d-electrons are therefore

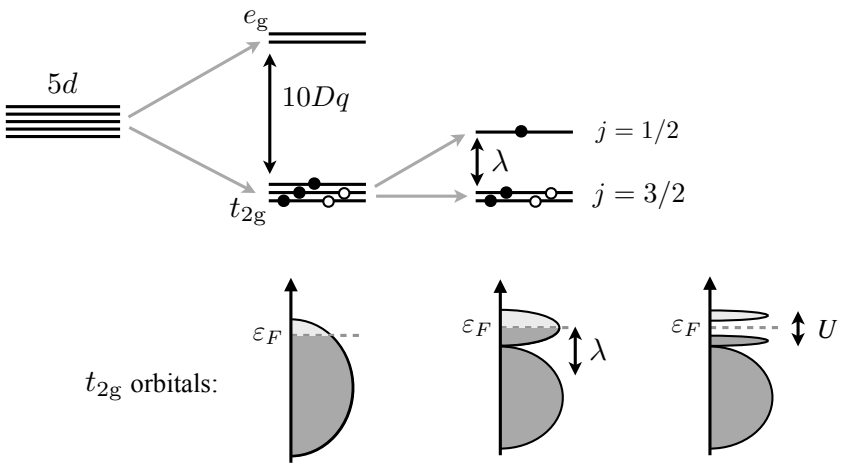

Figure 4.2.: $5d$ level splittings by the crystal field and the spin-orbit coupling, resulting in an effective $j = 1/2$ degree of freedom.

close to the oxygen ions and their energy is raised by the (repulsive) Coulomb interaction. On the other hand, the t_{2g} orbitals are oriented diagonally to the axes, i.e. *away* from the ligands. The Coulomb interaction is thus smaller and accordingly these three orbitals are energetically more favorable [8, 68]. The resulting energy difference between the t_{2g} and e_g states is historically called $10Dq$ [69], values for which are typically of the order of $\sim$ 2–3 eV [68]. The splitting into e_g and t_{2g} levels is shown schematically for the case of a $5d$ shell in Fig. 4.2.

4.1.3. Spin-orbit coupling and effective $j = 1/2$

So far we have considered a purely non-relativistic description of an atom. While this approximation is indeed justified for lighter atoms such as the hydrogen atom, it turns out that in transition metal oxides the electron spin and the subsequent relativistic spin-orbit coupling play an important role. In fact, they are the key ingredient leading to the existence of Mott-insulating effective $j = 1/2$ states in the Iridate transition metal oxides.

Spin-orbit coupling

Consider a single electron orbiting a nucleus with charge Ze, where Z is the atomic number and e the elementary charge, fixed at the center of the coordinate system. Changing our frame of reference to that of the electron, from special relativity we know that the moving nucleus induces a magnetic field which interacts with the spin of the electron. While this is just an intuitive picture, a rigorous result can be derived from the Dirac equation, which replaces the Schrödinger equation in the relativistic case. Expanding in small v/c, the first correction term due to spin-orbit coupling is then given by

$$H_{\mathrm{SOC}} = \lambda \mathbf{L} \cdot \mathbf{S}, \tag{4.4}$$

where $\mathbf{L} = (L^x, L^y, L^z)^T$ is the orbital angular momentum and $\mathbf{S} = (S^x, S^y, S^z)^T$ is the spin of the electron. Introducing the operator for the total angular momentum

$$\mathbf{J} = \mathbf{L} + \mathbf{S}, \tag{4.5}$$

the energy shift due to the spin-orbit contribution can be written as

$$\begin{aligned}\Delta E = \lambda \langle \mathbf{L} \cdot \mathbf{S} \rangle &= \frac{\lambda}{2} \left(\langle \mathbf{J} \rangle^2 - \langle \mathbf{L} \rangle^2 - \langle \mathbf{S} \rangle^2 \right) \\ &= \frac{\lambda}{2} \left(j(j+1) - \ell(\ell+1) - s(s+1) \right). \end{aligned} \tag{4.6}$$

Let us now discuss the coupling constant λ. From the expansion of the Dirac equation one finds that [70]

$$\lambda = \frac{1}{2m_e^2 c^2} \frac{1}{R} \frac{\mathrm{d}V(R)}{\mathrm{d}R}, \tag{4.7}$$

where R is the distance between electron and nucleus. The potential $V(R)$ created by a nucleus with $Z \in \mathbb{N}$ protons is given by

$$V(R) = -\frac{Ze^2}{R}. \tag{4.8}$$

Plugging Eq. (4.8) in Eq. (4.7) and using furthermore that the expectation value of $1/R^3$ is given by [71]

$$\left\langle \frac{1}{R^3} \right\rangle_{n\ell} = \frac{Z^3}{\ell \left(\ell + \frac{1}{2}\right) (\ell+1)\, n^3 a_B^3}, \tag{4.9}$$

with the Bohr radius a_B, we finally obtain that the coupling constant scales as

$$\lambda \sim Z^4. \tag{4.10}$$

This derivation only takes into account a single electron and a heavy nucleus, but the Iridates host, of course, more than one electron. These additional electrons, however, participate in a screening of the nucleus and comparison with experimental data reveals that Eq. (4.10) is still a good approximation.

In summary, the effective spin-orbit coupling can thus be roughly approximated to be proportional to the fourth power of the number of protons in the atom's nucleus, and in e.g. the heavier transition metals Rh, Ru, Os, and Ir, it cannot be neglected anymore. In fact, in Ir^{4+} ions with an atomic number of 77, it was found to be as large as $\lambda \sim 380\mathrm{meV}$ [72], far exceeding possible intersite interactions between its t_{2g} orbitals and spins [73].

Formation of $j = \frac{1}{2}$ in the Iridates

The large spin-orbit coupling of the Iridates has a crucial effect on their physical behavior. Combined with the effects of crystal field splitting it leads to an effective $j = \frac{1}{2}$ angular degree of freedom, combining both spin and orbital physics.

To see this, consider the typical Iridium valence Ir^{4+} which has a $5d^5$ configuration, i.e. the $5d$ shell is occupied by five electrons. Due to the crystal field splitting discussed in the last section, these orbitals are split up into the e_g and t_{2g} manifolds, differing by an energy of $10Dq$. From Hund's rule, we further know how to fill up the low-lying t_{2g} orbitals with the five electrons, resulting effectively in a single hole in the t_{2g} triplet, see Fig. 4.2.

In materials with an incomplete $3d$ shell, it is well understood that in this situation the large Coulomb interaction between electrons in the t_{2g} orbitals creates Mott insulating behavior. The $5d$ orbitals are spatially much more extended than the $3d$ orbitals and the Coulomb interaction is an order of magnitude smaller, which could lead to the assumption that these materials should be metallic. However, the fact that they are indeed Mott insulators with an effective $j = \frac{1}{2}$ degree of freedom can be understood from their strong

spin-orbit coupling. To see this, consider how the angular momentum operators act in the t_{2g} subspace. It will turn out to be convenient to perform a basis transformation in this subspace, so that the new basis vectors ϕ_i for the t_{2g} states are given as linear combinations of the d_{xy}, d_{yz}, and d_{zx} orbitals [74],

$$\phi_{+1} = \frac{1}{\sqrt{2}}\left(d_{zx} - i\, d_{yz}\right), \qquad \phi_0 = d_{xy}, \qquad \phi_{-1} = -\frac{1}{\sqrt{2}}\left(d_{zx} + i\, d_{yz}\right). \tag{4.11}$$

For the e_g states we keep the original basis vectors

$$\psi_1 = d_{z^2}, \qquad \psi_2 = d_{x^2-y^2}. \tag{4.12}$$

In this new basis, $\{\phi_1, \phi_0, \phi_{-1}, \psi_1, \psi_2\}$, the angular momentum operators have the following matrix representation,

$$L^x = -\frac{1}{\sqrt{2}}\left(\begin{array}{ccc|cc} 0 & 1 & 0 & \sqrt{3} & -1 \\ 1 & 0 & 1 & 0 & 0 \\ 0 & 1 & 0 & \sqrt{3} & 1 \\ \hline -\sqrt{3} & 0 & \sqrt{3} & 0 & 0 \\ -1 & 0 & 1 & 0 & 0 \end{array}\right), \tag{4.13a}$$

$$L^y = -\frac{i}{\sqrt{2}}\left(\begin{array}{ccc|cc} 0 & 1 & 0 & \sqrt{3} & -1 \\ -1 & 0 & 1 & 0 & 0 \\ 0 & -1 & 0 & \sqrt{3} & -1 \\ \hline -\sqrt{3} & 0 & -\sqrt{3} & 0 & 0 \\ 1 & 0 & 1 & 0 & 0 \end{array}\right), \tag{4.13b}$$

$$L^z = -\left(\begin{array}{ccc|cc} 1 & 0 & 0 & 0 & 0 \\ 0 & 0 & 0 & 0 & -2 \\ 0 & 0 & -1 & 0 & 0 \\ \hline 0 & 0 & 0 & 0 & 0 \\ 0 & -2 & 0 & 0 & 0 \end{array}\right). \tag{4.13c}$$

The upper left 3×3 block of each matrix thus corresponds to the t_{2g} manifold. Considering the action of the $\ell = 2$ angular momentum operator $\mathbf{L}^{\ell=2}$ in this subspace, we find that it is given exactly by the action of a $\ell = 1$ angular momentum operator[1], only with an overall negative sign [75, 76]. In other words: Projected onto the t_{2g} subspace, the $\ell = 2$ angular momentum operator $\mathbf{L}^{\ell=2}_{t_{2g}}$, acts like an effective $\ell = 1$ angular momentum operator with a negative sign, $-\mathbf{L}^{\ell=1}_{t_{2g}}$. We can check that the operators $\mathbf{L}^{\ell=1}_{t_{2g}}$ represented by the upper left 3×3 blocks of the matrices (4.13a)–(4.13c) indeed fulfill the commutation relations for a negative angular momentum:

$$[\, L^k, L^l \,] = -i\epsilon_{klm} L^m, \tag{4.14}$$

where ϵ_{klm} is the totally antisymmetric tensor. The effective angular momentum operator can thus be defined as $\mathbf{L}_{\text{eff}} = -\mathbf{L}^{\ell=1}_{t2g}$, and the spin-orbit term in the model can thus be recast into the form

$$\lambda \mathbf{L} \cdot \mathbf{S} \to -\lambda \mathbf{L}_{\text{eff}} \cdot \mathbf{S}, \tag{4.15}$$

with $\ell_{\text{eff}} = 1$. The total effective angular momentum operator then becomes $\mathbf{J}_{\text{eff}} =$

[1] The only purpose of our basis transformation was to see this immediately. Of course, this result is independent of the specific basis for the t_{2g} subspace.

$\mathbf{L}_{\text{eff}} + \mathbf{S}$, which yields two energy levels, given by a doublet state with $j_{\text{eff}} = \ell_{\text{eff}} - \sigma = \frac{1}{2}$ and a quartet state with $j_{\text{eff}} = \ell_{\text{eff}} + \sigma = \frac{3}{2}$, where $\sigma = \frac{1}{2}$ is the spin quantum number. Calculating the energy shift due to the spin-orbit coupling gives [77]

$$\Delta E_{\text{SOC}} = -\frac{\lambda}{2}\left[\mathbf{J}_{\text{eff}}^2 - \mathbf{L}_{\text{eff}}^2 - \mathbf{S}^2\right] = -\lambda\left[\frac{J_{\text{eff}}(J_{\text{eff}}+1)}{2} - \frac{11}{8}\right], \tag{4.16}$$

and we find that the $j_{\text{eff}} = \frac{1}{2}$ doublet has energy λ and the $j_{\text{eff}} = \frac{3}{2}$ quartet has *lower* energy $-\lambda/2$. We can again use Hund's rule to fill up states in the quartet with four of the five d^5 electrons. The remaining electron resides in the doublet band, see Fig. 4.2. The system can thus be described as a half-filled $j_{\text{eff}} = \frac{1}{2}$ single band system with a band narrow enough that even a small Coulomb interaction U can open a gap and create a Mott insulating state [63–65]. We schematically show the energy bands in the lower panel of Fig. 4.2.

4.2. Spin interactions

Mott insulators with orbital degrees of freedom have first been comprehensively studied in the 1980s by Kugel and Khomskiĭ [61], with the realization that the directional nature of the orbital degree of freedoms leads to spin-selective interactions [78]. The term *compass models* was coined at that time and has since been used to subsume a plethora of different models which are all characterized by the following two conditions [78]: (i) there is only an interaction between certain vector components of $\mathbf{S}$, and (ii) on different bonds in the lattice, different vector components interact. In general terms, the degree of freedom need not be a proper spin-$\frac{1}{2}$ but can be given by any type of pseudospin operator, however for our purposes we focus only on the former. In the Kitaev model which we discussed in Sec. 2.3, the interactions between two spins are given by $S_i^\gamma S_j^\gamma$, where $\gamma = x, y, z$ depends on the orientation of the bond, making the Kitaev model a special (because somewhat symmetric, compared to e.g. the 120 degree model [79]) specimem of a compass model. In the following we discuss how such "Kitaev-type" interactions can appear in transition metal oxides.

For a Mott-insulating $5d$ transition metal oxide, the magnetic interactions between two transition metal ions are mediated via the ligand oxygens by the mechanism of superexchange. Similar to the discussion of the Mott insulator in Sec. 2.2.2, this superexchange is facilitated by virtual hopping of electrons to intermediate states and back, only that here these processes happen via the oxygen atoms. We discussed the strongly anisotropic nature of the orbital degrees of freedom in the last sections and now, following Ref. [33], we show how this may lead to the realization of spin-selective interactions in such systems. These interactions are of the Kugel-Khomskiĭ type and, among other models, occur in the Kitaev model, see Sec. 2.3. The superexchange via a ligand oxygen can happen via two different dominant paths:

- **180° paths**. These are dominant when two oxygen cages of the transition metal oxides share a corner, as depicted in Fig. 4.3(a). The interaction happens along the line connecting the transition metal ions, hence the name 180°. In this case, equivalent orbitals are coupled via the $2d$ orbital of the oxygen, e.g. d_{yz} on the left ion with d_{yz} on the right ion. For these paths, the hopping is diagonal in the orbital index, and the effective Hamiltonian for two neighboring ions contains a Heisenberg-type

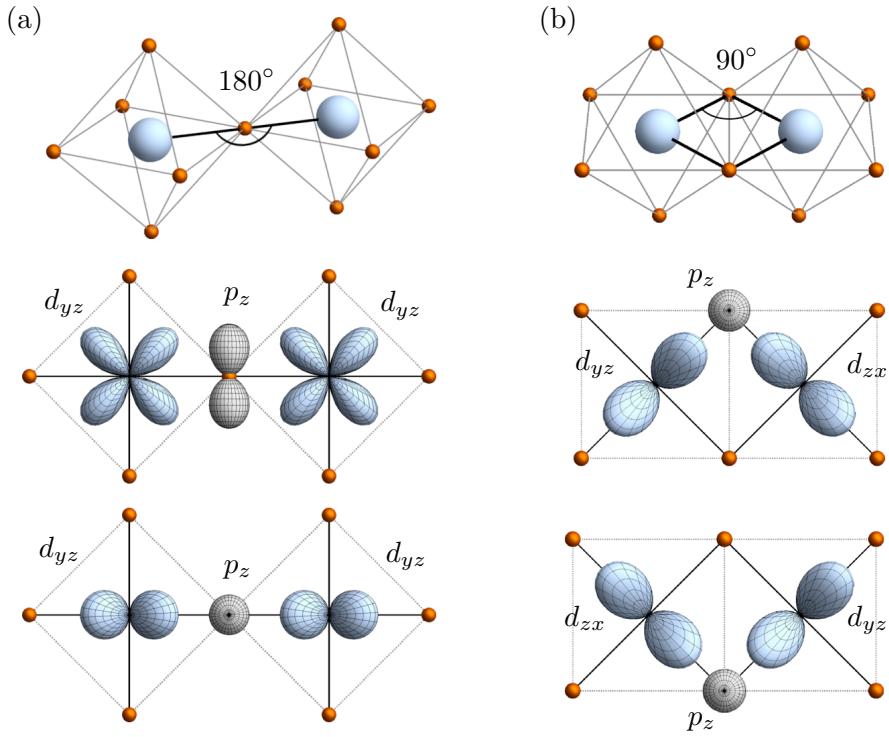

Figure 4.3.: Schematic of the two possible superexchange paths. The top row shows the two exchange paths, the center and bottom row show the alignment of the orbitals participating in the exchange. (a) 180° path coupling the same orbitals, yielding an isotropic Heisenberg interaction. The two lower figures show the same exemplary interaction from a side and top view, respectively. (b) 90° paths coupling different orbitals, resulting in an effective Kitaev interaction. Both lower figures are shown from a top view, each showing one half of the full 90° exchange path.

exchange interaction and an anisotropic term,

$$H_{ij}^{180^\circ} = J_1 \mathbf{S}_i \cdot \mathbf{S}_j + J_2 \left(\mathbf{S}_i \cdot \mathbf{e}_{ij}\right)\left(\mathbf{S}_j \cdot \mathbf{e}_{ij}\right), \tag{4.17}$$

where the operators $\mathbf{S}$ represent the effective $j = 1/2$ spin-orbital moments on the transition metal ions. The vectors $\mathbf{e}_{ij}$ are unit vectors parallel to the line connecting the two transition metal ions and the coupling constants $J_{1/2}$ depend on microscopic parameters [33]. In the limit of strong spin-orbit coupling $J_1 \gg J_2$ and the isotropic Heisenberg interaction dominates.

- **90° paths**. In these paths, the interaction happens at a 90° angle with respect to the line connecting the ions, see Fig. 4.3(b). In contrast to the 180° paths, here different orbitals are coupled and the hopping matrix has only non-diagonal entries. Along the two possible paths, the charge transfer amplitudes interfere destructively and the isotropic part the effective Hamiltonian vanishes *exactly* [33]. The remaining anisotropic interaction is given by

$$H_{ij}^{90^\circ} = -J S_i^\gamma S_j^\gamma, \tag{4.18}$$

where $\gamma \in \{x, y, z\}$ is given by the relevant orbital alignment of the intermediate oxygen ion. In Fig. 4.3(b) the oxygen orbital is p_z, thus here $\gamma = z$.

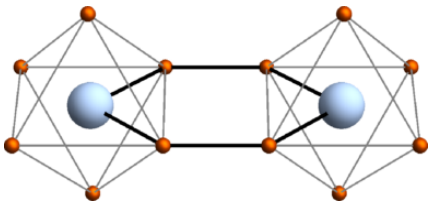

Figure 4.4.: The parallel-edge alignment of the transition metal oxides in $Ba_3IrTi_2O_9$. The Ir-O-O-Ir exchange paths are longer than the Ir-O-Ir paths in the honeycomb iridates, but they still lead to interactions of Kitaev type, albeit of somewhat smaller magnitude compared to the Heisenberg coupling.

4.3. Kitaev interactions in real materials

We have seen how transition metal oxides with a strong spin-orbit coupling can form a $j = 1/2$ ground state which, due to its orbital origin, has a strong anisotropic interaction behavior. The effective exchange interactions depend on microscopic parameters and edge-sharing octahedra lead to a Kitaev interaction. In realistic materials, however, one must expect other interactions to be present, mostly anisotropic Heisenberg interactions due to direct overlap of the transition metal orbitals [80]. Nonetheless, the spin liquid ground state of the Kitaev model (see Sec. 2.3) is stable against a small perturbation by an isotropic Heisenberg exchange [80], and a possible realization of Kitaev physics is therefore within reach. We now discuss two materials for which Heisenberg-Kitaev models have been proposed to be the relevant theoretical description.

4.3.1. The honeycomb iridates A_2IrO_3

Chaloupka et al. argued in 2010 [80] that A_2IrO_3 compounds (where typically $A = \mathrm{Na}$ or $A = \mathrm{Li}$) might be described by the so-called Heisenberg-Kitaev model, a mixture of both Heisenberg and Kitaev interactions:

$$H = J_H \sum_{\langle ij \rangle} \mathbf{S}_i \cdot \mathbf{S}_j + J_K \sum_{\langle ij \rangle \| \gamma} S_i^\gamma S_j^\gamma, \tag{4.19}$$

where the value of $\gamma \in \{x, y, z\}$ depends on the orientation of the nearest-neighbor link $\langle ij \rangle$. The effective spins on the Iridium ions form well-separated layers of honeycomb lattices in such a way that for each real-space bond direction a different spin component interacts [81]. The prospect of a possible realization of the Kitaev model, including its spin liquid ground state, has led to a vast amount of research devoted to such materials. An abundance of experimental data [64, 65, 82–84], ab initio calculations [85–88], and model simulations [89–95] for these hexagonal systems has fueled an ongoing discussion about the actual spin-orbital ordering mechanism in these materials.

Although the spin liquid ground state of the Kitaev model was shown [80] to be stable against small Heisenberg-type perturbations, in the honeycomb Iridates the Heisenberg interaction is still large enough to destroy the spin liquid. Experimental findings [86] do indeed indicate a magnetically ordered ground state.

4.3.2. The triangular iridate $Ba_3IrTi_2O_9$

A material which might be described by the Heisenberg-Kitaev model on the triangular lattice is $Ba_3IrTi_2O_9$ [96]. This compound crystallizes in a hexagonal structure consist-

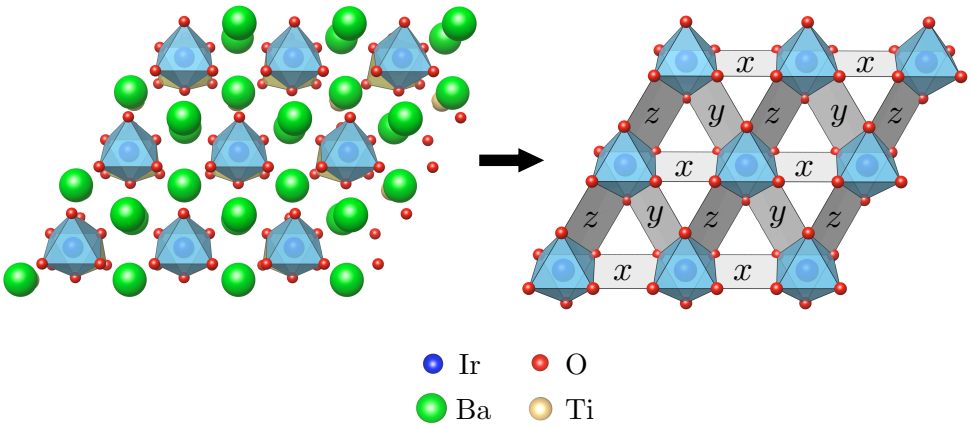

Figure 4.5.: The structure of $Ba_3IrTi_2O_9$. The right column shows the triangular lattice which emerges between the spins on the Iridium ions. The gray planes indicate that for each direction different orbitals become relevant, leading to the anisotropic Kitaev-type interactions.

ing of well-separated layers in which the Ir^{4+} ions form a triangular lattice, its structure is shown is shown in Fig. 4.5. Early experimental results measured a high antiferromagnetic Weiss temperature ($|\theta| > 400\mathrm{K}$) [97], indicating a strong coupling between the effective $j = 1/2$ degrees of freedom on the Ir^{4+} ions. The oxygen octahedra in the triangular lattice layers are separated from each other, but they are still oriented towards each other as in the previously discussed case of the honeycomb iridates: Any two neighboring octahedra have two parallel edges as shown in Fig. 4.5. The exchange path for the iridium ions in two neighboring oxygen cages is Ir-O-O-Ir (Fig. 4.4) and as such somewhat longer than in the honeycomb iridates in which the exchange path only runs via one ligand oxygen. However, this longer path still leads to destructive interference and the subsequent suppression of the isotropic Heisenberg exchange, resulting in an effective anisotropic Kitaev spin-coupling. Due to the longer exchange paths this contribution is of much smaller magnitude compared to the honeycomb iridates, and Heisenberg physics are expected to be dominant. In terms of the Heisenberg-Kitaev model, Eq. (4.19), this means that the experimentally relevant parameter regime should be assumed to be for $J_H \gg |J_K|$ with an antiferromagnetic Heisenberg coupling, $J_H > 0$.

Site disorder and spin liquid behavior

Since the ionic radii of the Ir^{4+} and Ti^{4+} ions are very similar, a site disorder may develop where a certain portion of the Iridium and Titanium ions exchange their positions. This disorder has been found to be fairly large, ranging from 21% [98] to 37% [96]. For these materials, no magnetic ordering down to lowest temperatures has been found, and a spin liquid has been suggested as a possible ground state [96]. However, it is unclear whether this absence of ordering must be contributed to the site disorder, and thus whether it would vanish in the case of a clean single crystal.

Chapter 5.

The Heisenberg-Kitaev model on the triangular lattice

In Secs. 2.2 and 2.3 we introduced the Heisenberg and Kitaev models, respectively. Both of these models are by themselves of great interest as they contain a plethora of exotic physical phenomena. The Heisenberg model has proven successful in the description of ferromagnetic and antiferromagnetic materials. The honeycomb Kitaev model, on the other hand, is celebrated for the existence of an exact solution and its spin-liquid ground states. While the Kitaev model originally had been investigated from a purely theoretical point of view, in the previous chapter we showed how spin-orbit coupling in transition metal oxides can lead to the appearance of Kitaev-type interactions in real materials. Kitaev introduced and solved his original model on the honeycomb lattice [31]. However, the Kitaev Hamiltonian can equally be defined on *any* lattice in which the bonds between sites can be subdivided into three sets of different spatial orientation [99], such as the triangular or kagome lattices [12,13]. In this work, we concentrate on the case of a triangular lattice. The exact solution of the Kitaev model in terms of Majorana fermions on the honeycomb lattice does not generalize to the triangular lattice, and so far the nature of its ground state is not clear. However, in materials such as the $Ba_3IrTi_2O_9$ compound discussed in the previous chapter, the appropriate model is proposed to be a combination of both types of interactions in the Heisenberg-Kitaev model.

Numerical results for the full phase diagram of the classical Heisenberg-Kitaev model on the triangular lattice have been reported in Ref. [12], with one of the main results being the observation of a phase close to the antiferromagnetic Heisenberg point, characterized by the formation of a lattice of $\mathbb{Z}_2$ vortices. In this chapter we complement these findings with analytical and numerical results for the classical and the quantum model. After first discussing the relevant physics of the Heisenberg model on the triangular lattice, we then consider the effect of adding a Kitaev interaction. We present the full phase diagram for both the classical and quantum models and proceed to consider each phase individually and in more detail.

5.1. The Heisenberg model on the triangular lattice

As a preparation to the discussion of the Heisenberg-Kitaev model on the triangular lattice, it is useful to first review the physics of the plain Heisenberg model without any Kitaev interactions,

$$H = J_H \sum_{\langle ij \rangle} \mathbf{S}_i \cdot \mathbf{S}_j. \tag{5.1}$$

In the ferromagnetic case, $J_H < 0$, the spins can trivially minimize their energy by aligning parallel to each other. In contrast, the nature of the quantum ground state for the antiferromagnetic model, $J_K > 0$, has long been debated. By now, however, it is under-

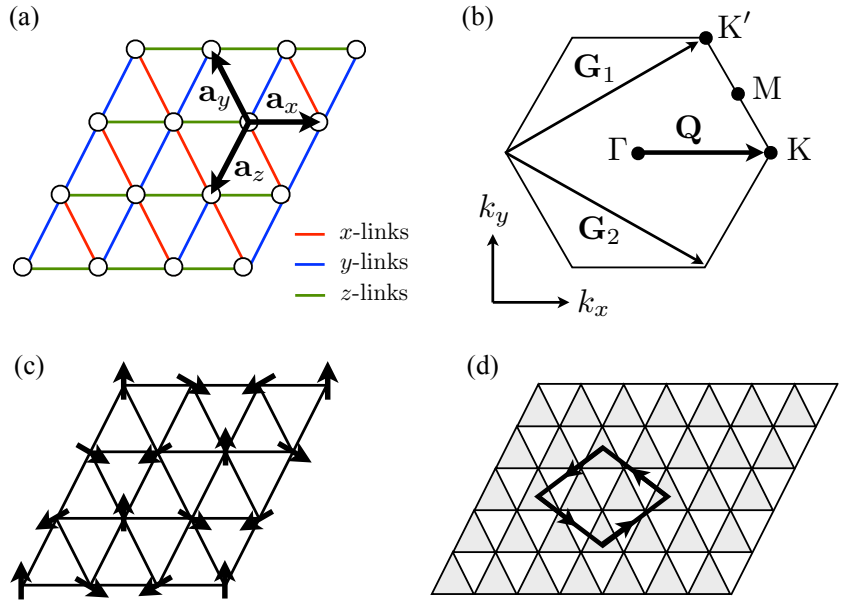

Figure 5.1.: (a) The triangular lattice and the three lattice vectors $\mathbf{a}_i$. (b) First Brillouin zone of the triangular lattice and the basis vectors of the reciprocal lattice $\mathbf{G}_i$, showing the four special points K and K′, Γ and M. (c) The 120° order of the triangular lattice. The three sublattices are colored differently. (d) Wilson loop on the upward pointing triangular lattices to calculate vorticity.

stood that the antiferromagnetic model has a ground state characterized by the so-called 120° order. This specific ordering and its topological properties play an important role in our subsequent discussion of the emergent $\mathbb{Z}_2$ vortex lattice phase.

5.1.1. 120° order of the antiferromagnetic model

The triangular lattice is shown in Fig. 5.1(a). It is spanned by the lattice vectors

$$\mathbf{a}_x = a\begin{pmatrix}1\\0\end{pmatrix}, \qquad \mathbf{a}_y = \frac{a}{2}\begin{pmatrix}-1\\\sqrt{3}\end{pmatrix}, \qquad \mathbf{a}_z = -\frac{a}{2}\begin{pmatrix}1\\\sqrt{3}\end{pmatrix}, \tag{5.2}$$

where a is the lattice constant which we will henceforth set to $a = 1$. Note that a two-dimensional lattice of course only requires two basis vectors and that $\mathbf{a}_z = -\mathbf{a}_x - \mathbf{a}_y$. However, in order to keep our mathematical formulation of the system more elegant we will use all three vectors. As each site in the triangular lattice has six direct neighbors, its first Brillouin zone is a hexagon, as shown in Fig. 5.1(b). The basis vectors $\mathbf{G}_i$ of the reciprocal lattice connect the centers of two Brillouin zones and are defined in the usual way by the condition that $\mathbf{G}_i \cdot \mathbf{a}_i = 2\pi\delta_{ij}$. They are (with $a = 1$) given by

$$\mathbf{G}_{1/2} = 2\pi\begin{pmatrix}1\\\pm\frac{1}{\sqrt{3}}\end{pmatrix}. \tag{5.3}$$

The magnetic order of the ground state of a given Hamiltonian naturally depends on the type of exchange interaction between individual spins. The nearest-neighbor Heisenberg model Eq. (5.1) contains only a single interaction J_H, which can be either ferromagnetic ($J_H < 0$) or antiferromagnetic ($J_H > 0$). On bipartite lattices, the antiferromag-

netic ground state at $T = 0$ is given by a perfectly *staggered* spin ordering: The two-sublattice structure allows for every spin to align perfectly antiparallel with all its neighbors. However, the triangular lattice is a prime example of a non-bipartite lattice where antiferromagnetic interactions lead to *frustration* due to the geometry of the lattice. Consider one triangular plaquette with three spins: While two spins can order antiferromagnetically, the third spin can never be antiparallel to both its neighbors at the same time. This frustration typically leads to a highly degenerate ground state, where quantum fluctuations are strongly enhanced. For the Heisenberg antiferromagnet on the triangular lattice it was argued by Anderson that the ground state of this system is given by resonating valence bonds [100,101] in which pairs of spins form singlet dimers, covering the entire lattice. While this idea was intriguing as it provided a connection to the pairing mechanisms in high-temperature superconductors, it is by now established that the antiferromagnetic ground state of the triangular spin-$\frac{1}{2}$ Heisenberg model at $T = 0$ is in fact given by a state with long-range magnetic order, characterized by the 120° ordering [102–107] of the spins. This order is shown in Fig. 5.1(c): The spins are all co-planar and the angle between any two neighboring spins is 120°, or $2\pi/3$.

Let us formulate more rigorously how this order comes about. We first introduce the Fourier transform of the spin operators,

$$\mathbf{S}_i = \frac{1}{\sqrt{N}} \sum_{\mathbf{k}\in 1.\mathrm{BZ}} \mathbf{S}_{\mathbf{k}} e^{i\mathbf{k}\cdot\mathbf{r}_i}, \tag{5.4}$$

where N is the number of spins and the summation of the momenta runs over the entire first Brillouin zone. We can now formulate the Heisenberg Hamiltonian in momentum space, which yields

$$H = \sum_{\mathbf{k}\in 1.\mathrm{BZ}} \mathcal{J}^0(\mathbf{k}) \mathbf{S}_{\mathbf{k}} \cdot \mathbf{S}_{-\mathbf{k}}, \tag{5.5}$$

with the exchange interaction in momentum space given by

$$\mathcal{J}^0(\mathbf{k}) = J_H \sum_{i=x,y,z} \cos(\mathbf{a}_i \cdot \mathbf{k}), \tag{5.6}$$

where the $\mathbf{a}_i$ are the lattice vectors defined above. Minimizing this expression, we immediately find that $\mathcal{J}^0(\mathbf{k})$ is minimal at the corners of the Brillouin zone. Each corner of the Brillouin zone is related to two other corners by the reciprocal lattice vectors, which leaves us with only two factually inequivalent corners, given by the K- and K′-points. For the description of the magnetic order, the two relevant wave vectors are thus the ones connecting the center of the Brillouin zone with these two points, given by

$$\mathbf{Q} = \pm \frac{4\pi}{3} \begin{pmatrix} 1 \\ 0 \end{pmatrix}. \tag{5.7}$$

As a next step, we use these two vectors to describe the spin order in the classical limit. To this end, we introduce the following notation to describe a general classical spin:

$$\mathbf{S}_i = S\hat{\mathbf{\Omega}}(\mathbf{r}_i), \tag{5.8}$$

where S is the length of the spin, $\mathbf{r}_i$ is the real-space vector pointing at lattice site i and $\hat{\mathbf{\Omega}}$ is a unit vector (which we throughout denote with a hat) in $\mathbb{R}^3$ determining the orientation of the spin. As the magnetic order is determined by the momenta at $\pm\mathbf{Q}$, we can

write the spin orientation as

$$\hat{\mathbf{\Omega}}(\mathbf{r}) = \mathbf{\Omega}_0 e^{i\mathbf{Q}\cdot\mathbf{r}} + \text{c.c.}, \tag{5.9}$$

where $\mathbf{\Omega}_0$ is a complex vector (which does not necessarily have to be of unit length) and c.c. means complex conjugation. The constraint that $\hat{\mathbf{\Omega}}(\mathbf{r})$ is a purely real vector which must be of length one at each site implies

$$\hat{\mathbf{\Omega}}^2(\mathbf{r}) = \mathbf{\Omega}_0^2 e^{2i\mathbf{Q}\cdot\mathbf{r}} + (\mathbf{\Omega}_0^*)^2 e^{-2i\mathbf{Q}\cdot\mathbf{r}} + 2|\mathbf{\Omega}_0|^2 \stackrel{!}{=} 1. \tag{5.10}$$

Except for the special case that $\mathbf{Q}\cdot\mathbf{r} = n\pi$ with $n \in \mathbb{N}_0$, this condition can only be fulfilled for *any* $\mathbf{r}$ if $\mathbf{\Omega}_0$ is *chiral*, i.e. $\mathbf{\Omega}_0^2 = (\mathbf{\Omega}_0^*)^2 = 0$. Thus, we can without loss of generality assume the spins to lie in the x-y-plane and set $\mathbf{\Omega}_0 = \frac{1}{\sqrt{2}}(1, i, 0)^T$. This leads to the following expression for the orientation vector to describe the classical spin order at zero temperature:

$$\hat{\mathbf{\Omega}}_{120^\circ}(\mathbf{r}) = \mathbf{e}_1 \cos(\mathbf{Q}\cdot\mathbf{r}) + \mathbf{e}_2 \sin(\mathbf{Q}\cdot\mathbf{r}). \tag{5.11}$$

The vectors $\mathbf{e}_i$ are the three orthonormal basis vectors in three-dimensional spin space, for which $\mathbf{e}_i \cdot \mathbf{e}_j = \delta_{ij}$ and $\mathbf{e}_1 \times \mathbf{e}_2 = \mathbf{e}_3$, and which we here identified with the Cartesian basis vectors. Finally, from the Hamiltonian Eq. (5.1) we can immediately find the energy per spin of this state. In the classical limit it is given by

$$\frac{\varepsilon_{120^\circ}}{N} = -S^2 \frac{3}{2} J_H. \tag{5.12}$$

5.1.2. $\mathbb{Z}_2$ vortices as topological point defects of the 120° order

An essential tool in the discussion of phase transitions is the order parameter as a measure of the degree of order in any given phase. But even when one is not directly concerned with phase transitions, the order parameter might reveal important information, such as the topological defects of the system. For the 120° state the order parameter consists of three distinguishable arrows in a plane [108], and the order parameter space is, in fact, isomorphic to the three-dimensional rotation group SO(3). This can be seen if we relate the spin order to the orthonormal frame defined by the vectors $\hat{\mathbf{e}}_i$ for which only rotations keep the internal structure intact.

How does a topological defect of the 120° order look like? In this context, we can define a topological defect as an irregularity in the 120° spin order which cannot be eliminated by a continuous transformation. In a different sense, a defect can be understood as a 'singularity' in the order parameter [109]. The classification, stability and existence of such defects is generally discussed by means of the *fundamental group* (or first homotopy group) of the order parameter space. In our case, the first homotopy group of SO(3) is

$$\Pi_1(SO(3)) = \mathbb{Z}_2, \tag{5.13}$$

which in 2D indicates that the system has stable point defects (in contrast to e.g. line defects). These defects manifest as vortices in the order parameter, which translates to a twisting of the 120° structure when going along a path around the vortex core. Precisely at the core, however, the order parameter diverges and it is not possible anymore to assign a 120° order here. A vortex can further be labeled by its winding number: The cumulative rotation of the order parameter along a closed path around the vortex core

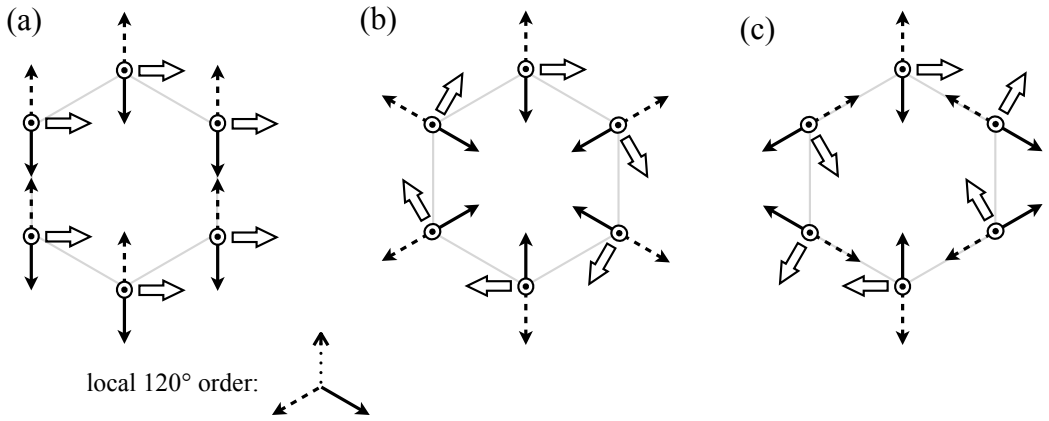

Figure 5.2.: Vortices in the 120° order. The SO(3) order parameter of the 120° order is determined by the orientation of three arrows (dotted, dashed, solid) which define the local spin order on a plaquette of the triangular lattice. The thicker white arrows illustrate the chirality vectors $\boldsymbol{\kappa}$, which by definition are orthogonal to the local spin structure. In the shown configurations, the dotted arrow points out of the plane of the page, i.e. the plane of the 120° order is perpendicular to the page. (a) shows a perfect 120° order with a homogeneous order parameter, (b) shows a vortex and (c) an anti-vortex. For a discussion we refer to the main text.

is always $\theta = 2\pi n$, where $n \in \mathbb{N}_0$ is the winding number. For the 120° order, however, Eq. (5.13) tells us that in this case the vortices have a $\mathbb{Z}_2$ structure. Accordingly, we only have one type of vortex, and any pair of vortices can be continuously transformed to yield a state where both are eliminated.

To measure the rigidity of the 120° order parameter we now define a chirality vector $\boldsymbol{\kappa}$ on each upward pointing triangle plaquette (the shaded triangles in Fig. 5.1(d)) as follows:

$$\boldsymbol{\kappa}(\mathbf{r}) = \frac{2}{3\sqrt{3}} \left(\mathbf{S}_{\mathbf{r}} \times \mathbf{S}_{\mathbf{r}+\mathbf{a}_x} + \mathbf{S}_{\mathbf{r}+\mathbf{a}_x} \times \mathbf{S}_{\mathbf{r}-\mathbf{a}_z} + \mathbf{S}_{\mathbf{r}-\mathbf{a}_z} \times \mathbf{S}_{\mathbf{r}} \right) \tag{5.14}$$

with the lattice vectors $\mathbf{a}_i$ as defined in Fig. 5.1. The vector $\boldsymbol{\kappa}(\mathbf{r})$ is perpendicular to the plane of the local 120° order of the plaquette defined by the position $\mathbf{r}$, and its length gives a measure of the quality of the 120° structure [108]. In a perfect 120° ordered state, the chirality vectors on all plaquettes are the same, $\boldsymbol{\kappa}(\mathbf{r}) \equiv \hat{\boldsymbol{\kappa}}_0$ and $|\hat{\boldsymbol{\kappa}}_0| = 1$. Any deviation from the perfect 120° order, however, immediately changes the texture of chirality vectors, and it vanishes as soon as two spins on a plaquette are parallel.

Fig. 5.2 shows what a vortex looks like in the chirality vectors. The vortex-free configuration is shown in (a), where the order parameter is the same for each plaquette and the chirality vectors are homogeneous. Fig. (b) shows a vortex configuration: The local 120° structure and thus the chirality vectors rotate clockwise when going around the closed path. The corresponding anti-vortex is shown in (c), where the order parameter rotates counter-clockwise. The vortex can be continuously transformed into the anti-vortex, but neither can be continuously transformed into the vortex-free configuration.

In order to finally calculate the number of vortices enclosed by any given closed path $\mathcal{C}$, we introduce the "vorticity" function, which is given by the cumulative rotation of chirality vectors along this path [108]. Due to the $\mathbb{Z}_2$ nature of the vortices, the total number of vortices measured this way will either be one or zero. To be able to resolve individual vortices, it is thus important to consider paths of appropriate size and shape. The

rhombic path shown in Fig. 5.1(d) was found to yield very good results [12], therefore we will use this path in our calculations, too. We define the rotation between two chirality vectors $\boldsymbol{\kappa}_i$ and $\boldsymbol{\kappa}_j$ by an angle ω_{ij} and a rotation axis $\hat{\mathbf{n}}_{ij}$:

$$\omega_{ij} = \arccos\left(\boldsymbol{\kappa}_i \cdot \boldsymbol{\kappa}_j\right), \tag{5.15a}$$

$$\hat{\mathbf{n}}_{ij} = \frac{\boldsymbol{\kappa}_i \times \boldsymbol{\kappa}_j}{|\boldsymbol{\kappa}_i \times \boldsymbol{\kappa}_j|}. \tag{5.15b}$$

At this point it is crucial to be able to distinguish between rotations by 0 (no rotation) and 2π. To achieve this, we use the special unitary group SU(2), which is a two-valued representation of SO(3). Any given rotation $(\omega, \hat{\mathbf{n}})$ can then be represented by the two following SU(2) matrices [108]:

$$U_{ij} = \pm \exp\left(\frac{\omega_{ij}}{2i}\hat{\mathbf{n}}_{ij} \cdot \boldsymbol{\sigma}\right), \tag{5.16}$$

where $\boldsymbol{\sigma} = (\sigma^x, \sigma^y, \sigma^z)^T$ is the vector of Pauli matrices, and replacing $\omega \leftrightarrow 2\pi - \omega$ and $\hat{\mathbf{n}} \leftrightarrow -\hat{\mathbf{n}}$ reverses the sign of U_{ij}. Let us consider now the product of these matrices along the closed contour $\mathcal{C}$ on the lattice of chirality vectors

$$U_{\mathcal{C}} = \prod_{(ij)\in\mathcal{C}} U_{ij} = \pm\mathbb{1}, \tag{5.17}$$

where $\mathbb{1}$ is the 2×2 identity matrix. Since SU(2) is non-abelian, the order of the multiplication is important and we define the direction for a contour to run in a counter-clockwise fashion. The result that for any closed contour, $U_{\mathcal{C}}$ is given by the identity matrix up to a sign follows directly from the definition in Eq. (5.16) and the fact that the sum of angles ω_{ij} along a closed path must add up to integer multiples of 2π. The vorticity of the contour $\mathcal{C}$ can then be simply defined via the trace of $U_{\mathcal{C}}$ as

$$V[\mathcal{C}] = \frac{1}{2}\operatorname{tr} U_{\mathcal{C}} = \pm 1. \tag{5.18}$$

In conclusion, once the chirality vectors are obtained directly from the spin configuration, the vorticity of any given closed path can be calculated. In our definition, a vorticity of $V[\mathcal{C}] = 1$ means that $\mathcal{C}$ contains no (or, equivalently, an even number of) vortices, whereas a negative vorticity $V[\mathcal{C}] = -1$, on the other hand, indicates that $\mathcal{C}$ contains a vortex (or an odd number of vortices).

5.1.3. Static spin structure factor

While theoretical analysis generally allows for the calculation of numerous different quantities, it is vital to provide links to experiment. In the treatment of magnetic systems, such a link is given by the *static spin structure factor* $\mathcal{S}$. It is commonly measured in magnetic neutron scattering experiments, and from its Bragg peak structure one can infer magnetic properties of the observed materials. In spin-$\frac{1}{2}$ systems, it is defined as the spatial Fourier transform of the equal-time spin-spin correlation function [110] for the spin component γ:

$$\mathcal{S}^{\gamma}(\mathbf{k}) = \sum_{i,j} e^{i\mathbf{k}\cdot(\mathbf{r}_i - \mathbf{r}_j)} \left\langle S_i^{\gamma} S_j^{\gamma} \right\rangle. \tag{5.19}$$

Summing over all spin components γ then yields the full spin structure factor $\mathcal{S}(\mathbf{k}) = \mathcal{S}^x(\mathbf{k}) + \mathcal{S}^y(\mathbf{k}) + \mathcal{S}^z(\mathbf{k})$, which is measured in scattering experiments with non-spin-polarized neutrons. In the classical limit at $T = 0$, fluctuations (both thermal and quantum) vanish, and the expectation value in Eq. (5.19) is trivially given by the product of the spin vectors, $\langle \mathbf{S}_i \cdot \mathbf{S}_j \rangle_{\text{classical},T=0} = \mathbf{S}_i \cdot \mathbf{S}_j$. In this case, we find

$$\mathcal{S}^\gamma(\mathbf{k}) = \big| \sum_i e^{i\mathbf{k}\cdot\mathbf{r}_i} S_i^\gamma \big|^2 \qquad (\text{fluctuation} - \text{free}). \tag{5.20}$$

The Bragg peaks in the structure factor indicate the dominant wave vectors which appear in the spin structure. For a state with commensurate magnetic order, these peaks thus directly identify the ordering vectors. Using Eq. (5.19) to calculate the structure factor of the (classical) 120° state given in Eq. (5.11), we find

$$\mathcal{S}^\gamma_{120^\circ}(\mathbf{k}) = \big| \sum_i e^{i(\mathbf{k}\pm\mathbf{Q})\cdot\mathbf{r}_i} \big|^2 \sim \delta(\mathbf{k} \pm \mathbf{Q}). \tag{5.21}$$

We have thus recovered the expected result that in the antiferromagnetic ground state of the triangular Heisenberg model at $T = 0$, all components of the spin structure factor are peaked in the corners of the Brillouin zone at $\pm\mathbf{Q}$.

5.2. The Heisenberg-Kitaev model

Let us now consider the Heisenberg-Kitaev model in which we add a Kitaev term to the Heisenberg model on the triangular lattice:

$$H = J_H \sum_{\langle ij \rangle} \mathbf{S}_i \cdot \mathbf{S}_j + J_K \sum_{\gamma=x,y,z} \sum_{\gamma-\text{links}} S_i^\gamma S_j^\gamma. \tag{5.22}$$

In the triangular lattice we can immediately identify three different spatial bond directions which we can label as x-, y- and z-links respectively. Due to the rotational C_6 symmetry of the lattice (a global rotation by $2\pi/6$ leaves the lattice invariant) the specific labeling of each group of links is arbitrary, but for the sake of consistency we define an $x-$link to be parallel to lattice vector $\mathbf{a}_x$, a y-link to be parallel to $\mathbf{a}_y$, and a z-link to be parallel to $\mathbf{a}_z$. This labeling is shown by a different coloring of the links in Fig. 5.1(a). The physical behavior of this Hamiltonian depends solely on the coupling parameters J_H and J_K. A convenient way to investigate all possible relative strengths of the two interactions is to parameterise J_H and J_K on the unit circle using an angle α:

$$J_H = \cos(\alpha), \quad J_K = \sin(\alpha), \tag{5.23}$$

where $\alpha \in [0, 2\pi)$. This way, we have reduced the effective parameters to only one parameter, and by running α from 0 to 2π one can access any point in the phase diagram. This parameterization is frequently used in discussions of the full phase diagram of the Heisenberg-Kitaev model [12, 94].

5.2.1. Klein duality and SU(2)-symmetric points

The particular form of the Heisenberg-Kitaev Hamiltonian Eq. (5.22) leads to an interesting property: A local basis transformation of the spin operators transforms the Hamiltonian in such a way that the form of the Hamiltonian is preserved but the coupling parame-

ters are changed. This feature was first discussed in Refs. [111,112] and is especially useful here as it reveals two additional SU(2)-symmetric points of the Hamiltonian (in addition to the two Heisenberg points at $\alpha = 0$ and $\alpha = \pi$). While this "trick" had been well-known for years, its underlying mathematical structure was first elucidated in Ref. [13], where it was shown that the structure of the basis transformation is that of the Klein four group $\mathbb{Z}_2 \times \mathbb{Z}_2$. Following this logic, we refer to the mapping as the *Klein duality*.

Consider the following representation of the Klein four group, given by the tuple $(\Gamma, \times)$ consisting of a set of elements Γ and a multiplication defined as follows[1]:

$$\Gamma = \{\mathbb{1}, x, y, z\} \tag{5.24a}$$

$$x \times x = y \times y = z \times z = x \times y \times z = \mathbb{1}. \tag{5.24b}$$

Each bond in the lattice can immediately be labeled with $\gamma_{ij} \in \{x, y, z\}$ according to the Kitaev interaction it carries. Using the group structure of $(\Gamma, \times)$, we then proceed to find labels $a_i \in \Gamma$ for each *site*. These site labels finally determine the type of basis rotation to be performed in spin space. To this end, we start by labeling a reference site i with the identity $\mathbb{1}$. The labels for the rest of the sites are then found by using the multiplication rules in Eq. (5.24b) on the bond labels along an arbitrary path connecting two sites. As an example, consider the reference site at i, labeled with $\mathbb{1}$ and a path connecting sites i and j (cf. Fig. 5.3(a)). Assume this path consists of the bond sequence $x \to y \to z \to x$. Then the site j will be labeled

$$\underbrace{x \times y \times z}_{=\mathbb{1}} \times x = \mathbb{1} \times x = x. \tag{5.25}$$

If the considered lattice is compatible with the duality transformation, the labels resulting from the outlined procedure do not depend on the chosen path. This is the most general way of constructing the sublattice labeling and works for arbitrary (Klein dual) lattices. The resulting structure for the case of the triangular lattice and the path from the example is shown in Fig. 5.3(a).

Once the lattice has been divided into the four sublattices determined by the site labels a_i, the spin basis on each site where $a_i \neq \mathbb{1}$ is rotated by π around the spin axis S^{a_i}. This rotation around one of the three axes effectively reverses the sign of the other two spin components. More explicitly, the transformations for the four types of sites are:

$$a_i = \mathbb{1}: \quad (S^x, S^y, S^z) \to (\ \ S^x, \ \ S^y, \ \ S^z) \tag{5.26a}$$

$$a_i = x: \quad (S^x, S^y, S^z) \to (\ \ S^x, -S^y, -S^z) \tag{5.26b}$$

$$a_i = y: \quad (S^x, S^y, S^z) \to (-S^x, \ \ S^y, -S^z) \tag{5.26c}$$

$$a_i = z: \quad (S^x, S^y, S^z) \to (-S^x, -S^y, \ \ S^z). \tag{5.26d}$$

After this transformation, the form of the Heisenberg-Kitaev Hamiltonian, Eq. (5.22), is unchanged, but the parameters are transformed:

$$\begin{aligned} J_H &\to -J_H, \\ J_K &\to 2J_H + J_K. \end{aligned} \tag{5.27}$$

It should be noted at this point that the duality transformation is a simple basis rotation, and thus two dual points on the phase diagram can be described by the same

[1] Note that the Klein group is abelian and the multiplication is thus commutative.

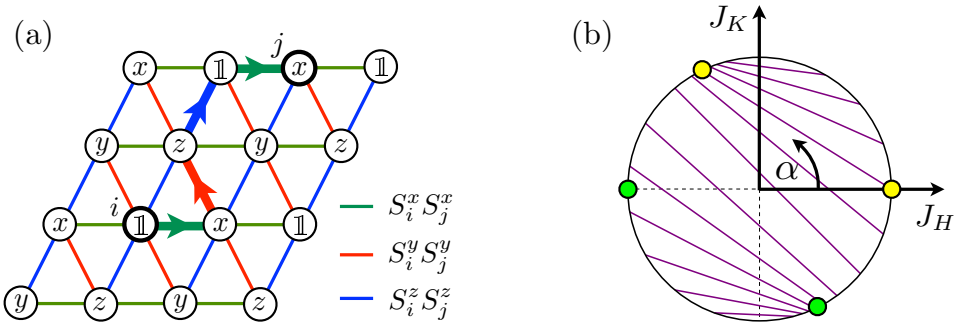

Figure 5.3.: (a) The four-color labeling of the triangular lattice. The bold arrows show the path used in the example in the text. (b) The angular parameterisation of the Heisenberg-Kitaev model with an angle $\alpha \in [0, 2\pi)$, where $J_H = \cos(\alpha)$ and $J_K = \sin(\alpha)$. The purple lines illustrate the structure of the mapping between two points in the phase diagram. The four dots indicate the location of the four $\mathrm{SU}(2)$-symmetric points: The yellow (green) pair corresponds to the antiferromagnetic (ferromagnetic) Heisenberg model and its dual Hamiltonian.

effective model, albeit with an enlarged/shrunk unit cell and different magnetic order, for an example see Fig. 5.4. Therefore, if one knows the ground state at any point in the phase diagram, by applying the duality transformation (i.e. the basis rotation) one immediately finds the ground state of the dual Hamiltonian. In the discussion of the phases of the Heisenberg-Kitaev model we repeatedly refer to this fact as it allows us to analyze only half of the phase diagram, while the other half can be immediately found by the Klein duality.

SU(2) symmetric points

The anisotropic spin interactions in the Kitaev Hamiltonian explicitly break the SU(2) invariance of the Heisenberg-Kitaev model. However, a closer inspection of Eqs. (5.27) shows that for the special case that

$$J_K = -2J_H \tag{5.28}$$

the Kitaev coupling J_K vanishes after the basis rotation and the transformed Hamiltonian consists only of the SU(2)-symmetric Heisenberg term. Thus it turns out that the phase diagram of the Heisenberg-Kitaev model has in fact *four* SU(2)-symmetric points: the ferro- and antiferromagnetic Heisenberg points at $J_H \neq 0$ and $J_K = 0$, and their dual counterparts given by Eq. (5.27).

A clearer picture of the Klein duality emerges in the angular parameterisation as given in Eq. (5.23). In this context, the Klein duality provides a (unique) mapping between the left hemisphere ($J_H < 0$) and the right ($J_H > 0$) on the circle defined by α, see Fig. 5.3(b) where the set of lines illustrates the mapping. The four SU(2) symmetric points are indicated by the yellow (green) circles, corresponding to the (anti-)ferromagnetic Heisenberg point and its dual.

Spin configurations at the SU(2) symmetric points

Fig. 5.4 shows the classical spin configurations at the four SU(2)-symmetric points along with the unit cells of each configuration, where the magnetic order at the dual points

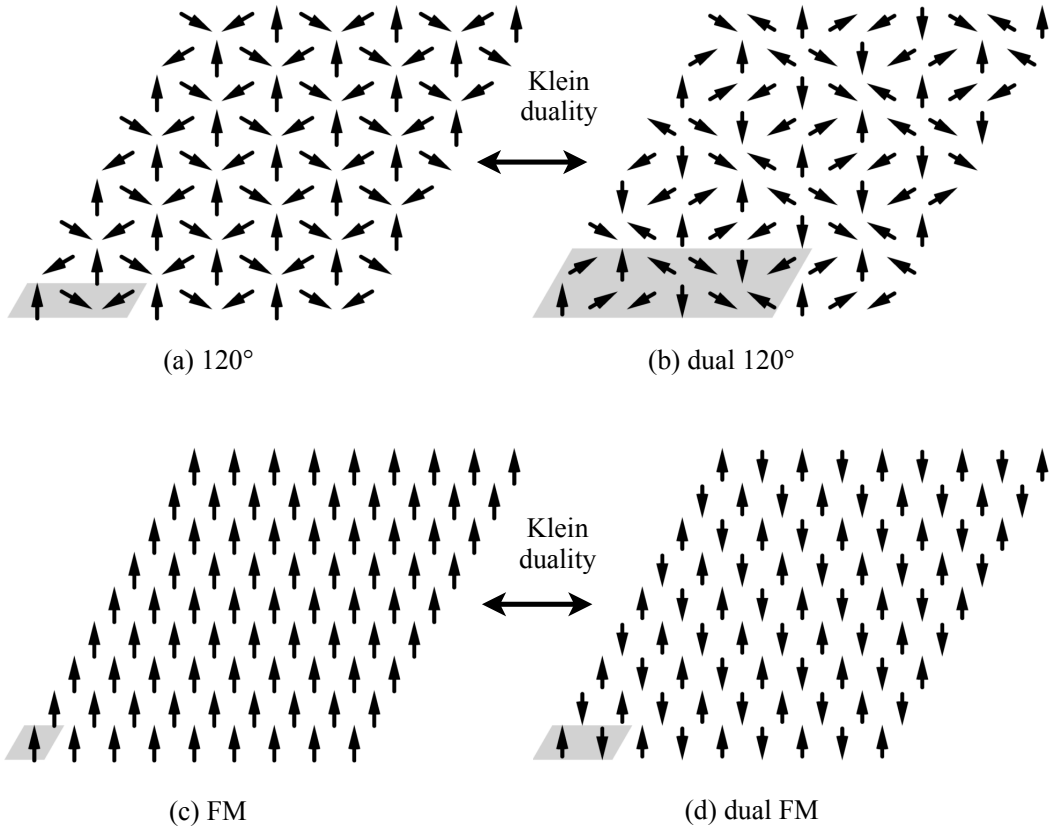

Figure 5.4.: Spin configurations and their dual configurations: (a) 120° order, (b) dual 120° order, (c) ferromagnet, and (d) dual ferromagnet. The gray diamond shows the unit cells of each configuration.

was obtained by a applying the basis transformation discussed above. This transformation Eq. (5.26d) doubles the size of the unit cell [112, 113], as indicated by the gray diamonds in the figure. While the 120° order gets transformed into a similar albeit larger structure, the dual ferromagnet is characterized by the formation of ferromangetically ordered chains with each chain oriented antiferromagnetically with respect to its two neighboring chains. Remarkably, although the dual ferromagnet exhibits antiferromagnetically ordered (i.e. staggered) spins, it is still an exact eigenstate of the Hamiltonian at that point and as such contains no quantum fluctuations, and it thus is an effectively classical ground state.

5.3. Phase diagram

With help of the Klein duality we could already identify four SU(2) symmetric points which each correspond to a different phase. Numerical simulations show, however, that in both the classical and the quantum model a fifth extended phase around the antiferromagnetic Kitaev point exists. Before discussing each phase in more detail below, we here give an overview of the phase diagram as obtained in Ref. [12] for the classical case and our own results for the quantum model.

5.3.1. Previous numerical results for the classical model

The full phase diagram for the *classical* Heisenberg-Kitaev model on the triangular lattice was examined numerically in Ref. [12]. Results obtained from classical Monte Carlo methods show the existence of a rich phase diagram, including a phase around the antiferromagnetic Heisenberg point characterized by a lattice of $\mathbb{Z}_2$ vortices. The classical phase diagram alongside schematic illustrations of the structure factors for each phase are shown in Fig. 5.5. In the following, we recap the results found in Ref. [12] as they serve as a motivation and starting point for our work.

Lattice of $\mathbb{Z}_2$ vortices

The arguably most intriguing phase is found around the antiferromagnetic Heisenberg point for $\alpha \approx 0$ ($J_H > 0$, $|J_K| \ll J_H$): While the classical ground state at exactly $J_K = 0$ is given by the 120° ordering of the spins, a small Kitaev exchange interaction locally preserves this order but distorts it on long distances. The order becomes incommensurate with the lattice and leads to the appearance of topological $\mathbb{Z}_2$ vortices discussed in Sec. 5.1.2. In the ground state these vortices form a triangular lattice with lattice vectors parallel to the microscopic ones. The distortion away from the 120° order is most clearly seen in the spin structure factor, where the dominant peaks of the components $\mathcal{S}^\gamma(\mathbf{k})$ each move slightly away from the K-point, depending on the component γ and the sign of J_K, as is shown schematically in Fig. 5.5.

Ferromagnetic phases

At the ferromagnetic Heisenberg point $\alpha = \pi$, the classical ground state is given by a homogeneous constant magnetization, as shown in Fig. 5.4(c). This state is, in fact, also an eigenstate of the full quantum-mechanical model. The phase around the ferromagnetic state (denotet FM in Fig. 5.5) was found to be somewhat stable against deviations from the exact SO(3) symmetric point by turning on Kitaev interactions. For a ferromagnetic Kitaev interaction $J_K < 0$, the phase indeed persists until the Heisenberg interaction vanishes exactly. By virtue of the Klein duality, one can map the FM phase to its dual phase FM'. Here, the spin order is *stripy* with a doubled unit cell as shown in Fig. 5.4(d).

The absence of any spatial modulation in the spin order of the ferromagnetic point at $\alpha = \pi$ implies that the dominant wave vector is simply $\mathbf{k} = \mathbf{0}$. This can be seen from Eq. (5.9): In the case of a constant $\hat{\mathbf{\Omega}}(\mathbf{r})$ the exponential function must be constant as well which can only hold for $\mathbf{Q} = \mathbf{0}$. This property is recovered in the spin structure factor, where for the entire FM phase the only Bragg peak is found in the center of the Brillouin zone at Γ. In contrast, the order in the FM' phase is non-constant. Here, for the particular ground state order each spin component is described by a different ordering vectors. This again translates to the structure factor, where the Bragg peaks now sit halfway between two Brillouin zone corners at the M points.

Kitaev points and nematic ordering

An interesting classical state is found at the Kitaev points $\alpha = \pm\pi/2$, where the Heisenberg interaction vanishes and the system is described entirely by the triangular Kitaev model. These points are self-dual (i.e. the Klein duality maps them to themselves) and must thus have a ground state which is invariant under the Klein basis transformation. The Monte Carlo results in Ref. [12] show that the spins form Ising chains along one of the

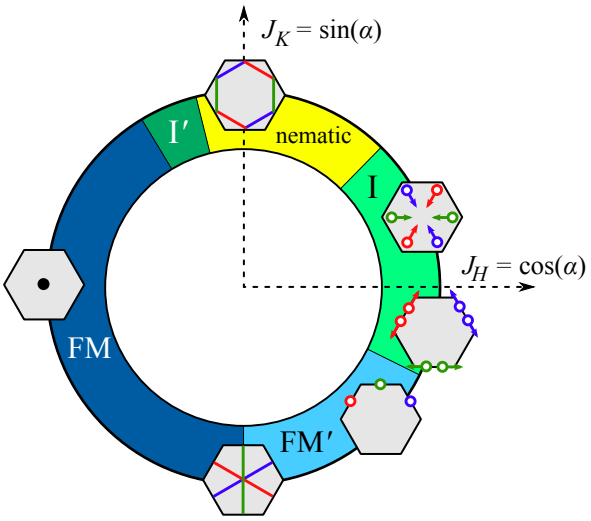

Figure 5.5.: Phase diagram of the classical model as obtained from classical Monte Carlo methods in Ref. [12]. I and I' denote the incommensurate $\mathbb{Z}_2$ vortex lattice phase and its dual, respectively. FM and FM' are the ferromagnet and its dual. The yellow shading around $\alpha = \pi/2$ indicates the nematic Kitaev phase. For each phase, the spin structure factor is shown schematically, with the peaks of the components $\mathcal{S}^\gamma(\mathbf{k})$ shown. The components γ are distinguished by three colors red, blue and green. Figure adapted from Ref. [12].

three lattice directions, where the chains are ordered antiferromagnetically for $\alpha = \pi/2$ and ferromagnetically for $\alpha = -\pi/2$. The type of Ising interaction is determined by the Kitaev coupling along the chosen lattice direction in which the chain forms, i.e. if the chains form along the direction of the Kitaev x-links, the effective Ising model for two spins on a chain is $H_{ij} = S_i^x S_j^x$. As the two remaining Kitaev interactions acting between two neighboring chains do not couple to this component, flipping the spins in a chain does not cost any energy. Thus, each chain is two-fold degenerate. Furthermore, the freedom of choosing any of the three lattice directions finally leads to a sub-extensive degeneracy of 3×2^L states, where L is the linear system size.

Deviating from the ferromagnetic Kitaev point immediately leads to the ferromagnetic order described in the previous section: Since flipping chains does not cost energy, any infinitesimal negative or positive Heisenberg interaction arranges the chains to the configurations Fig. 5.5(c) and (d), respectively. The classical Kitaev point at $\alpha = -\pi/2$ is thus indeed a (self-dual) *singular* point in the phase diagram.

The antiferromagnetic Kitaev point $\alpha = \pi/2$, however, appears stable against Heisenberg perturbations as each spin's neighbors in an adjacent Ising-AFM chain compensate each other [114]. This extended region is termed *nematic* in Fig. 5.5.

5.3.2. Phase diagram for the quantum model

The results from Ref. [12] cited in the last section were calculated for the classical model. An obvious question is how quantum fluctuations for the case of spin-$\frac{1}{2}$ degrees of freedom affect the phases. We performed sparse matrix diagonalization calculations using the Jacobi-Davidson [49,115] algorithm on various clusters consisting of up to 27 sites (for more detail see App. B). While the ground state energy itself provides a useful quantity to compare with analytics, its second derivative with respect to the parameter α helps indicate the phase boundaries, as the points at which $-\mathrm{d}^2 E_0/\mathrm{d}\alpha^2$ seems to diverge in-

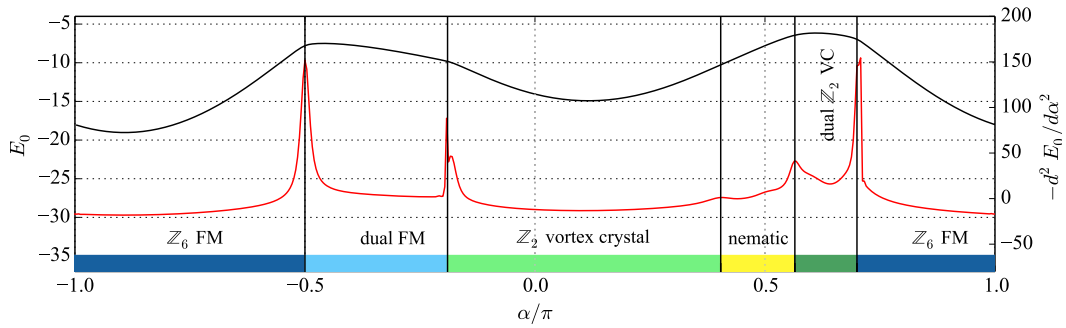

Figure 5.6.: Ground state energy E_0 (black line) and its second derivative, $-\mathrm{d}^2 E_0/\mathrm{d}\alpha^2$ (red line), with respect to the parameterization angle α. Peaks in the second derivative show the position of phase transitions. The data were obtained with sparse matrix diagonalization on a 24-sites cluster with periodic boundary conditions (see main text). The colored bar on the bottom refers to the color scheme of Fig. 5.7.

dicate phase transitions. The results are shown in Fig. 5.6 and the phase boundaries that we thus identified were used to create the quantum phase diagram shown in Fig. 5.7. Close investigation of the classical and quantum phase diagrams shows that some phase boundaries are shifted slightly (which might be a conspiracy of quantum fluctuations and finite-size effects due to the smaller cluster size for the exact diagonalization calculations), but all phases are present in both cases, which should be attributed to the mainly classical nature of the various ordered phases.

5.4. $\mathbb{Z}_2$ vortex lattice phase

In the discussion of the phases in the triangular Heisenberg-Kitaev model, we first focus on the vortex lattice phase around the antiferromagnetic Heisenberg point at $\alpha \approx 0$. In order to identify the ground state in this parameter regime, we first show that any finite Kitaev interaction immediately destabilizes the 120° order. Subsequently, from an approximative solution of the Hamiltonian in the continuum limit by means of an expanded Luttinger-Tisza method, we show that a lattice of $\mathbb{Z}_2$ vortices forms, which is in perfect agreement with the previously reported results obtained from classical Monte Carlo calculations [12].

5.4.1. Instability of the 120° order for finite Kitaev coupling

Let us first consider the fate of the classical 120° order in the presence of finite Kitaev interactions. It is a priori not clear how small anisotropic interactions affect the spin order, but we show that even an infinitesimal Kitaev coupling leads to an instability of the 120° state.

As the magnetic order of the spins discussed in Sec. 5.1.1 spontaneously breaks the (continuous) symmetry of the Hamiltonian, we expect the existence of three Goldstone modes. To identify these modes we consider small (i.e. long-wavelength) fluctuations of the spin vector. These fluctuations around the 120° order can be parameterized by two real fields $\pi_a(\mathbf{r})$ with $a = 1, 2$. Recalling our previous notation for classical spins, $\mathbf{S}_i = S\hat{\mathbf{\Omega}}(\mathbf{r}_i)$, the addition of fluctuations yields the following form for the orientation

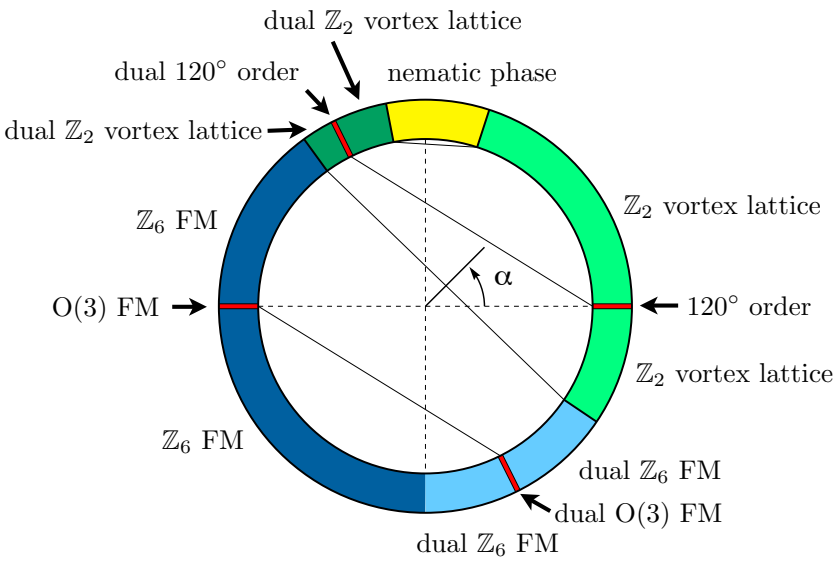

Figure 5.7.: Phase diagram of the quantum model obtained from exact diagonalization, with annotations labeling the phases based on both analytical and numerical calculations. This figure summarizes our results and should serve as a reference point.

vector:

$$\hat{\mathbf{\Omega}}(\mathbf{r}) = \hat{\mathbf{\Omega}}_{120^\circ}(\mathbf{r})\sqrt{1-(\pi_1(\mathbf{r}))^2-(\pi_2(\mathbf{r}))^2} + \delta\hat{\mathbf{\Omega}}(\mathbf{r}), \tag{5.29}$$

where $\hat{\mathbf{\Omega}}_{120^\circ}$ is given in Eq. (5.11) and the square-root ensures that $\hat{\mathbf{\Omega}}^2(\mathbf{r}) = 1$. The fluctuation term is given by

$$\delta\hat{\mathbf{\Omega}}(\mathbf{r}) = \pi_1(\mathbf{r})[-\mathbf{e}_1 \sin(\mathbf{Q}\cdot\mathbf{r}) + \mathbf{e}_2\cos(\mathbf{Q}\cdot\mathbf{r})] + \pi_2(\mathbf{r})\mathbf{e}_3. \tag{5.30}$$

Plugging this Ansatz in the Heisenberg-Kitaev Hamiltonian and expanding up to second order in the fluctuation fields π_a one obtains a second-order correction $\mathcal{E}^{(2)}$ to the energy, $\mathcal{E} = N\varepsilon_{120^\circ} + \mathcal{E}^{(2)}$, where the energy of the 120° order is given by Eq. (5.12) and N is the number of sites. The fluctuation part consists of two contributions,

$$\mathcal{E}^{(2)} = \mathcal{E}_0^{(2)} + \sum_{\gamma=x,y,z} \mathcal{E}_\gamma^{(2)}, \tag{5.31}$$

where $\mathcal{E}_0^{(2)}$ contains isotropic fluctuations due to the Heisenberg interaction and $\mathcal{E}_\gamma^{(2)}$ contains anisotropic fluctuations from the Kitaev interaction which are dependent on the bond-type γ. The full expressions for $\mathcal{E}^{(2)}$ are given in App. B. The eigenmodes of the fluctuations are found with the help of Fourier transformation,

$$\pi_a(\mathbf{r}_i) = \frac{1}{\sqrt{N}} \sum_{\mathbf{k}\in 1.\mathrm{BZ}} e^{i\mathbf{k}\mathbf{r}_i}\pi_a(\mathbf{k}). \tag{5.32}$$

No Kitaev interaction, $J_K = 0$

Let us first discuss the case of $J_K = 0$. In the absence of Kitaev interactions the anisotropic contribution vanishes, $\mathcal{E}^{(2)}\big|_{J_K=0} = \mathcal{E}_0^{(2)}$. The energy of the fluctuations

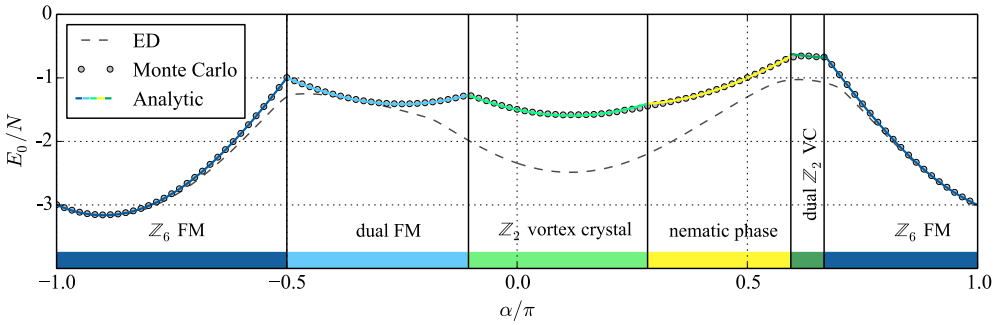

Figure 5.8.: Energies of the model: The exact diagonalization data was obtained on a 24 sites cluster, the Monte Carlo data on a 24×24 cluster at temperature $T = 0.005$. All five phases are present: The $\mathbb{Z}_6$ ferromagnet and its dual phase, the $\mathbb{Z}_2$ vortex crystal (VC) phase and its dual, and the "quantum" phase around the Kitaev point which is dominated by quantum fluctuations. The four $SU(2)$-symmetric points are shown as yellow spheres.

is then given by

$$\mathcal{E}_0^{(2)} = \frac{J_H S^2}{2} \sum_{\substack{\mathbf{k}\in 1.\mathrm{BZ} \\ \gamma=x,y,z}} \left[(1-\cos(\mathbf{k}\cdot\mathbf{a}_\gamma))\,|\pi_1(\mathbf{k})|^2 + (1+2\cos(\mathbf{k}\cdot\mathbf{a}_\gamma))|\pi_2(\mathbf{k})|^2 \right] \tag{5.33}$$

with $\pi_a^*(\mathbf{k}) = \pi_a(-\mathbf{k})$. The prefactor of the field π_1 vanishes in the center of the Brillouin zone at $\mathbf{k} = \mathbf{0}$. The field π_2, however, vanishes when $\mathbf{k}$ is in the corner of the Brillouin zone, e.g. $\mathbf{k} = \pm\mathbf{Q}$. When either field π_α drops out of the Hamiltonian, the corresponding fluctuations do not cost any energy, i.e. the modes become massless (or *soft*). These zero modes $\pi_1(\mathbf{k} = \mathbf{0})$ and $\pi_2(\pm\mathbf{Q})$ identify three Goldstone modes that correspond to a long-wavelength rotation and tilting of the local orthogonal frame, respectively. In particular, the energy dispersion of the tilting mode $\pi_2(\mathbf{k})$, i.e. the second term in the sum in Eq. (5.33), can be expanded around momentum $\mathbf{Q}$ and then, for $|\mathbf{q}| \ll |\mathbf{Q}|$, takes the form

$$\varepsilon^{\mathrm{tilt}}_{\mathbf{Q}+\mathbf{q}}\Big|_{J_K=0} \approx J_H S^2 \frac{3}{8}\mathbf{q}^2. \tag{5.34}$$

Finite Kitaev interaction, $J_K \neq 0$

For a finite Kitaev coupling we can still diagonalize the problem to obtain the eigenenergies perturbatively in J_K. If we consider the long-wavelength limit of small momenta $|\mathbf{q}| \ll |\mathbf{Q}|$, the three zero modes cannot couple to each other (as they are too far away from each other in momentum space). Then, to lowest order, the dispersion relation obtained for the tilting mode in this limit is given by

$$\varepsilon^{\mathrm{tilt}}_{\mathbf{Q}+\mathbf{q}} \approx J_H S^2 \frac{3}{4}\mathbf{q}^2 - 2J_K S^2 \sum_{\gamma=x,y,z} \mathbf{q}\cdot\mathbf{a}_\gamma \sin(\mathbf{Q}\cdot\mathbf{a}_\gamma)\,(e_3^\gamma)^2\,. \tag{5.35}$$

Any finite $J_K \neq 0$ results in a negative value of $\varepsilon^{\mathrm{tilt}}_{\mathbf{Q}+\mathbf{q}}$ at certain momenta $\mathbf{k}_{\mathrm{inst}}$, indicating that the ground state order becomes unstable. We have thus found that the tilting Goldstone modes trigger the instability of the 120° antiferromagnetic ordering in the presence of a finite Kitaev interaction J_K. The wavevector at which $\varepsilon^{\mathrm{tilt}}$ becomes maximally neg-

ative is given by

$$\begin{aligned}\mathbf{k}_{\text{inst}} &= \frac{J_K}{J_H}\frac{4}{3}\sum_{\gamma=x,y,z}\mathbf{a}_\gamma \sin(\mathbf{Q}\cdot\mathbf{a}_\gamma)(e_3^\gamma)^2 \\ &= \frac{J_K}{J_H}\frac{1}{\sqrt{3}}\begin{pmatrix}(e_3^y)^2+(e_3^z)^2-2\,(e_3^x)^2\\ \sqrt{3}\left[(e_3^z)^2-(e_3^y)^2\right]\end{pmatrix},\end{aligned} \tag{5.36}$$

which can be expressed entirely in terms of the vector $\mathbf{e}_3$. Without loss of generality, we can assume the spins of the 120° ordering to be confined within the x-y plane. Then $\mathbf{e}_3 = \hat{\mathbf{z}}$ and Eq. (5.36) reduces to

$$\mathbf{k}_{\text{inst}} = \frac{J_K}{J_H}\begin{pmatrix}1\\ \frac{1}{\sqrt{3}}\end{pmatrix} = \frac{J_K}{J_H}\frac{2}{\sqrt{3}}\mathbf{a}_z. \tag{5.37}$$

5.4.2. Continuum limit of the Heisenberg-Kitaev Hamiltonian

By establishing the instability of the antiferromagnetic ordering at $J_H > 0$ and infinitesimal Kitaev interaction J_K, we have shown that the 120° order cannot be the correct classical ground state. In fact, from the numerical results, we instead expect the ground state to be given by an incommensurate spin order forming a large-scale lattice of $\mathbb{Z}_2$ vortices. In the following section, by considering a continuum limit of the problem we present an analytical solution which indeed recovers such a state. Our solution is an approximation to the true ground state, but it still exhibits the characteristic properties found earlier in numerics.

Let us first formulate the full Heisenberg-Kitaev Hamiltonian in momentum space:

$$H = \sum_{\mathbf{k}\in 1.\text{BZ}} \mathbf{S}_{\mathbf{k}}\left[\mathcal{J}^0(\mathbf{k})\mathbb{1} + \mathcal{J}^K(\mathbf{k})\right]\mathbf{S}_{-\mathbf{k}}, \tag{5.38}$$

where the Heisenberg interaction $\mathcal{J}^0(\mathbf{k})$ is given by Eq. (5.6) and the Kitaev interaction is encoded in the matrix:

$$\mathcal{J}^K(\mathbf{k}) = J_K\begin{pmatrix}\cos(\mathbf{a}_x\cdot\mathbf{k}) & & \\ & \cos(\mathbf{a}_y\cdot\mathbf{k}) & \\ & & \cos(\mathbf{a}_z\cdot\mathbf{k})\end{pmatrix}. \tag{5.39}$$

From the classical Monte Carlo results we know that, on short length scales, the 120° order is preserved, albeit with a slowly varying spatial modulation which is the origin of the topological defects. It is therefore reasonable to approximate the problem by expanding the full Hamiltonian to second order around the wave vectors of the 120° order, $\pm\mathbf{Q}$. Assuming $\mathbf{k} = \mathbf{Q} + \mathbf{q}$ with $|\mathbf{q}| \ll 1$, this yields the continuum Hamiltonian in $\mathbf{k}$-space

$$H = \int_{|\mathbf{q}|<\Lambda} \mathrm{d}\mathbf{q}\,\mathbf{S}_{\mathbf{Q}+\mathbf{q}}\left[\tilde{\mathcal{J}}^0(\mathbf{q})\mathbb{1} + \frac{\sqrt{3}}{2}J_K\begin{pmatrix}\mathbf{a}_x\cdot\mathbf{q} & & \\ & \mathbf{a}_y\cdot\mathbf{q} & \\ & & \mathbf{a}_z\cdot\mathbf{q}\end{pmatrix}\right]\mathbf{S}_{-(\mathbf{Q}+\mathbf{q})} \tag{5.40}$$

with an infrared cut-off Λ and the exchange interaction

$$\tilde{\mathcal{J}}^0(\mathbf{q}) = -\frac{3J_H}{2}\left[1 + \frac{J_K}{3J_H} - \frac{\mathbf{q}^2}{4}\right]. \tag{5.41}$$

To allow for the spatial modulation of the orthonormal frame which locally defines the 120° order, we modify the expression in Eq. (5.11) by allowing the vectors $\mathbf{e}_i$ to depend on the position $\mathbf{r}$,

$$\mathbf{e}_i \to \mathbf{e}_i(\mathbf{r}). \tag{5.42}$$

In this formulation, the classical spin at site $\mathbf{r}$ can now be expressed as

$$\begin{aligned}\mathbf{S}(\mathbf{r}) = S\hat{\mathbf{\Omega}}(\mathbf{r}) &= S\left[\mathbf{e}_1(\mathbf{r})\cos(\mathbf{Q}\cdot\mathbf{r}) + \mathbf{e}_2(\mathbf{r})\sin(\mathbf{Q}\cdot\mathbf{r})\right] \\ &= \frac{S}{\sqrt{2}}\left[\mathbf{e}^-(\mathbf{r})e^{i\mathbf{Q}\cdot\mathbf{r}} + \mathbf{e}^+(\mathbf{r})e^{-i\mathbf{Q}\cdot\mathbf{r}}\right],\end{aligned} \tag{5.43}$$

where we defined $\mathbf{e}^\pm \equiv (\mathbf{e}_1 \pm i\mathbf{e}_2)/\sqrt{2}$. Back-transforming Eq. (5.40) to real-space then yields the Hamiltonian

$$H = \frac{3J_H S^2}{4}\int \mathrm{d}\mathbf{r} \sum_{\gamma=x,y,z} e_\gamma^-(\mathbf{r})\left[-\nabla^2 - i\frac{4J_K}{\sqrt{3}J_H}\mathbf{a}_\gamma\cdot\nabla\right]e_\gamma^+(\mathbf{r}) + \text{const.} \tag{5.44}$$

Again, for $J_K = 0$ this Hamiltonian reduces to the continuum limit of the Heisenberg model, but any finite Kitaev interaction induces a coupling to constant gauge fields, which are here given by the lattice vectors $\mathbf{a}_i$. The magnetization can thus minimize its energy by allowing for a spatial modulation of the SO(3) order parameter on length scales $\sim J_H/J_K$, which is the expected result.

5.4.3. Luttinger-Tisza approximation of the classical ground state

While the 120° order instability and the continuum Hamiltonian indicate on an analytical level the existence of an incommensurate ground state for finite J_K, it turns out that an exact classical ground state is difficult to obtain. This is mainly due to the strong condition that the spin length be strictly S at every site. However, one can loosen this constraint and obtain an approximate ground state with varying spin lengths. This is known as the Luttinger-Tisza approximation [116,117], in which the strong conditions that $|\mathbf{S}(\mathbf{r})| = S$ for any $\mathbf{r}$ are replaced by the weaker condition that the spin length must be conserved only *on average*. This yields a ground state which is a good approximation for large length scales, $J_K|\mathbf{r}|/J_H \gg 1$, or, alternatively, for small momenta $|\mathbf{q}| \ll J_K/J_H$.

To set up the Luttinger-Tisza approximation, we use the notation introduced in Sec. 5.1.1. However, the spin orientation vectors are no longer unit vectors, and here we formally define

$$\mathbf{S}(\mathbf{r}) = S\mathbf{\Omega}(\mathbf{r}), \tag{5.45}$$

for an arbitrary $\mathbb{R}^3$-vector $\mathbf{\Omega}$. The energy functional for the classical spins then assumes the following form:

$$\mathcal{E} = J_H S^2 \sum_{\langle ij\rangle} \mathbf{\Omega}_i\cdot\mathbf{\Omega}_j + J_K S^2 \sum_{\gamma\parallel\langle ij\rangle} \Omega_i^\gamma\Omega_j^\gamma - \sum_i \lambda_i(\mathbf{\Omega}_i^2 - 1), \tag{5.46}$$

where $\mathbf{\Omega}_i \equiv \mathbf{\Omega}(\mathbf{r}_i)$. This functional is given by the Heisenberg-Kitaev Hamiltonian and an additional term which locally imposes the unit length of the spin vector with the help of the Lagrange multiplier λ_i. In the simplest Luttinger-Tisza approximation, the N Lagrange multipliers are reduced to only one by changing the last term in Eq. (5.46) to

$$\lambda_0 \sum_i (\mathbf{\Omega}_i^2 - 1). \tag{5.47}$$

This way one effectively requires the *sum* of all spins squared to be N, but each individual spin can have arbitrary length. While within this approximation the problem becomes tractable, the approximation is fairly coarse. To see how it can be improved, however, we need to reformulate the problem in momentum space. Plugging in the Fourier transforms of the spin vectors,

$$\mathbf{\Omega}_i = \frac{1}{\sqrt{N}} \sum_{\mathbf{k}\in 1.\mathrm{BZ}} e^{i\mathbf{k}\cdot\mathbf{r}_i} \mathbf{\Omega}_{\mathbf{k}}, \tag{5.48}$$

the functional Eq. (5.46) then takes a form similar to Eq. 5.38:

$$\frac{\mathcal{E}}{NS^2} = \sum_{\mathbf{k}} \mathbf{\Omega}_{\mathbf{k}} \left[\mathcal{J}^0(\mathbf{k})\mathbb{1} + \mathcal{J}^K(\mathbf{k})\right] \mathbf{\Omega}_{-\mathbf{k}} + \sum_{\mathbf{k},\mathbf{k}'} \lambda_{-\mathbf{k}-\mathbf{k}'} \mathbf{\Omega}_{\mathbf{k}} \cdot \mathbf{\Omega}_{\mathbf{k}'} - \lambda_0 \tag{5.49}$$

where $\lambda_0 = \lambda_{\mathbf{k}=0}$, and the summations all run over the entire first Brillouin zone. In this formulation, softening the spin length conservation requirement as in (5.47) translates to keeping only the λ_0 multiplier, and setting $\lambda_{\mathbf{k}} = 0$ for any $\mathbf{k} \neq 0$. This reveals a dominant mode $\mathbf{k}^{(1)}$ and the corresponding amplitude $\mathbf{\Omega}^{(1)}_{\mathbf{k}}$ to be used in the Fourier expansion Eq. (5.48). By successively identifying further modes and their amplitudes, we can thus gradually improve our approximation.

At the Heisenberg point $J_K = 0$, we recover the results from Sec. 5.1.1 and find that the diagonal components of the matrix are minimal for momenta at the K and K′ points in the corner of the Brillouin zone. In this case, the system is fully described by only one dominant mode $\mathbf{k} = \mathbf{Q}$, thus leading to 120° ordering. Turning on Kitaev interactions $J_K \neq 0$, we see from Eq. (5.40) that the minimum is shifted away from the corners. For every spin component a different new minimum appears and the new dominant wave vectors then have the form

$$\mathbf{k}^{(1)}_{\gamma} = \mathbf{Q} - t\,\mathbf{a}_{\gamma}, \tag{5.50}$$

where $\gamma = x, y, z$, and $t \in \mathbb{R}$ is a function of J_K/J_H. These wave vectors are incommensurate with the lattice and lead to a modulation in the real-space spin configuration on length-scales of the order $\sim 1/t$. A consequence of the incommensurability of the $\mathbf{k}^{(1)}_{\gamma}$ vectors is that the Fourier components $\Omega^{\gamma}(\mathbf{k}^{(1)}_{\gamma})$ which belong to these wave vectors generally induce further finite Fourier components (higher harmonics) of the Lagrange multiplier as discussed above, they are given by $\lambda_{\pm 2\mathbf{k}^{(1)}_{\gamma}}$ with $\gamma = x, y, z$. These finite Lagrange multipliers in turn induce two finite secondary Fourier components $\Omega^{\alpha}(\mathbf{k}^{(2)}_{\alpha,\beta})$ with the secondary modes

$$\mathbf{k}^{(2)}_{\alpha,\beta} = \mathbf{Q} - t\,(2\mathbf{a}_{\beta} - \mathbf{a}_{\alpha}), \tag{5.51}$$

where $\alpha, \beta = x, y, z$ and $\beta \neq \alpha$. In this fashion, each mode $\mathbf{k}^{(i)}$ induces higher-order modes $\mathbf{k}^{(i+1)}$. The corresponding Fourier components $\Omega^{\alpha}(\mathbf{k}^{(i)})$ define the amplitude of these modes and can be found by straight-forward minimization of the Hamiltonian.

In our calculation, we keep the primary and secondary modes given above, and neglect all higher orders. Minimizing the functional in Eq. (5.49) we obtain for the energy per site in this approximation

$$\begin{aligned}\varepsilon_{\mathrm{LT}}(t) = -\frac{J_H}{9}\Bigg[&17\sin\frac{\pi-3t}{6} + \sin\frac{\pi+15t}{6} + \cos\frac{\pi+6t}{3} + 8\sin\frac{\pi+6t}{6} \\ &+ \frac{J_K}{J_H}\left(\cos\frac{\pi+6t}{3} + 8\sin\frac{\pi+6t}{6}\right)\Bigg],\end{aligned} \tag{5.52}$$

which still depends on the parameter t that quantifies the distance of the primary Bragg peaks $\mathbf{k}_\alpha^{(1)}$ from the corner of the Brillouin zone. To find the ground state energy $\varepsilon_{\mathrm{LT}}(t_{\min})$, one now needs to find $t_{\min}$ by minimizing Eq. (5.52). The result is shown as a green solid line in Fig. 5.8, and it is in excellent agreement with results from the classical Monte Carlo simulation. In particular, it is important to point out that the energy $\varepsilon_{\mathrm{LT}}(t_{\min})$ for $J_K \neq 0$ is lower than the energy of the 120° state, which for $J_K \neq 0$ is given by

$$\varepsilon_{120^\circ} = -S^2 \frac{1}{2}(3J_H + J_K). \tag{5.53}$$

It is now straight-forward to construct the corresponding classical ground state. The state resulting from the Luttinger-Tisza approximation is still a function of t. It is given by the spin components

$$\Omega_t^\alpha(\mathbf{r}) = \frac{4}{3\sqrt{3}} \mathrm{Re}\left\{ e^{i\phi} \left(e^{i(\mathbf{Q}-t\mathbf{a}_\alpha)\cdot(\mathbf{r}-\mathbf{r}_0)} + \frac{1}{4} \sum_{\substack{\beta=x,y,z \\ \beta\neq\alpha}} e^{i(\mathbf{Q}-t(2\mathbf{a}_\beta-\mathbf{a}_\alpha))\cdot(\mathbf{r}-\mathbf{r}_0)} \right) \right\}, \tag{5.54}$$

where $\phi \in \mathbb{R}$ is a phase and $\mathbf{r}_0 = (x_0, y_0)^T$ fixes an origin. The ground state is finally obtained by setting $t = t_{\min}$. The spin length $|\mathbf{\Omega}_t(\mathbf{r})|$ varies in space, but it nevertheless remains always finite so that the orientation of $\mathbf{\Omega}_t(\mathbf{r})$ is always well defined.

One shortcoming of this result is the fact that in the limit $J_K \to 0$ it does *not* recover the 120° order. The limit $|\mathbf{q}| \ll J_K/J_H$ does not commute with $J_K \to 0$, and, as a consequence, does not smoothly connect with the Heisenberg point. However, in the limit $J_K \to 0$ the value of $t_{\min} \to 0$ and $\varepsilon_{\mathrm{LT}}(0) = -S^2 3J_H/2$ still recovers the exact classical ground state energy. Furthermore, for finite J_K, the state Eq. (5.54) is in very good agreement with numerical results, as we will discuss now.

Vortices

The approximate classical ground state of Eq. (5.54) does indeed contain a lattice of $\mathbb{Z}_2$ vortices, thus confirming the numerical results in Ref. [12]. This can be easily seen by calculating the chirality in Eq. (5.14) and from this the vorticity. Fig. 5.9 compares both quantities obtained from the Monte Carlo results and the mean-field state.

Fig. 5.14 shows the obtained chirality vectors (top row), the length of the chirality vectors (middle row) and the calculated vorticity (bottom row). The lattices in the Monte Carlo simulation have a side-length of $L = 18$ and periodic boundary conditions. We performed $50\,000$ thermalization sweeps at a temperature $T = 0.05$, and then successively reduced the temperature to $T = 0$ in another $50\,000$ sweeps. The point on the phase diagram is $\alpha = 0.146\pi$, which yields a relative Kitaev coupling strength of $J_K/J_H = \tan\alpha \approx 0.49$.

After finding $t_{\min}$ numerically, the texture of the calculated chirality clearly resembles that of the Monte Carlo results. The orientation of the vortex crystal is fixed by the underlying triangular atomic crystal lattice, and its lattice constant grows by decreasing the Kitaev interaction J_K. One difference between numerics and analytics is that for a given value of J_K, the distance between to vortices is slightly overestimated in our analytical results. This can be attributed to two facts: Keeping only the first two dominant modes is a significant improvement over the simplest approximation but still omits a lot of information kept in higher modes. The more higher terms are kept, the less will each spin deviate from unity length, and one can expect that in this case the formation of topo-

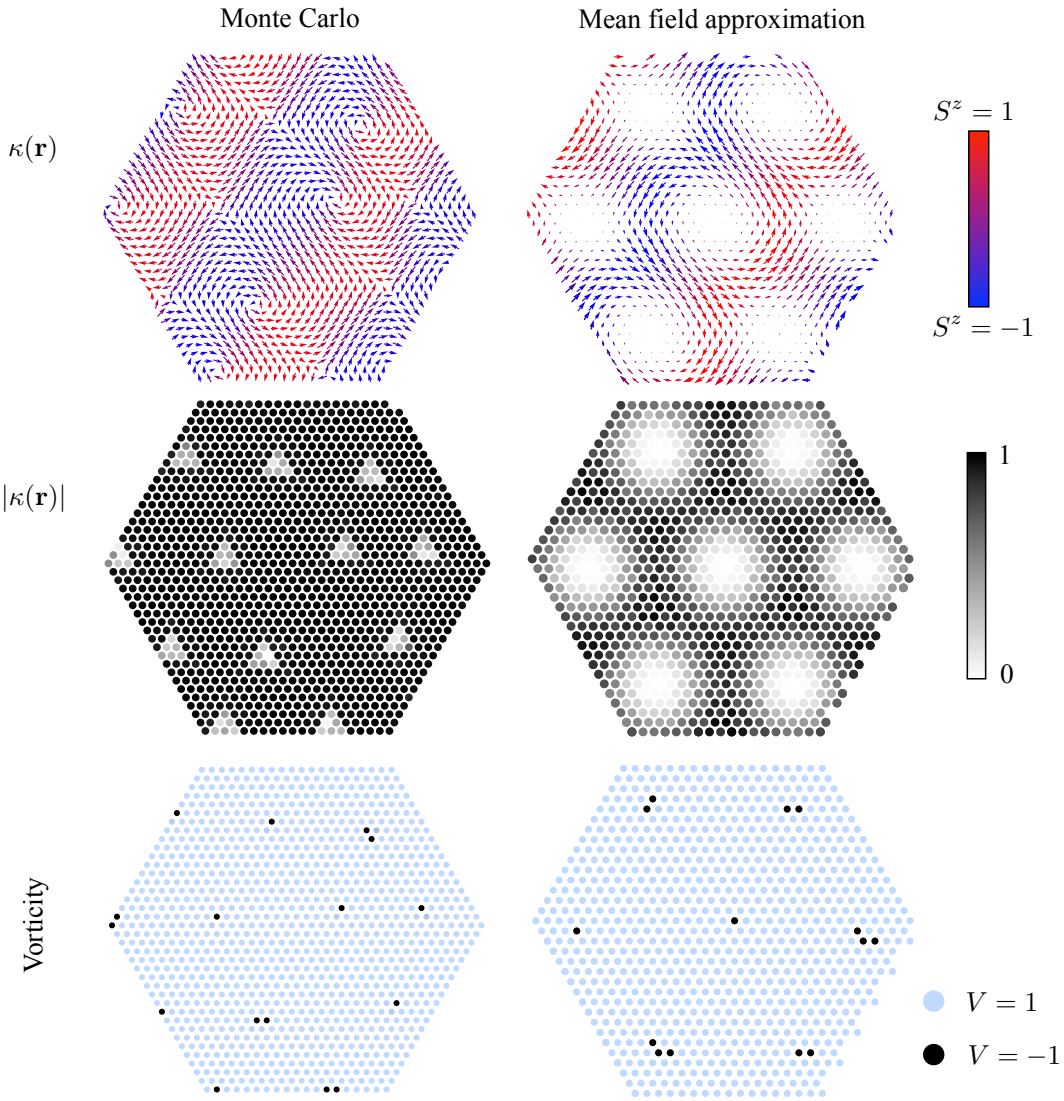

Figure 5.9.: Chirality and vorticity obtained from classical Monte Carlo simulations and the mean field result. The Monte Carlo simulations were performed for periodic boundary conditions at $T = 0.05$ with 50 000 thermalization sweeps and then 50 000 sweeps at $T = 0$. All results are obtained for $\alpha = 0.146\pi$. Top row: The (normalized) chirality vectors in which the vortices can be identified. The color code refers to the out-of-plane component S^z. Center row: The absolute value of the chirality vectors. In the core of the vortices the chirality vectors have minimal length, which is seen in both results. Bottom row: The vorticity $V[\mathcal{C}]$ calculated from the chirality vectors using the rhombic paths $\mathcal{C}$ discussed in Sec. 5.1.2, showing that the vortices are in fact $\mathbb{Z}_2$ vortices as defined in the main text.

logical defects is enhanced. Secondly, our analytical approximation has been performed for the case of small J_K. In the numerical simulations, on the other hand, the Kitaev coupling needs to be large enough to fit at least two vortices inside the lattice cluster.

However, the arguably most striking difference is that the length of the chirality vectors in the analytical results vanishes quickly as one approaches a vortex core, whereas the change in length is much less pronounced in the Monte Carlo results. This can be attributed to the fact that the spin length is not conserved in the analytical approach and thus the variation of the chiralities is allowed to be much stronger.

Spin structure factor

Further agreement between numerical and analytical results can be found in the spin structure factor. From Eqs. (5.20) and (5.54) it follows that the modes included in the analytical solution manifest themselves as Bragg peaks. A characteristic of the spin structure factor of the $\mathbb{Z}_2$ vortex lattice phase is the correlation between the position of magnetic Bragg peaks and the corresponding spin component: If we take into account only modes up to second order, we find that $\mathcal{S}^\alpha(\mathbf{k})$ has one dominant Bragg peak at position $\mathbf{k}_\alpha^{(1)}$ and two secondary Bragg peaks at $\mathbf{k}_{\alpha,\beta}^{(2)}$ for $\beta \neq \alpha$. Within our approximation the relative weight of secondary and primary Bragg peaks are predicted to be $1/4^2 = 1/16$ and, according to Eq. (5.50) the dominant primary Bragg peak of $\mathcal{S}^\alpha(\mathbf{k})$ are shifted away from the Brillouin zone corner by $t_{\min}$ in the direction $\mathbf{a}_\alpha$. Fig. 5.10 shows a comparison of the numerical data obtained from classical Monte Carlo and our analytical solution.

Both primary and secondary Bragg peaks are clearly present, with the analytical estimates (arrows) agreeing nicely. In the last section we argued that the distance of vortices is overestimated in our result. This small effect naturally translates to the structure factor where the distance of the Bragg peaks from the corners is accordingly slightly *under*estimated. Nonetheless, the analytical and numerical results are in very good agreement: The positions of the both primary and secondary Bragg peaks are reproduced very accurately.

Since we ran the Monte Carlo simulations at small but finite temperatures, we find a slight broadening of the Bragg peaks. Also, an exact commensurability of the vortex lattice with the size of the cluster of the microscopic lattice is generally not given and this frustration further affects the Monte Carlo averages. Comparing the relative heights of the primary and secondary Bragg peaks in the numerical results can therefore be expected to be somewhat unreliable. However, in our Monte Carlo results we find the ratio to be

$$\frac{\mathcal{S}(\mathbf{k}_\alpha^{(1)})}{\mathcal{S}(\mathbf{k}_\beta^{(2)})} \approx 19 \pm 4, \tag{5.55}$$

which, within error margins, agrees with our analytical prediction of $\mathcal{S}(\mathbf{k}_\alpha^{(1)})/\mathcal{S}(\mathbf{k}_\beta^{(2)}) = 16$.

5.4.4. Dual $\mathbb{Z}_2$ vortex lattice

With the help of the duality transformation in Eqs. (5.26d) and (5.27) one immediately obtains the energy and ground state of the phase dual to the $\mathbb{Z}_2$ vortex around $J_H < 0$ and $J_K = -2J_H > 0$. The energy is shown in Fig. 5.8.

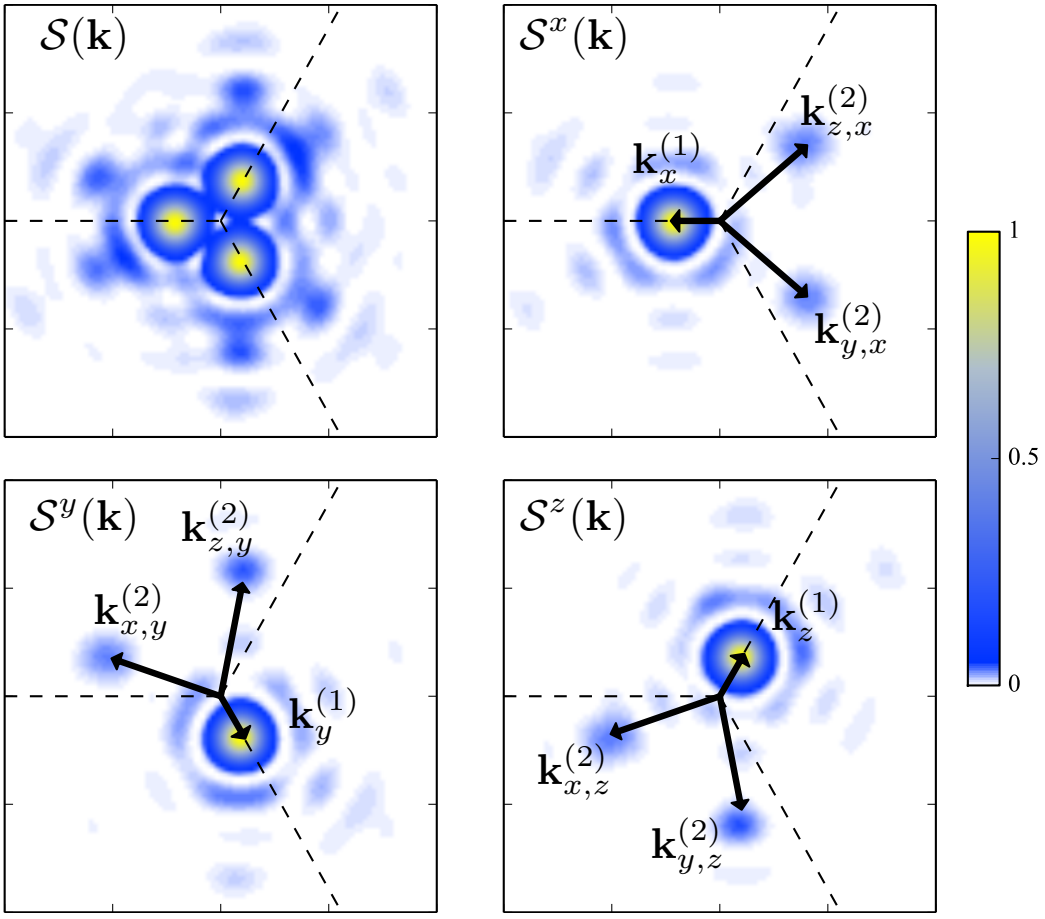

Figure 5.10.: The spin structure factor in the corner of the Brillouin zone around $\mathbf{k} = -\mathbf{Q}$, for $\alpha = 0.152\pi$, with a normalized scale such that the primary Bragg peaks have a height of 1. The numerical data was calculated on a C_6-symmetric cluster with an edge length of 20 sites. After $2\,000\,000$ thermalization sweeps at a temperature $T = 0.05$, another $2\,000\,000$ sweeps were run in which the temperature was gradually lowered to $T = 0$. The full spin structure factor (upper left panel) is given as the sum of its components, $\mathcal{S}(\mathbf{k}) = \mathcal{S}^x(\mathbf{k}) + \mathcal{S}^y(\mathbf{k}) + \mathcal{S}^z(\mathbf{k})$. The dashed lines indicate the Brillouin zone borders, and the arrows depict the analytical results for the primary and secondary Bragg peaks.

5.5. Ferromagnetic order

In contrast to the antiferromagnetic case, the ground state of the ferromagnetic Heisenberg model is given by a constant, homogeneous spin configuration, $\hat{\mathbf{\Omega}}(\mathbf{r}) \equiv \hat{\mathbf{\Omega}}$ with $\hat{\mathbf{\Omega}}^2 = 1$. This state is an exact eigenstate of the Hamiltonian and it contains no quantum fluctuations, which arise in the antiferromagnetic model e.g. due to spin-flip terms. The corresponding classical energy per site is easily found and independent of the orientation of $\hat{\mathbf{\Omega}}$. It is given by

$$\varepsilon_{\mathrm{FM}} = S^2 \left(3J_H + J_K\right). \tag{5.56}$$

At $J_K = 0$ (or $\alpha = \pi$) this corresponds to the exact ground state energy of the quantum mechanical system (see Fig. 5.8). However, any finite J_K gives rise to fluctuation corrections to the ground state. It turns out that these fluctuations lower the O(3) symmetry of the Heisenberg ferromagnet and discriminate between the various orientations of $\hat{\mathbf{\Omega}}$. We find that in this case, order-by-disorder leads to a minimization of the energy when

the spins align along one of the three spin-axes. This reduces the symmetry from O(3) to $\mathbb{Z}_6$ as only six possible directions for the magnetization remain. A similar result for the antiferromagnetic Heisenberg-Kitaev model on the honeycomb lattice was reported in Ref. [118].

Spin-wave analysis of the $\mathbb{Z}_6$ ferromagnet

To see how quantum fluctuations affect the ferromagnetic ground state we perform a $1/S$ expansion for $|J_K/J_H| \ll 1$ and $J_H < 0$. With the standard Holstein-Primakoff transformation we can express the spin operators in terms of bosonic operators:

$$\tilde{S}_i^z = S - a_i^\dagger a_i, \qquad \tilde{S}_i^+ = \sqrt{2S - a_i^\dagger a_i}\, a_i, \qquad \tilde{S}_i^- = a_i^\dagger \sqrt{2S - a_i^\dagger a_i}, \tag{5.57}$$

where $\tilde{S}_i^\pm = \tilde{S}_i^x \pm i\tilde{S}_i^y$. Here, $a_i^{(\dagger)}$ are bosonic annihilation (creation) operators for the site $i \equiv \mathbf{r}_i$, and we chose the operator $\tilde{S}^z$ to be aligned along the local z-axis. The spin operator $\mathbf{S}$ within the laboratory frame is related to $\tilde{\mathbf{S}} = (\tilde{S}^x, \tilde{S}^y, \tilde{S}^z)^T$ by a rotation $\mathbf{S} = R\tilde{\mathbf{S}}$ with the SO(3) matrix

$$R = \begin{pmatrix} -\sin\phi & -\cos\theta\cos\phi & \sin\theta\cos\phi \\ \cos\phi & -\cos\theta\sin\phi & \sin\theta\sin\phi \\ 0 & \sin\theta & \cos\theta \end{pmatrix}, \tag{5.58}$$

where $\phi \in [0, 2\pi)$ and $\theta \in [0, \pi]$. After reformulating the Hamiltonian in terms of the bosonic operators, we expand to second order in the $a_i^{(\dagger)}$'s. The first-order term vanishes and we find the two contributions $H = H^{(0)} + H^{(2)}$, where $H^{(0)} = N\varepsilon_{\mathrm{FM}}$ and

$$H^{(2)} = \frac{1}{2}\sum_{\mathbf{k}\in 1.\mathrm{BZ}} \left[\psi_{\mathbf{k}}^\dagger h_{\mathbf{k}} \psi_{\mathbf{k}} - S \sum_{\gamma=x,y,z} (\cos(\mathbf{k}\cdot\mathbf{a}_\gamma) - 1) \left(2J_H + J_K \left(1 - \hat{\Omega}_\gamma^2 \right) \right) \right], \tag{5.59}$$

where we defined the two-component spinor $\psi_{\mathbf{k}}^\dagger = \left(a_{\mathbf{k}}^\dagger, a_{-\mathbf{k}} \right)$ and the orientation vector is given by $\hat{\mathbf{\Omega}} = R(0,0,1)^T$. The expression for $h_{\mathbf{k}}$ is given in App. B, along with the fluctuation correction to the energy in lowest order in the Kitaev interaction which are obtained by a Bogoliubov transformation. Here we focus only on the result: the energy to second order in $|J_K|$ has the form $\varepsilon = N\varepsilon_{\mathrm{FM}} + \varepsilon_{\mathrm{FM}}^{(2)}$ with

$$\varepsilon_{\mathrm{FM}}^{(2)} = -\frac{S}{2}\frac{J_K^2}{|J_H|}\frac{3(2\sqrt{3}-\pi)}{8\pi}\left(1 + \hat{\Omega}_x^4 + \hat{\Omega}_y^4 + \hat{\Omega}_z^4 \right). \tag{5.60}$$

Because $2\sqrt{3} - \pi > 0$, this expression is negative for any finite value of J_K. With the constraint that $\hat{\mathbf{\Omega}}^2 = 1$, the correction $\varepsilon_{\mathrm{FM}}^{(2)}$ becomes maximally negative when the vector $\hat{\mathbf{\Omega}}$ points along one of the six equivalent $\langle 100 \rangle$ directions, i.e. any of the coordinate axes. At the Heisenberg point, $J_K = 0$, the ferromagnetic ground state manifold is the 2-sphere. Any finite Kitaev interaction, however, reduces this manifold to only six points corresponding to a $\mathbb{Z}_6$ ferromagnetic order parameter.

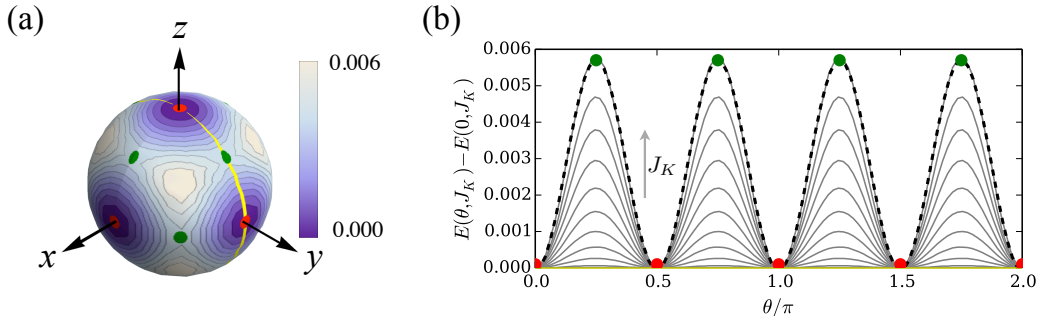

Figure 5.11.: (a) Ground state energy of the quantum ferromagnet in an external Zeeman field as a function of the direction of the applied magnetic field $\mathbf{B}$, where we have subtracted the ground state energy for $\mathbf{B} = \hat{\mathbf{z}}$. The Kitaev coupling strength is $J_K/J_H = \tan(11\pi/10) \approx 0.32$. The energy is minimal when the magnetization is pinned along one of the three axes, and maximal when pointing along the space diagonals. (b) The same results shown for the cut along the yellow line in (a). Each line corresponds to a different value of J_K/J_H. For $J_K/J_H = 0$ the ground state energy does not depend on the direction of the magnetization. Upon increasing J_K/J_H up to $J_K/J_H = \tan(11\pi/10)$, the directional dependence becomes more and more pronounced. The dashed line is a fit of Eq. (B.10).

5.5.1. Dual $\mathbb{Z}_6$ Ferromagnet

The dual point of the Heisenberg ferromagnet is located at $J_H > 0$ and $J_K = -2J_H$. The classical ground state energy of the dual ferromagnetic state is obtained from Eq. (5.56),

$$\varepsilon_{\mathrm{FM}'} = S^2\Big(-J_H + J_K\Big). \tag{5.61}$$

As before, the physical properties of the ferromagnetic Hamiltonian directly carry over to its dual point. Accordingly, the dual ferromagnetic state is also an exact ground state, and fluctuations arise for any $J_K \neq -2J_H$. The latter, following the arguments of the previous section, then favors a dual $\mathbb{Z}_6$ ferromagnetic ordering.

5.5.2. Numerical results

To further support the analytical results for the ferromagnet, we performed numerical simulations for both the quantum system with quantum fluctuations and the classical system with thermal fluctuations.

Quantum fluctuations: Fig. 5.11 shows the results for the ground state energy of a small cluster of 12 sites calculated by exact diagonalization. The lattice cluster is implemented with periodic boundary conditions and preserves the C_6 rotational symmetry of the lattice, thus it has no bias towards any direction in real space. To obtain the ground state energy as a function of the direction of the magnetization, we applied a magnetic field to each spin,

$$\mathbf{B} = B\begin{pmatrix}\cos(\phi)\sin(\theta)\\ \sin(\phi)\sin(\theta)\\ \cos(\theta)\end{pmatrix}, \tag{5.62}$$

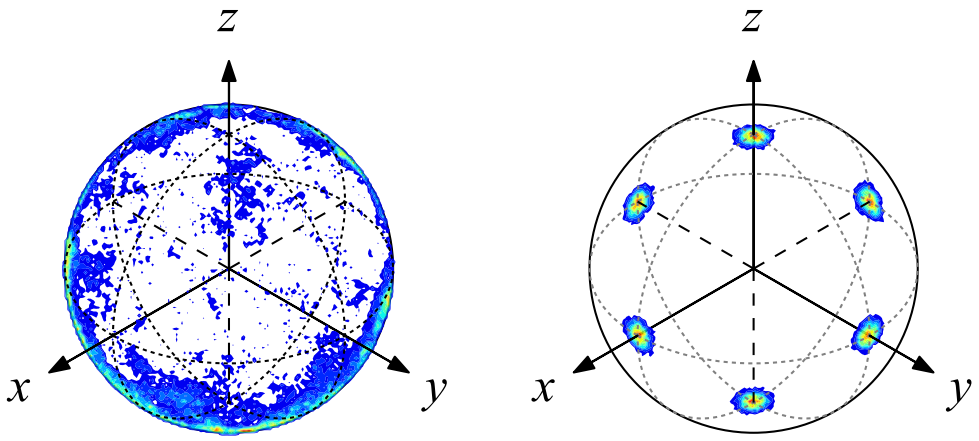

Figure 5.12.: Magnetization histograms from classical Monte Carlo simulations. The system is a C_6-symmetric cluster with periodic boundary conditions. The side length is $L = 12$, the total number of sites is $N = 3L^2 = 432$. Each image consists of the histograms for six Monte Carlo runs. Each run was performed at a temperature of $T = 0.005$, and comprised $6\,000\,000$ sweeps, of which $300\,000$ were thermalization sweeps. Left: Full SU(2) symmetry at the ferromagnetic point $\alpha = \pi$. Right: Pinning of the magnetization to the spin axes away from the ferromagnetic point at $\alpha = \frac{11}{8}\pi$ for a cluster of side length of $L = 12$ with fully periodic boundary conditions.

where $\phi \in [0, 2\pi)$ and $\theta \in [0, \pi]$. By changing the angles ϕ and θ, we adjusted the magnetization to point along different directions. In Fig. 5.11(a) we show results for the change in the ground state energy as a function of the orientation of $\mathbf{B}$, taken relative to the case when $\mathbf{B} \parallel \mathbf{z}$. The Kitaev coupling is taken to be $J_K/J_H = \tan(11\pi/10) \approx 0.32$. We find that, in agreement with our analysis above, the ground state energy of the system is minimal when the magnetization points along one of the three spin axes. A scan of the energies when changing the orientation of $\mathbf{B}$ along the yellow line shown in Fig. 5.11(a), we analyze the effect of different Kitaev couplings. In Fig. 5.11(b) each line corresponds to a different value of J_K. For $J_K = 0$, the energy does not depend on the direction of $\mathbf{B}$. For any finite $J_K \neq 0$, minima in the energy occur immediately, becoming more pronounced as J_K grows. The black dashed line in Fig. 5.11(b) is a fit of Eq. (B.10), showing perfect agreement.

Thermal fluctuations: Considering fluctuations, we find that thermal fluctuations in the classical system lead to the same result as the quantum fluctuations discussed before. To this end, we performed classical Monte Carlo calculations for a system with 432 spins for a fixed value of $\alpha = \frac{11}{8}\pi$. In Fig. 5.12 we show histograms of the magnetization obtained from a single Monte Carlo run. In the SO(3) symmetric case where $J_K = 0$ ($\alpha = \pi$), we find no preferred direction for the magnetization, and the histogram shows values distributed over the entire sphere. Once a finite Kitaev interaction is included, at $\alpha = \frac{11}{8}\pi$ the histogram shows that the magnetization is strongly focused along the spin axes, confirming the results obtained before for the case of quantum fluctuations.

5.6. Kitaev phase

Aside from the antiferromagnetic and ferromagnetic phases discussed so far, the numerical results for both classical and quantum models show the existence of an extended phase around the antiferromagnetic Kitaev point, $J_K > 0$. In the classical limit, the ground state of the Kitaev model on the triangular lattice, $J_H = 0$ and $J_K > 0$, is characterized by the formation of independent Ising-chains along one of the three lattice directions, thereby spontaneously breaking the C_6 lattice rotation symmetry. Before presenting our numerical results for the quantum model at the Kitaev point, we briefly discuss the Kitaev model on the triangular lattice from an analytical perspective.

5.6.1. Applicability of the Majorana fermion formalism

The Kitaev model on the honeycomb lattice can be solved exactly, so an obvious question is whether we can also solve it on the triangular lattice. While we cannot answer this question in general, it turns out that the solution by Majorana fermionization as presented in Sec. 2.3 is not applicable here. The key point in the solution of the honeycomb model is the presence of a sufficient number of conserved quantities (the plaquette operators), which commute with each other and the Hamiltonian. This property is lost on the triangular lattice. A different, slightly less rigorous but physically intuitive reasoning is given by noting that in the honeycomb lattice, each bond between two spins is modeled by two Majorana fermions, one from each site. Each spin is decomposed into four Majorana fermions, three of which participate in the three links to neighboring sites, and the remaining fourth one describes the site itself. The triangular lattice, however, has coordination number six, i.e. each site has six neighbors. Thus, the required number of Majorana fermions to employ the same scheme as in the honeycomb lattice is seven. This, however, is a nonsensical requirement as seven Majorana fermions would require a Hilbert space of dimension $\sqrt{2}^7 = 8\sqrt{2}$, which is both unphysical and in disagreement with the 4-dimensional Hilbert space of a spin-$\frac{1}{2}$.

5.6.2. Numerical results

In order to investigate the quantum mechanical ground state of the Kitaev model on the triangular lattice we carried out extensive numerical calculations using the density matrix renormalization group (DMRG, see Chap. 3) on triangular lattice strips of length L and width W with open boundary conditions. These lattice clusters break the C_6 rotational symmetry of the triangular lattice, and in the classical limit we expect a 2^W-fold ground state degeneracy with W independent Ising-chains forming along the longer direction. Considering the effects of quantum fluctuations on these classical states, our numerical results suggest that this degeneracy is lifted in the quantum model by an induced correlation between next-nearest neighbor chains. Directly neighboring chains, however, remain uncorrelated. Thus, for the lattices we used we end up with two sets of coupled chains, where chains within one set are correlated with each other, yielding a ground state degeneracy of 2^2, independent of system size. For system which do not break the rotational C_6 symmetry of the triangular lattice, this degeneracy should be expected along each of the three lattice directions, yielding a ground state degeneracy of 3×2^2 in the thermodynamic limit.

We investigated the degeneracy by calculating the lowest few energies of lattices with a width of up to $W = 4$, and a length of up to $L = 16$, for an antiferromagnetic Kitaev

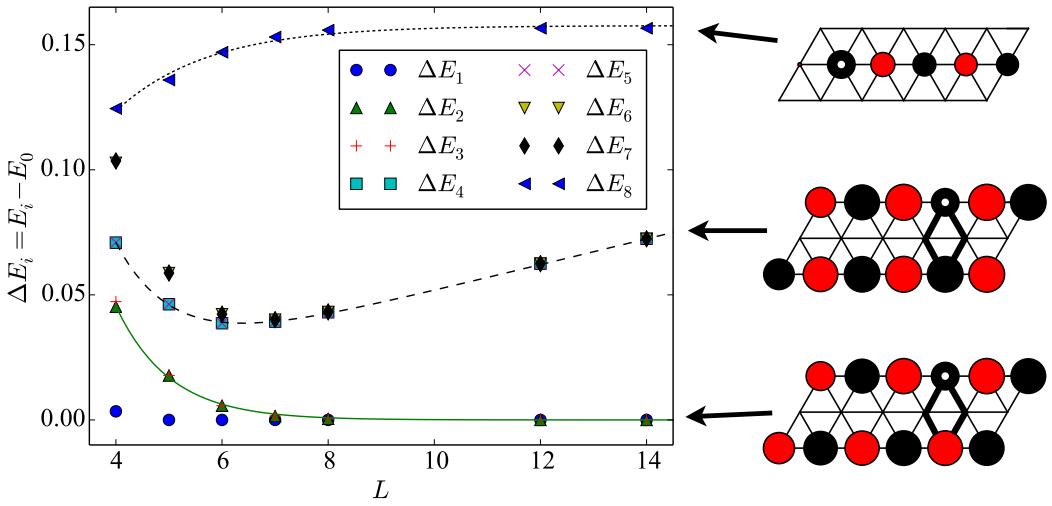

Figure 5.13.: Energy gaps of a $3 \times L$ triangular lattice strip with open boundary conditions. All values are given in relation to the ground state energy E_0, i.e. $\Delta E_1 = E_1 - E_0$. The figures on the right show numerical results for $\langle S^x(\mathbf{r}) S^x(\mathbf{r}_0)\rangle$ spin correlations, where the black disk with the white dot indicates the position $\mathbf{r}_0$, the diameter of the disks indicates the strength of the correlation and the color indicates the sign, with red corresponding to negative (antiferromagnetic) and black to positive (ferromagnetic) correlations. The lines are fits, dashed line: $f(x) = a_0 \exp(-x/a_1)$, dash-dotted line: $f(x) = a_0 \exp(-x/a_1) + a_2 x$, dotted line: $a_2 - a_0 \exp(-x/a_1)$

coupling, $J_K > 0$. In Fig. 5.13 we show results for the energy gaps of a system with $W = 3$ (a 3-leg ladder),

$$\Delta E_i = E_i - E_0, \tag{5.63}$$

where E_0 is the ground state energy and E_i is the i^{th} excited state. The first three excited states collapse exponentially onto the ground state energy as the length of the system increases, which is in perfect agreement with the 2^2-degeneracy conjectured above. The next four excited states collapse to the same energy, too, however with the gap to the ground state growing linearly in system length. Finally, the 8^{th} excited state exponentially approaches a constant value.

To identify the physical nature of the various states we calculated spin correlations functions, $\langle S^\gamma(\mathbf{r}) S^\gamma(\mathbf{r}_0)\rangle$ for $\gamma = x, y, z$. These correlations functions confirm the picture we have established so far: The four lowest states consists of chains along the L-direction, ordered antiferromagnetically in the x-component where the order is induced by the $S^x_i S^x_j$ Kitaev coupling along this direction. In the right panel of Fig. 5.13 we show exemplary correlation functions, in which we also see the clear absence of correlations between directly neighboring chains. In the ground state manifold two next-nearest neighbor chains are correlated antiferromagnetically, where the interchain coupling is mediated along the rhombic path shown as a thick line. In Fig. 5.14 we show results for the ground state of the 4-leg ladder. Here, we clearly find the suppression of spin-correlations along the two shorter directions (y and z), while the dominant direction (x) shows strong correlations.

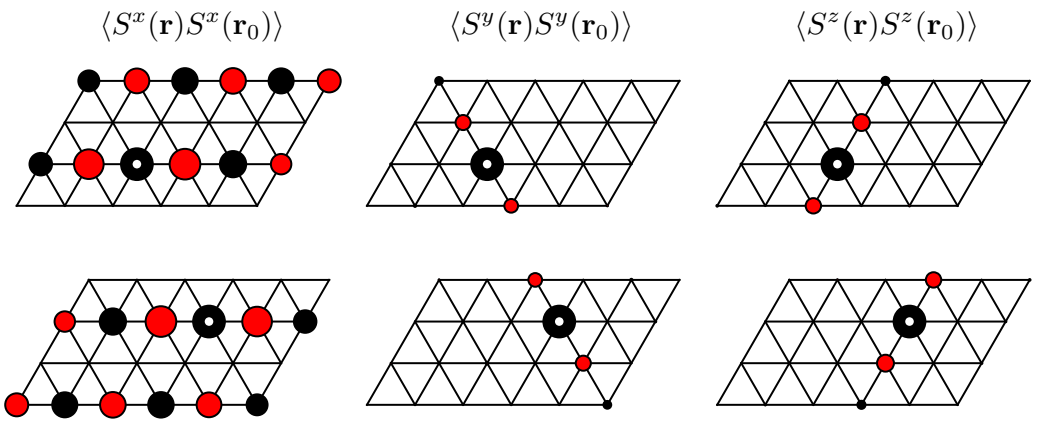

Figure 5.14.: Spin-spin correlations, $\langle S^\gamma(\mathbf{r})S^\gamma(\mathbf{r}_0)\rangle$, in the ground state of a 4×6 triangular Kitaev model. The white dot indicates the position $\mathbf{r}_0$. Red disks correspond to negative (antiferromagnetic) and black disks correspond to positive (ferromagnetic) correlations.

Excitations

Having identified the ground state, the question arises what the system's excitations in the thermodynamic limit are. From the spin correlators, see Fig. 5.13, we find that the linear growth of the energy gaps ΔE_4 through ΔE_7 is due to a breaking of the antiferromagnetic order between two chains. The energy cost associated with flipping an entire chain is linear in the system's length, and should clearly be forbidden in the thermodynamic limit.

The next excited state in our data, corresponding to the state with energy E_8, shows a breaking of spin correlations on a *single* site *within* a chain. The energy penalty associated with this local defect does not depend on system size, therefore we expect this to be the relevant excitation for the infinite system.

5.7. Summary and outlook

In conclusion, we have investigated the full phase diagram of the Heisenberg-Kitaev model formulated on the triangular lattice. The Heisenberg-Kitaev model is known to be compatible with the Klein duality [13]; a special basis transformation which provides a mapping between two halves of the phase diagram. This allows for the direct translation of results obtained for one phase to its dual phase. Motivated by previous numerical results for the classical model [12], we presented analytical approaches and numerical results for both the classical and the quantum model. Using exact diagonalization routines, we showed that the rich phase diagram of the classical model is preserved in the quantum case.

Ferromagnetic phases. We investigated the ferromagnetic phase analytically using a spin wave analysis, corroborated by numerical results using classical Monte Carlo and exact diagonalization. Close to the ferromagnetic Heisenberg point, the inclusion of a finite Kitaev interaction leads to an order-by-disorder effect which pins the magnetization along one of the three spin-axes, thereby lowering the ground state symmetry from O(3) in the classical and SU(2) in the quantum case to $\mathbb{Z}_6$. For the classical model, this

effect is mediated by thermal fluctuations, whereas quantum fluctuations drive the pinning in the quantum model. A similar effect has been observed before in the honeycomb Heisenberg-Kitaev model [118]. Our numerical results show very good agreement with the solutions we obtained in our sin wave analysis. Via the Klein duality, this physics directly translates to the dual ferromagnetic phase.

Kitaev points. In the absence of the Heisenberg interaction, the system reduces to the pure Kitaev Hamiltonian. While the honeycomb version of the model is exactly solvable using Majorana fermionization, this is not the case for the triangular lattice. Furthermore, in contrast to the spin liquid ground state of the honeycomb model, our numerical results indicate a ground state with nematic order. In the classical Kitaev model on the triangular lattice, the ground state is characterized by the formation of completely independent Ising-chains, generating a sub-extensive ground state degeneracy. We performed extensive DMRG simulations for triangular lattice ladders with a width of up to four legs. Calculating the first few lowest-lying states and spin correlation functions, we conjecture that the ground state of the quantum model is given by Ising-like chains, ordered (anti-)ferromagnetically at the (anti-)ferromagnetic Kitaev point. These chains, however, are not independent. Rather, quantum fluctuations induce correlations between next-nearest chains, reducing the ground state degeneracy to 3×2^2.

The ferromagnetic Kitaev model is a singular point in the phase diagram, as any finite Heisenberg interaction can immediately drive the ground state into the ferromagnetic or dual ferromagnetic order, depending on its sign. The antiferromagnetic Kitaev phase, on the other hand, is an extended phase. Our numerical simulations indicate, however, that any finite Heisenberg interaction breaks the ground state degeneracy. While our results for finite system sizes yield a clear picture of the ground state, it is at this point not clear if these results carry over to the thermodynamic limit.

Vortex lattice. The most interesting phase model forms around the antiferromagnetic Heisenberg point, when a small Kitaev interaction disturbs the 120° order. Previous numerical results indicate [12] that in this case the magnetic order is distorted on long length scales, leading to the formation of a lattice of topological point defects in the form of $\mathbb{Z}_2$ vortices. These results were first obtained from classical Monte Carlo simulations in Ref. [12]. In this chapter, we showed analytically that *any* finite Kitaev coupling immediately destroys the 120° order of the antiferromagnetic Heisenberg point. Furthermore, using an expanded Luttinger-Tisza approach, we could give an analytical approximation to the ground state which also confirms the build up of the $\mathbb{Z}_2$ vortex lattice, confirming to a very high degree of accuracy the Monte Carlo results.

Furthermore, we propose that the triangular Heisenberg-Kitaev model might be the relevant model to describe the low-energy physics of the transition metal oxide $Ba_3IrTi_2O_9$. In this material, the specific form of the exchange paths between to iridium ions is suggested to lead to the realization of Kitaev-type interactions, similar to honeycomb iridates [33, 64, 65, 81]. In $Ba_3IrTi_2O_9$, however, this interaction is thought to be much weaker, and we argue that the $\mathbb{Z}_2$ vortex lattice discussed above lies well within the experimentally relevant parameter regime.

Thus far, the synthesis of $Ba_3IrTi_2O_9$ has suffered from strong disorder due to site inversion effects as the Ti^{4+} and I^{4+} ions are of comparable size. However, with refined methods it might be possible to grow a non-disordered single crystal and perform polarized neutron spectroscopy. The static spin structure factor is an experimentally accessible observable with which the existence of a vortex lattice phase could be investigated.

Part III.

Real-space Kondo correlations in 1D and 2D

Chapter 6.

Friedel oscillations and the Kondo screening cloud

Since its first experimental observation and the subsequent theoretical description and solution, the Kondo effect (cf. Sec. 2.1) has been a cornerstone of condensed matter physics, from the early experiments with iron impurities in gold [19], to heavy fermion systems, to the highly topical search for Majorana fermions (cf. Chap. IV). Quantum impurity physics has been a ubiquitous and permanent field of study for more than 50 years, and the Kondo effect and many of its varieties and generalizations are by now well understood. In this light, it is deeply surprising that the real-space physics of the Kondo effect are still unclear and discussed controversially. The existence of a Kondo energy scale T_K suggests a real-space length scale $R_K = \hbar v_F / T_K$ where v_F is the Fermi velocity. This length scale is thought to define the extension of the many-body singlet between impurity and conduction electrons; the infamous *Kondo screening cloud*, the "holy grail" [9] of Kondo research. One way of observing this Kondo cloud is in the charge density oscillations surrounding a magnetic impurity [119–122]. These oscillations approach their standard form at long distances, while at shorter distances they are governed by Kondo physics [119]. However, for the typically exponentially small values of T_K, the size of the screening cloud is exponentially large, and so far no experimental evidence has been found. The absence of experimental proof has lead to criticism of the screening cloud concept [123], yet analytical and numerical calculations clearly show the appearance of such a length scale in various quantities [15, 124, 125]. Very recently, a refined scanning tunneling microscopy technique was used to observe Kondo signatures in the local density of states away from the impurity position [126], and an experimental verification of the Kondo cloud may finally be within reach.

In this chapter, we discuss general properties of the Kondo screening cloud. We review the occurrence of Friedel oscillations around potential-scattering impurities, and recapitulate previously found results on the Kondo cloud.

6.1. Occurrence of a length scale in Kondo physics

In the solution of the Kondo problem, using his NRG method, Wilson could prove that the Kondo groundstate is a singlet state. However, the precise structure of this state remains unclear. Below the characteristic energy/temperature scale T_K, the local magnetic moment on the impurity is dynamically screened by conduction electrons and a many-body singlet forms. We can relate an energy E to a wave-vector $\mathbf{k}$ via $|\mathbf{k}| = E/(\hbar v_F)$, where v_F is the Fermi velocity. Accordingly, it follows naturally that one can assign a length scale to the Kondo temperature by

$$R_K \sim \frac{\hbar v_F}{k_B T_K}, \tag{6.1}$$

which is the distance at which the effective Kondo coupling becomes large. Investigating the RG flow (see Sec. 2.1) of the Kondo and Anderson impurity models we find that going from high to low energies, the screening of the impurity moment sets in when $E \sim T_K$. Equivalently, R_K might be considered as the length scale which describes the spatial range of the Kondo effect. In a real-space RG sense, at the length R_K the antiferromagnetic coupling becomes large and at distances $r \gg R_K$ (corresponding to energies $E \ll T_K$ the system is described by the strong-coupling fixed point. In this regime, the impurity degrees of freedom are completely screened. This interpretation is indeed consistent with Fermi liquid theory in which one imagines conduction electrons not participating in the screening at $r \gg R_K$ to not be affected by the presence of the impurity. The question remains as to *where* the screening occurs?

6.2. The screening cloud scenario

The commonly adopted scenario in the literature (see e.g. Refs. [9,124]) is that of a screening cloud of a spatial extent R_K around the impurity. The cloud consists of electrons that have previously interacted with the local moment and accordingly contain information about the impurity, and thus, effectively, about each other [9]. The length scale R_K then defines the distance to the impurity at which the scattered electrons are not correlated anymore. The popular picture is that below T_K, the electrons inside this cloud form a many-body spin-singlet with the impurity spin. The implication is that the groundstate of a Kondo system should have the following real-space form:

$$|\mathrm{kondo-singlet}\rangle = \frac{1}{\sqrt{2}}\left(|\uparrow\rangle_{\mathrm{imp}}\,|\Downarrow\rangle_{\mathrm{cloud}} - |\downarrow\rangle_{\mathrm{imp}}\,|\Uparrow\rangle_{\mathrm{cloud}}\right). \tag{6.2}$$

The electrons in the cloud around the impurity collectively form a spin-$\frac{1}{2}$ degree of freedom (denoted by $|\sigma\rangle_{\mathrm{cloud}}$, with $\sigma = \Uparrow / \Downarrow$) which together with the impurity spin (denoted by $|\sigma\rangle_{\mathrm{imp}}$ with $\sigma = \uparrow / \downarrow$) form a spin-singlet. The extension of the $|\mathrm{kondo-singlet}\rangle$ object is R_K, and at distances greater than R_K the local moment on the impurity is 'hidden' inside the Kondo singlet. Thus, the rest of the system behaves like a Fermi liquid with altered boundary conditions (compared to the no-Kondo case) since a number of electrons is removed from the Fermi sea to participate in the screening cloud.

6.2.1. Spin-spin correlations

The Kondo effect is a direct result of spin-interactions and the groundstate is given by a spin singlet. Therefore, a length scale of the Kondo effect should be most directly visible in spin-spin correlations. In fact, assuming a groundstate of the form given in Eq. (6.2), the following quantity is suited to reveal information about the screening in real-space:

$$\chi_f(r) = \langle \hat{S}^z_f \hat{S}^z_f \rangle + \int_{|\mathbf{r}'|<r} \mathrm{d}\mathbf{r}'\, \langle \hat{S}^z_f \hat{S}^z_{\mathbf{r}'} \rangle\,, \tag{6.3}$$

where $\hat{S}^z_f$ and $\hat{S}^z_{\mathbf{r}}$ are the z-components of the impurity spin and the conduction electron at position $\mathbf{r}$, respectively.

In Ref. [127] a perturbative analysis of $\chi_f(r)$ in the weak-coupling regime close to the impurity, $r \ll R_K$ was performed. Moreover, the strong-coupling limit of $\chi_f(r)$ for distances $r \gg R_K$ was considered in Ref. [128], by application of Nozières' Fermi liquid

theory. In both cases, the spin-correlations are of the same form,

$$\langle \hat{S}_f^z \hat{S}_{\mathbf{r}}^z \rangle \sim \cos^2(k_F|\mathbf{r}|)/r^\alpha, \tag{6.4}$$

where the two regimes are distinguished by differing values of the exponent α. In particular, for a one-dimensional system the power-law behavior of the spin-correlators is

$$\langle \hat{S}_f^z \hat{S}_{\mathbf{r}}^z \rangle \sim \begin{cases} r^{-1}, & r \ll R_K, \\ r^{-2}, & r \gg R_K. \end{cases} \tag{6.5}$$

This result has been confirmed by various numerical calculations using different methods, such as Quantum Monte Carlo [129], an NRG method that was extended in such a way to be capable of calculating real-space correlations accurately [130], and DMRG calculations [131]. In Refs. [129, 131] the value of $\chi_f(\mathbf{r})$ was calculated and it was found that for $|\mathbf{r}| \gg R_K$ the screening is complete whereas it is not complete when $|\mathbf{r}| \ll R_K$.

6.3. Challenges to the screening cloud picture

The common picture described above is intuitive and straight-forwardly interprets the Kondo length scale as the extension of the the Kondo singlet. This interpretation nicely captures the Fermi liquid behavior of the conduction electrons in the region outside the cloud, $r \gg R_K$. However, it also suffers from some subtle problems, which indicate that the understanding of a Kondo length scale must be—at least slightly—adjusted. One immediately obvious issue arises when considering the limit of a vanishing Kondo coupling. From Eq. (2.14) we know that the Kondo temperature depends exponentially on the Kondo coupling J, so for the Kondo length scale one obtains

$$R_K \propto T_K^{-1} \propto e^{\frac{1}{\rho_0 J}}. \tag{6.6}$$

It is thus obvious that decreasing the coupling between impurity and conduction band leads to an increase in R_K, and in the limit of a decoupled impurity, $J \to 0$, the size of the cloud diverges, $R_K \to \infty$. The implication is that in this limit the screening cloud spreads out over the entire system and all conduction electrons participate in the singlet state screening the impurity. However, in the limit $J \to 0$ the impurity is strictly decoupled on the level of the bare Hamiltonian, and no screening takes place. Turning to the renormalization group point of view, for a decoupled impurity the system never flows from local moment to strong coupling and remains at the LM FP as $\omega \to 0$. The impurity entropy is $S(\omega \to 0) = \log(2)$, clearly indicating that the impurity retains a spin-$\frac{1}{2}$ degree of freedom in the ground state, and the latter it thus clearly not a singlet.

A second inconsistency arises from the effect of temperature, which introduces a length scale

$$R_T = \frac{\hbar v_F}{k_B T}. \tag{6.7}$$

This length scale interferes with the detection of the Kondo length scale [125, 130] and as soon as $T > T_K$ the Kondo effect is completely suppressed. However, for $T > T_K$ the numerical results show *no* change for the region inside the Kondo cloud, i.e. $r < R_K$, which is inconsistent with the destruction of a Kondo cloud singlet.

6.4. Kondo length scale in charge density oscillations

Spin correlation functions seem like the obvious quantity to show a Kondo length scale. However, numerical investigations of such correlators are currently only feasible using techniques such as e.g. the density matrix renormalization group (DMRG). Although the power of modern supercomputers allows for the treatment of fairly long 1D system (on the order of a few hundred sites), Kondo physics happen at exponentially small energies, requiring ideally an exponentially large host system. It turns out that charge density oscillations can be calculated much simpler, e.g. due to the possibility of expressing Green functions in 1D systems exactly as a simple algebraic formula. The charge density oscillations in the host system depend only on local impurity quantities, and the only interacting part of the problem is the impurity problem, which can be solved numerically exactly with the NRG. In this section we show how a Kondo length scale appears in the charge density oscillations, before turning to the discussion of numerical results in the next chapters.

6.4.1. Calculation of the charge density oscillations from Green functions

For our analysis of the Friedel (or charge density) oscillations, we now introduce some important quantities which help us in the actual calculations. A central object in our work is the retarded single-particle Green function. In its real-space formulation, it is a function of two positions $\mathbf{r}$ and $\mathbf{r}'$ and time $t - t'$, and it is defined as

$$G_{\sigma\sigma'}(\mathbf{r}, \mathbf{r}'; t - t') = -i\Theta(t - t') \left\langle \left\{ c_{\sigma\mathbf{r}}(t), c^\dagger_{\sigma'\mathbf{r}'}(t') \right\} \right\rangle , \tag{6.8}$$

where $\Theta(t)$ is the Heaviside step function which here ensures causality ($t > t'$), $\{a, b\} \equiv ab + ba$ is the anticommutator of operators a and b, and $c_{\mathbf{r}}(t)$ is the annihilation operator for an electron with spin σ at position $\mathbf{r}$ and time t. A physical interpretation of $G_{\sigma\sigma'}(\mathbf{r}, \mathbf{r}'; t - t')$ is that it gives the amplitude for a particle at $\mathbf{r}'$ inserted at time t' to propagate[1] into a state at position $\mathbf{r}$ and time t. With help of a Laplace transformation, the real-time Green function in Eq. (6.8) can be expressed in frequency space. For puerly real frequencies $\omega \in \mathbb{R}$ this transformation does not converge, therefore we need to perform an analytic continuation, i.e. adding an infinitesimal imaginary part to ω. We thus define the complex frequency argument $z \equiv \omega + i\delta$, where in this notation we henceforth imply taking the limit of $\delta \searrow 0$. This finally yields the expression

$$G_{\sigma\sigma'}(\mathbf{r}, \mathbf{r}'; z) \equiv \left\langle\langle c_{\sigma\mathbf{r}}; c^\dagger_{\sigma'\mathbf{r}'} \rangle\right\rangle_z = \int_0^\infty \mathrm{d}(t - t')\, e^{iz(t-t')} G_{\sigma\sigma'}(\mathbf{r}, \mathbf{r}'; t - t'), \tag{6.9}$$

where we introduced the double-bracket notation for the retarded Green function in frequency space. This notation on the one hand reminds us of the fact that the Green function is really a certain kind of correlation function of two fermionic operators, and it will on the other hand be convenient later on when applying equations of motion to the Green function.

The Green function is an essential tool in the description of many-body systems and it contains a lot of information [132,133]. From it, we can define another important quantity

[1] Green functions are often also called propagators.

in many-body physics, the *spectral function*

$$A(\mathbf{r};\omega) = \sum_{\sigma=\uparrow,\downarrow} \left(-\frac{1}{\pi} \lim_{\delta \searrow 0} \operatorname{Im} G_{\sigma\sigma}(\mathbf{r},\mathbf{r};\omega + i\delta) \right)$$
$$= -\frac{2}{\pi} \lim_{\delta \searrow 0} \operatorname{Im} G_{\sigma\sigma}(\mathbf{r},\mathbf{r};\omega + i\delta). \tag{6.10}$$

In the last equality we assumed the absence of an external magnetic field. In this case, the Green functions that are diagonal in the spin index are equal, $G_{\uparrow\uparrow}(\mathbf{r},\mathbf{r}';t-t') = G_{\downarrow\downarrow}(\mathbf{r},\mathbf{r}';t-t')$ and the summation yields a factor of 2. Following from the interpretation of the Green function, the spectral function can be understood as the probability density for putting in $(\omega > 0)$ or taking out $(\omega < 0)$ a particle at $\mathbf{r}$ and energy ω. As a probability density, it furthermore fulfills the sum rule

$$\int_{-\infty}^{\infty} \mathrm{d}\omega\, A(\mathbf{r},\omega) = 1. \tag{6.11}$$

In the cases we consider, the spectral function equals the energy-resolved local density of states and the charge densities at $\mathbf{r}$ and temperature T can thus be expressed in terms of the spectral function as [134]

$$n(\mathbf{r},T) = \int_{-\infty}^{\infty} \mathrm{d}\omega\, A(\mathbf{r};\omega) f(\omega,T), \tag{6.12}$$

where $f(\omega,T) = [\exp(\omega/T)) + 1]^{-1}$ is the Fermi distribution function. At zero temperature, $T = 0$, the Fermi function becomes a step function, $f(\omega,0) = \Theta(-\omega)$. For a system with half-bandwidth D the frequency summation only runs over $\omega \in [-D, D]$, and plugging in Eq. (6.10) with a Fermi level at $\varepsilon_F = 0$ yields for the charge density at position $\mathbf{r}$

$$n(\mathbf{r}) = -\frac{2}{\pi} \lim_{\delta \searrow 0} \operatorname{Im} \int_{-D}^{0} \mathrm{d}\omega\, G(\mathbf{r},\mathbf{r};\omega + i\delta). \tag{6.13}$$

The Green function contains all the required information about the system at hand. For an interacting system, such as a strongly-correlated impurity coupling to a metallic host, it is a highly complicated object. However, in the next section we show that it can be expressed in terms of two components; one contains all the information about the impurity physics, whereas the other only depends on the geometry of the host system.

6.4.2. Equations of motion and $\mathcal{T}$-matrix

Differentiating the Green function in Eq. (6.8) with respect to time, for a time-independent Hamiltonian H we find that $\langle\langle c_\lambda; c^\dagger_{\lambda'}\rangle\rangle_z$ has the following equations of motion:

$$z\,\langle\langle c_\lambda; c^\dagger_{\lambda'}\rangle\rangle + \langle\langle \mathscr{L} c_\lambda; c^\dagger_{\lambda'}\rangle\rangle_z = \langle\{c_\lambda, c^\dagger_{\lambda'}\}\rangle\,, \tag{6.14}$$

where λ is an arbitrary quantum number and $\mathscr{L}\cdot \equiv [H,\cdot]$ is the Liouville operator, which is defined as the commutator with the Hamiltonian. Using these equations of motion, for a quantum impurity system as introduced in Section 2.1 one can derive the following

important relation for the full Green function in real space, see App. A:

$$G(\mathbf{r},\mathbf{r}';z) = G^{(0)}(\mathbf{r},\mathbf{r}';z) + G^{(0)}(\mathbf{r},\mathbf{0};z)\mathcal{T}(z)G^{(0)}(\mathbf{0},\mathbf{r}';z), \tag{6.15}$$

where $\mathcal{T}(z)$ is the so-called scattering $\mathcal{T}$-matrix. The superscript $^{(0)}$ means that these Green functions are those of the same system *without* the impurity. These functions do not depend on the impurity and are entirely determined by the system's geometry, for a lattice geometry they are therefore often called 'lattice Green functions'. Conversely, Eq. (6.15) immediately shows that all information about the impurity is contained in the $\mathcal{T}$-matrix, which for the single-impurity Anderson model (cf. Sec. 2.1.1) is given in terms of the impurity Green function

$$\mathcal{T}(z) = V^2 \left\langle\langle f_\sigma; f_\sigma^\dagger\rangle\right\rangle_z = V^2 G_{\mathrm{imp}}(z), \tag{6.16}$$

where $f_\sigma^\dagger$ creates an electron with spin σ on the impurity orbital. Note that we have dropped spin indices as the Green functions do not depend on the spin. Summing over spins, as before, yields a trivial factor of 2. Eq. (6.15) can be understood in a very intuitive way: The second term contains the impurity's contribution to the non-local Green function between points $\mathbf{r}$ and $\mathbf{r}'$. This contribution is obtained by 'traveling' from $\mathbf{r}'$ to the impurity at $\mathbf{0}$, evaluating the local impurity $\mathcal{T}$-matrix, and then going from there to position $\mathbf{r}$.

Having discussed all ingredients to calculate charge densities, we show in Fig. 6.1 a diagrammatic representation of the logic we follow in our construction. The main constituent is the no-impurity ($V = 0$) real-space Green function $G^{(0)}(\mathbf{r},\mathbf{r}';z)$. Using Eq. (3.29), we can find the hybridization function of the system, which in turn serves as an input to the Numerical Renormalization Group. From there one obtains the impurity Green function and thus the $\mathcal{T}$-matrix. Finally, plugging Eq. (6.15) in Eq. (6.13) we then integrate over all negative frequencies to retrieve the charge densities at different points in space. The difference in charge densities compared to the no-impurity situation then follows directly from

$$\begin{aligned}
\Delta n(\mathbf{r}) &= n(\mathbf{r}) - n^{(0)}(\mathbf{r}) \\
&= -\frac{2}{\pi}\lim_{\delta\searrow 0}\mathrm{Im}\int_{-D}^{0}\mathrm{d}\omega\,\left[G(\mathbf{r},\mathbf{r};\omega+i\delta) - G^{(0)}(\mathbf{r},\mathbf{r};\omega+i\delta)\right] \\
&\overset{(6.15)}{=} -\frac{2}{\pi}\lim_{\delta\searrow 0}\mathrm{Im}\int_{-D}^{0}\mathrm{d}\omega\,\left[G^{(0)}(\mathbf{r},\mathbf{0};\omega+i\delta)\right]^2\mathcal{T}(\omega+i\delta),
\end{aligned} \tag{6.17}$$

where due to time-reversal invariance we could use $G^{(0)}(\mathbf{r},\mathbf{r}';z) = G^{(0)}(\mathbf{r}',\mathbf{r};z)$.

6.4.3. Friedel oscillations

Before considering magnetic impurities and the resulting Kondo physics, we first discuss the simpler case of a non-magnetic, purely potential-scattering impurity in a system of non-interacting electrons. The Hamiltonian of the host electrons is diagonal in momentum space and given by Eq. (2.2). The impurity is modeled by a local delta-function potential at position $\mathbf{r}_0$, which could be the result of e.g. a single site in a lattice system having a different level energy than the rest of the homogeneous system. Conduction

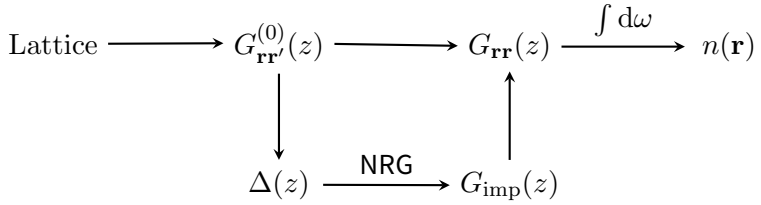

Figure 6.1.: Diagram depicting the underlying logic of our calculations. From the lattice Hamiltonian we calculate lattice Green functions $G^{(0)}_{\mathbf{rr}}(z)$. With these, the hybridization function $\Delta(z)$ can be obtained which serves as input to the NRG. After solving the impurity problem with the NRG and calculating the impurity Green function $G_d(z)$, we combine the latter with the lattice Green functions to calculate the full real-space Green function $G_{\mathbf{rr}}(z)$ and finally the charge densities $n(\mathbf{r})$.

electrons scatter from this potential and the full Hamiltonian for this system is given by

$$H = \sum_{\mathbf{k}\sigma} \varepsilon_{\mathbf{k}} c^\dagger_{\sigma\mathbf{k}} c_{\sigma\mathbf{k}} + \sum_{\mathbf{k}\mathbf{k}'\sigma} K_{\mathbf{k}\mathbf{k}'} c^\dagger_{\sigma\mathbf{k}} c_{\sigma\mathbf{k}'}, \tag{6.18}$$

where $K_{\mathbf{k}\mathbf{k}'} = \langle \sigma\mathbf{k}|\hat{V}^{\mathrm{eff}}_{\mathrm{imp}}|\sigma\mathbf{k}'\rangle$ is the scattering amplitude, and $|\sigma\mathbf{k}\rangle$ is a Bloch state in the lattice. The altered on-site energy at position $\mathbf{r}_0$ furthermore leads to a local change in the charge density. However, classical electrodynamics tell us that the excess charge at position $\mathbf{r}_0$ cannot create a sustained electric field in the metal. Rather, the free conduction electrons re-arrange themselves to compensate the impurity on a microscopic level. This charge compensation takes on the form of the so-called "Friedel oscillations" [14]: A repulsive potential leads to a build-up of charge surrounding the impurity. The spatial decay of these static charge displacements around the impurity is described by a power-law which is modulated by a characteristic oscillatory behavior with a period of $2k_F$, where k_F is the Fermi momentum. The leading asymptotic form in a d-dimensional isotropic system is

$$\Delta n(\mathbf{r}) \equiv n(\mathbf{r}) - n_0 \sim \frac{\cos(2k_F\,|\mathbf{r}-\mathbf{r}_0| + \eta_0)}{|\mathbf{r}-\mathbf{r}_0|^d}, \quad \text{for } |\mathbf{r}-\mathbf{r}_0| \to \infty, \tag{6.19}$$

where $n(\mathbf{r}) = \langle c^\dagger_{\mathbf{r}} c_{\mathbf{r}}\rangle$ is the charge density at position $\mathbf{r}$, and $n_0(\mathbf{r}) \equiv n_0$ is the constant charge density of the homogeneous system in the absence of an impurity. $\Delta n(\mathbf{r})$ thus measures the *excess* charge for a system with impurity compared to the same system without the impurity. The potential scattering also leads to a phase shift $\eta_0 \equiv \eta(\varepsilon_F)$ in the conduction electrons at the Fermi level, which depends on the scattering amplitude $K_{\mathbf{k}\mathbf{k}'}$. Friedel oscillations have successfully been studied experimentally using scanning tunneling microscopy measurements [135–138] for various systems.

The occurrence of such density oscillations is a direct result of the potential scattering. However, when the impurity is not only a potential scatterer, but also has a magnetic degree of freedom, the resulting Kondo physics affect the long-distance form of the Friedel oscillations in a distinctive way that evokes the elusive Kondo length scale, as we will discuss below.

6.4.4. Previous results for the Friedel oscillations in a free electron gas

The behavior of the Friedel oscillations around an impurity is completely determined by the non-interacting lattice Green functions and the scattering $\mathcal{T}$-matrix. The latter is a well-studied object [3, 139] and allows us to make some qualitative statements at this point. A signature of the Kondo effect is the characteristic resonance in the $\mathcal{T}$-matrix which occurs on the order of the Kondo temperature T_K. Below this energy scale, the magnetic impurity is screened by conduction electrons. This low energy regime relates to long distances in real-space, and, accordingly, far away from the impurity the system is not affected by the (screened) impurity. The only effect remaining at this length scale is the potential scattering phase shift, and therefore the charge density oscillations should approach their Friedel form for distances $r \gg \hbar v_F/T_K$ [15]. On short distances, however, the screening of the impurity is not complete and the impurity is still "visible" to the charge density oscillations. This purely qualitative analysis already indicates the existence of a crossover between the two real-space regions $r \ll \hbar v_F/T_K$ and $r \gg \hbar v_F/T_K$. The full Kondo Hamiltonian Eq. (2.6) contains the magnetic Heisenberg exchange interaction and also a potential scattering term. It is important to recall at this point that the potential scattering term vanishes for a particle-hole symmetric impurity. Zero potential scattering, of course, implies no charge density oscillations. Thus, it is necessary to have a particle-hole asymmetric impurity configuration in order to create density oscillations.

The occurrence of a Kondo length scale in the Friedel oscillations around an impurity was first discussed in Refs. [119, 121]. Recently, Affleck et al in Ref. [15] presented more detailed calculations supplemented by numerical results. There, the authors considered a Kondo impurity in an isotropic, translationally invariant host system of non-interacting conduction electrons in d dimensions. In this system the Friedel oscillations are modulated by a universal scaling function $F(r/R_K)$ which only depends on the Kondo scale:

$$\Delta n(\mathbf{r}) \sim \frac{1}{|\mathbf{r}|^d}\left[\cos\left(2k_F|\mathbf{r}| - \frac{\pi d}{2} + 2\eta_0\right) F(r/R_K) - \cos\left(2k_F r - \frac{\pi d}{2}\right)\right]. \quad (6.20)$$

Note that if $F(r)$ is constant this reduces to an expression proportional to the one in Eq. (6.19). Let us briefly discuss this result at particle-hole symmetry, where Friedel oscillations must vanish. To this end, consider a one-dimensional tight-binding system at particle-hole symmetry. There, the parameters become $d = 1$, $k_F = \pi/2$ and $\eta_0 = 0$. Since (for a lattice constant of one) r is restricted to integer values, the density oscillations $\Delta n(r)$ vanish exactly, as expected.

From perturbative expressions of the $\mathcal{T}$-matrix, the form of $F(r)$ for the short- and far-distance limits were derived. In the vicinity of the impurity, Kondo screening is not yet complete and

$$F(r/R_K) \to 1 - \frac{3\pi^2}{8\ln^2(R_K/r)}, \qquad (r \ll R_K). \quad (6.21)$$

The perturbative arguments used in the derivation of this behavior breaks down when r/R_K becomes of order 1. But for $r \gg R_K$, or equivalenty $\omega \ll T_K$, Nozière's Fermi liquid theory [3] becomes applicable and yields (up to second order in r/R_K):

$$F(r/R_K) \to -1 + \frac{\pi\mathcal{W}}{4(r/R_K)} - \frac{3\pi^2\mathcal{W}^2}{32(r/R_K)^2}, \qquad (r \gg R_K) \quad (6.22)$$

with the Wilson number $\mathcal{W} \approx 0.4128$. This number is a universal constant for the Kondo model which relates the Kondo scale T_K (which is calculated from perturbative high-

energy considerations) to the low-energy $T = 0$ impurity susceptibility, which is associated with the strong coupling regime [3]. Eqs. (6.21) and (6.22) imply a crossover in the density oscillations: In the absence of Kondo physics, $F \equiv 1$. However, when Kondo physics are present, $F(r/R_K)$ is close to 1 for $r \ll R_K$ and goes to -1 for $r \gg R_K$, which is equivalent to the potential scattering phase shift η_0 in Eq. (6.19) picking up an additional $\pi/2$ from the Kondo effect, $\eta_0 \to \eta_0 + \pi/2$. Numerical results calculated with the NRG method presented in Ref. [130] show a good agreement with these analytical expressions.

Chapter 7.

1D and Quasi-1D lattices

To expand on previous results in the literature, in this section we consider numerically the charge density oscillations in the single-impurity Anderson model on 1D and quasi-1D lattices. In Ref. [15] the crossover in the densities were studied for the Kondo Hamiltonian—a low-energy effective model of the single-impurity Anderson Hamiltonian (see Sec. 2.1). From the RG perspective, at the Kondo length $R_K \sim 1/T_K$ the system flows from the local moment fixed point to the strong coupling fixed point. However, in the single-impurity Anderson model, a second crossover exists at high energies, when the charge fluctuations are frozen out and the system flows from the free orbital fixed point to the local moment fixed point. In this chapter we show the existence of a second length scale given by this high-energy crossover, R_{LM}. In fact, the *entire* RG flow in frequency space is completely reproduced in the density oscillations.

In the first section, we consider the tight-binding limit of a semi-infinite chain with an Anderson impurity coupling to its end. Then, we show how to generalize the calculation of lattice Green functions for lattices of a finite width, such as ribbons or tubes. For these systems, although the geometry of the lattice alters the form of the charge density oscillations, we find equivalent results to the simple 1D case.

7.1. Lattice Green functions

From equation Eq. (6.15) we know that aside from the impurity Green function, the main ingredient in the calculation of the charge densities are the lattice Green functions $G^{(0)}_{\mathbf{r}\mathbf{r}'}(z)$. As discussed above, whereas the impurity Green function is a local quantity, the Green functions between two points in the system for the case that the impurity is *not* coupled to the system, i.e. $V = 0$, are non-local quantities. In the following we call these Green functions "free" Green functions if $V = 0$. For a 1D chain, a convenient way to calculate real-space propagators is to make use of the equations of motion in Eq. (6.14). This calculation can be extended to also work for systems with a finite width. Fig. 7.1 shows the geometries we consider. In this section, we present the equations of motion method and results for the lattice Green functions.

7.1.1. 1D chain

The simplest host system geometry we consider is a semi-infinite tight-binding 1D chain at half-filling. It is shown graphically in left part of Fig. 7.1(a). Let us recall the definition of the single-impurity Anderson model as discussed in Sec. 2.1:

$$H = H_{\mathrm{host}} + \epsilon_f \hat{n}_f + U \hat{n}_\uparrow \hat{n}_\downarrow + V \sum_\sigma \left(f^\dagger_\sigma c_{0\sigma} + \mathrm{H.c.} \right). \tag{7.1}$$

(a) 1D chain

(b) quasi-1D square lattice ribbon

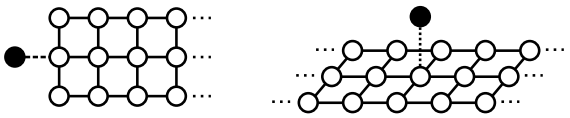

(c) honeycomb tube (periodic boundary conditions in width)

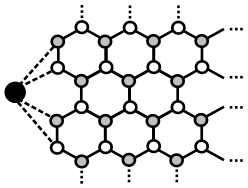

Figure 7.1.: The lattices considered in this section, the semi-infinite configuration is shown on the left and the infinite system on the right. In the lower illustration, on the left the honeycomb ribbon is shown with the impurity coupling to all sites.

The host Hamiltonian H_{host} for the semi-infinite 1D chain is given by

$$H_{\text{host}} = t \sum_{i=0}^{\infty} \sum_{\sigma} \left(c_{i\sigma}^{\dagger} c_{i+1\sigma} + \text{H.c.} \right). \tag{7.2}$$

Upon transforming the fermionic operators c_i into a diagonal basis, one finds the dispersion relation which in turn yields the bandwidth $D = 2|t|$ with the hopping amplitude t. As a first step, we calculate the free Green function at the end of the chain. As we show in App. A, for the lattice described by Eq. (7.2) it is given in a continued fraction expression as

$$G_{0,0}^{(0)}(z) = \cfrac{1}{z - \cfrac{t^2}{z - \cfrac{t^2}{z - \ddots}}} = \frac{1}{z - t^2 G_{0,0}^{(0)}(z)}, \tag{7.3}$$

where we introduced a slightly more compact notation for Green functions in 1D, $G_{i,j}(z) \equiv G(\mathbf{r}_i, \mathbf{r}_j; z)$. We can solve for $G_{00}^{(0)}(z)$ and find the closed expression

$$G_{0,0}^{(0)}(z) = \frac{z - \sqrt{z^2 - 4t^2}}{2t^2}. \tag{7.4}$$

Further application of the equations of motion then enables us to find arbitrary free Green functions on the chain, exploiting the important fact that our model only includes nearest-neighbor hoppings. Given a (not necessarily free) local Green function $G_{i,i}(z)$, the Green function on the next site is

$$G_{i,i}(z) = G_{0,0}^{(0)}(z) + t^2 G_{i-1,i-1}(z) \left[G_{0,0}^{(0)}(z) \right]^2, \tag{7.5}$$

Then, using Eqs. (7.5) and (7.4), one can iteratively calculate any local Green function on the chain. When $V > 0$ the impurity (which couples only locally to the chain site at $r = 0$) can be taken as the first site in the chain, albeit with a hopping to the next site given by V instead of t. From this perspective, once we obtained the impurity Green function $G_{\mathrm{imp}}(z)$ from the NRG, this function serves as a starting point in Eq. (7.5). Finally, for the *difference* of the Green functions with and without the impurity, $\Delta G_{r,r}(z) = G_{r,r}(z) - G^{(0)}_{r,r}(z)$ we find:

$$\Delta G_{r,r}(z) = \frac{V^2}{t^2} G_{\mathrm{imp}}(z) \left[t\, G^{(0)}_{0,0}(z) \right]^{2r+2}. \tag{7.6}$$

Let us remark on two important aspects here. First, in a translationally invariant system (regardless whether the symmetry is discrete or continuous), the Green functions generally only depend on the relative distance in real-space, i.e. $G_{\mathbf{r},\mathbf{r}'}(z) = G_{\mathbf{r}-\mathbf{r}'}(z)$. Of course, the coupling of an impurity to a particular site removes this invariance, but also in a semi-infinite chain with no impurity this symmetry is not given anymore, due to the chain ending. Second, by transforming only one of the operators in the Green function (see App. A) one finds the non-local free Green function

$$G^{(0)}_{0,r}(z) = \frac{1}{t} \left[t\, G^{(0)}(z) \right]^{r+1} = \frac{1}{t} e^{-i(r+1)\mathrm{acos}(z/(2t))}. \tag{7.7}$$

With this, we see that Eq. (7.6) is in fact equivalent to the Dyson equation Eq. (6.15):

$$G_{r,r}(z) = G^{(0)}_{r,r}(z) + G^{(0)}_{0,r}(z) \underbrace{V^2 G_{\mathrm{imp}}(z)}_{=\mathcal{T}(z)} G^{(0)}_{r,0}(z). \tag{7.8}$$

Fig. 7.2 shows the three first non-local free Green functions $G^{(0)}_{0,r}(z)$ for the semi-infinite 1D chain calculated from Eq. (7.7).

Infinite chain

So far we have calculated all relevant quantities for a semi-infinite chain. From equations of motion it follows directly that the infinite system (Fig. 7.1(a), right figure) is easily constructed by connecting two semi-infinite chains at $r = 0$. Consider the continued fraction expression in Eq. (7.3) for the Green function at the end of the semi-infinite chain. For the infinite system, this turns into

$$\tilde{G}^{(0)}_{0,0}(z) = \cfrac{1}{z - \cfrac{t^2}{z - \cfrac{t^2}{z - \ddots}} - \cfrac{t^2}{z - \cfrac{t^2}{z - \ddots}}} = \frac{1}{z - 2t^2 G^{(0)}_{0,0}(z)}. \tag{7.9}$$

Plugging this function in Eq. 7.5, the real-space Green functions in the infinite system are then found by

$$\tilde{G}_{i,i}(z) = \tilde{G}^{(0)}_{0,0}(z) + t^2 \tilde{G}_{i-1,i-1}(z) \left[G^{(0)}_{0,0}(z) \right]^2. \tag{7.10}$$

Note that only our starting point has changed: The function $G^{(0)}_{0,0}(z)$ in the last equation is still the Green function obtained for the semi-infinite chain, Eq. (7.4). In the lower panels of Fig. 7.2 we show exemplary results for the non-local Green functions of the infinite chain.

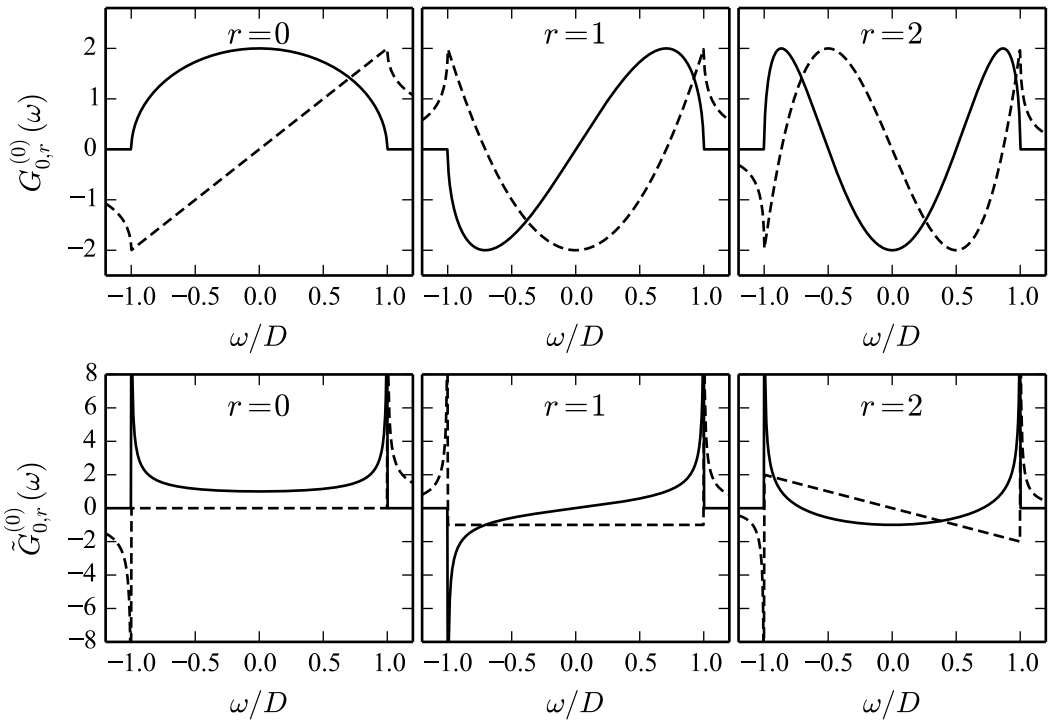

Figure 7.2.: Real (solid) and negative imaginary (dashed) parts of the free ($V = 0$) non-local lattice Green function for $t = -1/2$. The top tow shows results for the semi-infinite chain between sites 0 and r, the bottom row shows similar results for the infinite chain.

7.1.2. Square lattice and honeycomb lattice ribbons

In the method presented in the previous section, we used the equations of motion to relate one site to both its neighbors. Importantly, in a one-dimensional chain there is only a single path connecting two arbitrary sites, and by relating neighboring sites we could thus completely contain all required information in our calculations. In an infinite system of dimension > 1, this is no longer true: There is a generally infinite number of paths connecting any two sites, therefore a rigorous treatment with equations of motion in real-space cannot yield a result. In Chap. 8 we present alternative ways to deal with this situation. However, for the same reason it is clear that for systems infinite in one dimension but *finite* in the other dimensions, equations of motion are still appropriate. Here, we present a generalization [140] of the method from the last section, which at its core is exactly equivalent, albeit formulated in a slightly more elaborate fashion.

7.1.3. Square lattice ribbons

Consider a semi-infinite "ribbon" of square lattice geometry, see the left figure in the middle row of Fig. 7.1. Let us assume the ribbon to be of width $W = 2N + 1$, with $N \in \mathbb{N}$. The Hamiltonian of the ribbon (without the impurity) is then given by

$$H^{2D}_{\text{host}} = t \sum_{x=0}^{\infty} \sum_{y=-N}^{N} \left[c^{\dagger}_{(x,y),\sigma} c_{(x+1,y),\sigma} + c^{\dagger}_{(x,y),\sigma} c_{(x,y+1),\sigma} + \text{H.c.} \right], \tag{7.11}$$

where $c^\dagger_{(x,y),\sigma}$ creates an electron at site $\mathbf{r} = (x,y)^T$. The coordinate system we use here is shown graphically in Fig. 7.3. The main idea of how to proceed is to group all sites with the same x-coordinate (which we henceforth call a "column") into a vector-valued compound object. Then, we can reformulate the Hamiltonian Eq. (7.11) in a matrix notation. To this end, let us define the vector of operators

$$\mathbf{c}_{x,\sigma} = \begin{pmatrix} c_{(x,N),\sigma} \\ c_{(x,N-1),\sigma} \\ \vdots \\ c_{(x,-N+1),\sigma} \\ c_{(x,-N),\sigma} \end{pmatrix}, \tag{7.12}$$

which contains all annihilation operators for sites in column x. The Hamiltonian (7.11) can now be formulated as

$$H^{\mathrm{2D}}_{\mathrm{host}} = \sum_{x=0}^{\infty} \mathbf{c}^\dagger_{x,\sigma} \underline{M}_x \mathbf{c}_{x,\sigma} + t \sum_{x=0}^{\infty} \left(\mathbf{c}^\dagger_{x,\sigma} \cdot \mathbf{c}_{x+1,\sigma} + \mathrm{H.c.} \right), \tag{7.13}$$

where the matrix $\underline{M}_x$ defines the hopping between all sites *within* column x. For the sake of a precise notation, we henceforth denote matrices by an underline. The second term in the Hamiltonian is the hopping between two neighboring columns, and in the case of the square lattice is it simply given by the scalar product. Furthermore, as the system at hand is homogeneous, the hopping matrix $\underline{M}_x$ does not depend on the x-position of the column, thus $\underline{M}_x = \underline{M}$. For the square lattice it assumes tridiagonal form and is given as

$$\underline{M} = \begin{pmatrix} 0 & t & & & (t) \\ t & 0 & t & & \\ & t & 0 & t & \\ (t) & & \ddots & \ddots & \ddots \end{pmatrix}. \tag{7.14}$$

The entries in parentheses are only present for a "tube system", i.e. a ribbon with periodic boundary conditions in the y-direction. Fig. 7.3(a) shows an example of a subsystem described by the matrix $\underline{M}$.

With the matrix-valued formulation of the Hamiltonian (7.13), one can now proceed along the same lines as for the simple 1D case in order to calculate arbitrary free lattice Green functions between any two sites in the system. Starting, as before, with the calculation of the Green functions at the end of the semi-infinite system, one finds again a continued-fraction expression as in 1D, however for this system it is matrix-valued:

$$\begin{aligned} \underline{G}_0(z) &= [\underline{A}(z) - t^2[\underline{A}(z) - t^2[\underline{A}(z) - \ldots]^{-1}]^{-1}]^{-1} \\ &= [\underline{A}(z) - t^2 \underline{G}_0(z)]^{-1}, \end{aligned} \tag{7.15}$$

where the matrix $\underline{A}(z)$ is given by $\underline{A}(z) = z\mathbb{1} - \underline{M}$. $\underline{G}_0(z)$ is the $W \times W$-matrix of all free Green functions between operators in $\mathbf{c}_{0\sigma}$:

$$[\underline{G}_0(z)]_{ij} = G^{(0)}_{(0,i),(0,j)}(z) = \langle\langle c_{(0,i),\sigma}; c^\dagger_{(0,j),\sigma} \rangle\rangle^{(0)}_z, \tag{7.16}$$

where $i,j \in [-N,N] \subset \mathbb{Z}$. Note again that we have omitted spin indices in the Green functions (but not in the operators) as the Green functions in our scenarios do not depend on spin. Equally to the 1D case, a closed expression for $\underline{G}_0(z)$ can be found. It formally

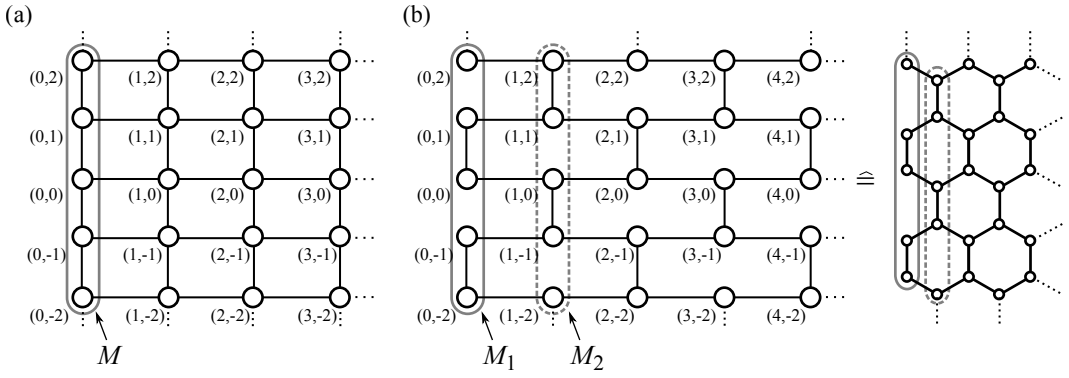

Figure 7.3.: (a) The coordinate convention for the square lattice ribbon. The blue bubble indicates the column of sites combined into the vector of operators $\mathbf{c}_{0\sigma}$ (see main text), the hoppings in which are given by the matrix $\underline{M}$. (b) Leaving out certain bonds generates a "brick wall" lattice which is topologically equivalent to the honeycomb lattice. Two inequivalent repeating columns are needed to describe this lattice (solid and dashed bubble), thus requiring two hopping matrices $\underline{M}_1$ and $\underline{M}_2$.

resembles the result for the 1D chain and is given as

$$\underline{G}_0(z) = \frac{\left(\sqrt{\underline{A}(z)^2 - 4t^2\mathbb{1}} + \underline{A}(z)\right)}{2t^2}. \tag{7.17}$$

Furthermore, Green functions between sites in column $x = 0$ and $x = n$ are obtained by (cf. Eq. (7.7))

$$\underline{G}_n(z) = \frac{1}{t}\left[t\,\underline{G}_0(z)\right]^{n+1}, \tag{7.18}$$

where the components of the matrix $\underline{G}_n(z)$ are the Green functions:

$$\left[\underline{G}_n(z)\right]_{ij} = G^{(0)}_{(0,i),(n,j)}(z) = \langle\langle c_{(0,i),\sigma}; c^\dagger_{(n,j),\sigma}\rangle\rangle^{(0)}_z. \tag{7.19}$$

Considering the technical features of this method we can thus summarize that the calculation of non-local Green functions in a semi-infinite squarelattice ribbon can be done by taking a $W \times W$-matrix to the $(n+1)$st power. This can be implemented efficiently by diagonalizing the matrix first and then multiplying the eigenvalues. As the final result of this section, we consider the $V \neq 0$ case with an impurity coupling to the site at $\mathbf{r} = (0,0)^T$. The charge density difference at position $\mathbf{r} = (x,y)^T$ can then be found with Eq. (6.17), and the Green function $\Delta G_{\mathbf{rr}}(z)$ is given by

$$\Delta G_{\mathbf{rr}}(z) = -V^2\, G_{\mathrm{imp}}(z) \left(\left[\underline{G}^{(0)}_x(z)\right]_{0y}\right)^2, \tag{7.20}$$

with the (scalar) impurity Green function $G_{\mathrm{imp}}(z)$.

In Fig. 7.4 we show the free Green functions $G^{(0)}_{\mathbf{0r}}(z)$ for a semi-infinite ribbon of width $W = 3$ and $\mathbf{r} = (r,0)^T$. A comparison with Fig. 7.2 reveals that the Green functions are of a similar structure, however decorated with more complex features. In the figures we have plotted the data in units of the half-bandwidth D.

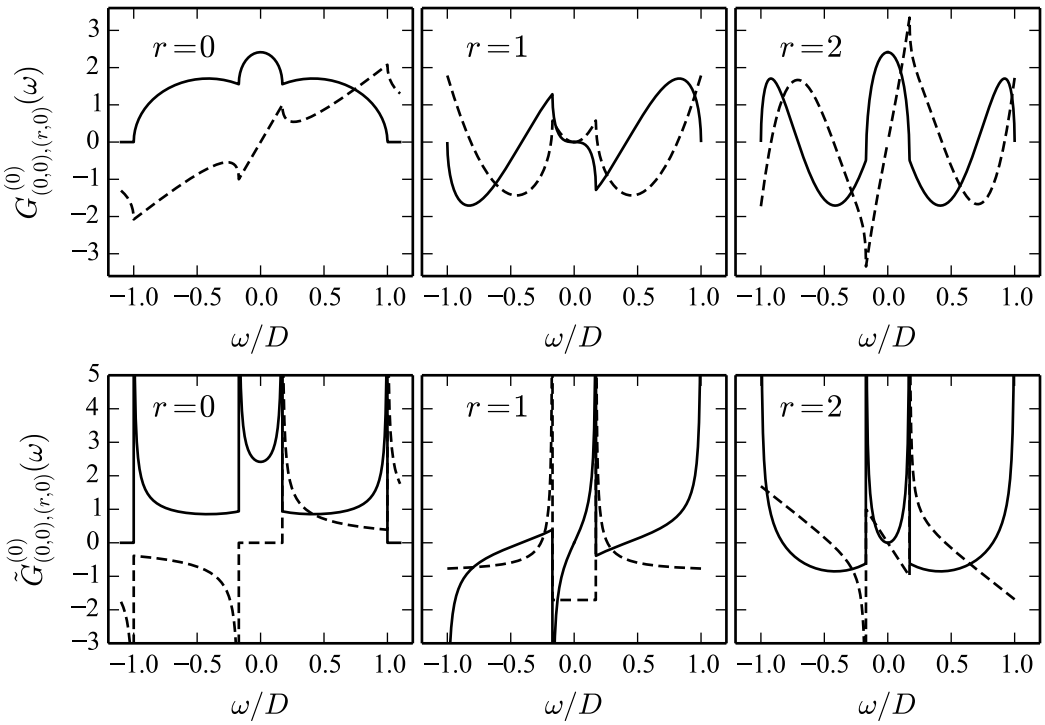

Figure 7.4.: Real (solid) and negative imaginary (dashed) parts of the free ($V = 0$) non-local lattice Green function for $t = -1/2$. The top shows results for the semi-infinite ribbon of width $W = 3$ between sites $\mathbf{r}_0 = \mathbf{0}$ and $\mathbf{r} = (r, 0)^T$, the bottom row shows similar results for the infinite system.

Bandwidth of the ribbon lattices

In the 1D chain, the half-bandwidth is given by $D = 2t$. For the ribbon systems, with increasing width W the bandwidth grows monotonously from the $D = 2t$ value and asymptotically approaches its 2D limit $D = 4t$, which is the half-bandwidth of the infinite square lattice.

Infinite ribbons

Along the same lines as discussed in the previous section, we can connect two semi-infinite ribbons to model an infinite one. Eq. (7.15) then assumes the form

$$\underline{\tilde{G}}_0(z) = [\underline{A}(z) - 2t^2 \underline{G}_0(z)]^{-1}, \tag{7.21}$$

while the remaining equations stay unchanged. As before, we show results for the non-local Green functions of an infinite ribbon in the bottom row in Fig. 7.4.

While in principle these results allow for precise calculations of arbitrary Green functions in (semi-)infinite 2D lattices of finite width, the size of the matrices and the increasing number of oscillations in the resulting functions quickly make wide systems unfeasible. However, this method still turns out to be very useful: With a slightly more involved approach (but following the same logic) that we discuss in the next section, the calculations can be extended to a honeycomb lattice, allowing for the precise calculation of Green functions in e.g. a tight-binding description of a carbon nanotube.

7.1.4. Honeycomb lattice tubes

The first theoretical description [141, 142] and subsequent experimental realization [143,144] of single-walled carbon nanotubes has led to remarkable progress in numerous fields such as engineering [145–147], science [148] and even medicine [149]. Due to their minute width, nanotubes can be modeled as 1D systems [141]. However, the method we present here describes the full tube in a tight-binding approximation and thus allows for a more detailed examination. From the point of view of our previous sections, a carbon nanotube can be viewed as a honeycomb lattice ribbon with periodic boundary conditions in the width-direction, see Fig. 7.1(c). The 1D chain and square lattice systems considered so far have a unit cell of one site. Furthermore, due to the spatially homogeneous geometry, after grouping sites in vectors $\mathbf{c}_i$, we required only a single matrix $\underline{M}$ and the identity $\mathbb{1}$ to describe the hopping in the system. The honeycomb lattice, however, is bipartite with a unit cell consisting of two sites, distinguished by a different shading in the figure. For our purposes, it is important to realize that, topologically, the honeycomb lattice is equivalent to a "brick wall" lattice, therefore allowing us to treat it as a square lattice with certain bonds missing.

A nanotube is typically characterized by the direction in which the graphene sheet has been "rolled up", i.e. the direction perpendicular to the tube axis. More specifically, going around the tube defines a vector in the plane of the graphene sheet,

$$\mathbf{C} = n\mathbf{a}_1 + m\mathbf{a}_2, \tag{7.22}$$

where $\mathbf{a}_{1/2}$ are the two lattice vectors of the honeycomb lattice, see Fig. 7.6b. Depending on the (relative) values of n and m, one discerns between three classes of nanotubes: zigzag $(n, 0)$, armchair (n, n) and chiral (n, m). While zigzag nanotubes are insulating, the armchair nanotubes are metallic [150]. Therefore, since we are interested in the Kondo in the tube, in the following we focus on the armchair geometry.

As shown in Fig. 7.3(b), a honeycomb lattice ribbon is composed of two inequivalent columns of sites, described by the two matrices $\underline{M}_1$ and $\underline{M}_2$, which alternate throughout the ribbon. The Hamiltonian for the tube is then given by

$$\begin{aligned} H_{\text{host}}^{\text{Honey}} = &\sum_{x\text{even}} \mathbf{c}_{x,\sigma}^\dagger \underline{M}_1 \mathbf{c}_{x,\sigma} + \sum_{x\text{odd}} \mathbf{c}_{x,\sigma}^\dagger \underline{M}_2 \mathbf{c}_{x,\sigma} \\ &+ \sum_{x=0}^{L-1} t \left(\mathbf{c}_{x,\sigma}^\dagger \cdot \mathbf{c}_{x+1,\sigma} + \text{H.c.} \right). \end{aligned} \tag{7.23}$$

As in the square lattice case, the matrices $\underline{M}_{1,2}$ describe the hopping between sites within a given column. For the armchair system

$$\underline{M}_1 = \begin{pmatrix} 0 & t & & & & & \\ t & 0 & 0 & & & & \\ & 0 & 0 & t & & & \\ & & t & 0 & 0 & & \\ & & & 0 & 0 & & \\ & & & & & \ddots & \\ & & & & & & 0 \end{pmatrix}, \quad \underline{M}_2 = \begin{pmatrix} 0 & 0 & & & & & t \\ 0 & 0 & t & & & & \\ & t & 0 & 0 & & & \\ & & 0 & 0 & t & & \\ & & & t & 0 & & \\ & & & & & \ddots & \\ t & & & & & & 0 \end{pmatrix} \tag{7.24}$$

respectively. The entries in the upper right and lower left corners of M_2 wrap the ribbon around to form a tube. As before, we can formulate a matrix-valued continued fraction

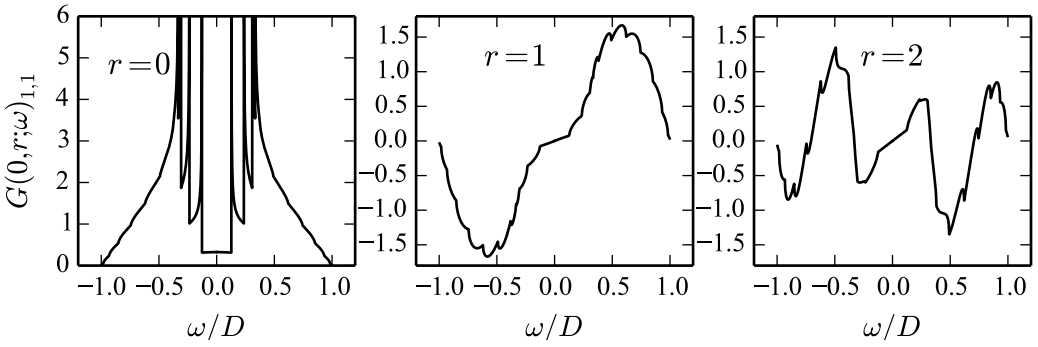

Figure 7.5.: Negative imaginary (dashed) parts of the free ($V = 0$) non-local lattice Green function on the semi-infinite honeycomb tube with a circumference of 16 sites. We leave out the real part for clarity. Note the different y-scale between the first and remaining two panels.

expression for the Green function at the end of a semi-infinite system. Defining, as before, matrices $\underline{A}_\alpha(z) = z\mathbb{1} - \underline{M}_\alpha$, with $\alpha = 1, 2$, the matrix of Green functions at the end of a semi-infinite system which ends in a column described by $\underline{M}_\alpha$ (for instance, the system shown in Fig. 7.3(b) ends on a column described by $\underline{M}_1$) can then be expressed by

$$\underline{G}_\alpha(z) = \left[\underline{A}_\alpha(z) - t^2 \underline{G}_{\bar{\alpha}}(z)\right]^{-1}, \tag{7.25}$$

where $\bar{\alpha} = 2$ for $\alpha = 1$ and vice versa. Since $\underline{A}_1$ and $\underline{A}_2$ are block-diagonal and have full rank they are invertible. Considering—without loss of generality—the matrix $\underline{G}_1$ we find (we omit the frequency arguments for notational clarity)

$$\underline{G}_1 = \frac{1}{2t^2} \underline{A}_1^{-1} \left(\sqrt{(\underline{A}_1 \underline{A}_2)^2 - 4t^2 \underline{A}_1 \underline{A}_2} + \underline{A}_1 \underline{A}_2 \right). \tag{7.26}$$

The matrix $\underline{G}_2$ can be obtained from $\underline{G}_1$ via $\underline{G}_2 = \underline{A}_1 \underline{G}_1 \underline{A}_2^{-1}$ and vice versa. While this expression is indeed *exact*, it is ambiguous since the square root of a $W \times W$-matrix leaves a choice of 2^W sign-combinations. However, there is *one* physical solution: Since the entries of the $\underline{G}_\alpha$ matrices are retarded Green functions, they need to fulfill the Kramers-Kronig relations.

Along the same lines as before, we can now find Green functions along the tube. For conciseness and clarity, we revert our notation to the one used previously: The matrix of Green functions connecting column n and column m are denoted by $\underline{G}(n, m; z)$. Then, assuming the Green function matrix $\underline{G}(0, 0; z)$ for the system in Fig. 7.3, we can obtain the matrix of Green functions connecting the zeroth column to the first column by multiplying with $\underline{G}_2$ from the right or left:

$$\underline{G}(0, 1; z) = t\, \underline{G}(0, 0; z)\, \underline{G}_2(z), \tag{7.27a}$$
$$\underline{G}(1, 0; z) = t\, \underline{G}_2(z)\, \underline{G}(0, 0; z). \tag{7.27b}$$

Using Eq. 6.15, the difference in Green functions in column one is then with and without the impurity

$$\Delta\underline{G}(1, 1; z) = \underbrace{t\underline{G}_2(z)\underline{G}_1(z)}_{\underline{G}(1,0;z)} \underbrace{V^2 G_d(z)}_{=\mathcal{T}(z)} \underline{B}_0 \underbrace{t\underline{G}_1(z)\underline{G}_2(z)}_{\underline{G}(0,1;z)}. \tag{7.28}$$

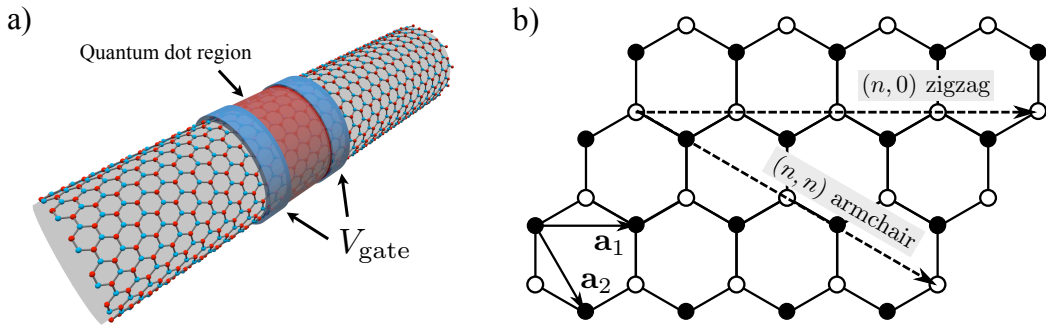

Figure 7.6.: (a) Schematic picture of an armchair nanotube, showing a region gated off from the rest of the tube by gates V_{gate}. This region functions as a quantum dot. We model such a setup by coupling the spin-$\frac{1}{2}$ impurity to all sites at the end of the nanotube. (b) The vector $n\mathbf{a}_1 + m\mathbf{a}_2$ in which the graphene sheet is "rolled up" determines its geometry. Shown are the two vectors (n,n) (armchair) and $(n,0)$ (zigzag) which lead to non-chiral nanotubes.

Where $\underline{B}_0$ is a $W \times W$-matrix determining how the impurity couples to the system. This result, of course, can be iterated and eventually leads to

$$\underline{G}(n,n;z) = t^2\, \underline{G}_\alpha(z)\, \underline{G}(n-1,n-1;z)\, \underline{G}_\alpha(z), \tag{7.29}$$

where α alternates between 1 and 2, reflecting the alternation of the geometries along the nanotube. In Fig. 7.5 we show results for the local and non-local Green functions obtained by application of Eq. (7.27a) for a tube of width $W = 16$. Because of the periodic boundary conditions in the y-direction, the system is translationally invariant in this direction. Recall that the entries of the matrix $\underline{G}(0,r;z)$ are the Green functions

$$\underline{G}(0,r;z)_{ij} = \langle\langle c_{(0,i)}; c^\dagger_{(r,j)}\rangle\rangle^{(0)}_z\,, \tag{7.30}$$

and from the translational invariance it follows that all diagonal entries must be identical. The imaginary part of the diagonal entries, $\mathrm{Im}\, G(0,0;\omega)_{ii}$, is gapless indicating a metallic behavior for the armchair nanotube [141].

Impurity setups in nanotubes

In real experiments with carbon nanotubes, the impurity is typically constructed by gating off a part of the tube, as shown in Fig. 7.6. The blue rings depict applied voltages that gate off the confined red region. This region functions as the quantum dot [151,152], whereas the rest of the tube is the lead. The important observation at this point is, that since the "impurity" is merely a part of the nanotube, it couples to *all* sites at the end. This justifies the picture in Fig. 7.1(c). We show in App. A how to determine the matrix $\underline{B}$ for arbitrary cases of the impurity coupling to multiple sites. In the case at hand, we find that the connection matrix consists only of 1's:

$$\underline{B}_0 = \begin{pmatrix} 1 & \dots & 1 \\ \vdots & \ddots & \vdots \\ 1 & \dots & 1 \end{pmatrix}. \tag{7.31}$$

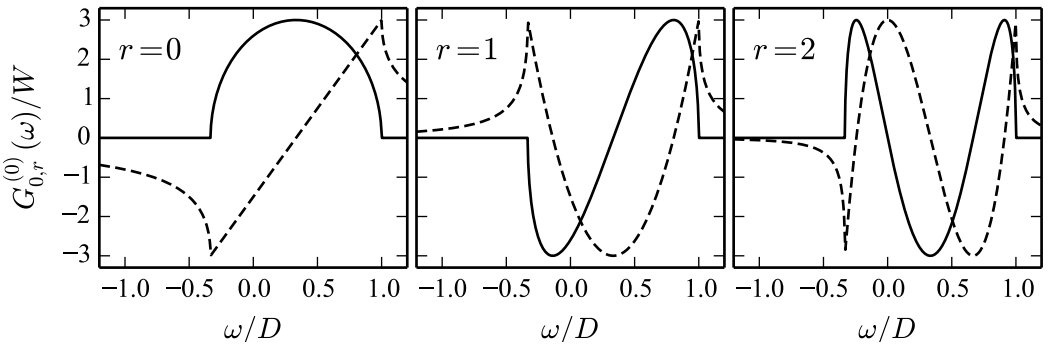

Figure 7.7.: Non-local Green functions appearing in the calculation of the charge densities in a semi-infinite nanotube where the impurity couples to all sites at the end. The functions are divided by the number of sites in the tube's circumference W.

Equivalence of a nanotube to a 1D chain

In Eq. (7.28) we have formulated the Dyson equation for the nanotube. As seen in the last section, for the situation which resembles most that of experiments, the impurity couples to all sites of the same sublattice at the end of the tube. With the corresponding matrix from Eq. (7.28), we find numerically that the hybridization function for the impurity is in fact equivalent to that of a 1D chain, albeit multiplied by the number of sites in the circumference of the tube and shifted by t. In fact, in this specific scenario, Eq. (7.28) can be formulated as

$$G^{\mathrm{nano}}_{r,r}(z) = W\left[G^{(0)}_{r,r}(z-t) + G^{(0)}_{0,r}(z-t)\; V^2 G_{\mathrm{imp}}(z-t)\; G^{(0)}_{r,0}(z-t)\right], \tag{7.32}$$

where W is the tube circumference, and all functions on the right-hand side are those of the simple 1D chain. The bandwidth of the nanotube system, however, is $D = 3t$, i.e. the band is given by $\omega \in [-3t, 3t]$. We show examples of the resulting Green functions in Fig. 7.7.

It is important to note that this special relation only holds when the impurity couples to the nanotube in the fashion described above. Therefore, the description of the Green functions in terms of the simple objects of the 1D chain can only be applied when using Eq. (7.28) since it is a direct consequence of the particular form of the matrix $\underline{B}_0$. If one considers e.g. the case of an impurity side-coupled to an infinite nanotube, this result is not valid anymore and the full matrix-valued method must be applied.

7.2. Impurity Green functions

The $\mathcal{T}$-matrix is proportional to the impurity Green function, see Eq. (6.16), which we calculate using the NRG. We discussed in Sec. 3.5 that all required information about the host system is contained in the hybridization function $\Delta(\omega)$, which is proportional to the local Green function of the site to which the impurity connects, see Eq. (3.29). In this section we present results for the impurity Green functions entering the calculation of the densities.

The negative imaginary parts of the local Green functions for the semi-infinite chain and the semi-infinite ribbons are shown in Figs. 7.2, 7.4, respectively. The Green functions for the effective 1D system of the armchair nanotube are shown in Fig. 7.7. Kondo

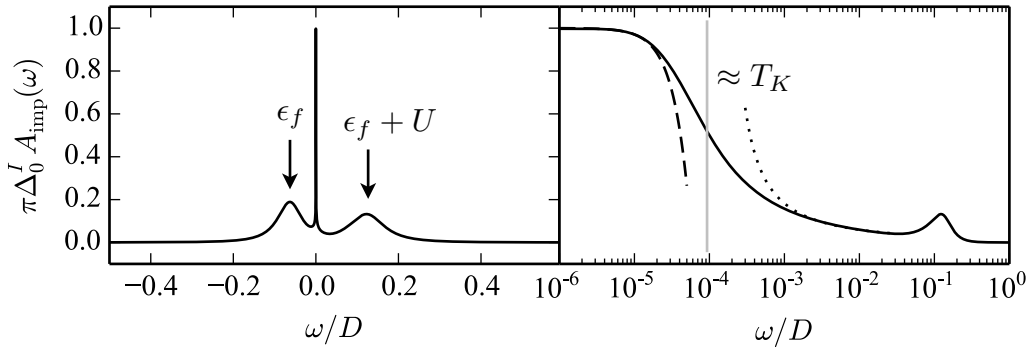

Figure 7.8.: Negativ imaginary part of the impurity Green function, $-\mathrm{Im}\, G_{\rm imp}(\omega)$, obtained for the semi-infinite 1D chain with impurity parameters $\epsilon_f/D = -0.07$, $U/D = 0.2$ and $V/D = 0.075$. In the left panel the "Hubbard satellites" are seen at energies ϵ_f and $\epsilon_f + U$, alongside the sharp, narrow Kondo resonance at the Fermi level, $\omega = 0$. The right panel shows the same data on a logarithmic scale. The Kondo temperature T_K can be defined as the full width at half maximum of the resonance, here indicated by a dashed line.

physics play out on exponentially low energy scales, and while the differences in the lattices we consider here lead to different features in the hybridization functions on energy scales of the band edge, $\omega \sim \mathcal{O}(D)$, around the Fermi level each system can be approximated by a constant hybridization function. Unsurprisingly, the corresponding impurity Green functions are highly similar, only differing slightly at higher energies. Whereas the spectral function in the host system is given by Eq. (6.10), the impurity spectral function is defined similarly as

$$A_{\rm imp}(\omega) = -\frac{2}{\pi} \lim_{\delta \searrow 0} \mathrm{Im}\, G_{\rm imp}(\omega + i\delta). \tag{7.33}$$

In Fig. 7.8 we show the spectral function obtained for an impurity at the end of a semi-infinite 1D chain, normalized so that the Kondo resonance has a maximum at 1. The charge fluctuations in the Anderson impurity model lead to two high energy resonances, known as the Hubbard satellites. These resonances are associated with the FO FP, they occur at energies relating to the energy cost of adding one electron (ϵ_f) and a second energy ($\epsilon_f + U$) to the unoccupied impurity. The slow rise of spectral weight, $\sim 1/\log(\omega)^2$, is characteristic of the LM FP, and finally at the Kondo scale, T_K, the Kondo resonance saturates. Here, the system is described by the SC FP, and results form Fermi liquid theory show an asymptotic behavior $\sim 1 - \omega^2$, whereas the asymptotic behavior for $\omega \gg T_K$ can be calculated perturbatively. The asymptotic functions are given as

$$\pi \mathrm{Im}\, \Delta A_{\rm imp}(\omega) = \begin{cases} 1 - a(\omega/T_K)^2 & \omega \ll T_K \\ \frac{b}{c + \log(\omega/T_K)^2} & \omega \gg T_K, \end{cases} \tag{7.34}$$

shown in the right panel of Fig. 7.8.

7.3. Real-space RG flow in the charge densities

Referring to the diagram in Fig. 6.1, we are now equipped with all necessary Green functions to calculate the charge density oscillations. We find that every relevant energy scale

in the impurity problem leads to the existence of a characteristic length scale in real space. In fact, the entire RG structure is reproduced in the charge density oscillations, which is our main result of this chapter. This confirms the results for the Kondo scale in Ref. [15], and extends them to a more comprehensive picture in terms of the entire RG flow.

7.3.1. 1D chain

A key point in our results is that the real-space charge densities are obtained from an integral transformation of the $\mathcal{T}$-matrix, given by Eq. (6.17). The lattice Green functions are complex objects, but generally become highly oscillatory for far distances [15]. For the 1D chain, using Eq. (7.7) and expanding to first order in $\omega \ll D$ the densities are given by

$$\Delta n(r) \overset{|\omega|\ll D}{=} -\frac{2}{\pi t^2}\mathrm{Im}\ (-1)^{r+1} \int_{-\infty}^{0} \mathrm{d}\omega\, e^{i\omega(r+1)/t}\, \mathcal{T}(\omega). \tag{7.35}$$

The important point is that in the $|\omega| \ll D$ limit in 1D, equation Eq. (6.17) takes on the form of a Fourier transformation. The inverse is generally well-defined and thus we expect all information contained in the $\mathcal{T}$-matrix to be equally contained in the density oscillations. Indeed, we find that the full RG structure of the underlying quantum impurity problem is *wholly* reproduced [125] in the spatial variation of $\Delta n(r)$, as shown in Fig. 7.9. There, we compare the energy dependence of the $\mathcal{T}$-matrix with the space dependence of the densities, normalized by the pure potential scattering contribution $\Delta n^{\mathrm{ps}}(r)$ at long distances. While the energy scale of the local moment crossover $T_{LM} \sim \mathcal{O}(U)$ was chosen to be similar for each system in the figure, the Kondo temperatures are widely differing. The difference between T_{LM} and T_K is deliberately tuned to be exaggerated to yield a clear energy and scale separation. The densities in the lower panel exhibit RG flow between all three fixed points as a function of distance. The crossover from local moment to strong coupling regime is given by a sign change in the oscillations, as discussed in Ref. [15] for the Kondo model.

The two crossover points at R_{LM} and R_K can be easily identified in the charge densities and we indeed find the expected results that $R_{LM} \sim 1/T_{LM}$ and $R_K \sim 1/T_K$. In particular, as the impurity-host coupling decreases, the length scale R_K grows and finally diverges, $R_K \to \infty$, for the case of an uncoupled impurity. The impurity then persists as a local magnetic moment and the long-distance behavior in real-space is described correspondingly by the local moment fixed point. In that sense, the region $r \ll R_K$ is not *per se* a "screening cloud", but contains an internal structure differentiating regions described by free orbital and local moment physics from regions at $\sim R_K$ in which screening occurs.

7.3.2. Square lattice ribbons

With the RG flow fully contained in the charge density oscillations of a 1D system, we now turn to quasi-1D systems of a finite width—the ribbons discussed above. As before, we use Eq. (6.17) to calculate the densities, with the lattice Green functions obtained from Eqs. (7.19) and (7.18).

Fig. 7.10 shows the structure in the charge density oscillations for ribbons of different widths with an impurity coupled to the site at $\mathbf{r} = (0, 0)$. The density oscillations are

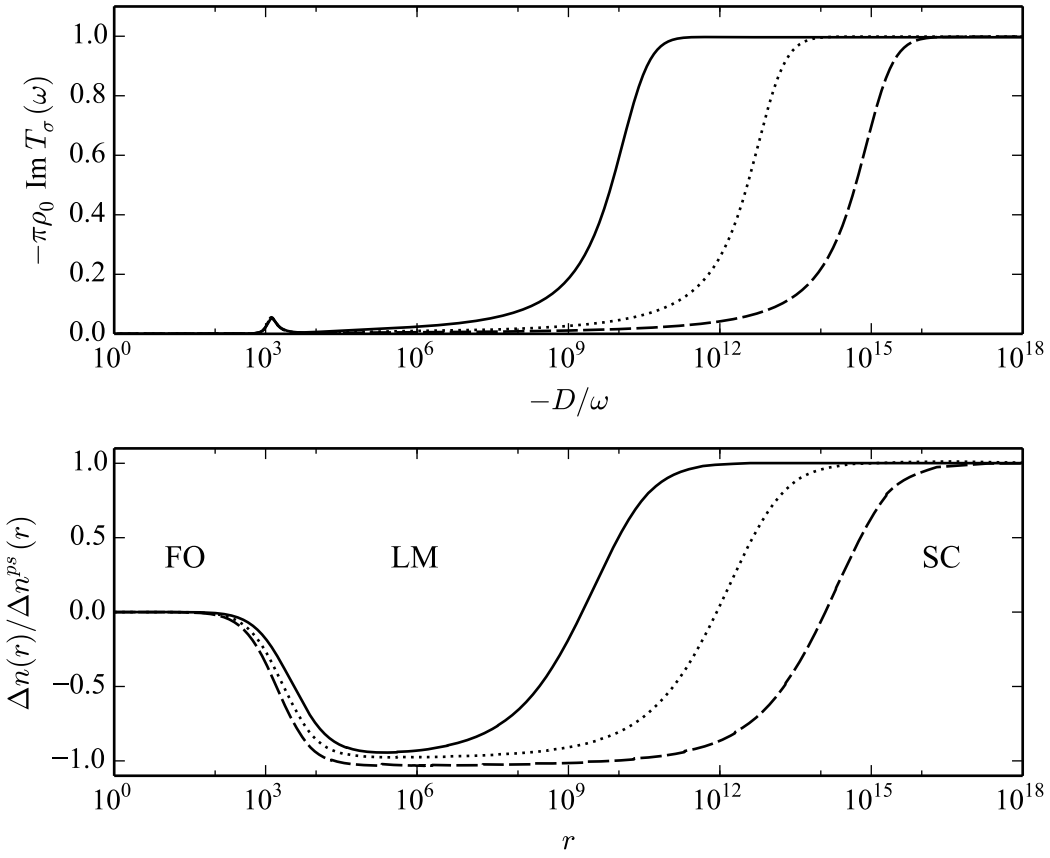

Figure 7.9.: Comparison of the spectrum vs. inverse frequency (upper panel) and the normalized excess charge density vs. distance (lower panel) for the $T = 0$ Anderson model on a semi-infinite 1D chain. The parameters of the Anderson model are for all systems $V/D = 3 \times 10^{-3}$ and $\epsilon_f/D = -0.8 \times 10^{-3}$. The Coulomb interaction was tuned to be $U/D = 1 \times 10^{-3}, 1.125/D \times 10^{-3}$ and 1.25×10^{-3} (solid, dotted, and dashed lines). The RG fixed points describing the different regions are given as free orbital (FO), local moment (LM) and strong coupling (SC).

strongest going diagonally away from the impurity. At the boundary of the system they are reflected, thus generating a characteristic zig-zag pattern. We discuss the origin of the focusing along the diagonals in more detail in Sec. 8.1. The more complex matrix structure of the problem does not allow us to investigate the behavior of the charge densities to such far distances as in the simple 1D case. However, by choosing parameters such that the Kondo temperature becomes large, we can push the Kondo length scale to small values, $R_K \sim \mathcal{O}(10^2)$, thus making it possible to examine the Kondo crossover without the need to go to very long distances. As seen in Fig. 8.1, when going away from the impurity along the central line where $y = 0$, the zig-zag pattern leads to the oscillations being strongest every $(W+1)$st site. The absolute values of the density oscillations on these sites, $|\Delta n(x, 0)|$, are shown in Fig. 7.11 for a strip of width $W = 9$. As in the 1D case discussed before, the density oscillations change sign at the Kondo length scale, which leads to a sharp dip in the absolute values. We find a good agreement with the expected behavior of $R_K \sim 1/T_K$ where the Kondo temperature is extracted from the thermodynamics, e.g. the impurity entropy. This behavior is demonstrated in Fig. 7.11 where the dip in the density oscillations moves toward the impurity for greater values

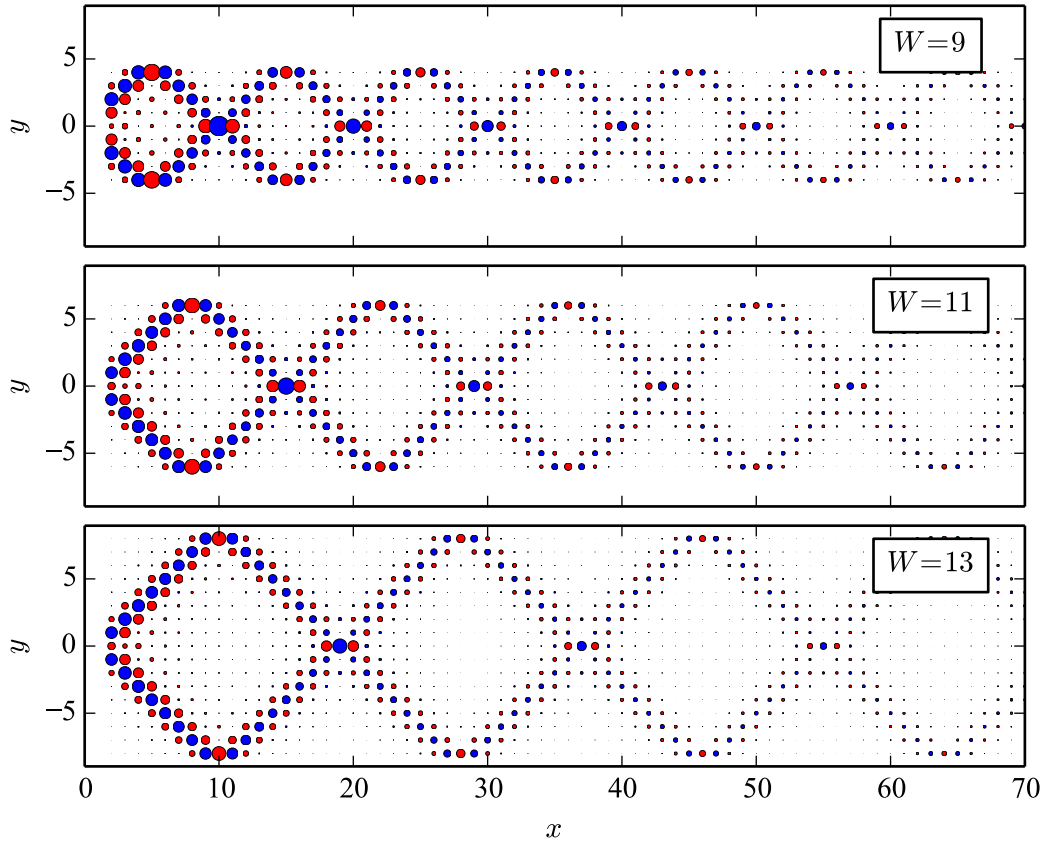

Figure 7.10.: Charge density oscillations for ribbons of widths $W = 9, 11, 13$. The size of the circles is proportional to the density differences $\Delta n(\mathbf{r})$, the red (blue) circles are > 0 (< 0). The density oscillations are clearly strongest diagonally away from the impurity, and reflected on the boundary. The impurity has a level energy of $\epsilon_f/D = -0.07$, an on-site Coulomb interaction of $U/D = 0.2$ and a hybridization strength $V/D = 0.075$.

of the hybridization V. From Eqs. (2.14) and (2.10) we know that the Kondo temperature grows with V, since

$$\frac{T_K}{D} \sim 2V\sqrt{\frac{\rho_0}{U}}e^{-\frac{U}{\rho_0 4V^2}}, \tag{7.36}$$

therefore confirming the observed behavior of the dips. The density oscillations in the square lattice ribbons possess a non-trivial structure, but the characteristic Kondo crossover is nevertheless still present.

The dimension of the matrices used in the calculation of the Green functions grows linearly in the width of the ribbons. The matrix multiplications and diagonalizations have a numerical complexity that scales as $\mathcal{O}(W^3)$. Furthermore the lattice Green functions obtain more features for wider systems, therefore requiring the numerical integration of Eq. (6.17) to be done more accurately. In the next chapter we present two different methods to investigate the infinite square lattice. However, it should be noted at this point that the equations of motion method introduced here has the advantage that it can be expanded to treat disordered system by introducing local level energies on each site, $\epsilon_{\mathbf{r}}$. Furthermore, this method can also be used to describe three-dimensional slab-type lattices.

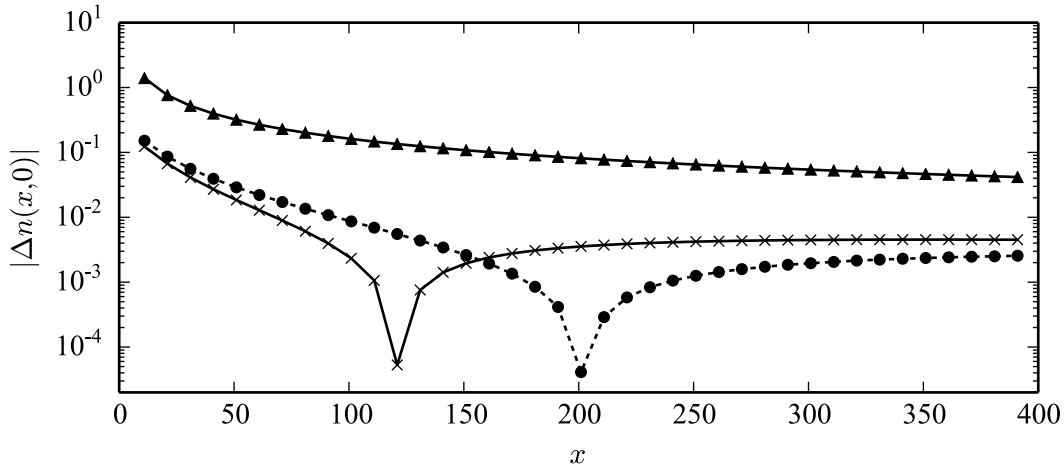

Figure 7.11.: Charge density oscillations for a ribbons of width $W = 9$, taken along the central line where $\mathbf{r} = (x, 0)$. Plotted are the absolute values on a log scale, where the sign change at $\sim R_K$ is shown as a sharp dip. The results shown are obtained for parameters $\epsilon_f/D = -0.07$, $U/D = 0.2$ and $V/D = 0.075$ (circles) and $V/D = 0.078$ (crosses, dotted line), respectively. The triangles show the oscillations for a pure potential scatterer where $\epsilon_f/D = -0.07$, $U = 0$ and $V = 0.075$.

7.3.3. Nanotubes

We discussed previously how the impurity setup that we employ for the nanotube leads to an effective 1D model for the densities. Using again Eq. (7.7) in Eq. (7.32) leads to an asymptotic expression for the charge oscillations along the tube:

$$\begin{aligned}\Delta n(r) &\overset{|\omega|\ll D}{=} -\frac{2}{\pi t^2}\mathrm{Im}\, e^{-i\frac{4\pi}{3}(r+1)} \int_{-\infty}^{0} \mathrm{d}\omega\, e^{-i\frac{2\omega}{\sqrt{3}t}(r+1)}\, \mathcal{T}(\omega) \\ &\overset{\omega\to\sqrt{3}\omega/2}{=} -\frac{\sqrt{3}}{\pi t^2}\mathrm{Im}\, e^{-i\frac{\pi}{3}(r+1)}(-1)^{r+1} \int_{-\infty}^{0} \mathrm{d}\omega\, e^{i\omega(r+1)/t}\, \mathcal{T}(\sqrt{3}\omega/2). \end{aligned} \tag{7.37}$$

The expression in the last line is essentially that for the 1D chain in Eq. (7.35), however multiplied by a factor $\sqrt{3}/2$ and with an additional modulation factor of $e^{-i\frac{\pi}{3}(r+1)}$. The argument of the $\mathcal{T}$-matrix is also rescaled by the factor $\sqrt{3}/2 \approx 0.86$, which slightly changes the Kondo temperature and accordingly the Kondo length scale. Assuming a non-interacting impurity, $U = 0$, the Friedel oscillations due to the potential scattering thus decay similarly to the simple 1D chain as $\sim 1/r$, superimposed by a modulation with a period of three sites. In Fig. 7.12 we compare results obtained numerically from Eq. (7.32) with the asymptotic result from Eq. (7.37), proving that the 1D description of the nanotube is justified.

For a correlated impurity, $U > 0$, we again find the RG flow contained in the density oscillations. However, the modulation of the densities results in essentially three sets of densities, see Fig. 7.12. In Fig. 7.13 we show the same comparison as in the simple 1D case. In the lower panel, each line connects densities belonging to one of the three subset of sites, given by $3n+i$, where $n \in \mathbb{N}$ and $i = 0, 1, 2$. At both length scales, the local moment scale R_{LM} and the Kondo scale R_K, we see a change in the density oscillations. How-

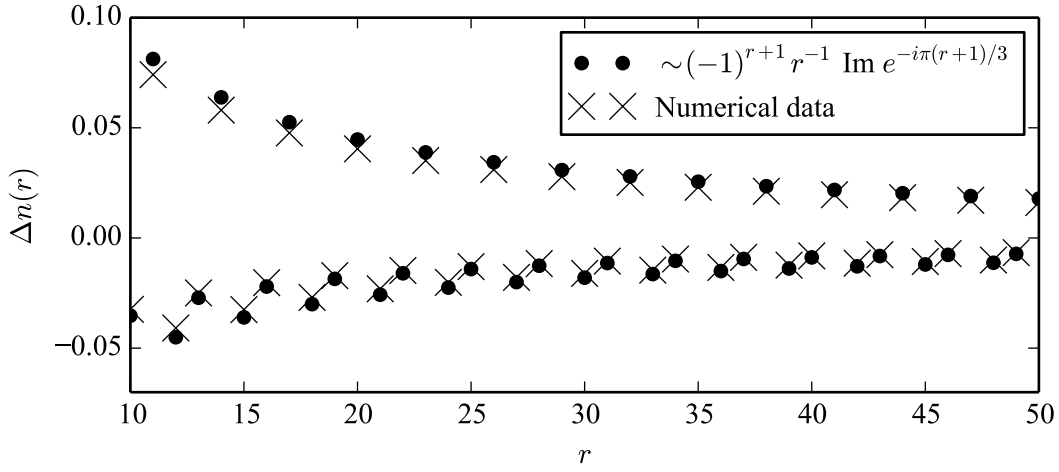

Figure 7.12.: Charge density oscillations along a nanotube for pure potential scattering at $U/D = 0, \epsilon/D = -0.1, V/D = 0.167$. The extra phase in the expression for the densities, Eq. (7.37), introduces a periodicity of three sites.

ever, contrary to the simple 1D case, the Kondo crossover does not show up as a simple sign change. Only one of the three subsets changes sign whereas the other two grow in magnitude. At distances $r \ll R_K$, the density oscillations are thus strongly suppressed and only at $r \gg R_K$ do they reach their simple potential scattering behavior.

7.3.4. Experimental observation

We have shown that the entire information of the full RG flow is contained in the charge density oscillations surrounding an Anderson impurity in a simple 1D chain, but also in quasi-1D nanoribbons and nanotubes. While the nanotube we described has a realistic circumference of 16 sites (or 8 hexagons, respectively), the density oscillations decay as a power-law and in a real system disorder and noise quickly render a measurement to the required accuracy impossible at this point in time. In fact, the recent success [126, 153–155] of measuring signatures of the Kondo effect in the local density of states only a few sites away from the impurity indicates that direct experimental results for the charge density oscillations hundreds of sites away from the impurity are currently out of the question.

Very recently, a different proposal for the measurement of the Kondo cloud has been put forth [156], however as of the writing of this thesis no experimental results to this end have been published.

7.4. Summary

We have calculated the static charge density oscillations due to a particle-hole asymmetric Anderson impurity in one-dimensional and quasi-one-dimensional lattices. The description of an impurity problem in terms of an RG framework is generically a function of energy or distance. The density oscillations are given in terms of an integral transformation of the $\mathcal{T}$-matrix, which itself is related to the impurity local density of states. As such, the entire information of the RG flow, which is contained in the $\mathcal{T}$-matrix, must equally be contained in the static density oscillations. We can directly confirm this concept numerically, showing that the RG flow including all fixed points is recovered in the

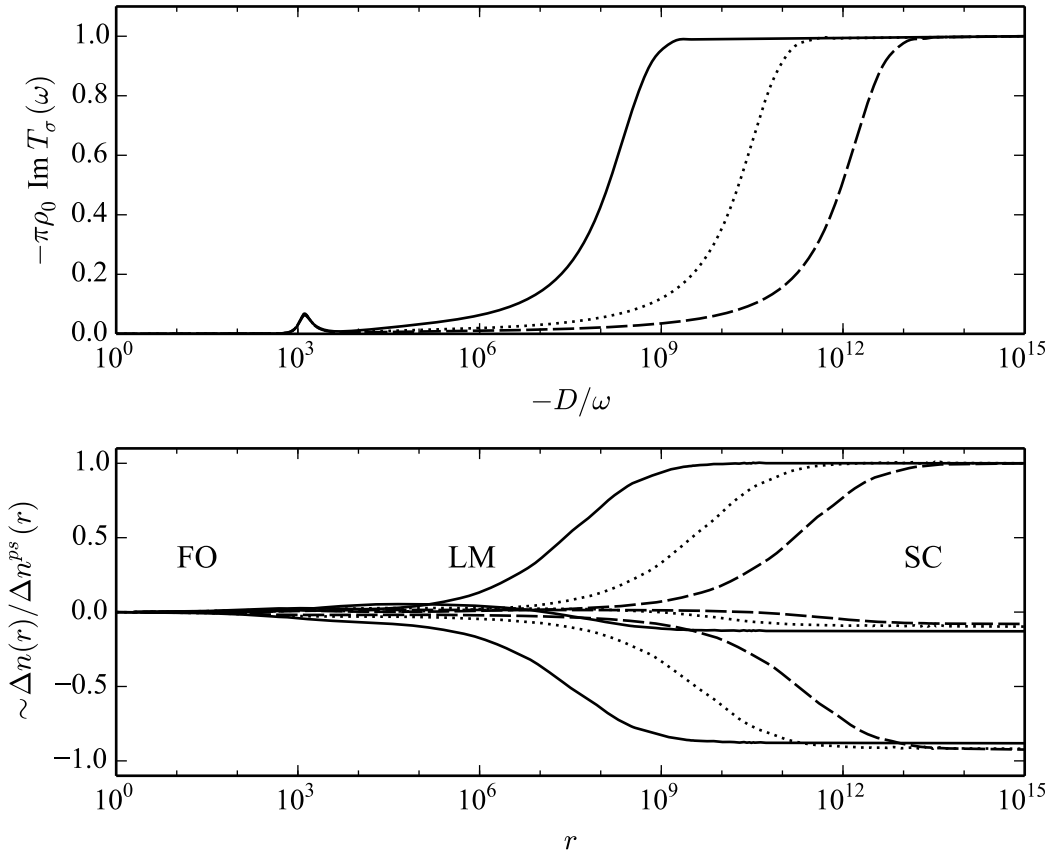

Figure 7.13.: Comparison of the spectrum vs. inverse frequency (upper panel) and the normalized excess charge density vs. distance (lower panel) for the $T = 0$ Anderson model on a semi-infinite 1D chain. The parameters of the Anderson model are for all systems $V = 0.75 \times 10^{-3}$ and $\epsilon = -0.8 \times 10^{-3}$. The Coulomb interaction was tuned to be $U = 1 \times 10^{-3}$, 1.125×10^{-3} and 1.25×10^{-3} (solid, dotted, and dashed lines).

envelope function of the density oscillations.

Furthermore, we used a matrix-valued equations of motion approach for the calculation of Green functions on square lattice ribbons and honeycomb lattice nanotubes. In the case of the latter, we can show that an experimentally relevant setup can be mapped to an effective 1D chain with an extra phase factor.

Finally, our results suggest a slightly adjusted understanding of the Kondo screening cloud. We conclude that the region inside the Kondo screening cloud is described by the local moment fixed point, and the region outside is described by the strong coupling fixed point — the screening of the impurity does not occur before the system flows to the strong coupling fixed point at distances on the order of $\sim R_K$.

Chapter 8.

Square lattice

Calculating Green functions for arbitrary lattices of dimension $d > 1$ to high accuracy is generally a formidable task. Using equations of motion works well in 1D and can be extended to quasi-1D (see the previous chapter). The computationally critical part in the calculation is the repeated inversion of a matrix, an operation with generally scales as $\mathcal{O}(N^3)$, and thus the complexity of the calculations grows strongly with the width of the system, making it intractable for an infinite 2D system. One could express the Green functions in $\mathbf{k}$-space and perform a Fourier transformation to generate the real-space representation. However, this involves a d-dimensional integral over highly oscillatory functions which is numerically hard, especially when the required accuracy of the result is as high as in our case. One thus has to look for more specialized methods tailored to the particular lattice under consideration.

For simple cubic lattices (such as the square lattice), arbitrary Green functions in d dimensions can in fact be calculated in a very efficient manner via their lower-dimensional counterparts. More specifically, square lattice Green functions are given by a convolution of two 1D Green functions. This result was presented for *local* Green functions in Refs. [157, 158].

Furthermore, recursive methods for various lattices—among them the square lattice–have been found which do not require any integrations [159, 160]. Although these methods are exact, they suffer greatly from build-up of numerical error, which so far can only be circumvented for certain high symmetry directions on the lattices. For the square lattice, such a direction is along the lattice diagonals. We argued in Sec. 8.1 that most of the intensity of charge density oscillations is focused along the diagonals and thus this method—which we will call Morita's method after its inventor [159]—allows us to examine these to high accuracy.

In the following we discuss some properties of the Friedel oscillations on a square lattice, then we briefly review the *convolution method* for arbitrary Green functions and *Morita's method* for functions along the diagonals. Finally, results for the densities and the Kondo RG flow are presented.

8.1. Friedel oscillations on the square lattice

The results for the density oscillations on the square lattie ribbons considered in Chap. 7 showed an example where the lattice geometry strongly influences the real-space physics. Turning to an infinite 2D system, the arguably simplest lattice configuration is that of a square lattice: Its lattice vectors are $\mathbf{a}_1 = a\hat{\mathbf{e}}_x$ and $\mathbf{a}_2 = a\hat{\mathbf{e}}_y$, where $\hat{\mathbf{e}}_{x/y}$ are the cartesian basis vectors and a is the lattice constant. The unit cell is given as a square of area a^2, containing one site. In reciprocal space, the first Brillouin zone is a square with an area of $a^2/(4\pi^2)$. For the remainder of this chapter, we set the lattice constant

to $a = 1$. The bath Hamiltonian we consider is

$$H_{\text{bath}} = t \sum_{\langle \mathbf{r}\mathbf{r}' \rangle \sigma} \left(c^{\dagger}_{\mathbf{r},\sigma} c_{\mathbf{r}',\sigma} + \text{H.c.} \right), \tag{8.1}$$

where the site positions are $\mathbf{r} = (x, y)^T = x\mathbf{a}_1 + y\mathbf{a}_2$ and the summation runs over nearest neighbors. This Hamiltonian describes non-interacting electrons and it can be diagonalized by Fourier transformation, yielding the dispersion relation

$$\varepsilon(\mathbf{k}) = t \left[\cos(k_x) + \cos(k_y) \right], \tag{8.2}$$

where $\mathbf{k} = (k_x, k_y)^T$ is a vector in the first Brillouin zone. The bandwidth $2D$ of the model is determined by the dispersion's extremal energies and is readily found to be $2D = 4t$.

Despite its geometrical simplicity, the square lattice gives rise to some interesting physics. Its influence on Friedel oscillations has been studied before [161,162], and in the following we would like to give an intuitive picture of the results, following the arguments in Ref. [163]. Green functions can be understood as a description of how electrons of energy ω move from a point source $\mathbf{r}'$ to other points $\mathbf{r}$ in the system. Furthermore, charge density oscillations in a system fundamentally result from scattering processes of conduction electrons on an impurity and can be calculated from the real-space Green function $G_{\mathbf{r}\mathbf{r}'}(\omega + i\delta)$, cf. Eq. (6.13). It is thus clear that the shape of the Friedel oscillations is directly related to the propagation of electrons in the system. Indeed, by examining the electron's group velocity (determined by the Fermi surface of the system), one can identify regions where electron transport and thus density oscillations are strong. The group velocity is given by [110]

$$\mathbf{v}_{\text{g}}(\mathbf{k}) = \frac{1}{\hbar} \nabla_{\mathbf{k}} \varepsilon(\mathbf{k}), \tag{8.3}$$

where $\varepsilon(\mathbf{k})$ is the band structure and the gradient is taken with respect to the wave vector $\mathbf{k}$. When many group velocity vectors point in a certain direction, electron flux in this direction will be greatly enhanced. This effect is called *electron focusing* [163] and in the following we examine this effect on the square lattice. At half-filling, the Fermi surface is determined by $\varepsilon(\mathbf{k}) = 0$, which for the square lattice dispersion from Eq. (8.2) is the contour given by $|k_x| + |k_y| = \pi$, as shown in Fig. 8.1. The group velocity is normal to the Fermi surface, and along the flat edges the group velocity vectors are all parallel, resulting in a very strong electron focusing along the lattice diagonals. Therefore, Friedel oscillations due to a potential scatterer have greatest intensity going diagonally away from the impurity [163, 164]. After presenting results for the full system, we specifically focus on the lattice diagonals since most of the charge density is centered along them.

8.2. Green functions on the infinite lattice

In principle, lattice Green functions for arbitrary lattice with translational symmetry can always be obtained from a straight-forward Fourier transformation. While this approach is of great usefulness in analytical treatments, it is usually only feasible when considering continuum limits in field theories. Here, we are rather interested in calculating (numerically accurate) effects of the microscopic features of the lattice. The Fourier transforma-

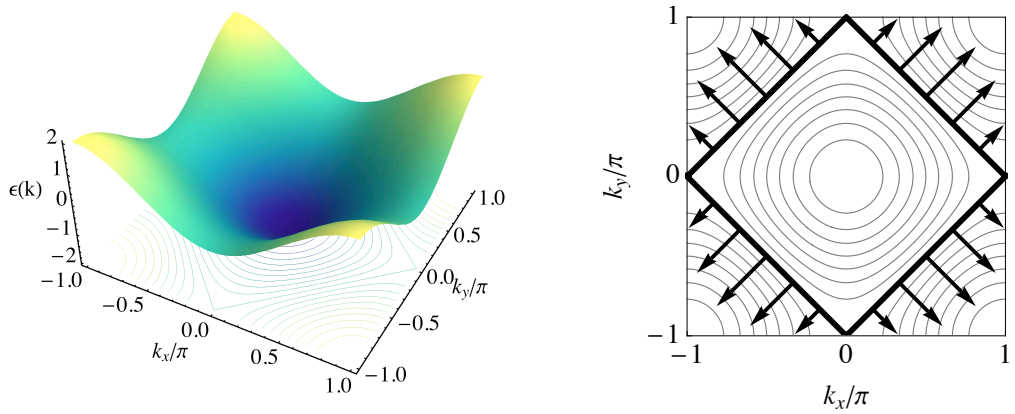

Figure 8.1.: Left panel: The dispersion $\varepsilon(\mathbf{k})$ of the square lattice in the first brillouin zone for $t = 1$. Right panel: The dispersion shown as contours of constant energy. The Fermi surface $\varepsilon(\mathbf{k}) = 0$ at half-filling is shown as the solid black diamond. The group velocity $\mathbf{v}_\mathrm{g}$ along the Fermi surface is strongly focused along four distinct directions (arrows). The group velocities are largest at the center of the flat edges of the Fermi surface.

tion for real-space Green functions on the square lattice are given as

$$\begin{aligned} G_{\mathbf{r}\mathbf{r}'}(z) &= \frac{1}{\sqrt{2\pi}} \int_{-D}^{D} \mathrm{d}\mathbf{k}\, e^{i\mathbf{k}\cdot(\mathbf{r}-\mathbf{r}')} G_{\mathbf{k},\mathbf{k}'}(z) \\ &= \frac{1}{\sqrt{2\pi}} \int_{-D}^{D} \mathrm{d}\mathbf{k}\, \frac{e^{i\mathbf{k}\cdot(\mathbf{r}-\mathbf{r}')}}{z - \varepsilon(\mathbf{k})}, \end{aligned} \tag{8.4}$$

with the square lattice dispersion $\varepsilon(\mathbf{k})$ given in Eq. (8.2). The main problem with this approach is the computationally involved 2D integral. Since this transformation has to be performed *per frequency* argument ω, it is unfeasible to perform the integration to the required accuracy each time. Another route could be to employ Discrete Fourier Transformation methods. There, however, the system effectively acquires a finite size. Furthermore, in both cases, to avoid divergencies in the integrand, we must always implement a finite δ in $z = \omega + i\delta$, which broadens the resulting Green functions and further decreases the accuracy.

While this approach is thus not viable for our purposes, we must resort to other methods of calculating the lattice Green functions. In the following, we present two such methods for the square lattice.

8.2.1. The convolution method

In Refs. [157, 158] a method was introduced to calculate lattice Green functions for a d-dimensional simple cubic lattice from a *convolution* of $(d-1)$-dimensional Green functions. In the case of the 2D square lattice, lattice Green functions can then be obtained from Green functions for the one-dimensional chain, viz.

$$G^{\mathrm{2D}}_{\mathbf{r}\mathbf{r}'}(\omega + i\delta) = \int_{-D}^{D} \mathrm{d}\omega'\, G^{\mathrm{1D}}_{x,x'}(\omega' - \omega + i\delta)\, G^{\mathrm{1D}}_{y,y'}(\omega + i\delta), \tag{8.5}$$

where $\mathbf{r} = (x, y)$ and $\mathbf{r}' = (x', y')$, and $G^{\mathrm{1D}}_{x,x'}(z) = \langle\langle c_x; c^\dagger_{x'}\rangle\rangle_z$ is the (non-local) lattice Green function for the chain as discussed in the previous chapter. Using the commonly adopted sign $*$ for the convolution operator we can rewrite this as

$$G^{\mathrm{2D}}_{\mathbf{rr}'}(z) = G^{\mathrm{1D}}_{x,x'}(z) * G^{\mathrm{1D}}_{y,y'}(z). \tag{8.6}$$

The usefulness of this result lies in two important facts:

- The 1D Green functions are simple objects for which a simple analytical expression exists, see Sec. 7.1, and they can thus be calculated very efficiently.
- The convolution of two functions is equivalent to a multiplication of their Fourier transforms. Thus, instead of Fourier transforming a 2D object, now we only need the Fourier transformation (and back-transformation) of a 1D Green function, a much simpler task. The Fourier transformation can be carried out numerically very efficiently using the Fast Fourier Transformation algorithm, an excellent implementation of which can be found in the `FFTW3` library [165].

We employ this method for the investigation of the shape and extension of the Kondo cloud in the square lattice in Sec. 8.4.

8.2.2. Morita's iterative method

The convolution method from the last subsection is a powerful tool for the calculation of Green functions. However, due to the non-trivial numerical operations such as the Fourier transformation, the accuracy is thus far high enough to produce satisfactory results for considering distances from the impurity of only a few hundred sites.

With regard to the exponentially large length scales associated with the Kondo effect, we now introduce a different method of calculating Green functions on the square lattice, which is constrained to work only along the lattice diagonals. As discussed in Sec. 8.1, however, this is in fact precisely the region that we expect to find the strongest density oscillations. For the sake of clarity, in this section we use a slightly different notation for the Green functions. We are only concerned with Green functions on the lattice diagonals and can therefore express the Green functions only in terms of the distance to the impurity along the diagonals,

$$G(n; z) \equiv G_{\mathbf{r0}}(z), \tag{8.7}$$

where $\mathbf{r} = n(\hat{\mathbf{e}}_x + \hat{\mathbf{e}}_y)$ and $n \in \mathbb{N}$.

The algorithm we use was first introduced by Morita in Ref. [159]. However, in its original formulation it is extremely sensitive to numerical errors and only generates reliable results when $|\mathbf{r}| \lesssim 30$. A refinement of this method was proposed in Ref. [160], strongly increasing its numerical stability. As a starting point we require the local lattice Green function $G^{(0)}(0; z)$, and the non-local Green function connecting the origin with its diagonal neighbor, $G^{(0)}(1; z)$. These can be expressed exactly as:

$$G^{(0)}(0; z) = \frac{2}{\pi z} K(D/z), \tag{8.8}$$

$$G^{(0)}(1; z) = \frac{2}{\pi z}\left(\frac{z^2}{8} - 1\right) K\left(4/z\right) - \frac{z}{4\pi} E(4/z), \tag{8.9}$$

with the half-bandwidth $D = 4t$. $K(x)$ is the complete elliptic integral of the first kind and $E(x)$ is the complete elliptic integral of the second kind. From here, Morita's method provides a recursive scheme which we briefly describe in the following.

The Green function $G^{(0)}(n;z)$ can be related to $G^{(0)}(n-1;z)$ via a (frequency- and distance-dependent) factor $R(n;z)$. The inital equation of the recursion is thus

$$G^{(0)}(1;z) = R(0,z)G^{(0)}(0;z). \tag{8.10}$$

Plugging in Eqs. (8.8) and (8.9) yields

$$R(0,z) = \frac{2z^2}{D^2}\left(1 - \frac{E(D/z)}{K(D/z)}\right) - 1. \tag{8.11}$$

The values of $R(n,z)$ for $n > 0$ are then given in terms of the previously found $R(n,z)$ by the following formula [160]:

$$R(n+1,z) = \frac{4(n+1)}{2n+3}\left(\frac{2z^2}{D^2} - 1\right) - \frac{\left(\frac{2n+1}{2n+3}\right)}{R(n,z)}. \tag{8.12}$$

Since $R(n+1,z)$ is given only in terms of $R(n,z)$, this way one can calculate lattice Green functions along the diagonal of the square lattice *iteratively* in a numerically very efficient manner. After calculating $R(m,z)$ for every $0 \leq m < n$, we find

$$G^{(0)}(n;z) = \left[\prod_{m=0}^{n-1} R(m,z)\right] G^{(0)}(0;z). \tag{8.13}$$

The resulting Green functions are those of an infinite lattice, that means we neither have to perform any broadening nor do we have to deal with finite size effects. Furthermore, once the functions in Eqs (8.8) and (8.9) are known, the remaining calculation is simple and can be performed very efficiently by a computer. Therefore, this method allows us to generate highly accurate results, which we use to discuss the real-space RG flow in the square lattice in Sec. 8.5.

8.2.3. Results for the Green functions

In Fig. 8.2 we show results for the square lattice Green functions, $G^{(0)}(n;z)$ for various values of n, calculated using the recursive Method by Morita. The arguably most striking feature of these functions is the van-Hove singularity at the Fermi level, where the imaginary part of the Green functions diverges logarithmically, which we discuss in more detail in the next section.

8.3. Impurity Green functions

In Sec. 7.2 we presented impurity Green functions for the Anderson model for the 1D and quasi-1D system. In these system, the host density of states near the Fermi level is approximately constant. The resulting impurity Green functions therefore all resembled those obtained for the simple flat band model [3]. The logarithmically diverging van-Hove singularity in the hybridization function for the Anderson model on the square lattice, shown in the upper left panel of Fig. 8.2, however, is qualitatively different from a flat band model and we now discuss the implications for the impurity problem and the NRG calculations.

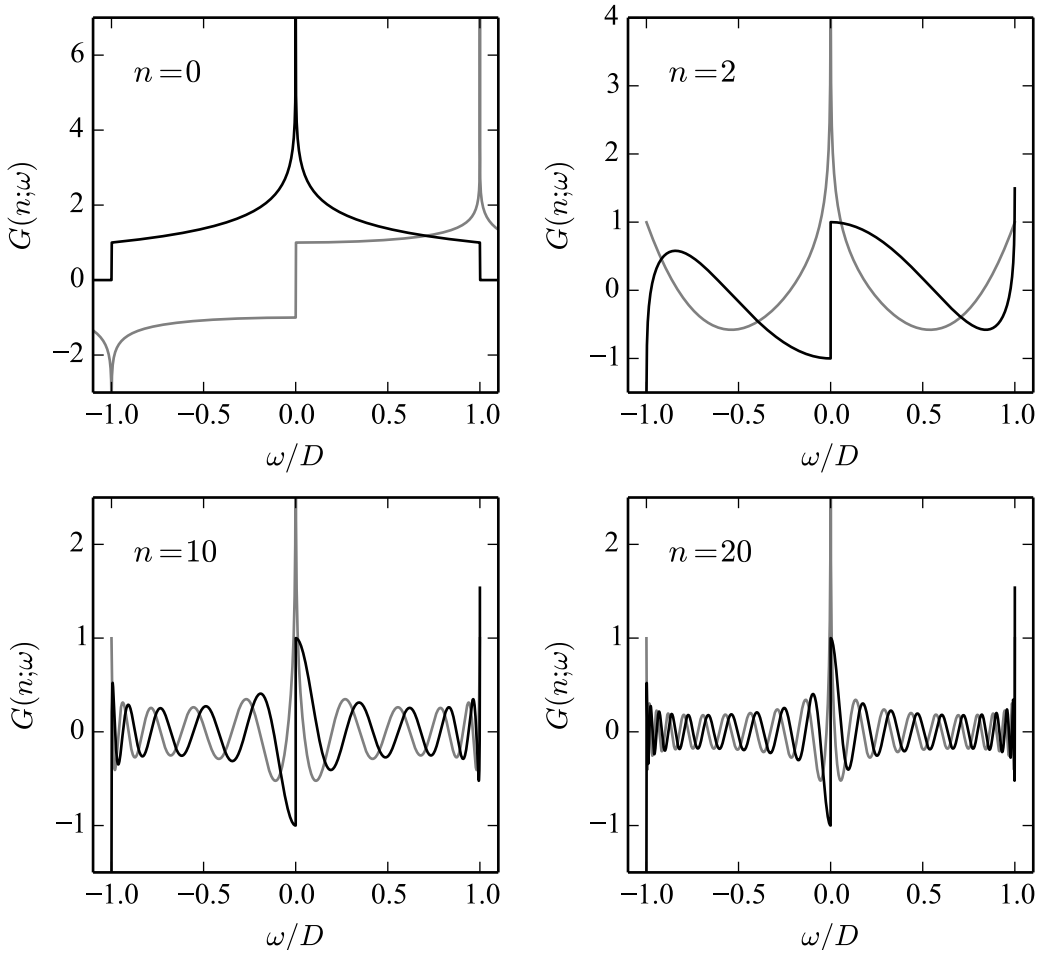

Figure 8.2.: Lattice Green functions $G^{(0)}_{\mathbf{r0}}(\omega)$ on the square lattice diagonal $\mathbf{r} = n(\hat{\mathbf{e}}_x + \hat{\mathbf{e}}_y)$, negative imaginary part (black line) and real part (gray line). The first figure shows the local Green function obtained directly from the exact definition in Eq. (8.8). The remaining Green functions are calculated with Morita's recursive method. The most important feature in the square lattice Green functions is the logarithmic divergence near the Fermi level.

8.3.1. Van-Hove singularity in the hybridization function

The problem of a logarithmically diverging hybridization function is discussed by means of the 'poor man's scaling' approach and numerically using NRG in Ref. [166]. Numerically, one accounts for the divergence in the hybridization function by constructing the Wilson chain long enough to resolve energies well below the Kondo scale, thereby capturing all relevant physics at T_K. The results agree well with those found from analytical approaches.

The main consequence of the divergence is the occurrence of non-Fermi liquid behavior when the van-Hove singularity is exactly at the Fermi level, as is the case in our setup. As $T \to 0$, the huge spectral weight around the Fermi level leads to an overcompensation in the screening process [166], similar to the overscreened Kondo problem [167]. This effect is visible in the thermodynamic impurity quantities, such as the susceptibility or the entropy, which show a nonmonotonous behavior as $T \to 0$. Furthermore, the Kondo resonance in the impurity Green function decays logarithmically, $A_{\mathrm{imp}}(\omega) \to 0$,

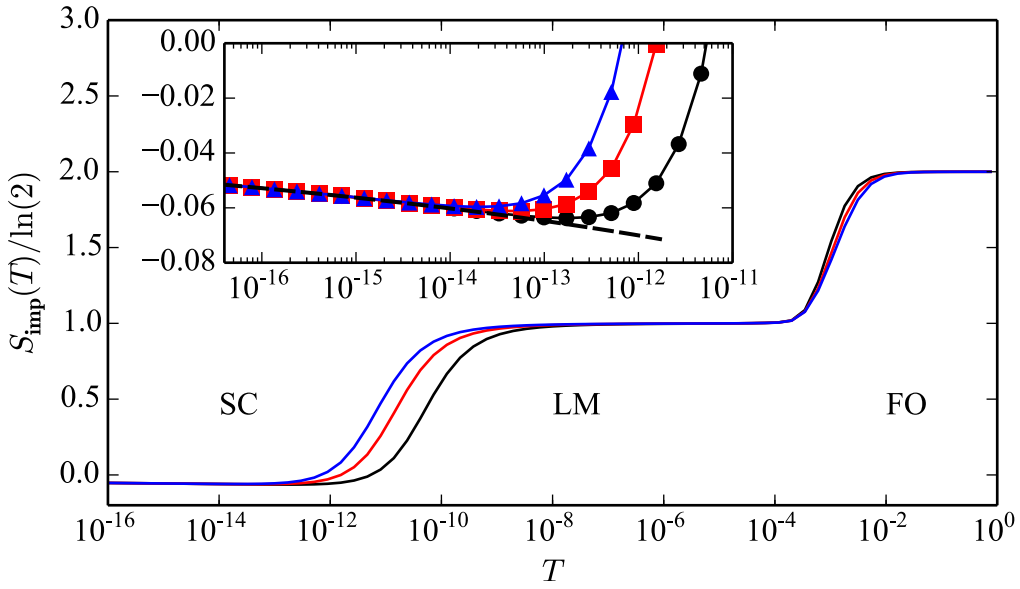

Figure 8.3.: Impurity entropy as a function of temperature for an impurity side-coupled to the square lattice. The three RG fixed points are clearly visible. In the strong coupling fixed point the impurity entropy becomes negative but logarithmically approaches zero. Parameters used are common $V/D = 3 \times 10^{-3}$ and $\epsilon_f/D = -1.5 \times 10^{-3}$, varying $U/D = 6 \times 10^{-3}, 5 \times 10^{-3}, 4 \times 10^{-3}$ (black, red and blue lines). The inset shows a closeup of the negative region. The dashed line is a fit $S(T) = -a/|\ln(T/D)|^{\delta}$, with $a = 1.25622$ and $\delta = 0.980212$.

for $\omega \ll T_K$.

8.3.2. Entropy and Green functions

In Ref. [166] the following estimate was given for the Kondo temperature in a square lattice system:

$$T_K \sim \sqrt{|J|} e^{-1/\sqrt{|bJ|}}, \tag{8.14}$$

where b is a constant on the order of the inverse bandwidth D^{-1}. From this, the low-temperature behavior of the impurity entropy could be derived and was found to be

$$S_{\mathrm{imp}}(T) = -\frac{a}{|\ln(T/D)|^{\delta}}, \tag{8.15}$$

with constants a and δ on the order of 1. The overcompensation of the dynamic screening leads to negative values in the impurity entropy as $T \to 0$, where logarithmically approaches zero upon further lowering the temperature [166,168,169]. Of course, this results holds for the impurity contribution to the entropy, and the entropy of the entire system is always non-negative. In Fig. 8.3 we show results from our NRG calculations for the impurity entropy as a function of temperature for three different parameter sets. Comparing with the flat band model results in Fig. 2.2, we find that all three fixed points of the Anderson impurity model are present and one can observe the change of T_K upon varying the impurity parameters. In the inset, a fit of Eqn. (8.15) to the low-temperature behavior is shown. The fit parameters were obtained to be $a = 1.25622$ and $\delta = 0.980212$.

Fig. 8.4 shows results for an impurity Green function. We recover the two Hubbard satellites at high energies, and see a narrow sharp resonance around the Fermi level.

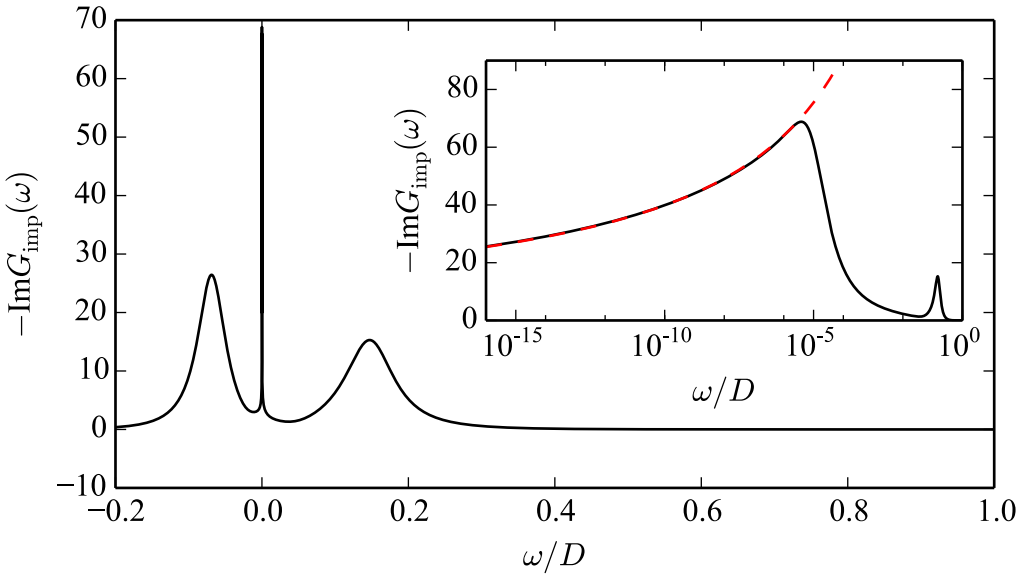

Figure 8.4.: Bottom panel: Negative imaginary part of the impurity Green function. The inset shows the logarithmic decay as $\omega \to 0$. The data was calculated for an Anderson impurity with parameters $\epsilon_f/D = 0.07$, $U/D = 0.22$ and $V/D = 0.04$.

As shown in the inset, this resonance builds up as $\omega \sim T_K$, but for $\omega \ll T_K$ decays logarithmically like

$$-\operatorname{Im} G_{\mathrm{imp}}(\omega) \overset{\omega\to 0}{\sim} \frac{1}{\log|D/\omega|}. \tag{8.16}$$

8.4. Shape of the screening cloud

In the 2D free electron gas, Friedel oscillations induced by a potential scatterer fall off radially with $\Delta n(r) \sim r^{-2}$ [14]. As discussed above, this anisotropy is broken in the square lattice and, at half filling, the flat areas of the Fermi surface lead to four discrete directions of maximum electron transport (Fig. 8.1), and accordingly, charge density oscillations are strongest along the lattice diagonals. Since a charge surplus on one site leads to a charge deficit on its four neighboring sites, the excess charge densities induced by a localized potential are thus always of the same sign when going along the lattice diagonally. In the case of a 1D chain discussed in Sec. 7.3, the excess charge densities oscillate symmetrically around zero, $\Delta n^{1D}(r) \sim (-1)^r/r$, with a changing envelope function of the oscillations as the system flows from the free orbital (FO) to local moment (LM), and from LM to the strong coupling (SC) fixed points.

In Fig. 8.5 we plot the absolute value of the charge density oscillations on a logarithmic scale. This difference decays smoothly and monotonously if the impurity is not correlated ($U = 0$) and thus only a potential scatterer. However, as soon as strong correlations on the impurity are present and the system flows to the SC fixed point, the oscillations change at specific distances from the impurity. Similar to Fig. 7.11, the data plotted in Fig. 8.5 has a *minimum* at the point where the oscillations change, which can be seen clearly as a dark line with a characteristic shape. Following the arguments given in Sec. 7.3 and the general notion of a correspondence between RG flow in inverse frequency space and real-space, the area enclosed by the minimum can be associated with the LM

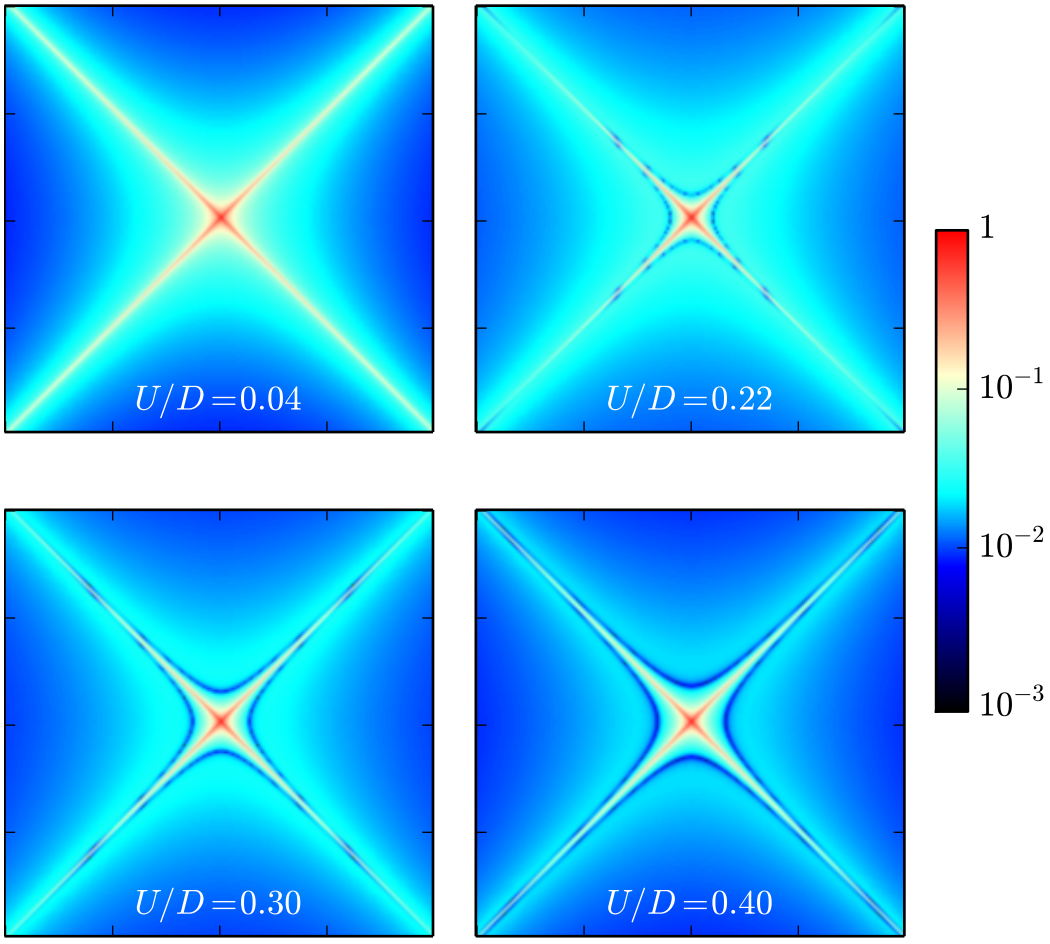

Figure 8.5.: Charge density oscillations in the square lattice. The Anderson impurity with parameters $\epsilon_f/D = -0.07$, $V/D = 0.04$ is coupling to the site in the center. Shown here are the logarithms of the absolute value of the charge density oscillations, $\log|\Delta n(\mathbf{r})|$. The dark line shows a minimum, which indicates the point where the oscillations change sign.

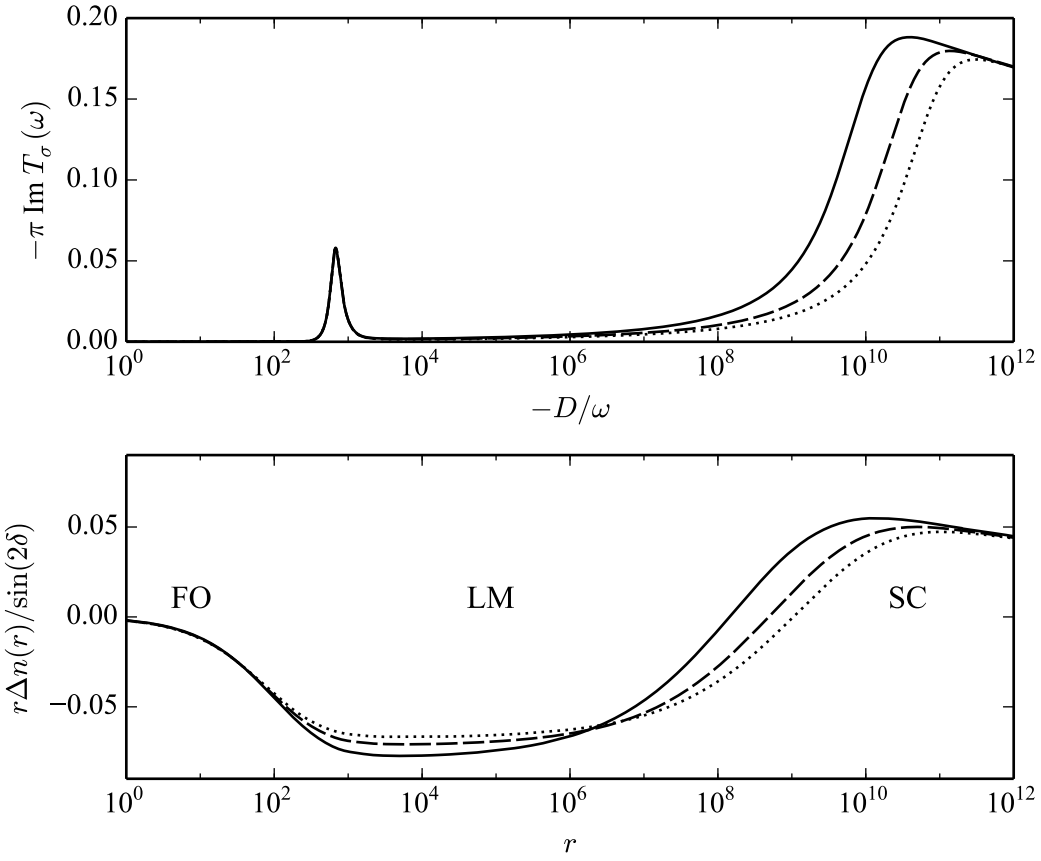

Figure 8.6.: Comparison of the spectrum vs. inverse frequency (upper panel) and the excess charge density vs. distance (lower panel) for the $T = 0$ Anderson model not the square lattice. The density oscillations are taken along the lattice diagonal. Parameters of the Anderson model are $V/D = 3 \times 10^{-3}$, $\epsilon_f/D = -1.5 \times 10^{-3}$, and varying $U/D = 6 \times 10^{-3}, 5 \times 10^{-3}, 4 \times 10^{-3}$ (dotted, dashed, solid lines). The RG fixed points describing the different regions are given as free orbital (FO), local moment (LM) and strong coupling (SC). Furthermore, the density oscillations have been normalized by the pure potential scattering contribution at long distances, $\sin(2\delta)$ with the scattering phase shift δ.

fixed point, whereas on the outside of it the system has reached the SC fixed point.

As expected, the strong electron focussing due to the flat edges of the Fermi surface (see Sec. 8.1) leads to the charge density oscillations being strongest along the lattice diagonals, where they are about an order of magnitude larger than in the directions of the x- or y-axis. Furthermore, the fact that the regions away from the diagonals contribute only very little to the screening of the impurity, the distance at which the crossover occurs does not follow the exponential growth which is found along the diagonals (see below).

8.5. RG flow in real space along lattice diagonals

Having established the real-space shape of the crossover from regions of weak to strong-coupling on the square lattice, we now turn to examining further the charge density oscillations along the lattice diagonals, using the iterative method described in Sec. 8.2.2. We can carry out this calculation to a much higher accuracy, and Fig. 8.6 shows our main result: In direct analogy to the 1D case discussed in Sec. 7.3, the full RG flow is contained

in the Friedel oscillations away from the impurity. Since frequency and distance are related by $r \sim \omega^{-1}$, we again plot in the upper panel the negative imaginary part of the $\mathcal{T}$-matrix as a function of *inverse* negative frequency. This way we can, as before, associate the relevant energy scales to a length scale.

We have found that, contrary to the isotropic case, the Friedel oscillations along the diagonal do *not* fall off as $1/r^2$, but rather $1/r$ with logarithmic corrections. The lower panel shows the Friedel oscillations divided by $1/r$. The crossovers between the different regions is clearly visible, furthermore we find a clear correspondence to the change in energy scales in the upper panel. Whereas for the full lattice we have previously established the existence of a crossover from local moment to strong coupling fixed point, these results show that the whole RG flow is reproduced.

We find that, as long as the the convolution method is computationally sensible, both methods produce the same results along the diagonals.

8.6. Summary

We have used two different exact methods for the calculations of lattice Green functions on the square lattice. From these Green functions, using the NRG to solve the impurity problem, we obtained the static charge density oscillations induced by an Anderson impurity side-coupled to the lattice. Similar to the 1D case discussed in the previous chapter, we recover the entire RG flow, including all three fixed points of the model. While previous analytical calculations have considered results for the free electron gas [15], we here investigated specifically the influence of the square lattice geometry. For one, the logarithmic divergence of the density of states at the Fermi energy directly influences the quantities under considerations: both the impurity entropy and the impurity spectral function exhibit logarithmic corrections at low energies. However, the most prominent effect of the lattice geometry is surely the electron focusing due to the flat edges of the Fermi surface: the directions of electronic transport—and therefore the charge density oscillations—are strongly centered along the diagonal lattice directions away from the impurity. Along these directions, we find that the envelope function of the oscillations changes for each fixed point, in direct correspondence with the 1D results.

Part IV.

Kondo and Majorana interactions in quantum dots

Chapter 9.

Majorana zero modes in quantum wires

The realization of a quantum computer is one of the great goals in modern science, bringing together researchers from fields such as engineering, computer science, theoretical and experimental physics. The computational power of qubits living in a quantum mechanical Hilbert space far exceeds that of any classical device [170]. However, constructing a quantum computation device is far from trivial, and thus far only very basic operations could be performed successfully [171, 172]. One of the main challenges is to avoid the decoherence, i.e. destruction, of a finely tuned quantum state by external influences. A lot of research has therefore gone into the study of fault-tolerant quantum computation [173]. It was suggested by A. Kitaev in Ref. [174] that a topologically ordered state can serve as physical analog of an error-correcting quantum code, opening up the field of *topological quantum computers*.

Consider two particles moving around each other so as to interchange their positions. This procedure leads to a multiplication of the overall quantum state by $e^{i\phi}$. In three dimensions, the process of moving a particle the whole way around another one (i.e. exchanging both particles twice) can be *continuously* deformed into a process where no exchange takes place. This means that in three dimensions, only one topological distinct way of swapping the particles exists. Two swaps are identical to no swap and the phase must be $e^{i\phi} = \pm 1$ [31]. In two dimensions, however, this exchange is topologically non-trivial and the phase can take on any rational multiple of 2π. The process of moving many such particles around each other in non-trivial ways is called *braiding*. If the order of the braiding operations matter, the anyons are called *non-abelian*, whereas in the other case they are *abelian*. In Ref. [175] it was proved that by braiding certain types of non-abelian anyons, universal quantum computation can be performed. Furthermore, the topological underpinnings of anyons provide a realization of a quantum memory that is protected from decoherence. This topological rigidity of anyons makes topological quantum computing one of the key candidates in the realization of a robust quantum computer.

An example of anyonic particles is given by Majorana bound states (MBS), where Majorana fermions are bound to some form of localized defect, e.g. a vortex core in a superconductor or the ends of a finite 1D wire. In fact, while MBS are intriguing even from a purely conceptual point of view, their possible application in quantum computation has played a big role in the recent quest for their detection. In this chapter, we introduce Kitaev's Majorana quantum wire, a "simple but rather unrealistic" [7] model exhibiting unpaired and spatially well-separated Majorana fermions, bound to the wire's ends. These MBS are robust and, in principle, could be manipulated to perform the braiding operations discussed above. Although originally a toy model, it turned out that a realization was possible, which we discuss in the end of this chapter. In the next chapter, we consider possible effects of quantum dots that might form naturally in realistic setups.

9.1. Kitaev's superconducting wire

In the quest for fault-tolerant quantum devices, A. Kitaev presented [7] a toy model of a one-dimensional system in which spatially separated, localized Majorana fermions occur naturally. These Majorana zero modes are decoherence-protected (since they are located far apart from each other) and could be used to engineer a reliable quantum memory device [7]. Consider the following superconducting system of spinless (or, equivalently, spin-polarized) fermions on a chain consisting of $L \gg 1$ sites. The system's tight-binding Hamiltonian is given by

$$H = \sum_{j=1}^{N} \left(-t c_j^\dagger c_{j+1} + \Delta c_j c_{j+1} + \text{H.c.} \right) - \mu \sum_{j=1}^{N} \left(c_j^\dagger c_j - \frac{1}{2} \right), \tag{9.1}$$

where t is the hopping amplitude, μ the chemical potential and Δ the superconducting gap. The operator c_i annihilates a spinless fermion at lattice site i. In Sec. 2.3 we have introduced Majorana fermions and shown how one Dirac fermion c_i can be split into a linear combination of two Majorana modes $\gamma_{i,1}$ and $\gamma_{i,2}$. Rewriting Eq. (9.1) in terms of these Majorana operators yields

$$H = \frac{i}{4} \left[-\sum_{j=1}^{N} \mu \gamma_{j,1} \gamma_{j,2} + \sum_{j=1}^{N-1} \left((\Delta + t) \gamma_{j,2} \gamma_{j+1,1} + (\Delta - t) \gamma_{j,1} \gamma_{j+1,2} \right) \right]. \tag{9.2}$$

Let us now consider two special cases. In the absence of superconductivity and hopping, $t = \Delta = 0$, the Hamiltonian reduces to

$$H = -\frac{i\mu}{4} \sum_{j=1}^{N} \gamma_{j,1} \gamma_{j,2}. \tag{9.3}$$

In this case, the two Majorana modes on each sites are paired up together. This is shown schematically in Fig. 9.1(a). In the second scenario, both superconducting and hopping terms are present, for simplicity we set $\Delta = t > 0$, and the chemical potential is $\mu = 0$. Then, the Hamiltonian takes on the form

$$H = \frac{it}{2} \sum_{j=1}^{N-1} \gamma_{j,2} \gamma_{j+1,1}. \tag{9.4}$$

Majoranas from *different* sites are paired together. Remarkably, the two Majorana modes at the end of the chain, $\gamma_{1,1}$ and $\gamma_{N,2}$, have entirely dropped out of the Hamiltonian! Simply put, there is no energy cost associated with the two modes, thus they occur at zero energy. Furthermore, even if $\mu \neq 0$ but $|\mu| < 2t$ and $\Delta \neq 0$, these boundary modes exist [7]. They are spatially separated and their overlap is exponentially small in system size, making them robust against perturbations.

9.2. A more realistic model: Topological superconductors

Kitaev's Majorana wire from the previous section is thus far a mere theoretical construct. However, various suggestions for experimental realization have since been put forth, the most promising ones are given by a one-dimensional heterostructure of a superconduc-

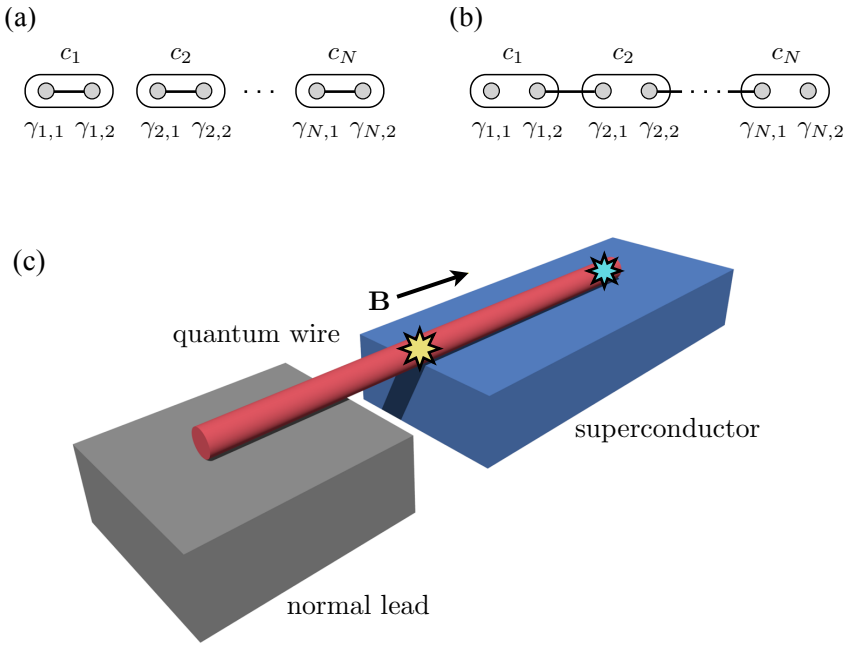

Figure 9.1.: (a) Kitaev's wire in the limiting case where Majorana fermions are paired up on each site. The bigger white shapes depict the Dirac fermions described by the operators c_j, whereas the small gray circles show the Majorana fermions, described by operators $\gamma_{j,n}$, $n = 1, 2$. Each Dirac fermion is composed of two Majoranas. (b) The same system in the opposing limit. Majoranas belonging to different sites pair up, leaving two unpaired Majorana modes at the two ends of the chain. (c) Experimental setup in the realization of Kitaev's quantum wire. The wire is placed on top of a superconductor and upon application of a magnetic field $\mathbf{B}$, Majorana edge states form, depicted by the two stars.

tor and a semiconductor [176–178]. In these structures, a semiconducting quantum wire with strong spin-orbit coupling is resting on a superconductor. Due to the close proximity of the two, the wire inherits a superconducting pairing mechanism. Upon application of an external magnetic field, this system can be driven into a so-called topological phase which effectively realizes Kitaev's system introduced above [179]. Recently, such a setup has famously been realized in experiment [16], in which transport measurements have indeed shown a conductance peak at the Fermi energy, strongly suggesting the experimental discovery of Majorana modes. The experimental setup is schematically shown in Fig. 9.1(c). The quantum wire is on top of the superconductor, and also connected to a normal metal lead. The stars indicate the expected position of the Majorana fermions [16].

We now closely follow Ref. [180] in presenting the model. Consider a one-dimensional semiconducting wire with spin-orbit coupling of strength α and an orthogonal magnetic field B_z. The proximity effect with a neighboring bulk superconductor induces an s-wave pairing field Δ in the wire. We furthermore include a local Coulomb interaction between

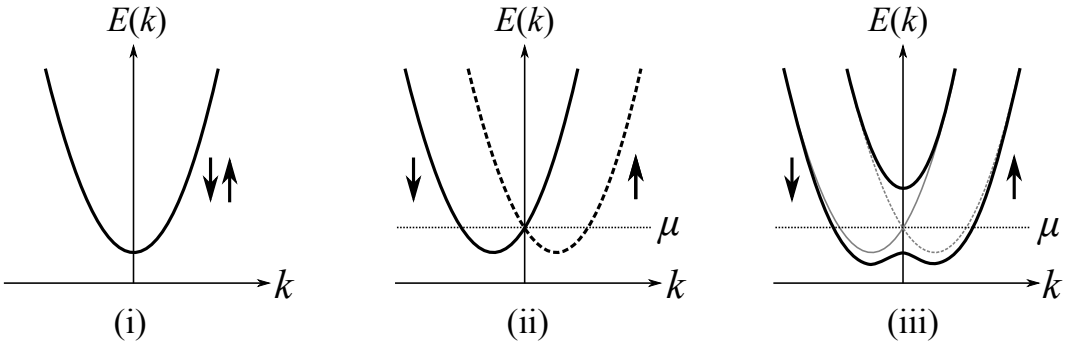

Figure 9.2.: Dispersion relations for various parameter regimes of the Hamiltonian in Eq. (9.5). For an explanation see the main text.

the electrons, leading to the following Hamiltonian:

$$\begin{aligned} H_{\mathrm{TSC}} = &- \sum_{j=0}^{N-1} \sum_{\sigma\sigma'} \frac{1}{2} \left(t\, c^\dagger_{j\sigma} c_{j+1\sigma} \delta_{\sigma,\sigma'} + \alpha\, c^\dagger_{j\sigma} i\sigma^y_{\sigma\sigma'} c_{j+1\sigma'} + \mathrm{H.c.} \right) \\ &+ \sum_{j=0}^{N} \sum_{\sigma,\sigma'} \Big[(t-\mu)\, c^\dagger_{j\sigma} c_{j\sigma} \delta_{\sigma\sigma'} + B_z c^\dagger_{j\sigma} \sigma^z_{\sigma\sigma'} c_{j\sigma'} \Big] \\ &+ \sum_{j=0}^{N} \Big[\Delta \left(c_{j\uparrow} c_{j\downarrow} + \mathrm{H.c.} \right) + U \hat{n}_{j\uparrow} \hat{n}_{j\downarrow} \Big], \end{aligned} \tag{9.5}$$

where σ^i is the ith Pauli matrix and $\hat{n}_{i\sigma} = c^\dagger_{i\sigma} c_{i\sigma}$ counts the spin-σ fermions at site i. To understand how this Hamiltonian leads to the appearance of Majorana modes, we now start with its simplest form and step by step include more terms and discuss their effects. The corresponding dispersion relations are shown in Fig. 9.2.

(i) Consider first the time-reversal invariant noninteracting limit where $\alpha = \Delta = B_z = U = 0$. In this case, the Hamiltonian describes free spinful fermions in a 1D wire with a hopping amplitude t and chemical potential μ. Its dispersion relation around the Fermi points is given by a parabola $\varepsilon_k \sim k^2$, as shown in Fig. 9.2(i).

(ii) Introducing spin-orbit coupling into the system, $\alpha > 0$, splits the dispersion relation into two parabolas, one for each spin alignment, see Fig. 9.2(ii). The spin-orbit coupling term favors aligning the spins along or against the y direction, depending on their momentum. In Fig. 9.2(ii), "right-moving" electrons with positive momentum will align their spins along the positive y-axis, whereas the spins of the "left-moving" electrons will align along the negative y-axis.

(iii) Turning on the magnetic field $B_z \neq 0$ changes the system crucially by canting the spins along the z-direction. This effectively couples the different spin-bands and, as shown by the two bold lines in Fig. 9.2(iii), opens up a gap at $k = 0$. We now have a finite region of the chemical potential μ (when μ is within the gap) in which the system only has two Fermi points and can thus effectively be viewed as a system of *spinless* fermions.

The system at this point connects smoothly to Kitaev's spinless fermions in Eq. (9.1). As discussed in the previous section, turning on a weak pairing field Δ couples electrons

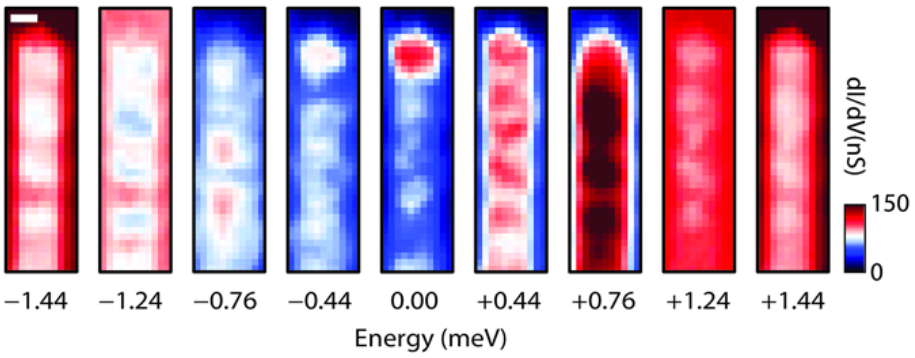

Figure 9.3.: Spatial and energy-resolved conductance maps of a Fe atomic chain close to its end. The conductance map at zero bias (middle panel) shows an increased conductance close to the end of the chain, indicating the existence of a Majorana quasi-particle mode. Figure taken from Ref. [181].

of opposite momentum, driving the system into a topologically superconducting phase. Thus, we obtain an experimental realization of Kitaev's Majorana quantum wire.

A quantitative analysis [178] shows that the topological superconducting state exists for parameter ranges

$$\begin{aligned} B_z &> 0, \\ -\sqrt{B_z^2 - \Delta^2} < \mu &< \sqrt{B_z^2 - \Delta}, \end{aligned} \tag{9.6}$$

as only in this regime the system maps to the spinless system in Eq. (9.1). So far we have not taken interactions between the electrons into account, $U = 0$. In Ref. [180] it was shown that the inclusion of a finite Coulomb interaction, $U > 0$, essentially leads to two important effects: The superconducting pairing is suppressed and hence the bulk gap protecting the topological phase decreases. This in turn leads to an increase in the localization length of the Majorana fermions, which is *per se* undesirable from an experimental standpoint. On the other hand, interactions increase the magnetization of the wire, leading to significant broadening of the chemical potential window in which the system connects to Kitaev's model, making the model somewhat more robust against perturbations and disorder.

In conclusion, within the right parameter regime, the system in Eq. (9.5) can be effectively described by Eq. (9.2). Interactions in the wire do not destroy these physics, but rather stabilize them against disorder. Hence, in a finite system with open boundary conditions, such systems exhibit exponentially localized Majorana modes at the left and right ends.

9.2.1. Experimental results

In 2012, the group around L. Kouwenhoven at TU Delft for the first time reported the observation of a zero-bias peak in transport measurements performed on the setup presented in the previous section [16]. This result was widely regarded as an answer to the question whether Majorana zero modes do exist [182], although such a conductance peak could also have been caused by the Kondo effect or disorder in the wire. Furthermore, very recently measurements in a mathematically related, yet experimentally somewhat different setup were performed [181]. There, ferromagnetic iron (Fe) atomic chains were placed on the surface of a superconducting lead. The onset of superconductivity was

accompanied by peaks in the conductance, which could be spatially resolved and were shown to appear at the ends of the wires. Part of their data is shown in Fig. 9.3, clearly showing a conductance peak forming close to the edge of the one-dimensional wire at zero bias. This experiment thus provides further evidence that Majorana modes do indeed form in such quantum wire setups.

Chapter 10.

Majorana fermions vs. the Kondo effect

A key observation in the experimental realizations of the model presented in the previous chapter was the observation of a zero-bias conductance peak at the end of the quantum wire. However, in the experimental setup used in Ref. [16] a setup as shown in Fig. 9.1(c) was used. Noteably, the confined region between the normal lead and the superconductor might lead to the formation of a quantum dot [16, 183–185]. In this case, such a quantum dot could host a single spin degree of freedom and eventually lead to a possible occurrence of the Kondo effect, see Sec. 2.1. A competition between the superconducting proximity effect and Kondo correlations has been shown to also lead to a zero-bias conductance peak [186,187] for certain values of the magnetic field in the setup. Therefore, it is crucial to understand the competition of Kondo and Majorana physics in this system in order to clearly distinguish the possible origins of such zero-bias peaks. In this Chapter, we investigate such a situation theoretically by considering a quantum dot coupled to a generally interacting lead on the one side, and a Majorana mode on the other side, as shown in Fig. 10.1.

10.1. The model

First we present our theoretical model. We consider a nanostructure comprised of a fermionic degree of freedom localized on a quantum dot. This local moment couples to an SU(2)-invariant, one-dimensional lead consisting of interacting fermions and to a Majorana mode in a topological superconductor, the setup is sketched in Fig. 10.1. Since we are interested in the low-energy physics, we can focus on the regime of a singly-occupied quantum dot, yielding an effective spin-$\frac{1}{2}$ degree of freedom. Furthermore, with energies well below the superconducting gap Δ, we do not need to incorporate the full topological superconductor. Instead, it suffices to effectively consider only the two Majorana modes γ_1 and γ_2, localized at its ends. The full Hamiltonian is then given by

$$H = H_{\mathrm{NM}} + H_{\mathrm{QD}} + H_{\mathrm{NM-QD}} + H_{\mathrm{TSC-QD}}. \tag{10.1}$$

The fermions in the lead are described in a tight-binding approximation with a hopping amplitude t and Coulomb interaction U_b by

$$H_{\mathrm{NM}} = -t \sum_{i,\sigma} \left(c^\dagger_{i\sigma} c_{i+1\sigma} + \mathrm{H.c.} \right) + U_b \sum_i \hat{n}_{i\uparrow} \hat{n}_{i\downarrow}, \tag{10.2}$$

where $\hat{n}_{i\sigma} = c^\dagger_{i\sigma} c_{i\sigma}$ counts the spin-σ fermions at site i. The quantum dot and its coupling to the lead are modeled by the single-impurity Anderson model, Eqs. (2.3) and (2.4), where the Hamiltonian for the isolated dot (i.e. the impurity) is

$$H_{\mathrm{QD}} = \epsilon_f \hat{n}_f + U \hat{n}_{f\uparrow} \hat{n}_{f\downarrow}, \tag{10.3}$$

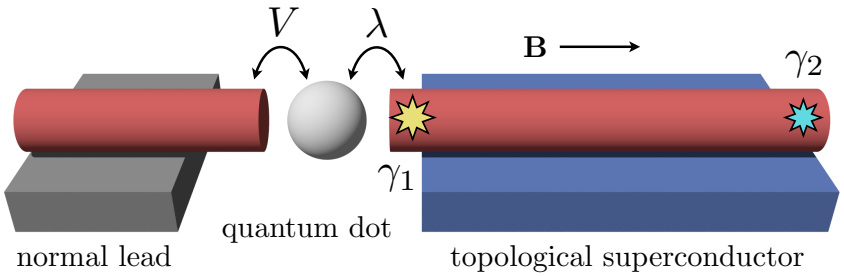

Figure 10.1.: The setup for our model: A normal metal lead is coupled to a quantum dot via a hopping V. On the other end, this quantum dot couples via a hopping λ to a topological superconductor, which hosts two Majorana zero modes at either end (γ_1 and γ_2). This setup is obtained from the one in Fig. 9.1 after including a quantum dot between lead and Majorana mode.

where the operator $f_\sigma^\dagger$ creates a spin-σ fermion on the quantum dot and $\hat{n}_f = f_\sigma^\dagger f_\sigma$. The quantum dot couples to the site at $i = 0$ in the lead by with a hopping V:

$$H_{\mathrm{NM-QD}} = V \sum_\sigma \left(f_\sigma^\dagger c_{0\sigma} + c_{0\sigma}^\dagger f_\sigma \right). \tag{10.4}$$

We assume the length of the superconductor to be much greater than the coherence length of the Majorana modes, ξ. The coupling between quantum dot and the Majorana mode at the far end of the superconductor of length L is exponential small in L/ξ, see Sec. 9.1, and we thus neglect it here. Hence, the tunneling between the dot and the Majorana mode γ_1 is given by

$$H_{\mathrm{TSC-QD}} = i\lambda\gamma_1 \left(f_\uparrow + f_\uparrow^\dagger \right), \tag{10.5}$$

with the hopping amplitude λ. The Majorana mode at the end of the TSC is spin-polarized [188], and we thus model here an interaction only with one spin-species on the quantum dot.

10.1.1. Low-energy effective theory for the quantum dot

In Sec. 2.1.2 we discussed that an effective low-energy theory of the single-impurity Anderson model is obtained by projecting out states in which the impurity is empty or doubly occupied by means of the Schrieffer-Wolff transformation. In the standard case this leads to the Kondo model. In our system, however, we have to take into account the coupling to the Majorana mode. After performing the transformation [189], the effective low-energy Hamiltonian for our setup is given as

$$H = H_{\mathrm{NL}} + H_{\mathrm{B}}, \tag{10.6}$$

with H_{NL} given in Eq. (10.16) and the boundary Hamiltonian H_B given by

$$\begin{aligned} H_B = &- |\lambda|^2 \xi_- S^z + |V|^2 \xi_+ \, \mathbf{S}_f \cdot \mathbf{s}_0 \\ &+ i\lambda|V|\gamma_1 \left[\left(c_{0\uparrow} + c_{0\uparrow}^\dagger \right) \left(\frac{\xi_-}{2} + \xi_+ S^z \right) + \xi_+ \left(c_{0\downarrow}^\dagger S^+ + c_{0\downarrow} S^- \right) \right], \end{aligned} \tag{10.7}$$

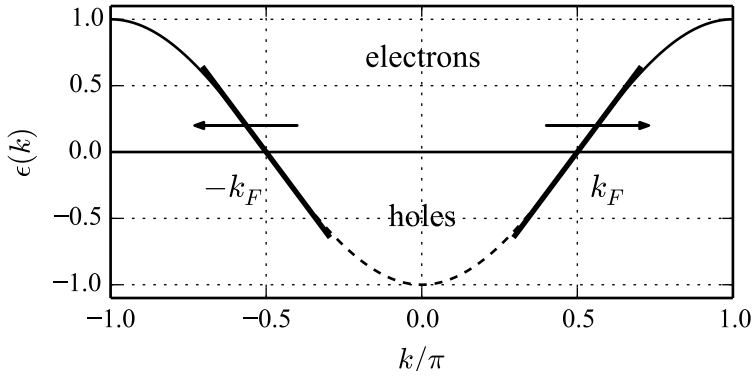

Figure 10.2.: Separation into left- and right-movers in the bosonization scheme. The dispersion relation is approximated linearly around the Fermi points k_F, for which $\epsilon(k_F) = \epsilon_F$. The modes with positive momentum, $k > 0$, are the right-movers and those with negative momentum, $k < 0$, are the left-movers.

Furthermore,

$$\mathbf{s}_x = \frac{1}{2} \sum_{\sigma\sigma'} c^\dagger_{x\sigma} \boldsymbol{\sigma}_{\sigma\sigma'} c_{x\sigma'} \tag{10.8}$$

is the spin operator at position x in the lead, $\mathbf{S}_f$ is the spin operator on the quantum dot, and we defined

$$\xi_\pm = \frac{1}{|\epsilon_f|} \pm \frac{1}{U - |\epsilon_f|}. \tag{10.9}$$

The first term in Eq. (10.7) describes an effective magnetic field acting on the quantum dot spin which is generated by virtual hopping of electrons from the topological superconductor to the quantum dot. The second term is the standard Kondo interaction between the lead and the dot. Finally, the third term is generated by processes in which an electron tunnels between the lead and the superconductor via a virtual state on the dot. We discuss the general case in Sec. 10.3 and the particle-hole symmetric model, $\epsilon_f = -U/2$, in Sec. 10.4.

10.2. Bosonization of the model

In order to carry out an RG analysis of our effective model, we use a bosonized version of the Hamiltonian, treating it as a Luttinger-Tomonaga liquid. In this formulation, by analyzing the various boundary conditions we can identify the low-energy fixed points of the effective model.

The Luttinger liquid approach is a powerful method to describe interacting Fermions in one-dimensional systems [190–192]. It was proposed by Tomonaga in 1950 and is based on the insight that, in one-dimensional systems, the relevant degrees of freedom are given by collective density waves rather than single particle excitations. The reason for this lies in the fact that moving fermions in one dimension cannot avoid each other and inevitably momentum is transferred to neighboring particles—a crucial difference to higher dimensional systems. This transfer of energy eventually leads to the emergence of collective bosonic density-wave degrees of freedom. Importantly, these collective excitations turn out to appear independently in the spin and charge channels, leading to the famous phenomenon of spin-charge separation [193], which was directly observed in experiment for the first time in 1996 [194].

In the Luttinger liquid approach, one commonly approximates the dispersion relation of the particles close to the Fermi energy, and then relates the single-particle creation and annihilation operators to string operators corresponding to the relevant charge and spin degrees of freedom. Linearizing the dispersion relation $\epsilon(k)$ around the Fermi points at k_F, see Fig. 10.2, yields

$$\epsilon(k) = \sum_{k\approx k_F} v_F(k + k_F) + \sum_{k\approx k_F} v_F(k - k_F), \tag{10.10}$$

where the Fermi velocity is given by $v_F = k_F/m_e$. The modes close to $-k_F$ are called left movers, and the ones close to k_F are called right movers, referring to the direction in which they propagate. By linearizing the model around the Fermi points, we implicitly focus on the physics on large length-scales, and it is thus reasonable to take the continuum limit also in the operators, viz.

$$c_{i,\sigma} \to \psi_\sigma(x). \tag{10.11}$$

In the spirit of the discussion above, one introduces bosonic fields for spin $\phi_{\uparrow/\downarrow}$ and charge $\theta_{\uparrow/\downarrow}$, from which we can construct the following fields

$$\begin{aligned}
\phi_\rho(x) &= \phi_\uparrow(x) + \phi_\downarrow(x) && \text{(charge density)}\\
\theta_\rho(x) &= \theta_\uparrow(x) + \theta_\downarrow(x) && \text{(charge current)}\\
\\
\phi_\sigma(x) &= \phi_\uparrow(x) - \phi_\downarrow(x) && \text{(spin density)}\\
\theta_\sigma(x) &= \theta_\uparrow(x) - \theta_\downarrow(x), && \text{(spin current)}
\end{aligned}$$

where the indices on the left refer to the spin fields (σ) and charge fields (ρ). To avoid unnecessary confusion, in this chapter we henceforth denote spin-indices by $s = \uparrow, \downarrow$ instead of σ. With these fields, we can express the fermionic annihilation operators for left- and right-moving particles in the continuum limit as [190]

$$\psi_{rs}(x) = \Gamma_{rs}\frac{1}{\sqrt{2\pi a}}\exp\left(-\frac{i}{\sqrt{2}}\left[(r\,\phi_\rho(x) - \theta_\rho(x)) + s\,(r\,\phi_\sigma(x) - \theta_\sigma(x))\right]\right), \tag{10.12}$$

with $r = \pm 1$ for right-/left-moving fermions and $s = \pm 1$ for spin $\uparrow/\downarrow$ respectively. Γ_{rs} is a factor preserving the correct commutation relations and a is the ultraviolet cut-off of the theory, given e.g. by the interatomic spacing. With these new operator definitions, the Hamiltonian can now be formulated entirely in terms of the two fields ϕ and θ. The interactions between particles are captured in the important Luttinger parameter K_ρ for the spin sector and K_ρ for the charge sector, where for each sector [133, 190]

$$K_\rho < 1, \quad K_\sigma > 1: \quad \text{repulsive interaction,} \tag{10.13}$$
$$K_\rho = 1, \quad K_\sigma = 1: \quad \text{no interaction,} \tag{10.14}$$
$$K_\rho > 1, \quad K_\sigma < 1: \quad \text{attractive interaction.} \tag{10.15}$$

With these operators, the bosonized lead Hamiltonian can then be expressed as a spinful Luttinger liquid in terms of the bosonic fields introduced above as

$$H_{\mathrm{NL}} = \sum_{\eta=\sigma,\rho}\frac{v_\eta}{2\pi}\int_0^\infty \mathrm{d}x\,\left[K_\eta\,(\nabla\theta_\eta)^2 + \frac{1}{K_\eta}\,(\nabla\phi_\eta)^2\right], \tag{10.16}$$

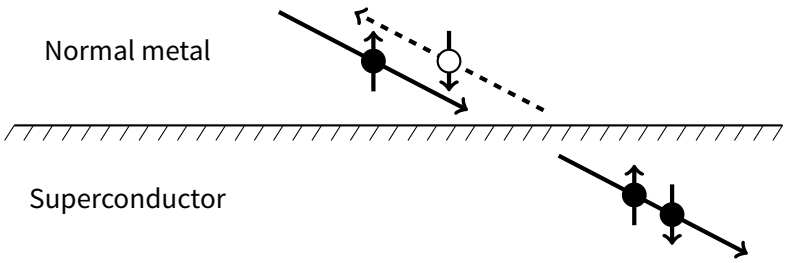

Figure 10.3.: Andreev reflection: At the boundary between a normal metal and a superconductor an incident spin-↑ electron creates a Cooper pair in the superconductor and a spin-↓ hole which is scattered back into the normal metal.

where $v_{\sigma/\rho}$ is the velocity for charge and spin modes, respectively.

10.2.1. Andreev reflection

We have formulated our setup as a boundary problem for a 1D wire. To this end, it is crucial to understand the nature of the various boundary conditions that might occur in the model. At this point we briefly sketch the physics of *Andreev reflection*, which will be used throughout the remainder of this chapter.

Let us consider the junction of a normal lead metal to a (topological) superconductor. Our focus lies on electrons with energies E traveling through a metallic system connected to the superconductor, occupying the half-plane with $y < 0$, see Fig. 10.3. The superconducting gap, below which no states can be formed, is $\Delta > 0$. What happens when the electrons hit the boundary of the superconductor? Naively one would expect that if the incident electrons have energies $E < \Delta$, they are backscattered into the metal since they lack the energy to break-up a Cooper pair. However, in 1964 Andreev showed [195] that something very different happens: Assume an incident spin-↑ electron. At the boundary to the superconductor this electron with wave vector $\mathbf{k}$ is scattered into a spin-↓ *hole*, with wave vector $-\mathbf{k}$, see Fig. 10.3. The incoming electron forms a Cooper pair in the superconductor, with the second required spin-↓ electron taken from the metal. This process does not violate time-reversal symmetry and thus the same can happen with an incident hole, scattering back an electron into the metal.

10.2.2. Boundary conditions of the effective model

Before examining the interplay of the Kondo and Majorana couplings, we now give a qualitative picture of the nature of the competing interactions and their corresponding boundary conditions in the system.

Coupling to the lead: In the limit of a vanishing Majorana coupling, $\lambda \to 0$, the full Hamiltonian reduces to that of the standard Kondo model. In this case, the ground state is described by the strong-coupling Kondo fixed point including the singlet formation discussed in Sec. 2.1. In terms of the boundary conditions for lead electrons, a phase shift is induced so that at the boundary

$$\psi_{R\sigma}(0) = e^{2i\eta_0}\psi_{L\sigma}(0), \tag{10.17}$$

with the scattering phase shift η_0 which depends on the potential at the boundary and is given by $\eta_0 = \pi/2$ in the particle-hole symmetric limit [196].

Coupling to the Majorana mode: The Majorana coupling λ, on the other hand, favors the formation of an entangled state with the fermion parity (even or odd number) in the lead. We describe this state in more detail when discussing the particle-hole symmetric model, see Sec. 10.4. In the absence of the quantum dot, such a system is characterized by a perfect Andreev reflection fixed point with boundary conditions

$$\psi_{R\sigma}(0) = \psi^\dagger_{L\sigma}(0), \tag{10.18}$$

which describes the phenomenon of a right-moving electron being scattered into a left-moving hole at the boundary (see above).

The difference in the boundary conditions clearly shows that the two essential couplings in our system (Kondo vs. Majorana) compete and, individually, drive the system to different fixed points.

10.3. Renormalization group analysis and numerical results

Having formulated the model in a field-theoretical description, we can now employ a renormalization group (RG) analysis to identify the low-energy fixed points of the system boundary. We can identify four couplings from Eq. (10.7) which appear in the RG equations:

$$\begin{aligned} h(0) &= -|\lambda|^2\xi_- && \text{(Zeeman field)} \\ J_{1,2}(0) &= \lambda|V|\xi_\mp && \text{(Majorana)} \\ J_3(0) &= |V|^2\xi_+. && \text{(Kondo)} \end{aligned}$$

We henceforth assume the electrons in the lead to have SU(2) symmetry, which means that the Luttinger parameter in the spin sector is $K_\sigma = 1$. The RG equations up to quadratic order are then given by

$$\frac{\mathrm{d}h(\ell)}{\mathrm{d}\ell} = h(\ell) - \frac{J_1(\ell)J_2(\ell)}{4\pi v_\sigma}\left(1+\frac{1}{K_\rho}\right) \tag{10.19a}$$

$$\frac{\mathrm{d}J_1(\ell)}{\mathrm{d}\ell} = \left(\frac{3}{4}-\frac{1}{4K_\rho}\right)J_1(\ell) \tag{10.19b}$$

$$\frac{\mathrm{d}J_2(\ell)}{\mathrm{d}\ell} = \left(\frac{3}{4}-\frac{1}{4K_\rho}\right)J_2(\ell) - \frac{J_2(\ell)J_3(\ell)}{2\pi v_\sigma} \tag{10.19c}$$

$$\frac{\mathrm{d}J_3(\ell)}{\mathrm{d}\ell} = \frac{J_3^2(\ell)}{2\pi v_\sigma}, \tag{10.19d}$$

where ℓ is the logarithmic length scale. The Zeeman operator $h(\ell)$ is relevant and leads to a polarization of the spin on the quantum dot. On the other hand, the Majorana couplings $J_1(\ell)$ and $J_2(\ell)$ are relevant if the Luttinger parameter in the charge sector is $K_\rho > \frac{1}{3}$. The Kondo coupling $J_3(\ell)$ is marginal. The competition between the Majorana and Kondo interactions appears as the second order correction $\sim J_2(\ell)J_3(\ell)$ in Eq. (10.19c) and is thus contained in the flow of the operator $J_2(\ell)$.

If the impurity-lead coupling is weak, $J_3(\ell)/(\pi v_\sigma) \ll 1$, the Majorana coupling $J_2(\ell)$ dominates the flow of the parameters and the system eventually flows to a fixed point described by the Majorana interaction rather than the Kondo interaction, and we conjecture that the same is true also for the case when the impurity is *strongly* coupled.

Characteristics of the Majorana-dominated fixed point

Let us now discuss in more detail the RG equations (10.19a)–(10.19d). The prefactor of the linear term for the Zeeman operator $h(\ell)$ is largest, and thus this operator grows strongest under the RG flow. On a given length scale ℓ^* it will become dominant, $h(\ell^*) \gg J_2(\ell^*)$; at this point the quantum dot feels an effective magnetic field and the spin will be completely polarized along the z-axis. Accordingly, the operator S^z acquires a classical expectation value and the terms containing spin raising and lowering operators $S^{\pm}$ in the boundary Hamiltonian Eq. (10.7) are strongly suppressed. The remaining term contains the coupling of spin-up electrons to the Majorana mode, $\sim i\gamma_1 \left(\psi_{0\uparrow} + \psi_{0\uparrow}^\dagger\right)$. Therefore, we can conclude that the boundary conditions of the lead are different for spin-up and spin-down electrons. Since spin-up electrons couple to the Majorana mode, the low-energy fixed point here corresponds to Andreev boundary conditions (ABC), which scatter right moving electrons into left-moving holes,

$$\psi_{R\uparrow}^\dagger(0) = \psi_{L\uparrow}(0). \tag{10.20}$$

Spin-down electrons, on the other hand, do *not* couple to the Majorana mode. They can only interact via the quantum dot through a virtual second-order spin-exchange process (remember that we have already projected the impurity down to single occupation). But since the impurity spin is strongly polarized it cannot be flipped, and a spin-down conduction electron must thus always be scattered back into a spin-down electron. This, effectively, yields "normal" boundary conditions (NBC):

$$\psi_{R\downarrow}(0) = \psi_{L\downarrow}(0). \tag{10.21}$$

We denote this fixed point as $A \otimes N$, for the Andreev reflection in the spin-up and the normal reflection in the spin-down sector, respectively.

10.3.1. Numerical results away from particle-hole symmetry

The RG analysis above relies on perturbative RG equations taken in the weak coupling limit. Therefore, strictly speaking, they are not valid at strong coupling. To examine this limit, we have performed DMRG calculations using the Hamiltonian in Eq. (10.7) to corroborate our conjecture in the strong coupling case. The fact that the systems flows to a fixed point described by the two different boundary conditions $A \otimes N$ can be seen in various static correlation functions, of which we have examined the superconducting triplet correlator, defined in the continuum limit as

$$\begin{aligned} T_\sigma(x) &= \langle \left(\psi_\sigma^\dagger(x)\, \partial_x \psi_\sigma^\dagger(x)\right) \left(\psi_\sigma(x')\, \partial_{x'} \psi_\sigma(x')\right) \rangle \Big|_{x'\to 0} \\ &\propto \langle e^{2i[\theta(x)-\theta(x')]} \rangle_{x'\to 0} \end{aligned} \tag{10.22}$$

In the bulk of the wire, this correlation function decays algebraically as [190]

$$T_\sigma(x, x') \propto |x - x'|^{-(K_\rho^{-1}+1)}. \tag{10.23}$$

Let us now discuss how this behavior is changed at the boundary, $x' \to 0$, for our boundary conditions. The behavior of the correlation function is still a power law given by

$$T_\sigma(x) \propto |x|^{d_\sigma}, \tag{10.24}$$

where the exponent d_σ depends on the spin σ. The Andreev boundary conditions for spin-up electrons lead to a strong suppression of fluctuations in the spin-up field $\theta_\uparrow$. The decay of the spin-tripled correlator must thus be slower than in the bulk, and we find

$$d_\uparrow = -\frac{1}{2}(K_\rho^{-1} + 1). \tag{10.25}$$

Accordingly, the spin-down field $\theta_\downarrow$ strongly fluctuates for the normal boundary conditions. Therefore, the decay of the spin-down correlator is stronger, leading to

$$d_\downarrow = -\frac{3}{2}(K_\rho^{-1} + 1). \tag{10.26}$$

Discretized system

For our DMRG calculations, we implement a discretized model using the tight-binding Hamiltonian Eq. (10.2) for the lead and the low-energy effective Hamiltonian Eq. (10.7) for the boundary. In a finite system, the Kondo effect depends strongly on the parity of the lead electrons, it is strongly suppressed if the number of conduction electrons in the lead is even [197]. Therefore, we always choose an odd number of sites in the lead in our simulations. We furthermore fix the lead to be at half-filling and set $U_b = 0$ to avoid certain instabilities like charge density waves or pairing instabilities. The non-interacting lead thus implies $K_\sigma = 1$.

The discretized version of the correlator in Eq. (10.22) is obtained by replacing the derivative of a fermion field with the difference in the site operators,

$$\partial_x \psi_\sigma(x) \to c_{i+1,\sigma} - c_{i,\sigma}, \tag{10.27}$$

where c_i is the annihilation operator for spin σ at site $x = x_i$. The triplet correlator then becomes

$$\begin{aligned} T_\sigma(x) \to T_\sigma(x_i) &= \langle \left(c_{i,\sigma}^\dagger c_{i+1,\sigma}^\dagger - c_{i,\sigma}^\dagger c_{i,\sigma}^\dagger\right)\left(c_{0,\sigma}c_{1,\sigma} - c_{0,\sigma}c_{0,\sigma}\right)\rangle \\ &= \langle c_{i,\sigma}^\dagger c_{i+1,\sigma}^\dagger c_{0,\sigma} c_{1,\sigma}\rangle\,, \end{aligned} \tag{10.28}$$

where in the second line we have taken into account that $c_\mu^\dagger c_\mu^\dagger = c_\mu c_\mu = 0$ for any set of quantum numbers μ.

The DMRG simulations were performed for system sizes of up to 127 sites, keeping up to $M = 800$ states in the calculations to ensure accurate results also for the gapless lead. Fig. 10.4 shows the numerical results: The correlation function $T_\sigma(x)$ shows a clearly different behavior depending on the value of the spin. From a scaling analysis of our numerical data we extract the exponents $d_\uparrow \approx -1$ and $d_\downarrow \approx -3$ for the thermodynamic limit, which is in perfect agreement with our predictions in Eqs. (10.25) and (10.26). This confirms that the strong coupling fixed point is indeed controlled by the Majorana interaction rather than the Kondo interaction.

10.4. Results at the particle-hole symmetric point

We now turn to the discussion of the special particle-hole symmetric point at $\epsilon_f = -U/2$. For these values of the parameters, $\xi_- = 0$. Furthermore, $\xi_+ = 4/U$, which leads to the appearance of a standard Kondo term $J_3 \mathbf{s}_0 \cdot \mathbf{S}$ with $J_3 = 4|V|^2/U$, see also Eq. (2.10).

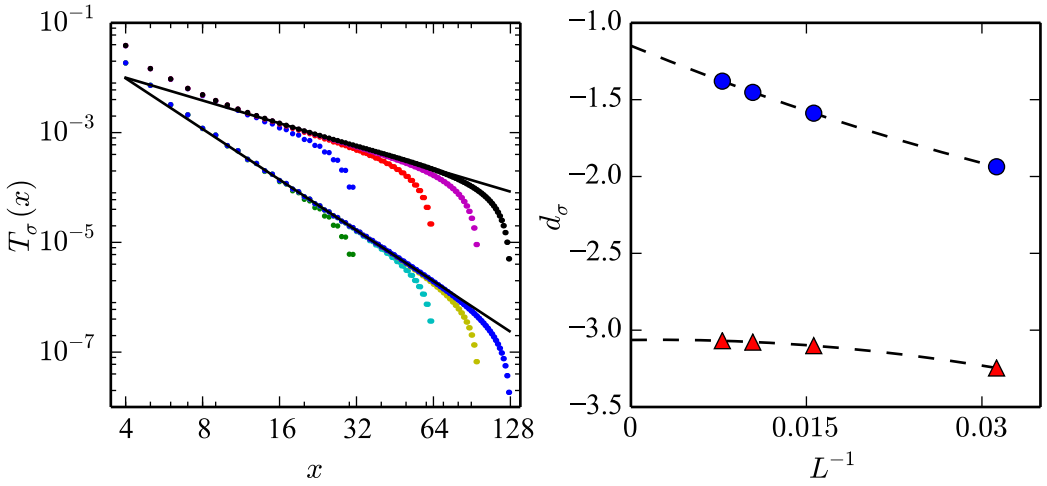

Figure 10.4.: Left panel: Triplet pairing correlation function $T_\sigma(x)$ for the couplings $h/t = 0.2$, $J_1/t = 0.2$, $J_2/t = 1$, $J_3/t = 0.5$ where t is the hopping in the lead. The upper set of lines show the correlation function for spin-↑ fermions, while the lower show the correlation function for spin-↓ fermions. Dashed lines indicate fits to a power-law decay. Right panel: Exponents $d_\uparrow$ (circles) and $d_\downarrow$ (triangles) extracted from the fits of the triple pairing correlation, as a function of inverse length.

The boundary Hamiltonian Eq. (10.7) therefore becomes

$$H_B = iJ_2\gamma_1\left[(\psi_\uparrow(0)+\psi_\uparrow^\dagger(0))S^z+\psi_\downarrow^\dagger(0)S^+ + \psi_\downarrow(0)S^-\right] + J_3\mathbf{s}_0\cdot\mathbf{S}. \tag{10.29}$$

This Hamiltonian can be brought to a somewhat simpler form by introducing the following set of Majorana operators:

$$\eta_x = \psi_\downarrow(0)+\psi_\downarrow^\dagger(0) \tag{10.30a}$$
$$\eta_y = i\left(\psi_\downarrow^\dagger(0)-\psi_\downarrow(0)\right) \tag{10.30b}$$
$$\eta_z = \psi_\uparrow(0)+\psi_\uparrow^\dagger(0). \tag{10.30c}$$

With these operators, Eq. (10.29) can be written as

$$H_B = iJ_2\sum_{\alpha=x,y,z}\gamma_1 S^\alpha\eta_\alpha + J_3\mathbf{s}_0\cdot\mathbf{S}. \tag{10.31}$$

In the absence of the parameters h and J_1, one can see from the RG equations Eqs. (10.19c) and (10.19d) that J_2 flows to strong coupling. As a result, the system forms an entangled state involving the fermion parity shared between the γ_1 and $\eta_\alpha(0)$ modes and the impurity spin. Before we discuss the first part of this statement, let us investigate how the spin fluctuations come about. The particle-hole symmetric Hamiltonian is invariant under the anti-unitary symmetry

$$\tilde{\mathcal{T}} = \mathcal{C}\mathcal{K}, \tag{10.32}$$

where $\mathcal{K}$ is complex conjugation and $\mathcal{C}$ is charge conjugation, i.e. $f_\sigma \to f_\sigma^\dagger$ and $\psi_\sigma \to \psi_\sigma^\dagger$. When acting on the quantum dot impurity spin, $\tilde{\mathcal{T}}$ is similar to the time-reversal symmetry, and [189]

$$\mathcal{T}\mathbf{S}\mathcal{T}^{-1} = -\mathbf{S}, \tag{10.33}$$

which implies that the spin strongly fluctuates, i.e. $\langle \mathbf{S} \rangle = 0$. Away from particle-hole symmetry, the $\tilde{\mathcal{T}}$-symmetry is broken and the impurity spin is polarized.

Entangled ground state

Now we turn to the action of the Majorana operators γ_1 and η_α. To this end, we remind ourselves that we can formulate each Majorana fermions in term of two Dirac fermions, see Eqs. (10.30). Here, we consider without loss of generality the the term $\gamma_1 \eta_x$.

$$\left.\begin{aligned} \gamma_1\eta_x |00\rangle &= |11\rangle \\ \gamma_1\eta_x |11\rangle &= |00\rangle \end{aligned}\right\} |00\rangle + |11\rangle \text{ is eigenstate if combined parity is even,} \quad (10.34a)$$

$$\left.\begin{aligned} \gamma_1\eta_x |01\rangle &= |10\rangle \\ \gamma_1\eta_x |10\rangle &= |01\rangle \end{aligned}\right\} |01\rangle + |10\rangle \text{ is eigenstate if combined parity is odd,} \quad (10.34b)$$

where in the state $|ij\rangle$ the first and second index correspond to the Hilbert space of the Dirac fermion associated with γ_1 and η_x, respectively. The inclusion of the fluctuating spin finally leads to the ground state taking on the form

$$|00\uparrow\rangle + |11\downarrow\rangle \quad \text{for even parity in the lead,} \quad (10.35a)$$
$$|01\uparrow\rangle + |10\downarrow\rangle \quad \text{for odd parity in the lead.} \quad (10.35b)$$

10.4.1. Numerical results at particle-hole symmetry

We now present our numerical results for the particle-hole point. First, we consider the superconducting triplet correlator already discussed away from particle-hole symmetry. Another interesting quantity is the spin-spin correlator which further indicates the absence of the Kondo effect for finite Majorana coupling. Finally, results for the static spin susceptibility of the quantum dot spin can be obtained exactly from the Hamiltonian Eq. (10.31) in the limit of vanishing Kondo coupling J_3. We compare these results for this case and also extend the numerical calculations to the case of finite J_3, agreeing nicely with analytical results.

Superconducting triplet correlation

We now present numerical results to verify the results at the particle-hole symmetric point. To this end, we consider the following form of the boundary Hamiltonian H_B in Eq. (10.7):

$$H_B = J_3 \, \mathbf{S}_f \cdot \mathbf{s}_0 + i J_2 \, \gamma_1 \left[\left(\psi_{0\uparrow} + \psi_{0\uparrow}^\dagger \right) S^z + \psi_{0\downarrow}^\dagger S^+ + \psi_{0,\downarrow} S^- \right], \quad (10.36)$$

where $J_1 = h = 0$ at the particle-hole symmetric point. We again consider the superconducting triplet correlation function $T_\sigma(x)$ from Eq. (10.22). In particular, we examine the dependence of the exponent d_σ on the Majorana coupling λ, see Fig. 10.5. We see that for zero Majorana coupling, $\lambda = 0$, the correlation function decays with the same exponent for both spin-up and spin-down electrons, $d_\uparrow = d_\downarrow$. However, including the Majorana coupling, the exponents immediately become different. We have calculated the exponents for systems of different sizes, and an extrapolation shows that they saturate at $d_\uparrow \approx -1$ and $d_\downarrow \approx -3$, which confirms that the strong-coupling fixed point is

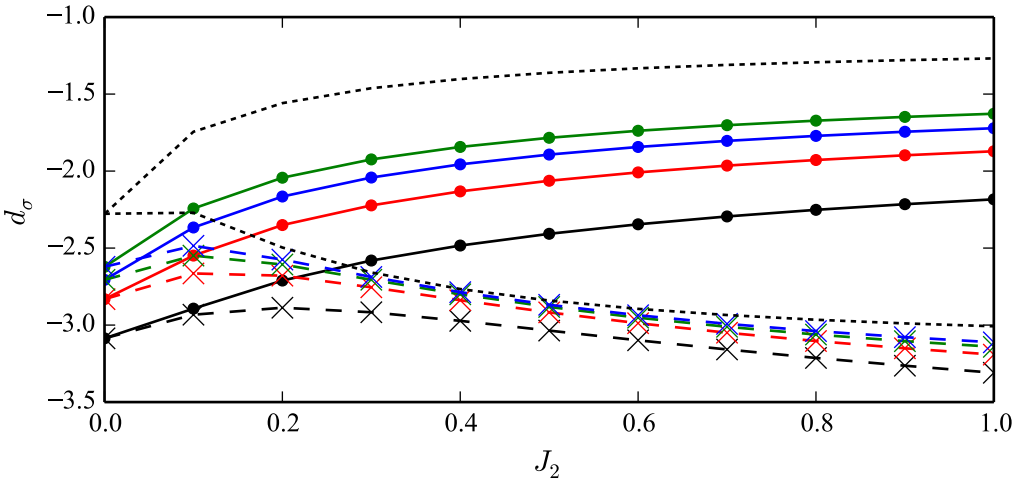

Figure 10.5.: Dependence of the exponent d_σ on the Majorana coupling J_2 for a fixed Kondo coupling $J_3/t = 0.5$, at the particle hole symmetric point with $J_1 = h = 0$. Solid lines correspond to $d_\uparrow$, dashed lines to $d_\downarrow$. System sizes are $L = 32, 64, 96, 128$ (black, red, blue, green), and an extrapolation to $L \to \infty$ is shown as a dotted line.

described by the $A \otimes N$ boundary conditions discussed above.

Static spin-spin correlator

Another quantity from which one can infer the dominating behavior in the strong-coupling limit is given by the equal-time spin-spin correlation function $\langle S_z(x) S_z(0)\rangle$. It was shown in Ref. [130] that the Kondo effect leads to a particular crossover in the correlations at a distance of the Kondo length scale R_K (see Sec. 6.2.1), where

$$\langle S^z(x) S^z(0)\rangle \sim \begin{cases} x^{-1} & \text{for } x \ll R_K, \\ x^{-2} & \text{for } x \gg R_K. \end{cases} \tag{10.37}$$

In Fig. 10.6 we show our numerical results. Plotted is the spin-spin correlator $\langle S^z(x) S^z(0)\rangle$ as a function of x at the particle-hole symmetric point, Eq. (10.29), and for different values of the Majorana coupling J_2. We tuned the Kondo coupling J_3 such that in for zero Majorana coupling, $J_2 = 0$, we see a clear sign of the Kondo crossover and can thus conclude that here the system is described by the Kondo strong-coupling fixed point. However, upon including the Majorana coupling we find that this crossover quickly disappears, and in the entire range the correlation function decays as x^{-2}, implying that there is no Kondo effect

Impurity spin susceptibility

Another interesting quantity to examine in the particle-hole symmetric limit is the impurity spin susceptibility. At the particle-hole symmetric point, $\epsilon = \epsilon_0 = -U/2$, the impurity spin is strongly fluctuating. Detuning the gate voltage by V_g, i.e. $\epsilon = \epsilon_0 + V_g$, we find that the impurity spin shows nontrivial behavior suited to distinguish between Kondo and Majorana physics. This difference is easily understood qualitatively: In the Kondo effect, a particle-hole asymmetric impurity does not affect the spin expectation value, and therefore $\langle \mathbf{S}\rangle = 0$ for all values of V_g. The Majorana coupling, on the other

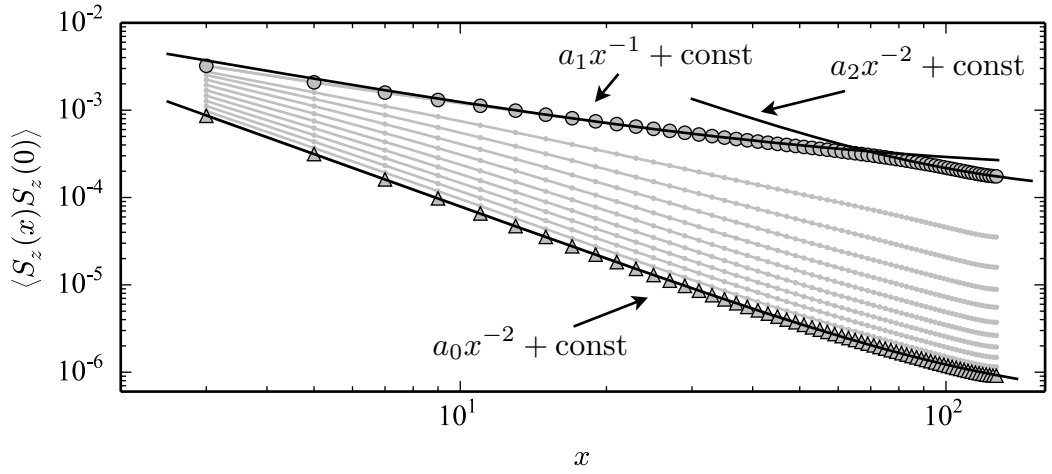

Figure 10.6.: $\langle S_z(x)Sz(0)\rangle$ away from the quantum dot boundary for $J_3 = 0.5$ and $J_2 = 0.1n$ with $n = 0, 1, \ldots, 10$ (top to bottom) at the particle-hole symmetric point. In the Kondo dominated regime ($J_2 = 0$, big circles) the correlation function shows a characteristic crossover from $1/x$-dependence at short distances $x \ll R_K$ to $1/x^2$ at $x \gg R_L$ [130]. Here R_K is the Kondo length scale. Clearly, the correlation function exhibits a different behavior in the Majorana-dominated regime ($J_2 \gg 0$, big triangles). There, the correlation function decays as $1/x^2$ in the entire range.

hand, polarized the spin along the z-axis for $V_g \neq 0$. To examine the effect of a finite V_g, consider the perturbation Hamiltonian obtained by introducing a small V_g:

$$H_V = eV_g \left(-\frac{8|\lambda|^2}{U^2} S^z + \frac{4i\lambda|t|}{U^2} \gamma_1 \eta_z(0) \right). \tag{10.38}$$

Using linear response theory, one finds the impurity spin susceptibility [189]

$$\left. \frac{\partial \langle S^z \rangle}{\partial V_g} \right|_{V_g=0} = \frac{2e}{U\pi^2} \log \left[\frac{16\pi V^2 v_F}{DU^2} e^{\frac{U}{4v_F V^2}} \lambda^2 \right], \tag{10.39}$$

where D is the half-bandwidth of the lead system and we have used that $J_2 = 4\lambda V/U$ at the particle-hole symmetric point. This behavior is very distinct from the Kondo case, thus we suggest that studies of impurity-spin fluctuations in TSC-QD-NL structures might be used to help in identifying Majorana zero-energy modes.

To confirm this behavior, we ran DMRG calculations of up to 64 sites of the Hamiltonian Eq. (10.7). We set $U = 8$ and $V = 1$, using up to $M = 400$ states and measuring $\langle S^z \rangle$ on the impurity. Slightly detuning the chemical potential in the range $V_g \in [-0.05, 0.05]$, we could extract the numerical derivative $\partial \langle S^z \rangle / \partial V_g$. To minimize effects due to the finite size of the system, we ran the calculations several times, each time multiplying the Kondo-coupling term by an additional factor κ to suppress or enhance the Kondo energy scale. The results are shown in Fig. 10.7. For intermediate values of λ we find that the susceptibility can be well fit by a function $\sim \log(b\lambda^2)$, as expected from Eq. (10.39). We furthermore see that an enhanced Kondo coupling suppresses the spin susceptibility, which can be easily understood from the fact that at the Kondo strong coupling fixed point the impurity participates in the formation of a spin-singlet and the susceptibility vanishes, $\langle \mathbf{S} \rangle \to 0$.

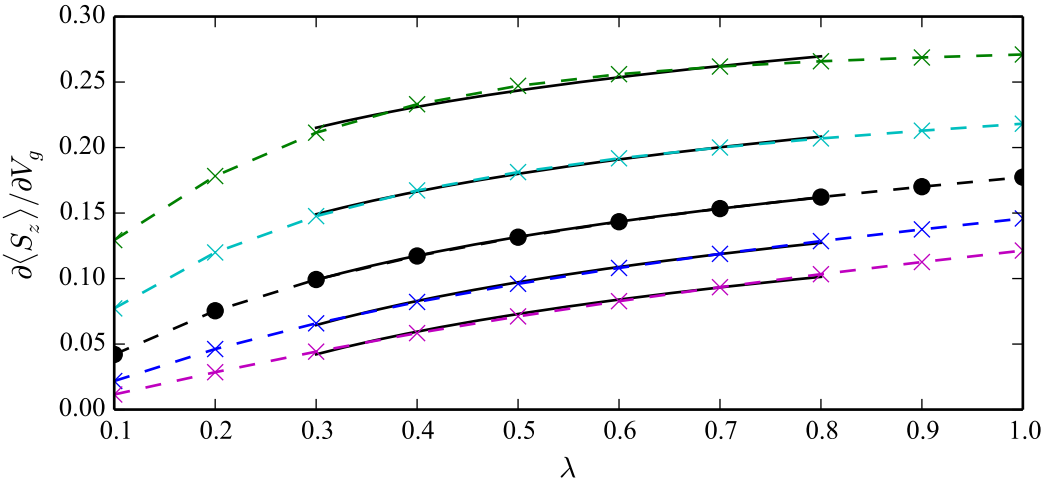

Figure 10.7.: Impurity spin susceptibility for a system of $L = 64$ sites with $U = 8$ and $V = 1$, where different dashed lines correspond to simulations where we have multiplied the Kondo term of Eq. (10.7) by $\kappa = 0, 0.5, 1, 1.5, 2$ (from top to bottom). The black line (round points) was obtained for $\kappa = 1$, i.e. it represents the unmodified Hamiltonian (10.7). The solid lines show a fit to $a\log(b\lambda^2)$ (see Eq. (10.39)), with a and b as fit parameters over a regime of intermediate λ.

The nice agreement of our numerical data with the results from Eq. (10.39) confirm that the spin susceptibility should provide an interesting experimental quantity to distinguish Kondo from Majorana physics in the setup we consider.

10.5. Summary

In conclusion, we have studied the physical properties of a quantum dot coupled to a 1D topological superconductor and a normal metallic lead. In the experimentally relevant parameter regime, the low energy theory for such a system involves Kondo and Majorana-induced interactions [189]. We focus on the competition between Majorana and Kondo couplings, where both drive the system to different many-body ground states. If the distance between the localized Majorana modes is taken to be far enough, we show that the low-energy infrared fixed point is governed by the Majorana physics rather than the Kondo effect. We found these results analytically using a perturbative RG scheme, and corroborate the emerging picture with numerical data obtained with the DMRG.

We consider the impurity spin susceptibility, an experimentally accessible quantity, and show how to distinguish between Kondo and Majorana physics in the lab. We predict that in the presence of a coupling to the Majorana mode the impurity spin polarization $\langle \mathbf{S} \rangle$ shows a strong dependence on tuning the gate voltage away from the particle-hole symmetric point: whereas it vanishes at the particle-hole symmetric point, the spin is polarized as the gate voltage is detuned. In fact, the impurity spin susceptibility's dependence on the Majorana coupling is highly non-trivial. In the Kondo-dominated regime, on the other hand, the impurity spin is strongly fluctuating for *all* values of V_g regardless whether the system is at the particle-hole symmetric point or not. These results have important ramifications for experiments trying to detect Majorana zero modes, where the natural formation of a local magnetic moment might interfere with the measurements. The exceptional degree of parameter control in quantum dot experiments, however, might turn out to be highly useful for distinguishing these different phenomena in

experiment.

Part V.

Appendices

Appendix A.

Real-space Green functions from equations of motion

A.1. Green functions for the semi-infinite 1D chain

The Hamiltonian for the Anderson impurity model defined on a 1D chain is given by

$$H = t\sum_{i=0}^{\infty}\sum_{\sigma}\left(c_{i\sigma}^{\dagger}c_{i+1\sigma} + \mathrm{H.c.}\right) + \epsilon_f \hat{n}_f + U\hat{n}_{\uparrow}\hat{n}_{\downarrow} + V\sum_{\sigma}\left(f_{\sigma}^{\dagger}c_{0\sigma} + \mathrm{H.c.}\right). \tag{A.1}$$

We now derive how local and non-local Green functions in this system can be obtained from equations of motion. To this end, we start by considering the same setup for a chain of finite length L. The chain Hamiltonian is then given by

$$H = t\sum_{i=0}^{L-1}\sum_{\sigma}\left(c_{i\sigma}^{\dagger}c_{i+1\sigma} + \mathrm{H.c.}\right). \tag{A.2}$$

The equations of motion for the Green function $G_{n,m;\sigma}(z) \equiv \langle\langle c_{n\sigma}; c_{m\sigma}^{\dagger}\rangle\rangle_z$ for $n, m > 1$ are then straight-forwardly obtained from Eq. (6.14) as

$$G_{n,m} = \frac{t}{z}\left(G_{n-1,m} + G_{n+1,m}\right) + \frac{1}{z}\delta_{n,m}, \tag{A.3}$$

where we have omitted spin and frequency indices for clarity. For real parameters $t, V \in \mathbb{R}$, this expression is symmetric in n and m:

$$G_{n,m} = \frac{t}{z}\left(G_{n,m-1} + G_{n,m+1}\right) + \frac{1}{z}\delta_{n,m}. \tag{A.4}$$

In the first step we consider the chain without the impurity by setting $V = 0$, and calculate the local Green function at one of its ends, $G_{0,0}^{(0)}(z)$. Starting at the other end of the chain, we find the following relations:

$$\begin{aligned} G_{0,N}^{(0)} &= \frac{t}{z}G_{0,N-1}^{(0)} \\ G_{0,N-1}^{(0)} &= \frac{t}{z}\left(G_{0,N-2}^{(0)} + G_{0,N}^{(0)}\right) \\ \Rightarrow G_{0,N-1}^{(0)} &= \frac{t}{z - \frac{t^2}{z}}G_{0,N-2}^{(0)}. \end{aligned} \tag{A.5}$$

Continuing this calculation down the chain, we eventually obtain

$$G_{0,0}^{(0)} = \cfrac{1}{z - \cfrac{t^2}{z - \cfrac{t^2}{\ddots}}}, \tag{A.6}$$

with a fraction of depth L. Taking the limit $L \to \infty$, this expression becomes a continued fraction and we can write it in a closed form as

$$G_{0,0}^{(0)} = \frac{1}{z - t^2\, G_{0,0}^{(0)}} \quad \Rightarrow \quad G_{0,0}^{(0)} = \frac{z \pm \sqrt{z^2 - 4t^2}}{2t^2}. \tag{A.7}$$

The negative imaginary part of $G_{0,0}^{(0)}$ is proportional to the spectral function $A_{n=0}$ and we must thus choose the sign of the square root such that the *negative* imaginary part of $G_{0,0}^{(0)}$ is strictly non-negative. Before reintroducing the impurity to the system, we summarize four important relations which are readily obtained from the equations of motion calculation:

$$G_{n,n} = \frac{1}{z} + \frac{t}{z}\left(G_{n-1,n} + G_{n+1,n}\right) \tag{A.8a}$$

$$G_{n+1,n} = G_{0,0}^{(0)}\, t\, G_{n,n} \tag{A.8b}$$

$$G_{n+1,n-1} = G_{0,0}^{(0)}\, t\, G_{n,n-1} \tag{A.8c}$$

$$G_{n-1,n} = G_{n,n-1} = \frac{t}{z} G_{n-1,n-1} + \frac{t}{z} G_{n+1,n-1}., \tag{A.8d}$$

where Eqs. (A.8a) and (A.8d) follow directly from Eq. (A.4), and Eqs. (A.8b) and (A.8c) follow from Eq. (A.5) in the limit $L \to 0$. From these expressions, we can obtain a general expression for the local Green function $G_{n,n}$ at a point $n > 1$ in the system:

$$G_{n,n} = G_{0,0}^{(0)} + t^2\, G_{n-1,n-1} \left[G_{0,0}^{(0)}\right]^2 \tag{A.9}$$

which allows us to traverse the chain site by site in order to calculate the local Green function at arbitrary sites.

When the impurity couples to the site at $n = 0$, these calculations are valid as long as $n > 1$. With the impurity reinstated, $V \neq 0$, using the equations of motion for $G_{0,0}$ we find

$$\begin{aligned} z\, G_{0,0} &= V\, G_{f,0} + t\, G_{1,0} + 1 \\ &= V\, G_{f,0} + t^2\, G_{0,0}^{(0)}\, G_{0,0} + 1 \\ \Rightarrow G_{0,0} &= G_{0,0}^{(0)} + V\, G_{0,0}^{(0)}\, G_{f,0}, \end{aligned} \tag{A.10}$$

where $G_{f,n} \equiv \langle\langle f; c_n^\dagger \rangle\rangle$. Again applying the equations of motion to $G_{f,0}$ yields

$$G_{f,0} = \frac{V}{z} G_{f,f} + \frac{t}{z} G_{f,1}. \tag{A.11}$$

Using the expression from Eqs. (A.8) finally gives us

$$G_{f,0} = \frac{V}{z}\, G_{f,f} + G^{(0)}_{0,0}\, \frac{t^2}{z}\, G_{f,0} = V\, G^{(0)}_{0,0}\, G_{f,f}. \tag{A.12}$$

Plugging this into (A.10) gives us the final expression for $G_{0,0}$:

$$G_{0,0} = G^{(0)}_{0,0} + V^2\, G_{f,f}\, \left(G^{(0)}_{0,0}\right)^2. \tag{A.13}$$

which, in combinations with Eq. (A.9), allows us to calculate arbitrary Green functions in the system. The difference in the Green functions for systems with and without the impurity are readily calculated. Consider for simplicity the difference in the local Green functions at position $n = 1$:

$$\begin{aligned}
\Delta G_{1,1} &= G_{1,1} - G^{(0)}_{1,1} \\
&= G^{(0)}_{0,0} + t^2 \left[G^{(0)}_{0,0} + V^2\, G_{\mathrm{imp}}\, \left(G^{(0)}_{0,0}\right)^2\right] \left(G^{(0)}_{0,0}\right)^2 - \left[G^{(0)}_{0,0} + t^2\, \left(G^{(0)}_{0,0}\right)^3\right] \\
&= t^2 V^2\, G_{\mathrm{imp}}\, \left(G^{(0)}_{0,0}\right)^4 \\
&= \frac{V^2}{t^2}\, G_{\mathrm{imp}} \left[t\, G^{(0)}_{0,0}\right]^4,
\end{aligned} \tag{A.14}$$

which recovers the result in Eq. (7.6) for $n = 1$.

Extended systems

The extension of the calculation from the previous section readily generalized to systems of finite size. One simply regroups all Green functions in the way discussed in Sec. 7.1.2. After applying equations of motion to each Green function, the calculation can be performed in a matrix-vector formalism and has the same form as the calculation or the 1D chain. In the next section we discuss the calculation for the nanotube system, which is a special case of the square lattice ribbons.

A.2. Green functions for ribbons and tubes

The extension of the calculation from the previous section readily generalized to systems of finite width. One simply regroups all Green functions in the way discussed in Sec. 7.1.2. Upon applying equations of motion to each Green function, one finds that the calculation can be performed in a matrix-vector formalism and has the same form as the calculation or the 1D chain.

Here we derive the relevant equations for the calculation of lattice Green functions for the nanotube. This calculation can immediately be transferred to the (simpler) square lattice ribbon systems. In the nanotube setup, we must distinguish between two types of matrices 1 and 2, which alternate through the system. This issue does not occur in the squarelattice ribbons, where only one hopping matrix is required.

We introduced the hopping matrices $\underline{M}_1$ and $\underline{M}_2$ for the nanotube in Sec. 7.1.2. The matrix of Green functions connecting to the first column is given as $\underline{G}_n(z)$. Assuming that the column at position n is described by matrix $\underline{M}_1$, after applying the equations of

motion to each coefficient of the matrix $\underline{G}_n$, for $n > 1$ we find,

$$[z\mathbb{1} - \underline{M}_1]\,\underline{G}_n(z) = t\,\underline{G}_{n-1}(z) + t\,\underline{G}_{n+1}(z) + \delta_{n,0}\mathbb{1}. \tag{A.15}$$

Defining the two matrices $\underline{A}_{1/2}(z) \equiv z\mathbb{1} - \underline{M}_{1/2}$, we can perform a calculation along the lines of the previous section, starting with a finite tube of length L, with the last column described by $\underline{M}_1$ (again omitting frequency arguments for clarity):

$$\underline{A}_1\underline{G}_L = t\,\underline{G}_{L-1} \tag{A.16}$$

$$\underline{A}_2\underline{G}_{L-1} = t\,\underline{G}_{L-2} + t\underline{G}_L \tag{A.17}$$

$$\Rightarrow \underline{G}_{L-1} = \left[\underline{A}_2 - t^2\underline{A}_1^{-1}\right]^{-1}\, t\,\underline{G}_{L-2}. \tag{A.18}$$

Continuation of this scheme yields

$$\underline{G}_n = [\underline{A}_2 - t^2[\underline{A}_1 - t^2[\underline{A}_2 - \ldots]^{-1}]^{-1}]^{-1} t\,\underline{G}_{n-1}. \tag{A.19}$$

For the case that the impurity is absent from the system, and the first column is described by $\underline{M}_1$, this becomes (due to the delta function in Eq. (A.15))

$$\underline{G}_0^{(1)} = [\underline{A}_1 - t^2[\underline{A}_2 - t^2[\underline{A}_1 - \ldots]^{-1}]^{-1}]^{-1}, \tag{A.20}$$

and if the system's first column is described by $\underline{M}_2$,

$$\underline{G}_0^{(2)} = [\underline{A}_2 - t^2[\underline{A}_1 - t^2[\underline{A}_2 - \ldots]^{-1}]^{-1}]^{-1}, \tag{A.21}$$

with which we recover Eq. (7.25):

$$\underline{G}_0^{(1)} = \left[\underline{A}_1 - t^2\,\underline{G}^{(2)}\right]^{-1}, \tag{A.22a}$$

$$\underline{G}_0^{(2)} = \left[\underline{A}_2 - t^2\,\underline{G}^{(1)}\right]^{-1}. \tag{A.22b}$$

By plugging Eq. (A.22b) into (A.22a) and recalling that $\underline{A}_1$ and $\underline{A}_2$ commute and are invertible, one can solve for $\underline{G}_0^{(1)}$ and finds

$$\underline{G}_0^{(1)} = \frac{1}{2t^2}\underline{A}_1^{-1}\left(\sqrt{(\underline{A}_1\underline{A}_2)^2 - 4t^2\underline{A}_1\underline{A}_2} + \underline{A}_1\underline{A}_2\right). \tag{A.23}$$

Combining the previous results, the find furthermore that to advance a local Green function by one column in real space, we must apply the matrix $\underline{G}_0^{(1)}$ or $\underline{G}_0^{(2)}$ (depending on the lattice geometry of this step), once from both sides. Thus, advancing a local Green function one and two steps becomes (due to the alternating columns 1 and 2):

$$\underline{G}_{n+1} = t^2\,\underline{G}_0^{(1)}\,\underline{G}_n\,\underline{G}_0^{(1)}, \tag{A.24a}$$

$$\underline{G}_{n+2} = t^2\,\underline{G}_0^{(2)}\,\underline{G}_0^{(1)}\,\underline{G}_n\,\underline{G}_0^{(1)}\,\underline{G}_0^{(2)}, \tag{A.24b}$$

an so forth.

Result for the square lattice ribbons

As mentioned above, the square lattice ribbons only require a single set of matrices. Indeed, by simply replacing $\underline{A} = \underline{A}_1 = \underline{A}_2$ in Eq. (A.23), we recover the result for the square

lattice ribbons:

$$\underline{G}^{(1)} = \frac{1}{2t^2}\left(\sqrt{A^2 - 4t^2\mathbb{1}} + \underline{A}\right). \tag{A.25}$$

A.2.1. Impurity coupling to more than one site

Let us now discuss a generalized method of coupling the impurity to the systems considered here. The impurity Green function obtained from the NRG is a scalar function: it is therefore *a priori* not clear how to combine it with the matrix formalism which we constructed. To this end, we define a *connection vector*, $\mathbf{1}_c$, which describes to which sites the impurity couples. For a system of width W, the vector has length W and the nth coefficient in it describes the coupling between the impurity and the site in the host at position $\mathbf{r} = (0, n)$, and a 1 indicates a coupling, and a 0 indicates now coupling. For the case of the armchair nanotube considered in Sec. 7.1.2, we considered the situation where *every* site in the first column of the nanotube couples to the impurity. Therefore, the connection vector in this setup takes on the form

$$\mathbf{1}_c = [1, 1, 1, 1, \ldots, 1]^T. \tag{A.26}$$

Again, careful application of the equations of motion yields the following expression for the matrix of Green functions at the end of the system,

$$\underline{G}_0 = V^2\, G_{\mathrm{imp}}\, \underline{G}_0^{(\alpha)} \underbrace{\mathbf{1}_c \mathbf{1}_c^T}_{=\underline{B}_0} \underline{G}_0^{(\alpha)}, \tag{A.27}$$

where $\alpha \in \{1, 2\}$ again determines the type of column at the end of the tube, and we have defined the *connection matrix*

$$\underline{B}_0 \equiv \mathbf{1}_c \mathbf{1}_c^T. \tag{A.28}$$

In the case of Eq. (A.26) this becomes,

$$\underline{B}_0 = \begin{bmatrix} 1 \\ \vdots \\ 1 \end{bmatrix} [1, \ldots, 1] = \begin{bmatrix} 1 & \ldots & 1 \\ \vdots & \ddots & \vdots \\ 1 & \ldots & 1 \end{bmatrix}. \tag{A.29}$$

Appendix B.

Calculations for the triangular Kitaev model

B.1. Lattice clusters used in the numerical calculations

In Sec. 5.3 we presented results for the ground state of the Heisenberg-Kitaev model on the triangular lattice obtained from sparse-matrix diagonalization. To reliably reproduce the phase boundaries of the entire phase diagram, the lattice under consideration should be compatible with all different phases. Fig. B.1 shows the four lattice clusters we used. To minimize finite size effects, all clusters are implemented with periodic boundary conditions. Except for the 12-site cluster, the periodic boundary conditions require compromising on the symmetries. We immediately see that only clusters (i) and (iv) implement the discrete C_6 rotational symmetry of the triangular lattice. Accordingly, in the two other clusters one direction is special. The following table summarizes the symmetries of each cluster:

Cluster	#spins	Klein	C_6	120°	AFM chains
(i)	12	✓	✓	✓	✓
(ii)	24	✓	✗	✗	✓
(iii)	24	✓	✗	✓	✓
(iv)	27	✗	✓	✓	✗

The next biggest cluster after the 12-site cluster that incorporates all symmetries is comprised of 48 sites, which is currently intractable with exact diagonalization routines. However, a comparison of the results for all lattices in Fig. B.1 shows that in each case all phases are present, albeit with slightly shifted boundaries. Lattice cluster (iii) only breaks the C_6 rotational symmetry, which only affects the nematic phase around the Kitaev point by lifting the ground state degeneracy. Therefore, the results shown in Fig. 5.6 were obtained using cluster (iii).

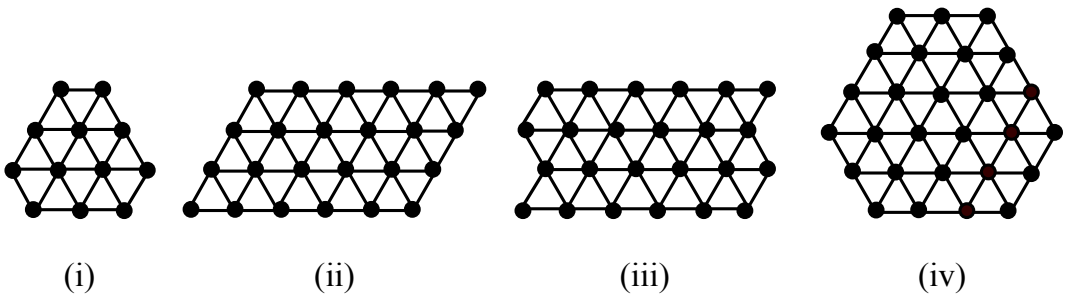

Figure B.1.: Lattice clusters used in the exact diagonalization calculations.

B.2. Instability of the 120° order

The second order correction to the energy of the 120° induced by fluctuations has the form

$$\mathcal{E}^{(2)} = \mathcal{E}_0 + \sum_{x-\text{links}} \mathcal{E}_x^{(2)} + \sum_{y-\text{links}} \mathcal{E}_y^{(2)} + \sum_{z-\text{links}} \mathcal{E}_z^{(2)}. \tag{B.1}$$

The first term corresponds to the correction coming from the Heisenberg interaction. It is given by

$$\mathcal{E}_0^{(2)} = -\sum_{\langle ij \rangle} \left[\left(\varepsilon_{120^\circ} \delta_{ij} + \frac{J_H S^2}{2} \right) \pi_{1i} \pi_{1j} + \left(\varepsilon_{120^\circ} \delta_{ij} - J_H S^2 \right) \pi_{2i} \pi_{2j} \right], \tag{B.2}$$

where the summation runs over all nearest-neighbor links. The contribution due to the anisotropic Kitaev interaction is given by

$$\begin{aligned} \mathcal{E}_\gamma^{(2)} = J_K S^2 \Bigg[& \Big(e_1^\gamma e_1^\gamma \cos(\mathbf{Q}\cdot\mathbf{r}_i)\cos(\mathbf{Q}\cdot\mathbf{r}_j) + e_2^\gamma e_2^\gamma \sin(\mathbf{Q}\cdot\mathbf{r}_i)\sin(\mathbf{Q}\cdot\mathbf{r}_j) \\ & - e_1^\gamma e_2^\gamma \Big[\cos(\mathbf{Q}\cdot\mathbf{r}_i)\sin(\mathbf{Q}\cdot\mathbf{r}_j) + \sin(\mathbf{Q}\cdot\mathbf{r}_i)\cos(\mathbf{Q}\cdot\mathbf{r}_j) \Big] \Big) \pi_{1i}\pi_{1j} \\ & + e_3^\gamma e_3^\gamma \pi_{2i}\pi_{2j} \\ & + \Big(-e_1^\gamma \sin(\mathbf{Q}\cdot\mathbf{r}_i) + e_2^\gamma \cos(\mathbf{Q}\cdot\mathbf{r}_i) \Big) e_3^\gamma \pi_{1i}\pi_{2j} \\ & + \Big(-e_1^\gamma \sin(\mathbf{Q}\cdot\mathbf{r}_j) + e_2^\gamma \cos(\mathbf{Q}\cdot\mathbf{r}_j) \Big) e_3^\gamma \pi_{1j}\pi_{2i} \Bigg], \end{aligned} \tag{B.3}$$

where we have used $\pi_{ai} \equiv \pi_a(\mathbf{r}_i)$ with $a = 1, 2$ and $\gamma = x, y, z$.

B.3. Spin-wave analysis of the ferromagnet

The second order correction to the ferromagnetic Hamiltonian in the spin-wave analysis is given by

$$H^{(2)} = \frac{1}{2} \sum_{\mathbf{k} \in 1.\text{BZ}} \left[\psi_{\mathbf{k}}^\dagger \underline{h}_{\mathbf{k}} \psi_{\mathbf{k}} - S \sum_{\gamma = x,y,z} \left(\cos(\mathbf{k}\cdot\mathbf{a}_\gamma) - 1 \right) \left(2J_H + J_K \left(1 - \hat{\Omega}_\gamma^2 \right) \right) \right], \tag{B.4}$$

with the two-component spinor $\psi_{\mathbf{k}}^\dagger = \left(a_{\mathbf{k}}^\dagger, a_{-\mathbf{k}} \right)$. The spin orientation vector is given by

$$\hat{\mathbf{\Omega}} = \underbrace{\begin{pmatrix} -\sin\phi & -\cos\theta\cos\phi & \sin\theta\cos\phi \\ \cos\phi & -\cos\theta\sin\phi & \sin\theta\sin\phi \\ 0 & \sin\theta & \cos\theta \end{pmatrix}}_{\equiv R} \begin{pmatrix} 0 \\ 0 \\ 1 \end{pmatrix} \tag{B.5}$$

with $R \in SO(3)$ being a rotation matrix. The matrix $\underline{h}_{\mathbf{k}}$ is given by

$$\begin{aligned}\underline{h}_{\mathbf{k}} = 2S\Big[& J_H \sum_{\gamma=x,y,z} (\cos(\mathbf{k}\cdot\mathbf{a}_\gamma)-1)\mathbb{1} \\ & + J_K\Big\{(\cos(\mathbf{k}\cdot\mathbf{a}_x)-1)\Big(e_x^+e_x^-\mathbb{1} + (e_x^+)^2\sigma^+ + (e_x^-)^2\sigma^-\Big) \\ & \quad + (\cos(\mathbf{k}\cdot\mathbf{a}_y)-1)\Big(e_y^+e_y^-\mathbb{1} + (e_y^+)^2\sigma^+ + (e_y^-)^2\sigma^-\Big) \\ & \quad + (\cos(\mathbf{k}\cdot\mathbf{a}_z)-1)e_z^+e_z^-(\mathbb{1}-\sigma^x)\Big\}\Big],\end{aligned} \tag{B.6}$$

with the Pauli matrices σ^x, σ^y, and σ^z, and we used the abbreviations $\mathbf{e}^\pm = \frac{1}{\sqrt{2}}R(1,\pm i,0)^T$ and $\sigma^\pm = \frac{1}{2}(\sigma^x \pm i\sigma^y)$. With the help of a Bogoliubov transformation we can compute the correction $\delta\varepsilon_{\mathrm{FM}}$ to the classical ground state energy (5.56). To elucidate the analytical structure we focus on the contribution to this correction only to lowest order in the Kitaev interaction,

$$\begin{aligned}\delta\varepsilon_{\mathrm{FM}} &= -\frac{1}{4N}\sum_{\mathbf{k}\in 1.\mathrm{BZ}} \frac{h_{21}(\mathbf{k})h_{12}(\mathbf{k})}{h_{11}(\mathbf{k})|_{J_K=0}} \\ &= \frac{S}{2N}\frac{J_K^2}{|J_H|}\sum_{\mathbf{k}\in 1.\mathrm{BZ}} \frac{\left|c_x e_x^+e_x^+ + c_y e_y^+e_y^+ - c_z e_z^+e_z^-\right|^2}{c_x+c_y+c_z},\end{aligned} \tag{B.7}$$

where we have defined the shorthand $c_\gamma \equiv (\cos(\mathbf{k}\cdot\mathbf{a}_\gamma)-1)$. To evaluate this expression we need the following integrals over the Brillouin zone

$$\begin{aligned}&\frac{1}{N}\sum_{\mathbf{k}\in 1.\mathrm{BZ}} \frac{c_\alpha c_\beta}{c_x+c_y+c_z} \overset{N\to\infty}{\longrightarrow} \\ &\frac{1}{\mathcal{V}_{1.\mathrm{BZ}}}\int_{1.\mathrm{BZ}} \mathrm{d}\mathbf{k}\frac{c_\alpha c_\beta}{c_x+c_y+c_z} = -\frac{6\sqrt{3}-2\pi}{3\pi}\delta_{\alpha\beta} - \frac{5\pi-6\sqrt{3}}{6\pi}(1-\delta_{\alpha\beta}).\end{aligned} \tag{B.8}$$

We evaluated here the integrals in the thermodynamic limit, $N\to\infty$, with the volume of the first Brillouin zone given by $\mathcal{V}_{1.\mathrm{BZ}} = \frac{8\pi^2}{\sqrt{3}}$.

Furthermore, we need the following identity:

$$\begin{aligned}\sum_{\gamma=x,y,z}(e_\gamma^+e_\gamma^-)^2 &= -(e_x^+e_y^-)^2 - (e_y^+e_x^-)^2 + \left[(e_x^+)^2 + (e_y^+)^2 + (\hat{e}_x^-)^2 + (\hat{e}_y^-)^2\right]\hat{e}_z^+\hat{e}_z^- \\ &= \frac{1}{4}\left(1+\hat{\Omega}_x^4+\hat{\Omega}_y^4+\hat{\Omega}_z^4\right).\end{aligned} \tag{B.9}$$

Putting these results together yields the second-order energy correction in Eq. (B.10):

$$\varepsilon_{\mathrm{FM}}^{(2)} = -\frac{S}{2}\frac{J_K^2}{|J_H|}\frac{3(2\sqrt{3}-\pi)}{8\pi}\left(1+\hat{\Omega}_x^4+\hat{\Omega}_y^4+\hat{\Omega}_z^4\right). \tag{B.10}$$

Acknowledgements

First and foremost I would like to thank my advisors Simon Trebst and Ralf Bulla for their continuous support, the fruitful discussions and overall for giving me the opportunity to write this thesis. I greatly enjoyed working on the highly topical and interesting research projects that they introduced me to. Furthermore, I want to especially thank Simon Trebst for making it possible for me to spend ten weeks at Microsoft Station Q, at the University of California at Santa Barbara. This experience was surely one of the highlights of my PhD. Go Gauchos!

I am grateful to Markus Garst, Andrew Mitchell, Lars Fritz, and Maria Hermanns for numerous enlightening discussions, and their overall help and collaboration in the projects presented in this thesis. Special thanks go out to Bela Bauer, who taught me a lot, not only about the delicacies of the DMRG and numerics in general, and who made me feel welcome in California. Also, I want to thank Meng Cheng for his patience during numerous Skype chats in the final stages of this thesis.

I have to thank Andrew Mitchell and Bela Bauer a second time for providing me with their computer codes. Both Andrew's NRG and Bela's DMRG are state-of-the-art, and surely belong to the best performing implementations currently in the community. Let's fight the NIH syndrome in research!

I greatly enjoyed my time in the institute in Cologne, much of which is due to the great companionship of my colleagues: Jonathan, Mario, Matthias & Karin, Tobias, Christoph, Stephan M., Lucas, Etienne, Alex, Carolin, Robert, Peter, Max Gerlach, Max Genske, Johannes H., Kevin, Johannes W., Stefan B., Stefan W., Jan A., and Jan M. Thank you for a great time!

Thank you, Fanny and Patrick, for allowing me to go to lunch with you (every now and then), and tolerating my bad jokes. You were trusty allies during the good and the bad times!

Zu guter Letzt gebührt der größte Dank meinen Eltern: Ohne ihre bedingungslose Unterstützung wäre diese Arbeit sicherlich nicht zustand gekommen. Danke!

Bibliography

[1] P. W. Anderson. *More Is Different*. Science **177**(4047), 393–396 (1972)

[2] R. de Picciotto et al. *Direct observation of a fractional charge*. Nature **389**, 162–164 (1997)

[3] A. C. Hewson. *The Kondo Problem to Heavy Fermions* (Cambridge University Press, 1993)

[4] C. Nayak et al. *Non-Abelian Anyons and Topological Quantum Computation*. Rev. Mod. Phys. **80**, 1083 (2008)

[5] A. J. Leggett. *What DO we know about high T_c?* Nature **2**, 134–136 (2006)

[6] X.-L. Qi. *Topological insulators and superconductors*. Rev. Mod. Phys. **83**(1057) (2011)

[7] A. Y. Kitaev. *Unpaired Majorana fermions in quantum wires*. Phys.-Usp. **44**(131) (2000)

[8] D. I. Khomskii. *Basic Aspects of the Quantum Theory of Solids* (Cambridge University Press, 2010)

[9] L. P. Kouwenhoven and L. I. Glazman. *Revival of the Kondo effect*. Phys. World **14**(33) (2001)

[10] K. G. Wilson. *The renormalization group: Critical phenomena and the Kondo problem*. Rev. Mod. Phys. **47**, 773 (1975)

[11] S. R. White. *Density Matrix Formulation for Quantum Renormalization Groups*. Phys. Rev. Lett. **69**, 2863 (1992)

[12] I. Rousochatzakis, U. K. Rössler, J. van den Brink, and M. Daghofer. *$\mathbb{Z}_2$-vortex lattice in the ground state of the triangular Kitaev-Heisenberg model*. arXiv:1209.5895 (2012)

[13] I. Kimchi and A. Vishwanath. *Kitaev-Heisenberg models for iridates on the triangular, hyperkagome, kagome, fcc, and pyrochlore lattices*. Phys. Rev. B **89**(014414) (2014)

[14] J. Friedel. *Metallic alloys*. Nuovo Cimento Suppl. **7**, 287 (1958)

[15] I. Affleck, L. Borda, and H. Saleur. *Friedel oscillations and the Kondo screening cloud*. Phys. Rev. B **77**(18), 180404 (2008)

[16] V. Mourik et al. *Signatures of Majorana Fermions in Hybrid Superconductor-Semiconductor Nanowire Devices*. Science **336**(6084), 1003–1007 (2012)

[17] A. K. Geim and K. S. Novoselov. *The rise of graphene*. Nature Materials **6**, 183–191 (2007)

[18] G. Finocchio et al. *Magnetization reversal driven by spin-polarized current in exchange-biased nanoscale spin valves*. Phys. Rev. B **76**(174408) (2007)

[19] W. J. de Haas, J. de Boer, and G. J. van den Berg. *The electrical resistance of gold, copper and lead at low temperatures*. Physica **1**(7), 1115–1124 (1934)

[20] J. Kondo. *Resistance minimum in dilute magnetic alloys*. Prog. Theor. Phys. **32**(1) (1964)

[21] P. W. Anderson. *A poor man's derivation of scaling laws for the Kondo problem*. Journal of Physics C: Solid State Physics **3**(12), 2436 (1970)

[22] H. R. Krishnamurthy, J. W. Wilkins, and K. G. Wilson. *Renormalization-group approach to the Anderson model of dilute magnetic alloys. I. Static properties for the symmetric case*. Phys. Rev. B **21**(1003) (1980)

[23] P. W. Anderson. *Localized Magnetic States in Metals*. Phys. Rev. B **124** (1961)

[24] J. R. Shrieffer and P. A. Wolff. *Relation between the Anderson and Kondo Hamiltonians*. Phys. Rev. **149**(491) (1966)

[25] L. P. Kadanoff. *Scaling laws for Ising models near* T_c. Physics **2**(263) (1966)

[26] D. Goldhaber-Gordon et al. *Kondo effect in a single electron transistor*. Nature **391**, 156–159 (1998)

[27] W. G. van der Wiel et al. *The Kondo effect in the unitary limit*. Science **289**(2105) (2000)

[28] J. Hubbard. *Electron Correlations in Narrow Energy Bands*. Proc. R. Soc. Lond. A **276**(1365), 238–257 (1963)

[29] P. W. Anderson. *The Theory of Superconductivity in the High-*T_c *Cuprates* (Princeton Univ. Press, 1997)

[30] N. F. Mott. *The Basis of the Electron Theory of Metals, with Special Reference to the Transition Metals*. Proc. Phys. Soc. A **62**(7) (1949)

[31] A. Y. Kitaev. *Anyons in an exactly solved model and beyond*. Ann. of Phys. **321** (2006)

[32] G. Baskaran, S. Mandal, and R. Shankar. *Exact Results for Spin Dynamics and Fractionalization in the Kitaev Model*. Phys. Rev. Lett. **98**, 247201 (2007)

[33] G. Khaliullin and G. Jackeli. *Mott Insulators in the Strong Spin-Orbit Coupling Limit: From Heisenberg to a Quantum Compass and Kitaev Models*. Phys. Rev. Lett. **102**, 017205 (2009)

[34] E. Majorana. *Teoria simmetrica dell'elettrone e del positrone*. Il Nuovo Cimento **14**, 171–184 (1937)

[35] F. Wilczek. *Majorana returns*. Nature Physics **5**(9), 614 (2009)

[36] G. Bertone, D. Hooper, and J. Silk. *Particle dark matter: evidence, candidates and constraints*. J. Phys. Rep. **405**, 279–390 (2005)

[37] E. H. Lieb. *Flux phase of the half-filled band*. Phys. Rev. Lett **73**, 2158–2161 (1994)

[38] L. Balents. *Spin liquids in frustrated magnets*. Nature **464**, 199–208 (2010)

[39] A. Y. Kitaev. *Proceedings of the 3rd International Conference of Quantum Communication and Measurement*, pp. 181–188 (Plenum, 1997)

[40] U. Schollwöck. *The density-matrix renormalization group in the age of matrix product states*. Ann. of Phys. **326**(96) (2011)

[41] M. Srednicki. *Entropy and area*. Phys. Rev. Lett. **71**, 666–669 (1993)

[42] J. Eisert, M. Cramer, and M. B. Plenio. *Colloquium: Area laws for the entanglement entropy"*. Rev. Mod. Phys. **82**, 277–306 (2010)

[43] R. Orus. *A Practical Introduction to Tensor Networks: Matrix Product States and Projected Entangled Pair States*. Ann. of Phys. **349**, 117–158 (2014)

[44] M. B. Hastings. *Solving gapped Hamiltonians locally*. Phys. Rev. B **73**, 085115 (2006)

[45] U. Schollwöck. *The density-matrix renormalization group*. Rev. Mod. Phys. **77**, 259 (2005)

[46] B. Bauer et al. *The ALPS project release 2.0: open source software for strongly correlated systems*. J. Stat. Mech. p. 05001 (2011)

[47] M. Dolfi et al. *Matrix product state applications for the ALPS project*. Comput. Phys. Commun. (2014)

[48] J. Cullum and R. A. Willoughby. *Computing Eigenvalues of Very Large Symmetric Matrices — An Implementation of a Lanczos Algorithm with No Reorthogonalization*. J. Comp. Phys. **44**(329) (1981)

[49] G. L. G. Sleijpen and H. A. van der Vorst. *A Jacobi–Davidson iteration method for linear eigenvalue problems*. SIAM J. Matrix Anal. Appl. **17**, 401–425 (1996)

[50] S. R. White. *Density-matrix algorithms for quantum renormalization groups*. Phys. Rev. B **48**(10345) (1993)

[51] J. Dukelsky, M. A. Martin-Delgado, T. Nishino, and G. Sierra. *Equivalence of the variational matrix product method and the density matrix renormalization group applied to spin chains*. Europhys. Lett. **43**, 457 (1998)

[52] S. R. White. *Density matrix renormalization group algorithms with a single center site*. Phys. Rev. B **72**(180403(R)) (2005)

[53] E. M. Stoudenmire and S. R. White. *Studying Two Dimensional Systems With the Density Matrix Renormalization Group*. Ann. Rev. of Cond. Mat. Phys. **3**, 111–128 (2012)

[54] S. Liang and H. Pang. *Approximate diagonalization using the density-matrix renormalization-group method: A two-dimensional perspective*. Phys. Rev. B **49**(9214) (1994)

[55] R. Bulla, T. Pruschke, and A. Hewson. *Anderson impurity in pseudo-gap Fermi systems*. J. Phys.: Condens. Matter **9**, 10463 (1997)

[56] R. Bulla, T. A. Costi, and T. Pruschke. *Numerical Renormalization Group method for quantum impurity systems*. Rev. Mod. Phys. **80**(2), 395–450 (2008)

[57] A. Weichselbaum, F. Verstraete, U. Schollwöck, J. I. Cirac, and J. von Delft. *Variational matrix-product-state approach to quantum impurity models*. Phys. Rev. B **80**, 165117 (2009)

[58] T. A. Costi, A. C. Hewson, and V. Zlatic. *Transport coefficients of the Anderson model via the numerical renormalization group*. J. Phys.: Cond. Matt. **6**(13), 2519 (1994)

[59] O. Sakai, Y. Shimiza, and T. Kasuya. *Single-Particle and Magnetic Excitation Spectra of Degenerate Anderson Model with Finite $f - f$ Coulomb Interaction*. J. Phys. Soc. Jpn. **58**, 3666–3678 (1989)

[60] S.-W. Cheong. *Transition metal oxides: The exciting world of orbitals*. Nature Materials **6**, 927–928 (2007)

[61] K. I. Kugel and D. I. Khomskiĭ. *The Jahn-Teller effect and magnetism: transition metal compounds*. Sov. Phys. Usp. **25**(4) (1982)

[62] W. Witczak-Krempa, G. Chen, Y. B. Kim, and L. Balents. *Correlated Quantum Phenomena in the Strong Spin-Orbit Regime*. Ann. Rev. of Cond. Mat. Phys. **5**, 57–82 (2014)

[63] B. Kim et al. *Novel $J_{\text{eff}} = 1/2$ Mott State Induced by Relativistic Spin-Orbit Coupling in Sr_2IrO_4*. Phys. Rev. Lett. **101**, 076402 (2008)

[64] R. Comin et al. *Na_2IrO_3 as a Novel Relativistic Mott Insulator with a 340-meV Gap*. Phys. Rev. Lett. **109**, 266406 (2012)

[65] H. Gretarsson et al. *Crystal-Field Splitting and Correlation Effect on the Electronic Structure of A_2IrO_3*. Phys. Rev. Lett. **110**, 076402 (2013)

[66] F. Hund. *Zur Deutung verwickelter Spektren, insbesondere der Elemente Scandium bis Nickel*. Z Physik **33**, 345–371 (1925)

[67] F. Hund. *Linienspektren und periodisches System der Elemente* (Springer-Verlag, 1927)

[68] S. Maekawa et al. *Physics of Transition Metal Oxides* (Springer-Verlag, 2004)

[69] P. O'Donnell Offenhartz. *On the Calculation of $10Dq$*. J. Am. Chem. Soc. **91**(21) (1969)

[70] C. Cohen-Tannoudji. *Quantum Mechanics (Volume 2)* (Wiley-VCH, 1991), 2nd edition

[71] A. Wacther and H. Hoeber. *Repetitorium Theoretische Physik* (Springer-Verlag (Berlin), 1998)

[72] O. Schirmer et al. *Paramagnetic resonance and near-infrared optical absorption of $SrTiO_3$: Ir^{4+}*. J. of Phys. C **17**(1321) (1984)

[73] G. Jackeli and G. Khaliullin. *Mott Insulators in the Strong Spin-Orbit Coupling Limit: From Heisenberg to a Quantum Compass and Kitaev Models*. Phys. Rev. Lett. **102**, 017205 (2009)

[74] P. Fazekas. *Lecture Notes on Electron Correlation and Magnetism* (World Scientific Publishing, 1999)

[75] A. Abragam and M. H. L. Pryce. *Theory of the Nuclear Hyperfine Structure of Paramagnetic Resonance Spectra in Crystals*. Proc. Roy. Soc. A **205** (1951)

[76] C. J. Ballhausen. *Introduction to Ligand Field Theory* (McGraw-Hill Book Co., 1962)

[77] L. J. P. Ament, G. Khaliullin, and J. van den Brink. *Theory of resonant inelastic x-ray scattering in iridium oxide compounds: Probing spin-orbit-entangled ground states and excitations*. Phys. Rev. B **84**(020403(R)) (2011)

[78] Z. Nussinov and J. van den Brink. *Compass and Kitaev models — Theory and Physical Motivations*. arxiv:1303.5922 (2013)

[79] M. Biskup, L. Chayes, and Z. Nussinov. *Orbital orering in transition-metal compounds: I. the 120-degree model*. Comm. Math. Phys. **255**(253) (2005)

[80] J. Chaloupka, G. Jackeli, and G. Khaliullin. *Kitaev-Heisenberg Model on a Honeycomb Lattice: Possible Exotic Phases in Iridium Oxides A_2IrO_3*. Phys. Rev. Lett. **105**, 027204 (2012)

[81] Y. Singh et al. *Relevance of the Heisenberg-Kitaev model for the honeycomb lattice iridates A_22IrO_3*. Phys. Rev. Lett. **108**, 127203 (2012)

[82] S. K. Choi et al. *Spin Waves and Revised Crystal Structure of Honeycomb Iridate Na_2IrO_3*. Phys. Rev. Lett. **108**, 127204 (2012)

[83] F. Ye et al. *Direct evidence of a zigzag spin-chain structure in the honeycomb lattice: A neutron and x-ray diffraction investigation of single-crystal Na_2IrO_3*. Phys. Rev. B **85**(180403) (2012)

[84] H. Gretarsson et al. *Magnetic excitation spectrum of Na_2IrO_3 probed with resonant inelastic x-ray scattering*. Phys. Rev. B **87**(220407) (2013)

[85] I. I. Mazin et al. *Na_2IrO_3 as a Molecular Orbital Crystal*. Phys. Rev. Lett. **109**, 197201 (2012)

[86] K. Foyevtsova et al. *Ab initio analysis of the tight-binding parameters and magnetic interactions in Na_2IrO_3*. Phys. Rev. B **88**(035107) (2013)

[87] I. I. Mazin et al. *Origin of the insulating state in honeycomb iridates and rhodates*. Phys. Rev. B **88**(035115) (2013)

[88] C. H. Sohn et al. *Mixing between $J_{\text{eff}} = \frac{1}{2}$ and $\frac{3}{2}$ orbitals in Na_2IrO_3: A spectroscopic and density functional calculation study*. Phys. Rev. B **88**(085125) (2013)

[89] A. Shitade et al. *Quantum Spin Hall Effect in a Transition Metal Oxide Na_2IrO_3*. Phys. Rev. Lett. **102**, 256403 (2009)

[90] H.-C. Jiang et al. *Possible proximity of the Mott insulating iridate Na_2IrO_3 to a topological phase: Phase diagram of the Heisenberg-Kitaev model in a magnetic field*. Phys. Rev. B **83**(245104) (2011)

[91] J. Reuther, R. Thomale, and S. Trebst. *Finite-temperature phase diagram of the Heisenberg-Kitaev model*. Phys. Rev. B **84**(100406(R)) (2011)

[92] C. C. Price and N. B. Perkins. *Critical Properties of the Kitaev-Heisenberg Model*. Phys. Rev. Lett. **109**, 187201 (2012)

[93] S. Bhattacharjee, S.-S. Lee, and Y. B. Kim. *Spin–orbital locking, emergent pseudo-spin and magnetic order in honeycomb lattice iridates*. New J. Phys. **14**(073015) (2012)

[94] J. Chaloupka, G. Jackeli, and G. Khaliullin. *On the Origin of Zigzag Magnetic Order in Iridium Oxide Na2IrO3*. Phys. Rev. Lett. **110**, 097204 (2013)

[95] C. Price and N. B. Perkins. *Finite-temperature phase diagram of the classical Kitaev-Heisenberg model*. Phys. Rev. B **88**(024410) (2013)

[96] T. Dey et al. *Spin-liquid behavior in $J_{eff} = 1/2$ triangular lattice compound $Ba_3IrTi_2O_9$*. Phys. Rev. B **86**(140405(R)) (2012)

[97] R. C. Byrne and C. W. Moeller. *Magnetic interactions of ruthenium, rhodium, and iridium in the hexagonal barium titanate structure*. J. Solid State Chem. **2**(228) (1970)

[98] T. Sakamoto, Y. Doi, and Y. Hinatsu. *Crystal structures and magnetic properties of 6H-perovskite-type oxides $Ba_3MIr_2O_9$ (M =Mg, Ca, Sc, Ti, Zn, Sr, Zr, Cd and In)*. J. Solid State Chem. **179**(2595) (2006)

[99] G. Khaliullin. *Order from disorder: Quantum spin gap in magnon spectra of $LaTiO_3$*. Phys. Rev. B **64**(212405) (2001)

[100] P. Anderson. *Resonating valence bonds: A new kind of insulator?* Mater. Res. Bull. **8**(153) (1973)

[101] P. Fazekas and P. Anderson. *On the ground state properties of the anisotropic triangular antiferromagnet*. Philos. Mag. **30**(423) (1974)

[102] S. Miyake. *Spin-Wave Results for the Staggered Magnetization of Triangular Heisenberg Antiferromagnet*. J. Phys. Soc. Jpn. **61**, 983–988 (1992)

[103] N. Read and S. Sachdev. *Large-N expansion for frustrated quantum antiferromagnets*. Phys. Rev. Lett. **66**(13), 1773 (1991)

[104] S. Sachdev. *Kagomé- and triangular-lattice Heisenberg antiferromagnets: Ordering from quantum fluctuations and quantum-disordered ground states with unconfined bosonic spinons*. Phys. Rev. B **45**(21) (1992)

[105] B. Bernu, C. Lhuillier, and L. Pierre. *Signature of Néel order in exact spectra of quantum antiferromagnets on finite lattices*. Phys. Rev. Lett. **69**, 2590 (1992)

[106] B. Bernu, P. Lecheminant, C. Lhuillier, and L. Pierre. *Exact spectra, spin susceptibilities, and order parameter of the quantum Heisenberg antiferromagnet on the triangular lattice*. Phys. Rev. B **50**(10048) (1994)

[107] N. Elstner, R. R. P. Singh, and A. P. Young. *Finite temperature properties of the spin-1/2 Heisenberg antiferromagnet on the triangular lattice*. Phys. Rev. Lett. **71**, 1629 (1993)

[108] H. Kawamura and S. Miyashita. *Phase Transition of the Two-Dimensional Heisenberg Antiferromagnet on the Triangular Lattice*. J. Phys. Soc. Jpn. **53**, 4138–4154 (1984)

[109] N. Mermin. *The topological theory of defects in ordered media*. Rev. Mod. Phys. **51** (1979)

[110] N. W. Ashcroft and N. D. Mermin. *Solid State Physics* (Thomson Learning, 1976)

[111] G. Khaliullin and S. Okamoto. *Quantum Behavior of Orbitals in Ferromagnetic Titanates: Novel Orderings and Excitations*. Phys. Rev. Lett. **89**, 167201 (2002)

[112] G. Khaliullin. *Orbital Order and Fluctuations in Mott Insulators*. Prog. Theor. Phys. Supplement **160**, 155–202 (2005)

[113] J. Reuther, R. Thomale, and S. Rachel. *Magnetic ordering phenomena of interacting quantum spin Hall models*. Phys. Rev. B **86**(155127) (2012)

[114] T. P. Eggarter. *Triangular antiferromagnetic Ising model*. Phys. Rev. B **12**(1933) (1975)

[115] E. R. Davidson. *The iterative calculation of a few of the lowest eigenvalues and corresponding eigenvectors of large real-symmetric matrices*. J. Comp. Phys. **17**, 87–94 (1975)

[116] J. Luttinger and L. Tisza. *Theory of dipole interactions in crystals*. Phys. Rev. **70**(954) (1946)

[117] J. Luttinger. *A note on the ground state in antiferromagnetics*. Phys. Rev. **81**(1015) (1951)

[118] E. Sela, H.-C. Jian, M. H. Gerlach, and S. Trebst. *Order-by-disorder and spin-orbital liquids in a distorted Heisenberg-Kitaev model*. Phys. Rev. B **90**(035113) (2014)

[119] F. Mezei and G. Grüner. *Theory of Anomalous Charge Oscillation around Resonant Scattering Impurities*. Rev. Rev. Lett. **29**, 1465 (1979)

[120] G. Grüner and F. Zawadowski. *Magnetic impurities in non-magnetic metals*. Rep. Prog. Phys. **1497**(37) (1974)

[121] G. Grüner and C. Hargitai. *Temperature Dependence of the Charge Oscillation Around Nearly Magnetic Impurities*. Phys. Rev. Lett. **772**(26) (1972)

[122] V. Z. Šokčević and B. Horvatić. *Charge-density oscillations in intermediate-valence and Kondo systems*. Phys. Rev. B **39**(603) (1989)

[123] P. Coleman. *Local moment physics in heavy electron systems*. In F. Mancini, editor, *Lectures on the Physics of Highly Correlated Electron Systems VI*, pp. 79–160 (American Institute of Physics, New York, 2002)

[124] I. Affleck. *The Kondo screening cloud: What It Is And How to Observe it*. In A. Aharony and O. Entin-Wohlman, editors, *Perspectives of Mesoscopic Physics: Dedicated to Yoseph Imry's 70th Birthday* (World Scientific Publishing, 2010)

[125] A. K. Mitchell, M. Becker, and R. Bulla. *Real-space renormalization group flow in quantum impurity systems: Local moment formation and the Kondo screening cloud*. Phys. Rev. B **84**, 115120 (2011)

[126] H. Prüser et al. *Long-range Kondo signature of a single magnetic impurity*. Nature Physics **10**, 1038 (2011)

[127] V. Barzykin and I. Affleck. *Screening cloud in the k-channel Kondo model: Perturbative and large-k results*. Phys. Rev. B **57**, 432–448 (1998)

[128] H. Ishii. *Spin correlations in dilute magnetic alloys*. J. Low. Temp. **32**(3/4) (1978)

[129] J. E. Gubernatis, J. E. Hirsch, and D. J. Scalapino. *Spin and charge correlations around an Anderson magnetic impurity*. Phys. Rev. B **35**(16) (1987)

[130] L. Borda. *Kondo screening cloud in a one-dimensional wire: Numerical renormalization group study*. Phys. Rev. B **75**, 041307 (2007)

[131] A. Holzner, I. P. McCulloch, U. Schollwöck, J. v. Delft, and F. Heidrich-Meisner. *Kondo screening cloud in the single-impurity Anderson model: A density matrix renormalization group study*. Phys. Rev. B **80** (2009)

[132] E. N. Economou. *Green's Functions in Quantum Physics* (Springer-Verlag, 2006)

[133] A. Altland and B. Simons. *Condensed Matter Field Theory* (Cambridge University Press, 2006)

[134] H. Bruus and K. Flensberg. *Many-Body Quantum Theory in Condensed Matter Physics* (Oxford University Press, 2004)

[135] A. Zettl. *Making waves with electrons*. Nature **363**, 496–497 (1993)

[136] K. Kanisawa, M. J. Butcher, H. Yamaguchi, and Y. Hirayama. *Imaging of Friedel Oscillation Patterns of Two-Dimensionally Accumulated Electrons at Epitaxially Grown InAs(111)A Surfaces*. Phys. Rev. Lett. **86**, 3384 (2001)

[137] M. F. Crommie, C. P. Lutz, D. M. Eigler, and E. J. Heller. *Quantum corrals*. Physica D **83**(98) (1995)

[138] H. Knorr et al. *Long-range adsorbate interactions mediated by a two-dimensional electron gas*. Phys. Rev. B **65**(115420) (2002)

[139] R. K. M. Chow and H. U. Everts. *Numerical Study of the t Matrix in the Kondo Problem*. Phys. Rev. **188**(947) (1969)

[140] G. Metalidis and P. Bruno. *Green's function technique for studying electron flow in two-dimensional mesoscopic samples*. Phys. Rev. B **72**(235304) (2005)

[141] J. W. Mintmire, B. I. Dunlap, and C. T. White. *Are fullerene tubules metallic?* Phys. Rev. Lett. **68**, 631 (1992)

[142] H. Noriaki, S. Shin-Ichi, and A. Oshiyama. *New one-dimensional conductors: Graphitic microtubules*. Phys. Rev. Lett. **68**, 1579 (1992)

[143] S. Iijima and T. Ichihashi. *Single-shell carbon nanotubes of 1-nm diameter*. Nature **363**, 603–605 (1993)

[144] D. S. Bethune et al. *Cobalt-catalysed growth of carbon nanotubes with single-atomic-layer walls*. Nature **363**, 605–607 (1993)

[145] S. J. Tans et al. *Individual single-wall carbon nanotubes as quantum wires*. Nature **386**, 474–477 (1997)

[146] M. Bockrath et al. *Single-Electron Transport in Ropes of Carbon Nanotubes*. Science **275**(5308), 1922–1925 (1997)

[147] M. M. Shulaker et al. *Carbon nanotube computer*. Nature **501**, 526–530 (2013)

[148] A. Goodsell, T. Ristroph, J. A. Golovchenko, and L. Vestergaard Hau. *Field Ionization of Cold Atoms near the Wall of a Single Carbon Nanotube*. Phys. Rev. Lett. **104**, 133002 (2010)

[149] R. G. Ellis-Behnke et al. *Nano neuro knitting: Peptide nanofiber scaffold for brain repair and axon regeneration with functional return of vision*. Proc. Natl. Acad. Sci. USA **103**(13), 5054–5059 (2012)

[150] N. Hamada et al. *New One-Dimensional Conductors: Graphitic Microtubules*. Phys. Rev. Lett. **68**, 1579 (1992)

[151] J. Nygård, D. H. Cobden, and P. E. Lindelof. *Kondo physics in carbon nanotubes*. Nature **408**, 342–346 (2000)

[152] M. R. Galpin, F. W. Jyatilaka, D. E. Logan, and F. B. Anders. *Interplay between Kondo physics and spin-orbit coupling in carbon nanotube quantum dots*. Phys. Rev. B **81**(075437) (2010)

[153] V. Madhavan et al. *Tunneling into a Single Magnetic Atom: Spectroscopic Evidence of the Kondo Resonance*. Science **280**(567) (1998)

[154] H. C. Manoharan, C. P. Lutz, and D. M. Eigler. *Quantum mirages formed by coherent projection of electronic structure*. Nature **403**(512) (2000)

[155] Y.-S. Fu et al. *Manipulating the Kondo Resonance through Quantum Size Effects*. Phys. Rev. Lett. **99**, 256601 (2007)

[156] J. Park et al. *How to Directly Measure a Kondo Cloud's Length*. Phys. Rev. Lett. **110**, 246603 (2013)

[157] A. Losev. *A convolution technique for the calculation of local densities of states*. J. Phys.: Cond. Matt. **11**(7501) (1999)

[158] A. Losev. *The convolution method for calculations of local densities of states*. J. Phys.: Cond. Matt. **15**(1007) (2003)

[159] T. Morita. *Useful Procedure for Computing the Lattice Green's Function-Square Tetragonal, and bcc Lattices*. J. Math. Phys. **12**(1744) (1971)

[160] M. Berciu. *On computing the square lattice Green's function without any integrations*. J. Phys. A: Math. Theor. **42**(39), 395207 (2009)

[161] G. D. Mahan. *Friedel oscillations on a square lattice*. International Journal of Modern Physics B **9**(11), 1327–1341 (1995)

[162] P. Hofmann et al. *Anisotropic Two-Dimensional Friedel Oscillations*. Phys. Rev. Lett. **79**, 265 (1997)

[163] A. Weismann et al. *Seeing the Fermi Surface in Real Space by Nanoscale Electron Focusing*. Science **323**(5918) (2009)

[164] E. C. Andrade, E. Miranda, and V. Dobrosavljević. *Quantum Ripples in Strongly Correlated Metals*. Phys. Rev. Lett. **104**, 236401 (2010)

[165] M. Frigo and S. G. Johnson. *The Design and Implementation of FFTW3*. Proceedings of the IEEE **93**(2), 216–231. Special issue on "Program Generation, Optimization, and Platform Adaptation" (2005)

[166] A. K. Zhuravlev. *Negative Impurity Magnetic Susceptibility and Heat Capacity in a Kondo Model with Narrow Peaks in the Local Density of Electron States*. Phys. Met. Metallogr. (USSR) **108**(2), 107–115 (2009)

[167] P. Coleman, L. B. Ioffe, and A. Tsvelik. *Simple formulation of the two-channel Kondo model*. Phys. Rev. B **52**(6611) (1995)

[168] A. O. Gogolin. *On the theory of the Kondo effect in two-dimensional metals*. Z. Phys. B **92**(1), 55–59 (1993)

[169] A. K. Zhuravlev and V. Y. Irkhin. *Kondo effect in the presence of van Hove singularities: A numerical renormalization group study*. Phys. Rev. B **84**(245111) (2011)

[170] M. A. Nielsen and I. L. Chuang. *Quantum Computation and Quantum Information* (Cambridge University Press, 2000)

[171] L. DiCarlo et al. *Demonstration of two-qubit algorithms with a superconducting quantum processor*. Nature **460**, 240–244 (2009)

[172] N. Xu et al. *Quantum Factorization of 143 on a Dipolar-Coupling Nuclear Magnetic Resonance System*. Phys. Rev. Lett. **108**, 130501 (2012)

[173] J. Preskill. *Fault-tolerant quantum computation*. In H. Lo, T. Spiller, and S. Popescu, editors, *Introduction to Quantum Computation and Information* (World Scientific Publishing, 1998)

[174] A. Y. Kitaev. *Fault-tolerant quantum computation by anyons*. Ann. of Phys. **303**(1), 2–30 (2003)

[175] M. H. Freedman, M. Larsen, and Z. Wang. *A modular functor which is universal for quantum computation*. Comm. Math. Phys. **227**(3), 605–622 (2002)

[176] J. D. Sau, R. M. Lutchyn, S. Tewari, and S. Das Sarma. *Generic New Platform for Topological Quantum Computation Using Semiconductor Heterostructures*. Phys. Rev. Lett. **104**, 040502 (2010)

[177] J. Alicea. *Majorana fermions in a tunable semiconductor device*. Phys. Rev. B **81**, 125318 (2010)

[178] R. M. Lutchyn, J. D. Sau, and S. Das Sarma. *Majorana Fermions and a Topological Phase Transition in Semiconductor-Superconductor Heterostructures*. Phys. Rev. Lett. **105**, 077001 (2010)

[179] Y. Oreg, G. Refael, and F. von Oppen. *Helical Liquids and Majorana Bound States in Quantum Wires*. Phys. Rev. Lett. **105**, 177002 (2010)

[180] E. M. Stoudenmire, J. Alicea, O. A. Starykh, and M. P. A. Fisher. *Interaction effects in topological superconducting wires supporting Majorana fermions*. Phys. Rev. B **84**(014503) (2011)

[181] S. Nadj-Perge et al. *Observation of Majorana fermions in ferromagnetic atomic chains on a superconductor*. Science Express (2014)

[182] E. S. Reich. *A solid case for Majorana fermions*. Nature **483**(7388) (2012)

[183] A. Das, Y. Ronen, Y. Most, Y. Oreg, M. Heiblum, and H. Shtrikman. *Zero-bias peaks and splitting in an Al-InAs nanowire topological superconductor as a signature of Majorana fermions*. Nat Phys **8**(12), 887–895 (2012)

[184] A. D. K. Finck et al. *Anomalous Modulation of a Zero-Bias Peak in a Hybrid Nanowire-Superconductor Device*. Phys. Rev. Lett. **110**, 126406 (2013)

[185] H. O. H. Churchill et al. *Superconductor-nanowire devices from tunneling to the multichannel regime: Zero-bias oscillations and magnetoconductance crossover*. Phys. Rev. B **87**, 241401(R) (2013)

[186] J.-D. Pillet, P. Joyez, R. Žitko, and M. F. Goffman. *Tunneling spectroscopy of a single quantum dot coupled to a superconductor: From Kondo ridge to Andreev bound states*. Phys. Rev. B **88**, 045101 (2013)

[187] E. J. H. Lee et al. *Spin-resolved Andreev levels and parity crossings in hybrid superconductor-semiconductor nanostructures*. Nature Nanotechnology **9**(1), 79–84 (2014)

[188] D. Sticlet, C. Bena, and P. Simon. *Spin and Majorana Polarization in Topological Superconducting Wires*. Phys. Rev. Lett. **108**, 096802 (2012)

[189] M. Cheng, M. Becker, B. Bauer, and R. M. Lutchyn. *Interplay between Kondo and Majorana Interactions in Quantum Dots*. Phys. Rev. X **4**(031051) (2014)

[190] T. Giamarchi. *Quantum Physics in One Dimension* (Clarendon Press, 2004)

[191] J. M. Luttinger. *An exactly soluble model of a many-fermion system*. J. Math. Phys. **4**(1154) (1963)

[192] S.-I. Tomonaga. *Remarks on Bloch's Method of Sound waves applied to Many-Fermion Problems*. Prog. Theor. Phys. **5**(544) (1950)

[193] F. D. M. Haldane. *Luttinger liquid theory' of one-dimensional quantum fluids. I. Properties of the Luttinger model and their extension to the general 1D interacting spinless Fermi gas*. J. Phys. C: Solid State Phys. **14**, 2585 (1981)

[194] C. Kim et al. *Observation of Spin-Charge Separation in One-Dimensional $SrCuO_2$*. Phys. Rev. Lett. **77**, 4054 (1996)

[195] A. F. Andreev. *Thermal conductivity of the intermediate state of superconductors*. Sov. Phys. JETP **19**(1228) (1964)

[196] I. Affleck. *Conformal Field Theory Approach to the Kondo Effect*. Acta Phys. Polon. B **26**, 1869–1932 (1995)

[197] W. B. Thimm, J. Kroha, and J. von Delft. *Kondo Box: A Magnetic Impurity in an Ultrasmall Metallic Grain*. Phys. Rev. Lett. **82**, 2143 (1999)

Publications

M. Cheng, M. Becker, B. Bauer, and R. M. Lutchyn. "*Interplay between Kondo and Majorana interactions in quantum dots.*" Phys. Rev. X **4**, 031051 (2014)

A. K. Mitchell, M. Becker, and R. Bulla. "*Real-space renormalization group flow in quantum impurity systems: Local moment formation and the Kondo screening cloud.*" Phys. Rev. B **84**, 115120 (2011)

Submitted manuscript:

M. Becker, M. Hermanns, B. Bauer, M. Garst, and S. Trebst. "*Spin-orbit physics of $j = 1/2$ Mott insulators on the triangular lattice.*" `arXiv`:1409.6972. (2014)